Cation ordered and Anion-vacancy Ordered Perovskite Materials

A thesis submitted to the
Board of the Faculty of Physical Sciences
in partial fulfilment of the requirements
for the degree of Doctor of Philosophy

by

Kun Luo

New College

Michaelmas Term 2013

Cation Ordered and Anion-vacancy Ordered Perovskite Materials

Kun Luo, New College, University of Oxford

Submitted for the degree of Doctor of Philosophy, Michaelmas Term 2013

Abstract

The investigation in this thesis focuses on the synthesis of cation-ordered perovskite phases by introducing anion vacancies into the structure.

Complex cation-ordered phases Ba_2YMO_5 and $Ba_3YM_2O_{7.5}$ (M = Fe, Co) have been synthesized using ceramic or citrate gel methods under flowing argon. Close inspection reveals that the structures are constructed from $Y_2M_2O_{10}$ $_2$ basic units which consist of two YO_6 octahedra and two MO_4 tetrahedra in a rock-salt type arrangement. In the structure of Ba_2YMO_5 (M = Fe, Co), the neighbouring $Y_2M_2O_{10}$ $_2$ units are connected with an equivalent one in the *yz*-plane with YO_6 octahedra sharing an apex. In the structure of $Ba_3YM_2O_{7.5}$ (M = Fe, Co), the basic units are connected to each other by the M_2O_7 dimers via a chain of Y – O – M – O – M – O – Y bonds. Complex cation ordering can be achieved by carefully controlling the anion vacancies and selecting the cations with different ionic radii.

The anion vacancies present in Ba_2YMO_5 (M = Fe, Co) (space group $P2_1/n$) allow the intercalation of anions like O^{2-} and F^- into the lattice. The fluorination of Ba_2YCoO_5 leads to the formation of a new orthorhombic phase $Ba_2YCoO_5F_{0.42}$ (space group *Pbnm*) in which the inserted fluoride ions are distributed in a disordered manner. In contrast, the topochemical oxidation of Ba_2YFeO_5 leads to the formation of a new orthorhombic phase $Ba_2YFeO_{5.5}$ (space group $Pb2_1m$), in which Fe^{4+} centres are located in 4-coordinate tetrahedral sites and 5-coordinate pyramidal sites, respectively. The polar structure of $Ba_2YFeO_{5.5}$ is confirmed by the observation of second-harmonic generation activity and pyroelectric behaviour. $Ba_2YFeO_{5.5}$ also exhibits a combination of ferromagnetic and antiferromagnetic behaviours at low temperature.

$LaCa_2Fe_2GaO_8$ adopts a six-layer structure consisting of an OOT_LOOT_R stacking sequence of layers of $(Fe/Ga)O_6$ octahedra (O) and $(Fe/Ga)O_4$ tetrahedra (T), related to that of the four-layer brownmillerite structure (space group *Pbma*). The chains of tetrahedra in the structure of $LaCa_2Fe_2GaO_8$ exhibit a cooperative twisting distortion in which the twisting direction of the chains of tetrahedra alternates in adjacent tetrahedral layers.

$La_xSr_{2-x}CoGaO_{5+\delta}$ ($0.5 < x < 1$) adopts brownmillerite structures which consist of octahedral and tetrahedral layers with mixed valence of Co^{2+}/Co^{3+}. The members with x = 0.5, 0.6 and 0.7 adopt structures with *I2mb* space group symmetry, in which all the tetrahedra twist in the same direction. The members with x = 0.8, 0.9 and 1.0 adopt structures with *Imma* space group symmetry, in which the chains of the tetrahedra twist in a disordered manner. A change in the Co^{3+} spin state from high spin (HS) to low spin (LS) is observed as the La/Sr ratio increases. The change of the Co^{3+} spin state can be rationalized on the basis of internal chemical pressure.

Declaration

The work described in this thesis was carried out at the Inorganic Chemistry Laboratory at the University of Oxford between October 2010 and October 2013 under the supervision of Dr. M. A. Hayward. All the work is my own, except where I have either acknowledged help from a named person or given a reference to a published source, and has not been submitted by the author for any other degree at this, or any other university.

Kun LUO

October 2013

Dedicated to My Parents

Acknowledgements

I would like to thank my supervisor, Dr. Michael A. Hayward for his expert guidance, support and encouragement during the course of my D.Phil. I have learnt a lot from him about the solid state chemistry and academic career, which is helpful for my future career life. There are also many people I would like to express my gratitude to. Firstly, Prof. P. Shiv Halasyamani and Thao T. Tran at Houston University, USA conducted the second-harmonic generation measurements, which help confirm the centrosymmetric or noncentrosymmetric structures. Secondly, Prof. Paolo G. Radaelli and Dr. Roger D. Johnson collected valuable temperature-dependant pyrocurrent and dielectric data, which help understand the polar behaviour of $Ba_2YFeO_{5.5}$ phase in Chapter 5. Finally, I would like to thank the beam scientists at ISIS, Diamond and ILL for collecting the neutron powder diffraction data, especially Dr. Ron Smith and Dr. Emma Suard.

I have enjoyed the time in Hayward group and would like to thank all the D.Phils who make my time at Oxford so enjoyable. In particular, I'd like to thank Ed for answering endless questions from me at the start of my studies. Fabio showed me how to use all the instruments in the lab. I would also like to thank Midori for spending overnight with me on collecting neutron diffraction data at ISIS.

I would also like to thank all the Part IIs in the group. I enjoyed the Thursday cakes so much. The Catalyst Football Tournaments every year offer me an opportunity to enjoy the football with all the members in Hayward and SJC groups.

Contents

Chapter 1 Introduction

1.1 The perovskite structure

Complex transition metal oxides based on perovskite structures are an important class of materials due to the wide variety of physical and electronic properties they exhibit. The perovskite materials adopt a general stiochoimetric formula ABO_3, where the large A-site cations are located in 12-coordinate sites and the smaller B-site cations are in 6-coordinate octahedral sites, as shown in Figure 1.1a. The relationship between < A - O > and < B - O > (the A - O and B - O bond lengths) in perovskite structures can be described using the tolerance factor:

$$t = \frac{< A - O >}{\sqrt{2} < B - O >}$$

The perfect perovskite phase, where t = 1, adopts a cubic structure (Figure 1.1a). The size mismatches between cations in perovskite structures can cause an internal strain which leads to the cooperative tilting or twisting of BO_6 octahedra. The introduction of large A-site cations or the small B-site cations (t > 1) leads to a hexagonal structure (Figure 1.1b). When t < 1, the structures undergo cooperative distortions (Figure 1.1c).

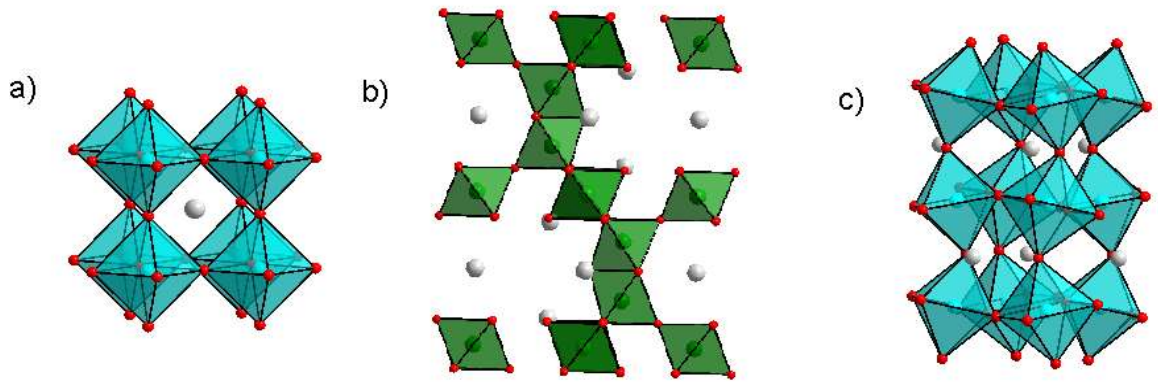

Figure 1.1 Structures of a) $SrTiO_3$[1]; b) $BaCrO_3$[2]; c) $CaTiO_3$[3].

The materials with perovskite structures are a class of interesting materials because the angle of metal – oxygen – metal bonds in perovskite structures are close to 180^{o}. This class of materials exhibit a wide range of interesting properties. For example, $SrMoO_3$ is a highly metallic conductor[4] and $SrRuO_3$ exhibit ferromagnetic behaviour.[5] $La_xCa_{1-x}MnO_3$ exhibits a magnetoresistive behaviour.[6] All these interesting physical behaviours motivate chemists and materials scientists to develop the investigations on materials with perovskite structures.

1.2 B-site cation ordering in perovskite structures

In addition to the many interesting physical properties mentioned above, perovskite structures can tolerate a broad range of chemical substitutions because perovskite structures can undergo a cooperative distortion when cations with different sizes are introduced into the lattice. The flexible and diverse stoichiometry of perovskite phases allows the materials with perovskite structures to accommodate a variety of different metal cations within the structural lattices. Partial substitution of metal cations in A- and/or B- sites offers the possibility of forming cation-ordered extended perovskite frameworks such as $AA'B_2O_6$ and $A_2BB'O_6$.[7] More interestingly, cation-ordered materials can exhibit physical behaviours that are significantly different from those of the disordered analogues. For example, Sr_2FeMoO_6 adopts a rock-salt type cation-ordered structure (Figure 1.2a) and exhibits a magnetoresistive behaviour, which is not observed in the disordered analogue $SrFe_{0.5}Mo_{0.5}O_3$.[8]

The common cation ordering patterns in perovskite structures are the rock-salt, columnar and layered patterns[7] as shown in Figure 1.2. The normal driving force for B-site cation ordering is the retention of local charge neutrality and lowering the local lattice strain when the pairs of cations with different charges and/or sizes are introduced into the lattice. For

example, the rock-salt type structure (Figure 1.2a) is one of the most common cation-ordered structures in double perovskites, because the 3D cation ordering can minimize the local lattice strain.

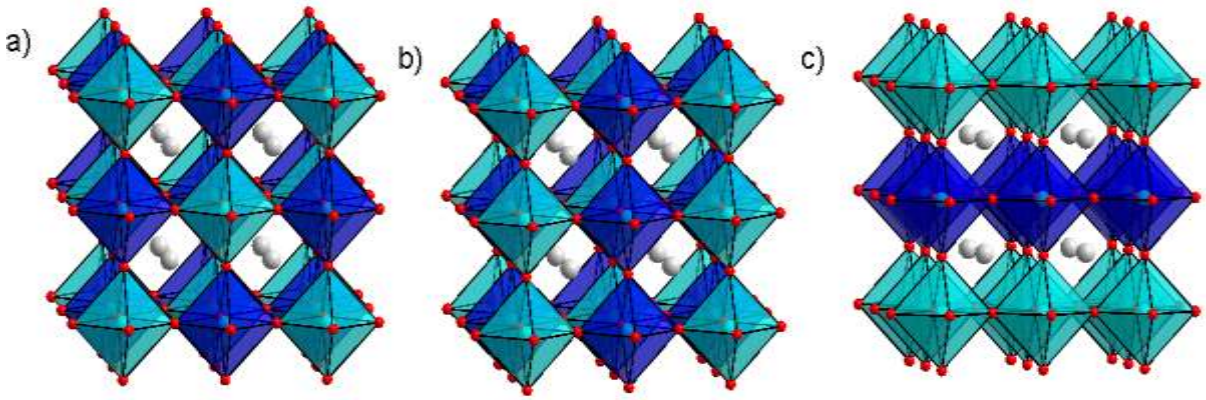

Figure 1.2 B-site cation ordering schemes in perovskite structures a) Rock-salt; b) Columar; c) Layered.[3]

The preparation of cation-ordered phases is very challenging. High-temperature synthesis conditions employed to prepare metal oxides lead to disordered products, which would be attributed to the domination of entropy in the reactions ($\Delta G = \Delta H - T\Delta S$). Thus possible cation-ordered structures are generally not preferred. A strong enthalpic motivation is necessary to form ordered phases, which can be provided by a large size difference between two cations because minimum local lattice strain can be achieved in a cation-ordered structure. For example, the size difference between Y^{3+} (0.90 Å) and Ta^{5+} (0.64 Å) cations in Sr_2YTaO_6 yields a rock-salt type cation-ordered arrangement[9] (Figure 1.2a). Cation ordering can also be achieved by involving pairs of cations with a large charge difference because cation-ordered structures can neutralize the local charge difference. For example, Ca_2CoNbO_6 adopts a disordered arrangement of Co^{3+} and Nb^{5+} cations in the lattice. Partial substitution of Ca^{2+} with La^{3+} cations in the A sites yields the formation of a new $LaCaCoNbO_6$ phase in which the increased charge difference between Co^{2+} and Nb^{5+} cations leads to cation order.[10]

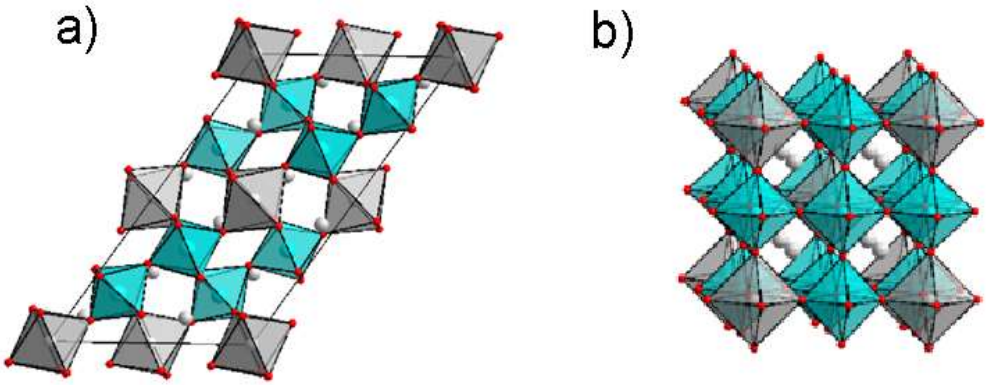

Figure 1.3 Structures of a) $Sr_3CaRu_2O_9$; c) $Ba_4NaSb_3O_{12}$.

By changing the ratio of B-site cations, more complicated cation ordering patterns can be achieved. For example, a 1:2 B-site cation ordered pattern has been reported in a perovskite ruthenate.[11,12] As shown in Figure 1.3a, an ordered arrangement of apex-linked RuO_6 octahedra and CaO_6 octahedra is observed in a cubic network of $Sr_3CaRu_2O_9$.[11] The 1:3 B-site-ordered patterns have also been reported. The size and charge differences between Na^+ and Sb^{5+} cations cause complicated cation ordering in the lattice of $Ba_4NaSb_3O_{12}$ in which each NaO_6 octahedron is surrounded by six SbO_6 octahedra[13] as shown in Figure 1.3b.

Complex cation ordering is also observed in some hexagonal lattices. The charge difference between Cu^{2+}/Co^{2+} and Sb^{5+} cations leads to the formation of cation-ordered $Ba_3MSb_2O_9$ (M = Cu, Co) phases, in which the non-magnetic Sb^{5+} cations are located in face-sharing octahedral sites and the paramagnetic cations Co^{2+}/Cu^{2+} are in apex-linked octahedral sites (Figure 1.4a).[14-16] Comparatively, $Ba_3CoNb_2O_9$ adopts a different cation ordered structure (Figure 1.4b) in which the d^0 Nb^{5+} cations are located in the apex-linked octahedral sites[17]. The absence of M – O – M interactions and the triangular lattice of paramagnetic layers in these two kinds of cation-ordered structures can lead to magnetic frustration.

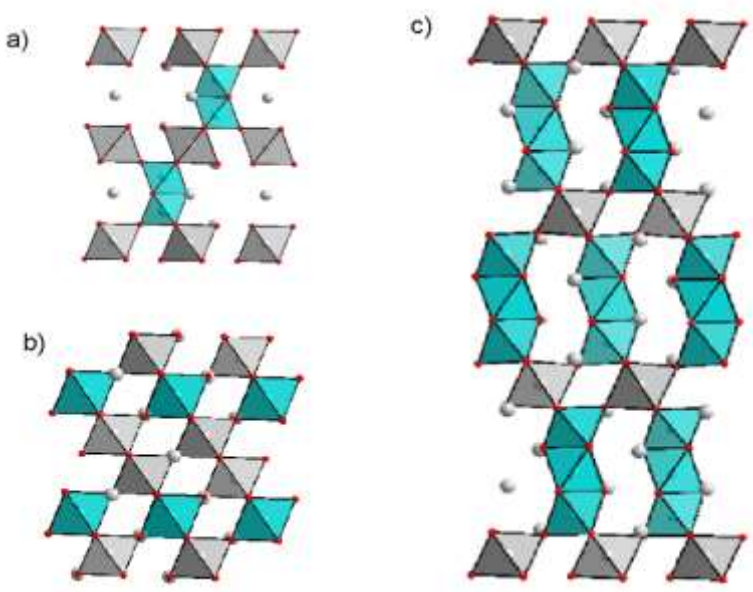

Figure 1.4 Structures of a) $Ba_3CoSb_2O_9$; b) $Ba_3CoNb_2O_9$; c) $Ba_4LnRu_3O_{12}$.

The 1:3 B-site $Ba_4LnRu_3O_{12}$ (Ln = lanthanides) phases adopt a complicated structure consisting of Ru_3O_{12} trimers and LnO_6 octahedra (Figure 1.4c).[18] Although some cation-ordered structures are achieved by carefully selecting the cations with different sizes and/or charges, the requirements for cation-ordered structures (size and/or charge of cations) seriously limit the diversity of cations that can be ordered and the variety of cation-ordered patterns.

1.3 Anion-deficient cation-ordered perovskite structures

The flexible stoichiometry of perovskite structures not only allows the substitution of different metal cations into structural lattices, but can also tolerate a broad range of oxygen nonstoichiometry to form ABO_{3-x} phases. The incorporation of non-octahedral coordination sites, such as tetrahedral and pyramidal sites, into structural lattices due to the presence of anion vacancies motivates an alternative strategy to order cations in perovskite structures. Some transition metal cations prefer a particular coordination number and/or geometry due to the size and electronic configuration of the cation. For example, Mn^{3+} prefers to be

located into octahedral sites as it undergoes a Jahn-Teller distortion due to a d^4 electronic configuration. Fe^{3+} has a d^5 electronic configuration, indicating no preference for specific coordination environment. Thus it can be seen in Figure 1.6a that Ca_2MnFeO_5 adopts a brownmillerite structure consisting of MnO_6 octahedral layers and FeO_4 tetrahedral layers.[19]

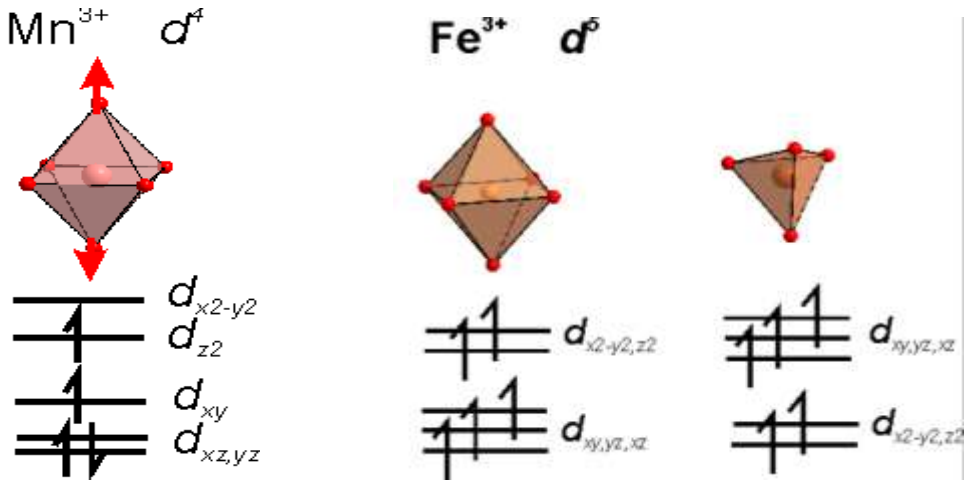

Figure 1.5 Electron configurations of Mn^{3+} and Fe^{3+} cations

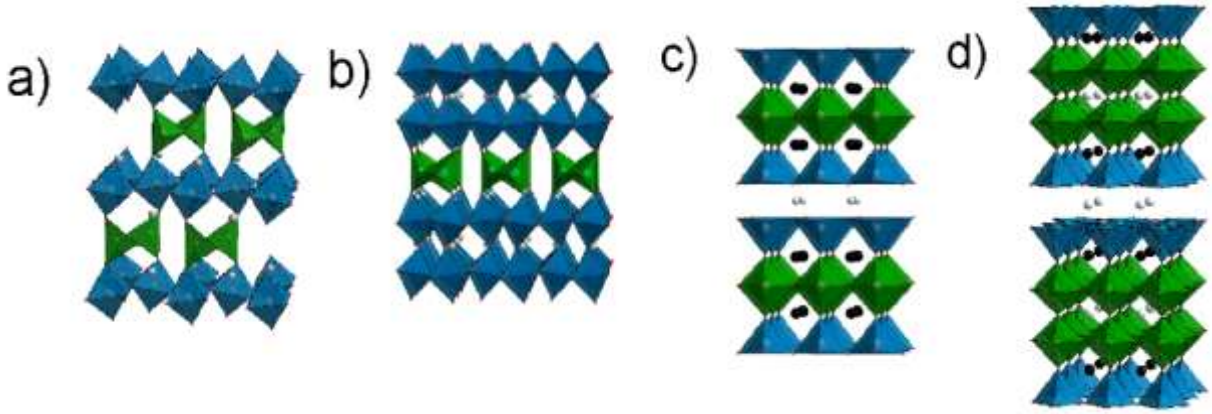

Figure 1.6 Structures of a) Ca_2MnFeO_5; b) $Ca_{2.5}Sr_{0.5}GaMn_2O_8$; c) $LaBa_2NbCu_2O_8$; d) $La_2Ba_2Ti_2Cu_2O_{11}$

By adjusting the ratio of B-site cations, a 1:2 B-site-ordered $Ca_{2.5}Sr_{0.5}GaMn_2O_8$ phase was synthesized, in which Mn^{3+} and Mn^{4+} cations are located in the octahedral sites and Ga^{3+} cations are located in tetrahedral sites,[20] as shown in Figure 1.6b. Transition metal cations with a d^0 electron configuration, such as Ti^{4+} and Nb^{5+} cations, prefer six-coordinate octahedral sites. The combination of d^0 and d^n cations provides another opportunity to

synthesize cation-ordered phases when anion vacancies are introduced into structural lattices. Thus $LaBa_2NbCu_2O_8$[21] and $La_2Ba_2Ti_2Cu_2O_{11}$[22] adopt cation-ordered layered structures in which Nb^{5+} and Ti^{4+} cations occupy octahedral sites and Cu^{2+} cations occupy 5-coordinate pyramidal sites, as shown in Figure 1.6c,d.

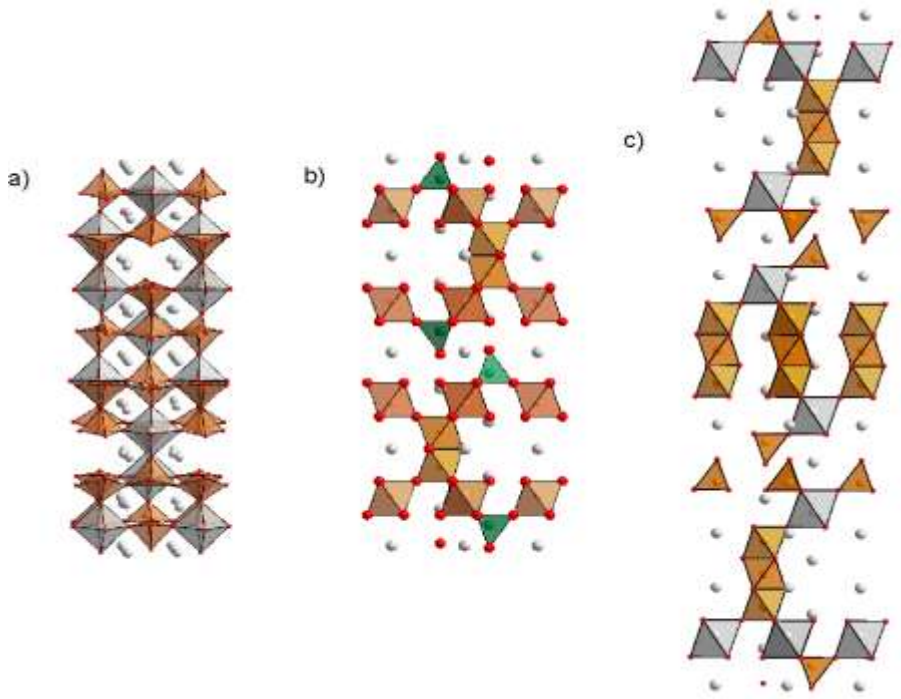

Figure 1.7 Structures of a) $Ba_4CaFe_3O_{9.5}$; b) $Ba_6Mn_4Cr_2O_{17}$; c) $Ba_7Ca_2Mn_5O_{20}$.

Even more complex cation ordering patterns have been reported in perovskite structures with a non-stoichiometric oxygen content. For example, $Ba_4CaFe_3O_{9.5}$ has been reported to adopt a complex structure in which Ca^{2+} and Fe^{3+} cations are ordered in the B-sites of the cubic perovskite lattice, as shown in Figure 1.7a.[23] The anion-deficient perovskite phase contains octahedral Ca^{2+} cations and 4- and 5-coordinate Fe^{3+} cations in a complex arrangement driven by the need to effectively order both cations and anion vacancies. The complex cation ordering in $Ba_4CaFe_3O_{9.5}$ breaks the inversion symmetry of the host lattice, allowing this material to exhibit second-harmonic generation activity. In addition, the

presence of the paramagnetic Fe^{3+} cation in the noncentrosymmetric lattice makes $Ba_4CaFe_3O_{9.5}$ a potential multiferroic material[23].

Complex cation ordering has also been observed in some anion-deficient hexagonal lattices. As shown in Figure 1.7c, $Ba_7Ca_2Mn_5O_{20}$ adopts a layered structure consisting of CaO_6 octahedra (grey), MnO_6 octahedra (orange) and MnO_4 tetrahedra (orange).[24] The presence of anion vacancies leads to the disconnection of the tetrahedral MnO_4 layers. Based on the observation that small Cr^{6+} cations favour tetrahedral sites, chemical substitutions have been carried out on the basis of the layered hexagonal lattices to give $(Ba/Sr)_{5+n}Mn_{3+n}Cr_2O_{3n+14}$ (n = 1 and 2) phases.[25,26] The n = 1 member adopts a 12-layered structure, as shown in Figure 1.7b, in which Cr^{6+} cations occupy the tetrahedral sites. The charge ordering of Mn^{2+} and Mn^{4+} in octahedral sites can be observed in the lattice. The n = 2 member adopts a 14-layered structure in which the majority of Cr^{6+} cations occupy the tetrahedral sites and the Mn^{2+}/Mn^{4+} charge ordering is also observed. The cation-ordered arrangement and Mn^{2+}/Mn^{4+} charge ordering in these two lattices lead to a tuneable magnetic behaviour. As shown in Figure 1.8, the n = 1 member adopts an antiferromagnetic order while the n = 2 member exhibits ferrimagnetic behaviour.

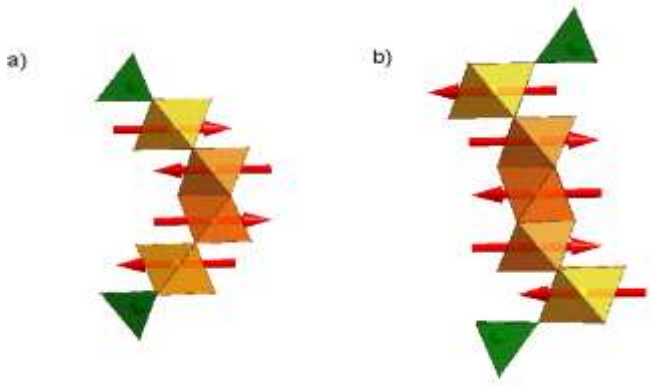

Figure 1.8 Magnetic structures of a) $(Ba_{0.5}Sr_{0.5})_6Mn_4Cr_2O_{17}$; b) $Ba_7Mn_5Cr_2O_{20}$.

It is thus believed that complex cation ordering patterns can be achieved by introducing anion vacancies and cations with a preference for a specific coordination number and

geometries, which provides an opportunity to synthesize more complicated cation ordering patterns.

1.4 Brownmillerite structures

The brownmillerite structure ($A_2B_2O_5$) is one of the most common anion-vacancy ordered structures. It consists of a stacking sequence – BO_2 – AO – BO – AO – with alternating layers of apex-linked BO_6 octahedra and BO_4 tetrahedra, as shown in Figure 1.9a. The chains of BO_4 tetrahedra within brownmillerite structures undergo a cooperative twisting distortion, which can occur in either a clockwise or anti-clockwise sense, to yield 'left' or 'right' handed chains, as shown in Figure 1.9b. The different arrangements of the chains of tetrahedra with different twisting directions leads to the formation of three different structural variants (*I2mb*, *Pnma* and *Imma*)[27], as shown in Figure 1.9a.

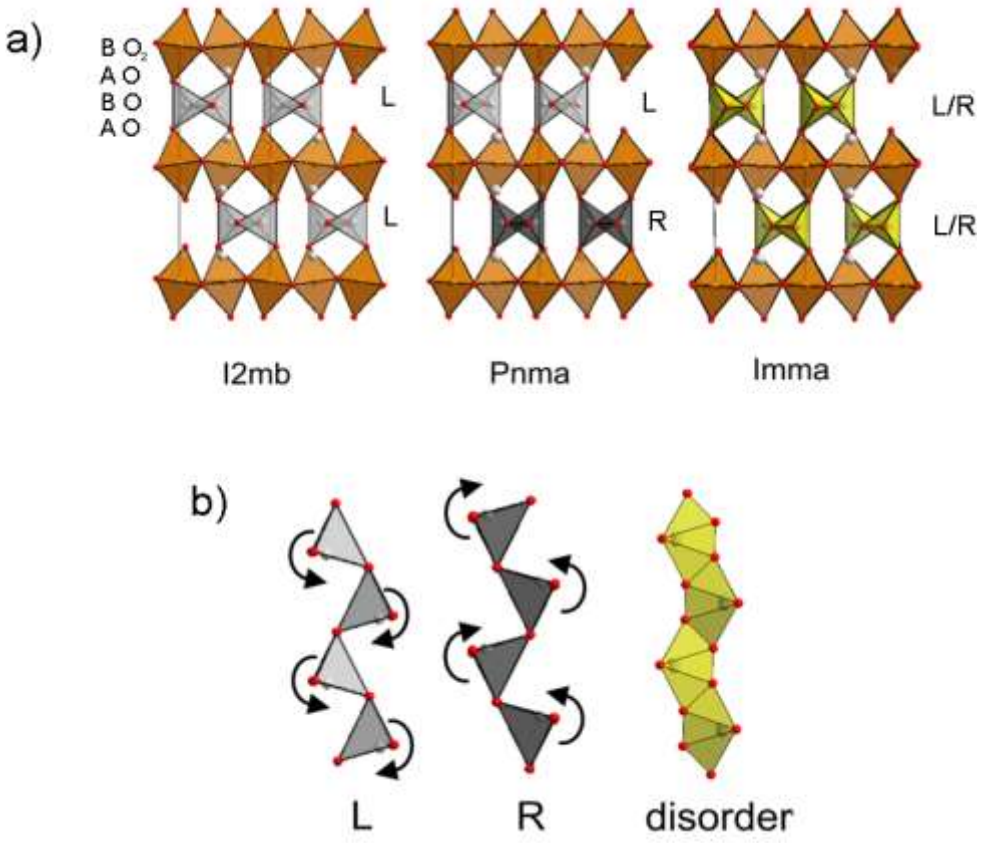

Figure 1.9 (a) The three common variants of the $A_2B_2O_5$ brownmillerite structure. (b) The cooperatively twisted chains of corner-linked BO_4 tetrahedral in the brownmillerite.

The arrangement of the chains of tetrahedra or the structural variant adopted by a phase is determined by the following factors.

Dipole cancellation. The particular brownmillerite structural variant adopted by a phase can be rationalized by observing that the cooperative twisting distortion induces a dipole moment into each chain of corner-linked tetrahedra (Figure 1.10) and that the specific structural variant adopted by a phase is driven by the need to effectively cancel the dipole moments and is a function of dipole size (degree of tetrahedral chain twisting, φ) and tetrahedral layer separation (l) (Figure 1.11) [27-29]

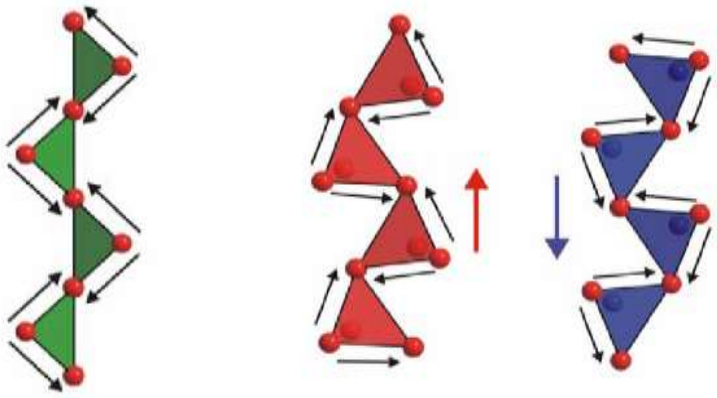

Figure 1.10 The dipole moments are shown for an undistorted tetrahedral chain (left) and the two possible distorted tetrahedral chains (right). The dipole moments result in the net dipole moments in the tetrahedral layer.

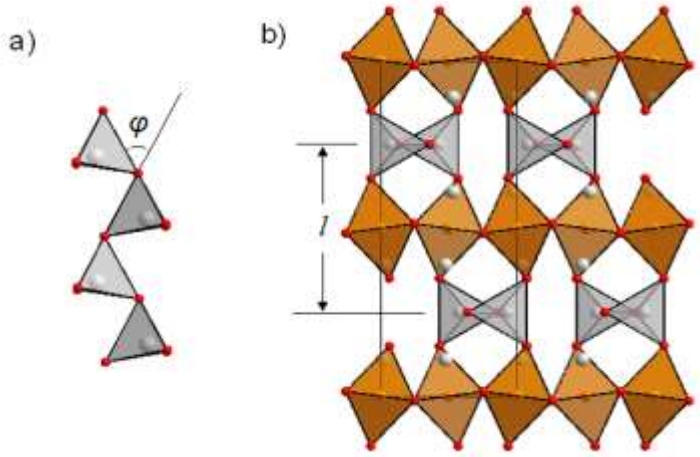

Figure 1.11 Tetrahedral chain twist angle, φ(a), tetrahedral layer separation, l (b) of brownmillerite structures.

For example, the phases with a small distortion in the chains of tetrahedra adopt a polar *I2mb* structure in which dipole moment in each layer is compensated by the formation of small polar domains, which means that all the tetrahedra twist in the same direction. As the distortion of tetrahedra increases (e.g. the twisting angle of tetrahedra increases), the formation of polar micro-domains cannot effectively cancel the dipole moment in the lattice. Thus a new arrangement of the chains of tetrahedra is adopted which inverts the twisting direction of the tetrahedra in adjacent layers, leading to the formation of the *Pnma* variant. Alternatively, when the separation between tetrahedral layers increases, a further structural change is observed. The twisting of tetrahedra in each layer adopts a disordered arrangement, to yield an *Imma* variant.

Disruption by additional oxide ions. The brownmillerite structural variant adopted by a phase can also be influenced by the stoichiometry of a particular phase. The presence of anion vacancies in the brownmillerite lattice allows the insertion of oxide ions into the lattice, yielding a composition of $A_2B_2O_{5+\delta}$. The additional oxide ions are located in the tetrahedral layers, converting 4-coordinate tetrahedra into 5-coordinate pyramids and even 6-coordinate octahedra, which lead to a disruption of the arrangement of the tetrahedral chains. For example, $Ba_2In_2O_5$ adopts an *I2mb*-type brownmillerite structure, in which all the tetrahedra twist in the same direction.[30] Partial substitution of In^{3+} with Mn^{5+} cations in the 'tetrahedral' sites leads to the formation of $Ba_2In_{2-x}Mn_xO_{5+x}$, in which the additional oxide ions in the tetrahedral layers disrupt the arrangement of the chains of tetrahedra, leading to an *Imma*-type brownmillerite structure.[31] Even a tetragonal structure is observed when a large of amount of additional oxide ions is present in the brownmillerite structure[32] (e.g. $Sr_2Al_{0.78}Mn_{1.22}O_{5.2}$, *P4/mmm*), as shown in Figure 1.12.

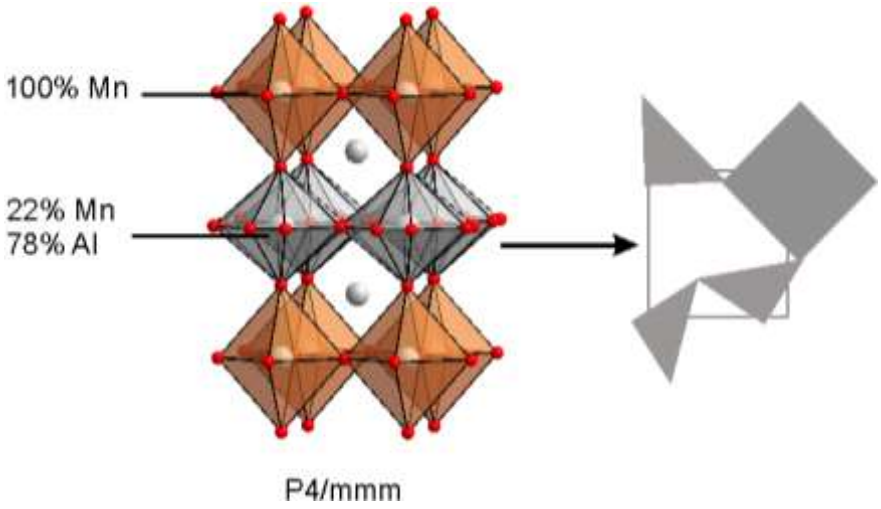

Figure 1.12 Structures of $Sr_2Al_{0.78}Mn_{1.22}O_{5.2}$.

Electronic factors. Some other factors can also be considered to influence the twisting manners of the chains of tetrahedra in the brownmillerite lattice. As discussed above, the brownmillerite structure with a large distortion in the chains of tetrahedra adopts a *Pnma* type structural variant, in which the chains of tetrahedra twist oppositely in the adjacent layers. When the separation of tetrahedral layers is even larger, the complicated arrangement of tetrahedral chains is observed. For example, *Pcmb*-type brownmillerite structure (Figure 1.13a) is observed in $La_xA_{1-x}MnO_{2.5}$ (A = Ba, Sr and Ca), in which the chains of tetrahedra with different twisting directions are arranged alternatively in the same tetrahedral layer.[27,33]

It should be noted that $La_xA_{1-x}MnO_{2.5}$ (A = Ba, Sr and Ca) series have a mixed valence of Mn^{2+}/Mn^{3+}. The Jahn-Teller active Mn^{3+} cations could lead to an internal lattice strain along *y*-axis (Figure 1.13a). The size differences between Mn^{2+} (CN = 6 HS 0.83 Å) and Mn^{3+} (CN = 6 HS 0.645 Å) could lead to an internal lattice strain in *ac*-plane (Figure 1.13b). The internal strain can be relieved by forming a *C2/c*-type brownmillerite variant (Figure 1.13a), which has a Mn^{2+}/Mn^{3+} ordered arrangement in the octahedral layers. Thus local Jahn-Teller

distortion and charge ordering can also influence the structural variant adopted by a brownmillerite phase.

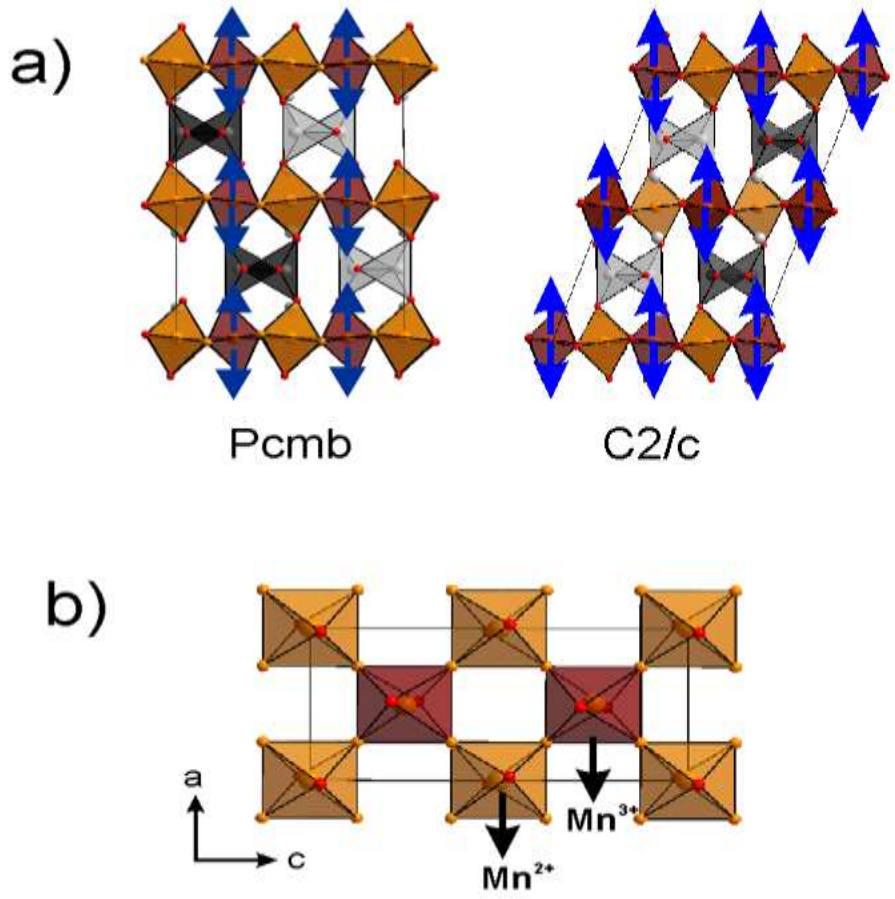

Figure 1.13 Jahn-Teller distortion (a) and charge ordering (b) in *Pcmb* and *C2/c* brownmillerite variants.

1.5 Low-temperature topochemical oxidation

The anion vacancies present in the lattice of perovskite structures can lead to complex cation ordering. In addition, the presence of anion vacancies allows modifications to cation-ordered phases to be made, such as the insertion of oxide ions or fluoride ions into the lattice, thus manipulating the oxidation states of some transition metals in the host lattice. The physical and chemical properties are usually related to the electron configurations of the transition metals and the band gap of the compounds, which are directly influenced by the oxidation states of transition metals. Low-temperature topochemical oxidation allows the tuning of the oxidation

state of transition metals in complex oxides, whilst maintaining the cation arrangement within the host lattice. For example, $BaFeO_{2.5}$ has been reported to be oxidized under an ozone atmosphere to form a cubic $BaFeO_3$ phase, which exhibits a ferromagnetic behaviour.[34] Another strategy to topochemically oxidize the materials is to utilize a fluorination reaction. For example, the Ruddlesden-Popper phase $Sr_3Ru_2O_7$ can react with CuF_2 to form a new layered $Sr_3Ru_2O_7F_2$ phase, which exhibits a canted antiferromagnetic behaviour.[35]

1.6 Noncentrosymmetric structures

The transition metal oxides with noncentrosymmetric (NCS) structures can exhibit interesting physical behaviours, such as ferrolectricity, piezoelectricity and second-harmonic generation (SHG) activity[36-38]. In order to prepare NCS materials, it is important to break the inversion symmetry of a structural lattice and form an acentric structure. However, the preparation of NCS compounds is rather challenging. Transition metal centres prefer to be located in a centric coordination environment (e.g. octahedra) to cancel any local directional polarization.

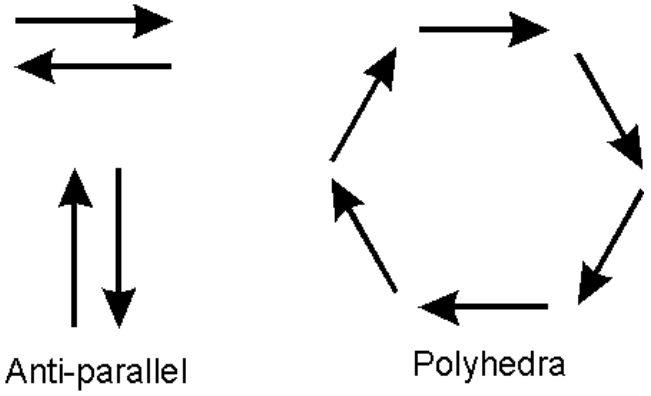

Figure 1.14 Illustration of the coupled dipole moment.

Although some directional interactions or local directional centres can be observed in transition metal oxides, these local directional components tend to anti-parallel or form local

coordination polyhedra to cancel the tendency to form NCS structures, as shown in Figure 1.14. As a result, the materials with NCS structures are very rare and most known phases adopt centrosymmetric structures.

In order to achieve an NCS structure, acentric units have to be incorporated into the lattice and arranged in an NCS manner. The acentric units can be constructed based on the following methods.

Electronic-driven local noncentrosymmetry. The most common strategy to be utilized is to incorporate some particular cations, which electronically induce a structural distortion, to break local inversion symmetry of the lattice. Two classes of metal cations can lead to this effect.

a) d^0 transition metal cations (e.g. Ti^{4+}, Nb^{5+}, Ta^{5+}). These cations can have a second-order Jahn-Teller (SOJT) distortion. The *d*-orbital of these metal cations can hybridize with oxygen *2p* orbital, which leads to a spontaneous symmetry breaking distortion and local acentric coordination environment.[39]

b) 'lone-pair' cations (e.g. Pb^{2+}, Bi^{3+}). These cations have ns^2 electronic configuration. The hybridization of metal cations *s*- and *p*-orbitals with oxygen *2p* orbitals also leads to a structural distortion and a breaking of local symmetry.[39]

Thus NCS structures can be achieved by incorporating these two classes of metal cations into the lattice. Typically, in perovskite structures, the inversion symmetry of the lattice can be lifted by either introducing d^0 transition metals in the B-sites (e.g. $NaNbO_3$[40]) or 'lone-pair' cations in the-A sites (e.g. $BiFeO_3$[41]).

Noncentrosymmetric basic units. Poeppelmeier et al., proposed that some specific acentric basic building units (BBUs) can be designed using mixed anions (e.g. oxy-fluorides) [42-46]. The difference in bond lengths and bond strengths between metal-oxide bonds and

metal-fluoride bonds offers the possibility of forming noncentrosymmetric units. The directional BBUs can be constructed by arranging the metal-oxide and metal-fluoride bonds in an NCS manner, yielding NCS units. Typical noncentrosymmetric basic units are transition metal oxy-fluorides like $NbOF_5^{2-}$ and $MoO_2F_4^{2-}$ (Figure 1.15). In principle, the mechanism of NCS basis units such as oxy-fluorides is similar to that of d^0 transition metal centres.

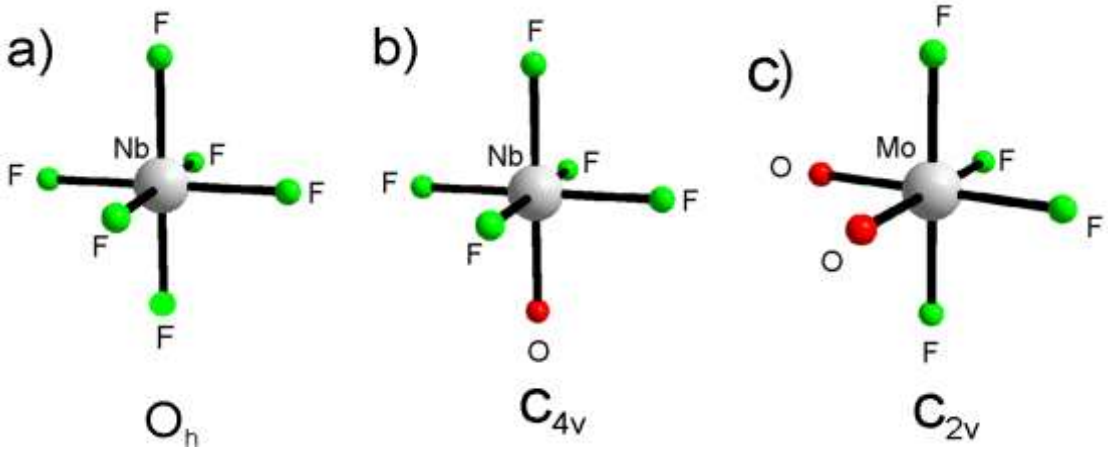

Figure 1.15 Structures of polar units. a) NbF_6, b) $NbOF_5^{2-}$and c) $MoO_2F_4^{2-}$.

Noncentrosymmetric polyhedra. In a perovskite structure, non-octahedral polyhedra, such as 5-coordinate pyramids and 4-coordinate distorted tetrahedra, are also acentric, as shown in Figure 1.16a, b. These directional polyhedra are led by noncentrosymmetric coordination environments and can be achieved in two methods.

a) The NCS polyhedra can be constructed by introducing anion vacancies into a lattice. For example, in the structure of anion-deficient perovskite $Ba_4CaFe_3O_{9.5}$, the presence of NCS FeO_5 pyramids and distorted FeO_4 tetrahedra, combined with the complex cation ordering, leads to a noncentrosymmetric structure[22].

b) 'lone-pair' cations, e.g. Se^{4+} or I^{5+}. Similar to Pb^{2+} and Bi^{3+} cations, these cations also have ns^2 electronic configurations and can interact with three oxides to form SeO_3[47,48]

or IO_3^{49-51} groups, as shown in Figure 1.16c. The presence of 'lone-pair' electrons yields noncentrosymetric coordination environments of Se^{4+} or I^{5+} cations and forms NCS units.

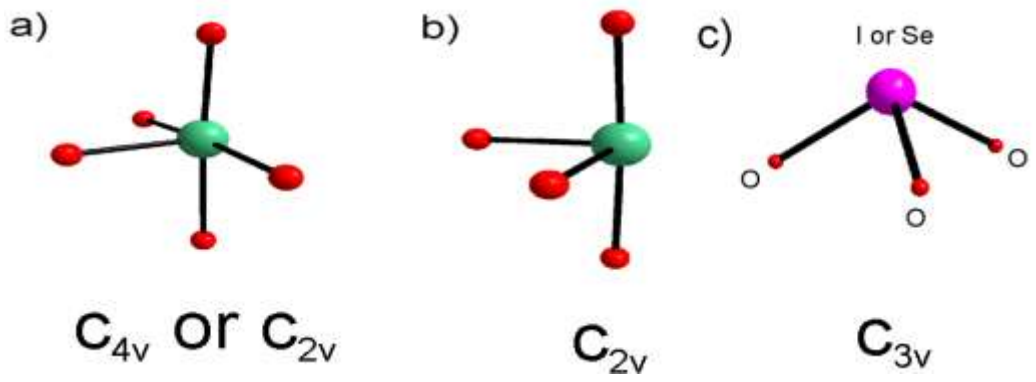

Figure 1.16 Structures of polar units. a) MO_5, b) MO_4; c) SeO_3 or IO_3.

However, the presence of these NCS components in the lattice is not a guarantee of a noncentrosymmetric structure. Centrosymmetric structures are more favourable, in which the dipolar couplings can be formed to anti-align any directional components. Thus, long-range centrosymmetric arrangement in the lattice is preferred. Previous studies indicated four main factors should be considered in order to direct the crystallization of directional units in an NCS manner: a) lattice strain; b) extended bond network; c) cation-cation repulsions; d) electronic effect.[52] Noncentrosymmetric structures can be achieved by carefully controlling these factors.

In the preparation of NCS materials, it is rather important to direct the polar units to crystallize in an NCS manner. NCS structures can be achieved by carefully controlling the structural framework. For example, $CsNaNbOF_5$ adopts a centrosymmetric structure in spite of polar $NbOF_5^-$ units present in the lattice[53], as shown in Figure 1.17. The substitution of Cs^+ cation with the smaller K^+ cation disrupts the simple packing in centrosymmetric $CsNaNbOF_5$ and leads to an NCS $KNaNbOF_5$ structure. This structural change is induced by a change of internal lattice strain when an A-site cation with different size is introduced.

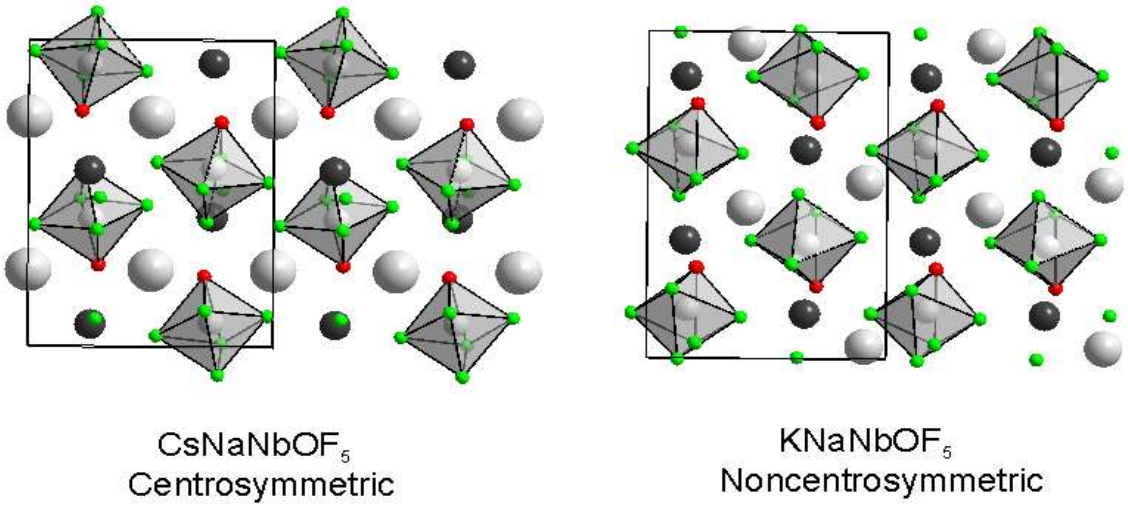

Figure 1.17 Structures of $CsNaNbOF_5$ (centrosymmetric) and $KNaNbOF_5$ (noncentrosymmetric). Solid lines indicate the respective unit cells. Gray octahedra represent $NbOF_5$ units, gray spheres Cs^+ or K^+ cations, black spheres Na^+ cations, red spheres O^{2-} anions and green spheres F^- anions.

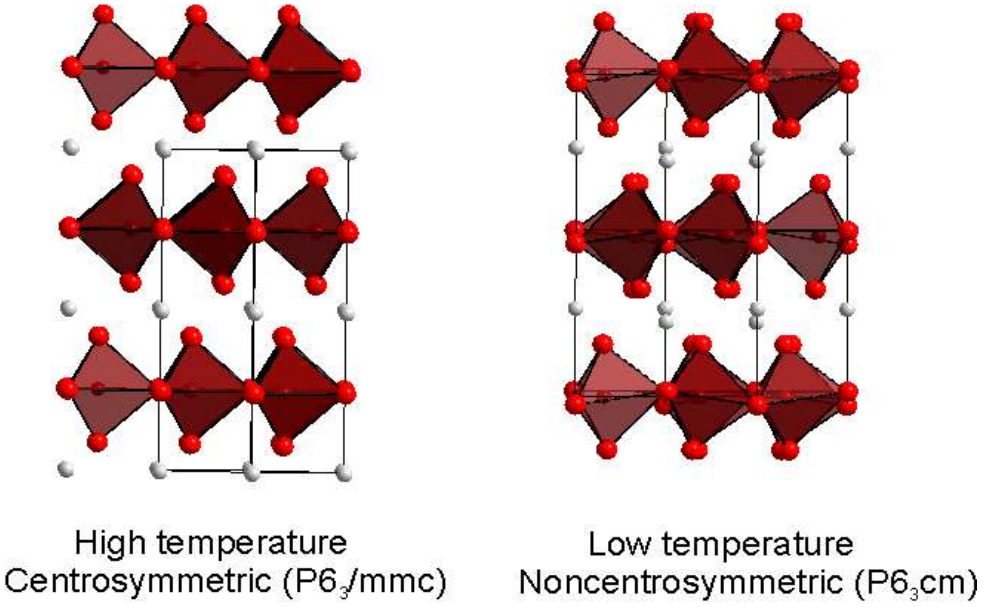

Figure 1.18 Structures of $YMnO_3$ (centrosymmetric at HT) and (noncentrosymmetric at LT). Solid lines indicate the respective unit cells. Brown polyhedra represent MnO_5 units, gray spheres Y^{3+} cations.

A similar effect is observed in a multiferroic $YMnO_3$ phase.[54] $YMnO_3$ adopts a centrosymmetric hexagonal structure at high temperature, as shown in Figure 1.18. When the temperature cools down, $YMnO_3$ undergoes a structural transition from centrosymmetric (*$P6_3/mmc$*) to noncentrosymmetric (*$P6_3cm$*). The lattice strain and bond network on the basis

of small Y^{3+} cations in the A sites provide the major driving force for the symmetry breaking in the $YMnO_3$ lattice, which leads to a distortion of the lattice and the polarization of the structure.[54]

Noncentrosymmetric structures can also be constructed by forming complex cation ordered bond networks and controlling the lattice strain.[23] The complex cation ordering in $Ba_4CaFe_3O_{9.5}$ is driven by cation size difference and preference of cations for different coordination environments, in which Ca^{2+} cations are in the octahedral sites and Fe^{3+} cations are in tetrahedral or pyramidal sites. The complex cation ordering, combined with acentric polyhedra (FeO_5 pyramids and distorted FeO_4 tetrahedra), breaks the inversion symmetry of the host lattice, allowing the material to exhibit SHG activity.

1.7 Aims of the present research

In this thesis, a series of cation-ordered and anion-vacancy ordered perovskite phases are described. The structure and magnetic behaviours are systematically investigated. In Chapter 3, the synthesis and characterization of complex cation-ordered phases Ba_2YMO_5 (M = Fe, Co) are presented. The relationship of cations, anion vacancies and cation ordered patterns has been illustrated. Furthermore, $Ba_3YM_2O_{7.5}$ (M = Fe, Co) were prepared and structural studies indicated $Ba_3YM_2O_{7.5}$ adopts a different cation ordered structure from Ba_2YMO_5. The structure and magnetic behaviour are detailed in Chapter 4.

Topochemical manipulations allow modifications to the structural lattice and oxidation state of transition metal cations to be made, whilst maintaining the arrangement of cation arrangement in the host lattice. In chapter 5, topochemical oxidation of cation-ordered Ba_2YFeO_5 leads to the formation of a new anion-vacancy ordered $Ba_2YFeO_{5.5}$ phase, which exhibits pyroelectric and ferromagnetic behaviours. The structure, magnetic and electric

properties of the oxidized phase are described. Chapter 6 describes the fluorination of Ba_2YCoO_5 which leads to the formation of $Ba_2YCoO_5F_{0.42}$. The processes of anion insertion into the two anion-vacancy ordered Ba_2YMO_5 (M = Fe, Co) phases are discussed.

In addition to the complex cation ordering described in Chapter 3-6, the layered brownmillerite structure ($A_2B_2O_5$) is one of the most common anion-deficient perovskite structures, which adopts an OTOT stacking sequence of octahedral(O) and tetrahedral(T) layers. Triple layer structure ($A_3B_3O_8$) can be regarded as an extension of brownmillerite structure, which adopts an OOTOOT stacking sequence of octahedral and tetrahedral layers. Thus these two types of anion-vacancy ordered structures are also included in this thesis. Chapter 7 introduces a new six-layered anion-deficient perovskite phase $LaCa_2GaFe_2O_8$ with *Pbma* space group symmetry. In Chapter 8, the new brownmillerite phases $La_xSr_{2-x}CoGaO_{5+\delta}$ ($0.5 < x < 1.0$) with a mixed Co^{2+}/Co^{3+} valence are described. Magnetization data indicate a composition-dependant Co^{3+} spin state in this series of materials, which could be rationalized on the basis of applied chemical pressure.

Chapter 2 Experimental Methods

2.1 Sample synthesis

2.1.1 Solid-state method

Mixtures of metal oxides and/or carbonates in an appropriate stoichiometric ratio were weighed out and ground together thoroughly using an agate pestle and mortar to obtain homogeneous powders. The mixtures were heated in alumina crucibles at 1000 ^{o}C for 12 h to decompose the carbonates, and then reground and pressed into pellets using a pressure of 5 tons. The syntheses were conducted at the appropriate temperatures (1100 - 1425 ^{o}C) under different atmospheres (typically argon or air) for 2 periods of 40 h with an intermediate grinding in order to form thermodynamically stable phases. The structures of the products were determined by X-ray powder diffraction measurements.

2.1.2 Citrate gel method

Suitable ratios of chemicals were dissolved in a 1:1 mixture of 6 M nitric acid and distilled water. Three mole equivalents of citric acid and about 5 mL of analar ethylene glycol were added into the solution. The solutions were stirred and heated to 150 ^{o}C to decompose the nitric acid and form a gel. The gel was then heated to 500 ^{o}C to decompose the organic residue. The resulting powder was transferred to an aluminium crucible and heated slowly to 850 ^{o}C in air to decompose the remaining organic residue. The powder was then ground and pressed into pellets for high-temperature synthesis.

2.2 Topotactic oxidation

Some samples in this thesis were synthesized in a topotactic oxidation reaction in an oxygen atmosphere at lower temperatures (250 - 450 ^{o}C). Under these conditions, oxide ions

can be inserted into the vacant positions of the host lattice and new phases retain the arrangement of cations within the host phases.

2.2.1 High pressure oxidation

Sometimes low-temperature oxidation cannot be achieved under atmosphere pressure and then oxidation under high pressure of oxygen is attempted. The oxidation reaction under high pressure is carried out in a Parr Series 4740 Pressure Vessel (Figure 2.1), which can withstand a maximum pressure of 2000 psi. The vessel was sealed by a Teflon gasket and stabilized by 6 bolts after the samples were placed into it. The vessel was connected to a pressure control system which consists of a 3-way tap, pressure gauge and oxygen supply. The entire vessel was then placed into a furnace and heated to the target temperature.

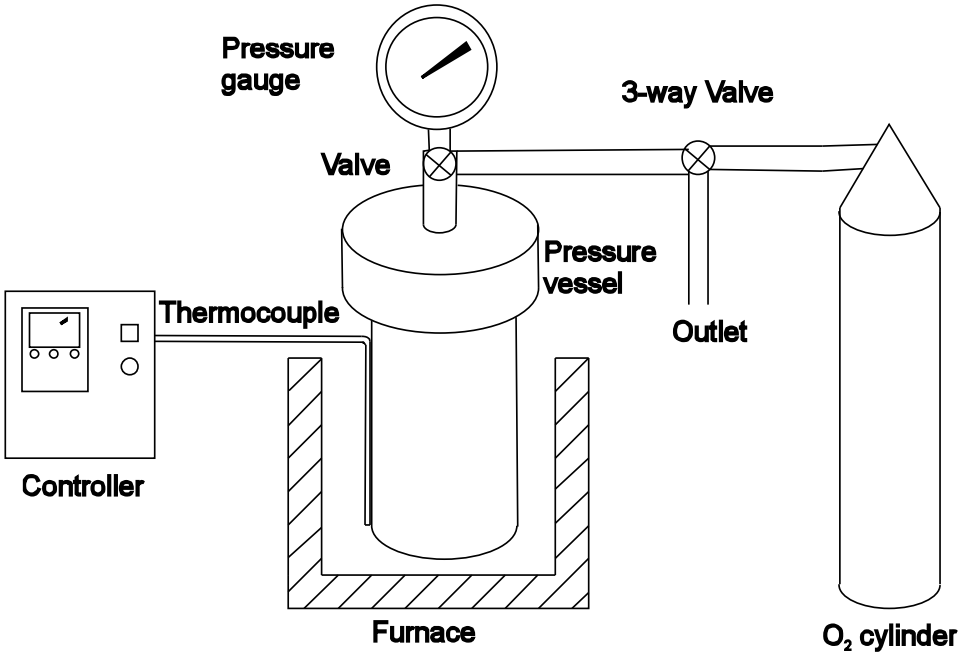

Figure 2.1 High-pressure system

2.2.2 Fluorination

In addition to the insertion of oxide ions, fluoride ions can also be inserted into the structure of anion-deficient perovskites. Fluorination reactions can be carried out under

flowing fluorine gas. However, the impurity of hydrofluoric acid in fluorine gas will lead to the decomposition of the sample and the formation of metal fluorides. Thus fluorination reactions in this thesis were carried out using copper fluoride as a fluorine agent according to the following reaction.

$$MO_x + CuF_2 \xrightarrow{O_2} MO_xF_y + CuO$$

The fluorinated sample prepared in this method is contaminated by CuO, which leads to a complication in magnetic or optical measurements. Thus an attempt to separate the reactions above is carried out using the following method.

$$CuF_2 \xrightarrow{O_2} F_2 + CuO; \qquad MO_x + F_2 \longrightarrow MO_xF_y$$

The CuF_2 and as-prepared perovskite sample were separately placed in two aluminium boats in a silica glass tube, as shown in Figure 2.2. CuF_2 was heated under flowing oxygen at 500 ^oC. The generated F_2 gas mixed with O_2 then flowed through the sample, which is held at a fixed temperature.

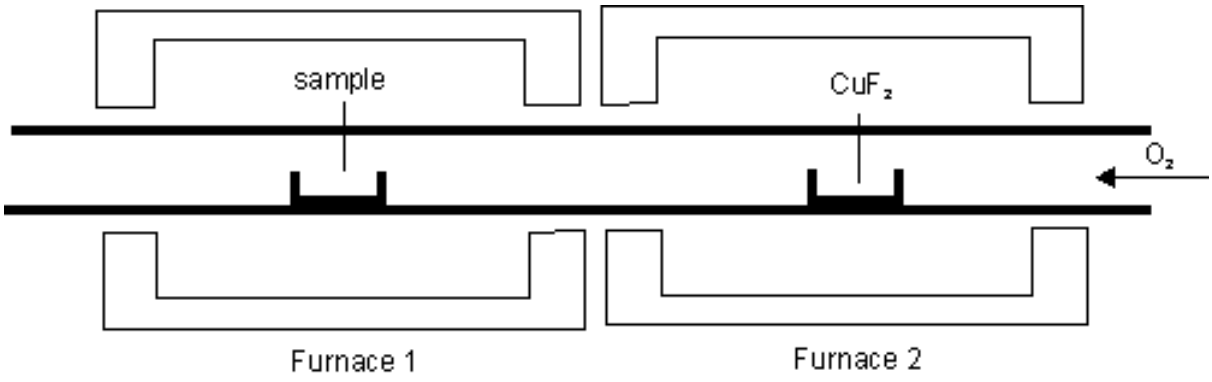

Figure 2.2 Fluorination reaction system.

2.3 Powder diffraction

Powder diffraction is a useful technique to monitor the reaction progress and determine structural information in solid-state chemistry. In a crystal structure, diffraction can occur

where the wavelength of the incident beam is similar to the spacing between the lattice planes. The lattice planes have Miller indices *hkl* which depend on the symmetry of the crystal. In the case of a cubic structure, the spacing between *hkl* planes is described as:

$$\frac{1}{d_{hkl}^{\ 2}} = \frac{h^2 + k^2 + l^2}{a^2}$$

where *a* is the lattice parameter. Hence, the spacing is smaller between the lattice planes with larger Miller indices.

The conditions for the appearance of diffracted beams can be described by Bragg's Law:

$$n\,\lambda = 2\,d_{hkl}\sin\theta$$

where *n* is an integer, λ is the wavelength of incident radiation, *d* is the distance between atomic planes and θ is the angle of incidence.

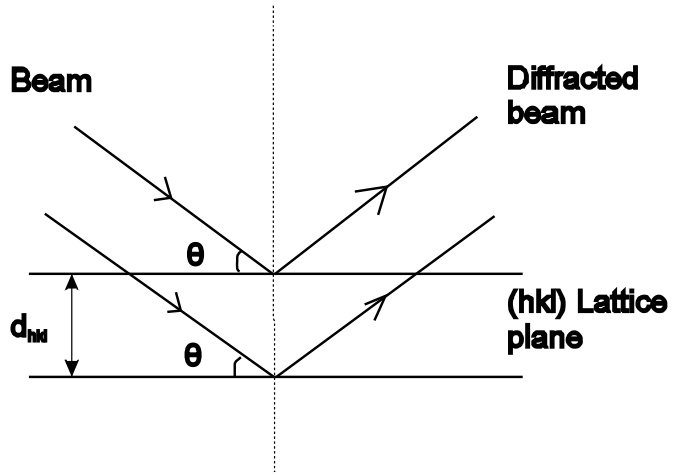

Figure2.3 Diffraction from a set of lattice planes (*hkl*) separated by a distance d_{hkl}.

Constructive interference occurs at a characteristic angle for each atomic plane and is dependent on the distance between planes. In this investigation, the structural determination is made by analyzing diffraction data of X-ray, neutron and electron beams. Figure 2.3 illustrates the principle when a beam of X-ray is diffracted by a crystal.

While Bragg's Law defines the conditions of characteristic diffraction, the intensity of the diffracted beam, I_{hkl}, is given by the following relationship:

$$I_{hkl} \propto LmA|\ F_{hkl}|^2$$

where L is the sample-independent Lorentz-polarisation factor, m is the multiplicity of a reflection, A is the absorption factor and F_{hkl} is the structure factor.

$$F_{hkl} = \sum_n f_n exp[2\pi i(hx_n + ky_n + lz_n)] \exp\left[\frac{-8\pi^2 U_{iso_n} sin^2\theta_{hkl}}{\lambda^2}\right]$$

where f_n is the atomic scattering factor and x_n, y_n and z_n are the fractional coordinates of the n^{th} atom in the unit cell. The second exponential term is a correction to the structure factor. $Uiso_n$ is the atomic isotropic thermal factor that determines the magnitude of reduction in the diffraction intensity as the scattering angle changes.

2.3.1 X-ray diffraction

The angles of diffraction reflections give information on the structural composition and lattice parameters of the unit cell, while the intensities of the peaks offer insight into the atomic positions in the unit cell. The X-ray powder diffraction data are compared to the STOE database to determine the phase composition. Furthermore, the structural model can be refined using General Structure Analysis System (GSAS).

2.3.1.1 Philips PW1720 diffractometer

The diffraction data collected from the Philips PW1720 diffractometer was used to monitor reaction progress. It operates in Bragg-Brentano Geometry using Cu $K\alpha_1$ (1.5406 Å) and $K\alpha_2$ (1.5444 Å) radiation from a generating tube operating at 30 mA with a voltage of 40 kV. Samples were loaded in an aluminium or glass slide. The diffraction data were collected at a

rate of 0.04^o 2θ s^{-1} between $3^o < 2\theta < 70^o$. Aluminium diffracts at around 38.5^o, 44.8^o and 65.1^o.

2.3.1.2 PANalytical X'pert diffractometer

The PANalytical X'pert diffractometer was used to collect high-quality data for Rietveld refinements. The diffractometer also operates in Bragg Brentano Geometry and a germanium monochromator was installed to selectively use Cu $K\alpha_1$ radiation. Sample powders were dispersed on the surface of a silicon slide with Dow-Corning high vacuum grease. The standard program measured a continuous scan over a range of $3° < 2\theta < 90°$ with a scan rate of $0.006° 2\theta$ s^{-1}.

2.3.2 Neutron diffraction

Neutron powder diffraction is an important technique to determine the structure of new phases. The principle of neutron diffraction is similar to that of X-ray diffraction. However, compared to X-rays, which are scattered by the periodic electron density of a crystalline solid, neutron beams are scattered by an interaction with atomic nuclei. Thus neutron powder diffraction technique has several advantages in solving a new structure.

1. As a nucleus approximates to a point source, the diffraction intensity will not drop off as the diffracted angle increases. The diffraction intensity of X-ray scattering falls off rapidly with the increasing scattering angle, which cause difficulties in unambiguously analyzing the structural information.
2. The neutron scattering lengths of all atoms are similar, which allows the determination of the positions of light atoms, such as oxygen and fluorine, in the presence of heavy atoms. Thus it is important to utilize neutron diffraction in this thesis to determine the positions of anion vacancies in the perovskite structure.

3. Neutron diffraction data can distinguish between the positions of elements with similar atomic numbers, which allows the identification of cation ordering in the structure.
4. Neutrons can interact with unpaired electrons. Scattering from an ordered array of electron spins gives additional diffraction features. In this thesis, magnetic structures are characterized by analyzing these additional diffraction features from neutron diffraction data.

The magnetic scattering structure factor $\boldsymbol{F}_{mag}^{hkl}$ can be described as follows:

$$\boldsymbol{F}_{mag}^{hkl} = \sum_{j} q_j p_j e^{2\pi i h x_j}$$

where q_j is the magnetic interaction vector, p_j is the magnetic scattering length, h is the magnetic scattering vector and x_j is the position vector of the magnetic atom within the unit cell. The diffraction intensity of the magnetic reflection $I_{mag,hkl}$ can be described as a function of magnetic scattering structure factor, $\boldsymbol{F}_{mag}^{hkl}$ and the angle between the magnetic scattering structure vector and relevant lattice plane, α.

$$I_{mag,hkl} = |\boldsymbol{F}_{mag}^{hkl}|^2 cos^2\alpha$$

Neutron powder diffraction is widely used in this thesis to determine the structural information, like cation and anion-vacancy ordering. The sample was loaded in a vanadium container in the measurements. Neutron diffraction data can be collected at variable temperatures using crystats (low temperature) or a vacuum furnace (high temperature). The main stations for neutron diffraction measurements are the Institut Laue Langevin (ILL) in France and ISIS in UK.

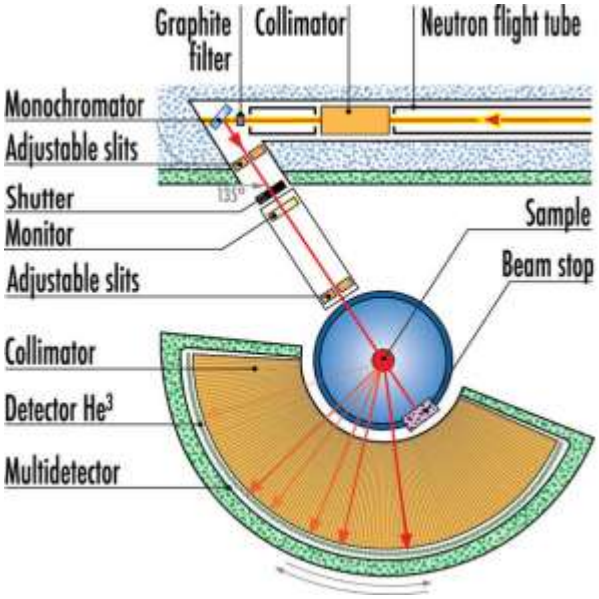

Figure 2.4 D2B instrument at the ILL facility[55]

2.3.2.1 D2B at Institute Laue Langevin (ILL)

The neutron diffractometer D2B in ILL, France is a high-resolution two-axis diffractometer, which is characterized by a high take-off angle of 135^{o} for the monochromator. Scans were carried out over the range $5 < 2\theta/^{o} < 160$ with 64 detectors spaced at 2.5^{o} intervals. During the experiments the detector bank is moved in 2.5^{o} steps to cover the overall range. Several scans were repeated and summed up to improve the statistics. The wavelength can be selected by rotating the germanium crystal monochromator. All the data collected in this thesis was carried out using a wavelength of $\lambda \approx 1.594$ Å. Figure 2.4 shows the picture of D2B instrument at ILL facility.

2.3.2.2 POLARIS at ISIS

The ISIS neutron facility is located at the Rutherford Appleton Laboratory in UK. Proton beams are accelerated in a synchrotron and passed through aluminium oxide to remove electrons. The proton beam was accelerated to the energy of 800 MeV in the synchrotron

and fired at a tantalum target. The collision of protons with the tantalum target excites the pulsed neutrons. The neutrons produced have very high energies and velocities and have to be slowed down using hydrogenous moderators. This method produces a continuous distribution of neutron wavelengths for the time-of-flight measurements.

In the D2B facility, the wavelength diffractometers adopted the incident radiation with a constant wavelength and the diffraction patterns were measured as a function of scattering angle. Comparatively, the time-of-flight diffractometers adopted a fixed angle detector and the diffraction patterns were measured as a function of wavelength determined by velocity of radiation, which follows the De Broglie relationship:

$$\lambda = \frac{h}{m} \cdot \frac{t}{l}$$

where h is Planck constant, m is the neutron mass and t is the time needed for the neutron to travel a distance L from the moderator to the detector.

The resolution of a time-of-flight diffractometer, $\Delta d/d$, can be described by the following relationship:

$$\frac{\Delta d}{d} = \sqrt{((\frac{\Delta t}{t})^2 + (\frac{\Delta L}{L})^2 + (\Delta\theta cot\theta)^2)}$$

where Δt is the time uncertainty, ΔL is the distance uncertainty and $\Delta\theta$ is the angular uncertainty.

POLARIS is a medium resolution, high intensity diffractometer with ZnS scintillator detector arranged into six detector banks, as shown in Table 2.1. The intense neutron flux, combined with a large detector solid angle allows the experiments to be conducted using a small amount of sample.

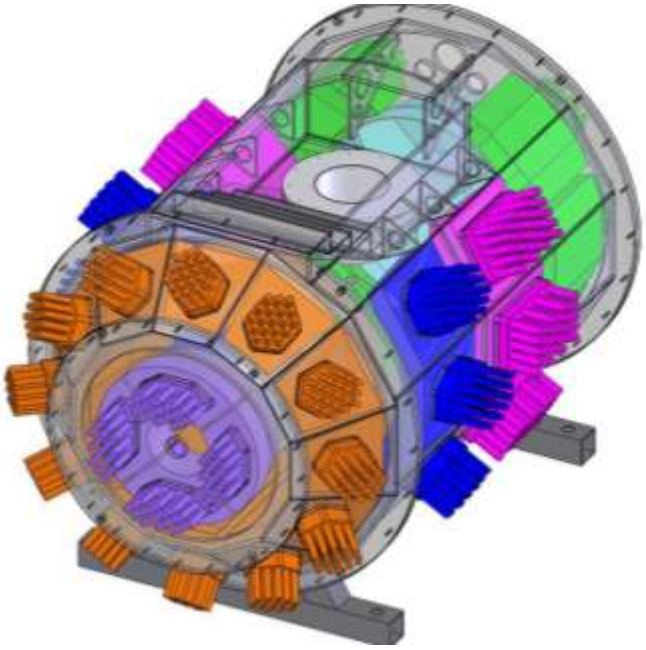

Figure 2.5 POLARIS instrument at the ISIS facility[56]

Detector	Bank	2θ	Solid Angle	Count rate	$\Delta d/d$(%)	d_{max}
Very low angle	1	6-14	0.26	~21	>2.7	19.6
Low angles	2	19-34	1.04	~29	1.2-1.9	8.7
	3	60-67	0.92		0.85	7.0
90 degrees	4	75-113	1.33	~3.0	0.51	3.2
Back-scattering	5	135-143	0.59	~3.6	0.3	2.7
	6	146-168	1.53			

Table 2.1 The performance parameters of the POLARIS instrument.[57]

2.3.2.3 GEM at ISIS

The General Materials (GEM) diffractometer is a new generation neutron diffractometer constructed at ISIS. A schematic of the detector array is shown in Figure 2.6. The GEM detectors cover a scattering angle range from 1.1 ° to 169.3 °. The incident flight path is 17.0 metres. GEM can be used to perform high-intensity, high-resolution experiments to study the structure of disordered materials and crystalline powders.

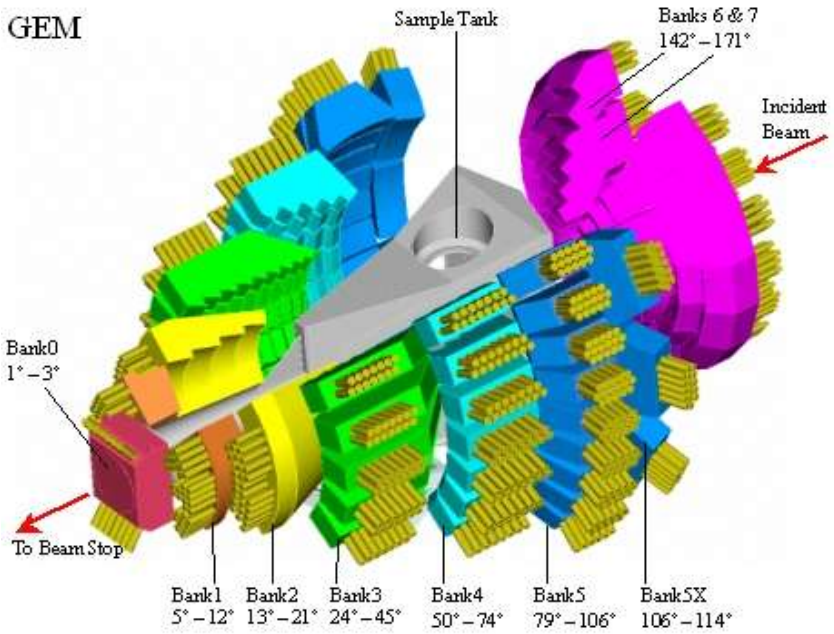

Figure 2.6 GEM instrument at the ISIS facility[58]

Bank	2 theta (^{o})	Minimum d-spacing (Å)	Maximum d-spacing (Å)
1	9.10	2.0	30
2	18.0	1.0	14
3	35.0	0.8	7
4	64.0	0.7	4
5	91.5	0.5	2.5
6	154	0.3	1.7

Table 2.2 GEM bank settings[59]

2.3.3 Electron diffraction

Electron diffraction is frequently used in solid state physics and chemistry to study the crystal structure of solids. In this investigation, electron microscopy was used to obtain information on the symmetry and the unit cell expansion of the crystal. Similar to X-rays and neutrons, electrons are diffracted by interaction with periodic variations within a crystal.

Electron diffraction measurements in this investigation were carried out using a JEOL JEM-2000FX Transmission Electron Microscope. Samples were ground into fine particles an agate pestle and mortar and then dispersed in chloroform. A drop of the suspension was pipetted onto a copper grid and placed in the microscope. Figure 2.7 shows the pathway of diffracted electron beams during the measurements.

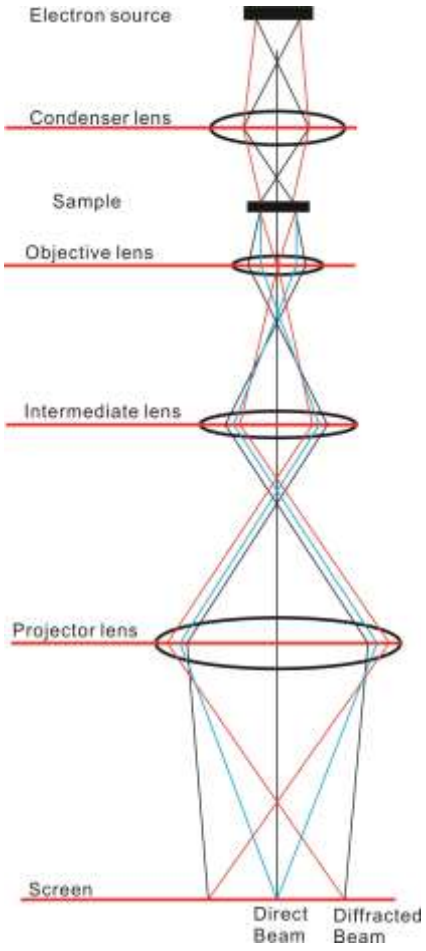

Figure 2.7 The pathway of diffracted electron beams

The diffraction patterns were analysed by measuring the distances between the central spot and the spots around it. The *d*-spacings were calculated using the following equation:

$$d_{hkl} = \frac{\lambda L}{R}$$

where d_{hkl} is the *d*-spacing of the *hkl* plane, λL is the camera constant, *R* is the distance between te centre spot and the diffracted spot. Thus, the *hkl* values were assigned.

2.4 Rietveld refinement

The Rietveld method of profile refinement was applied to obtain crystal structural information (e.g. structural symmetry, lattice parameters) by analyzing neutron and X-ray powder diffraction data. Before the refinement process, structural models are constructed on the basis of known information. The structural model and lattice parameters are then refined against the neutron and X-ray powder diffraction data collected from the samples. The principle of the refinement process is to minimize the differences between the observed intensity of each point in the experimental diffraction patterns and the calculated intensity of each point on the basis of the constructed models. The quantitative standard for this optimisation progress can be expressed as an S_y value.

$$S_y = \sum_i w_i \, (y_{i,obs} - y_{i,cal})^2$$

where w_i is the weighting factor, $y_{i,obs}$ is the observed intensity at the i^{th} point and $y_{i,cal}$ is the calculated intensity at the i^{th} point. The weighting factor w_i ensures the equal significance of each point.

In this thesis, the structural models are constructed using Diamond software. The General Structure Analysis System (GSAS) suite of programs is employed for the refinement process. The lattice parameters, the atomic positions and the fractional occupancies of the sites are allowed to be refined.

2.4.1 Background modelling

The neutron and X-ray diffraction data collected from the samples not only contain information on crystalline structures of the samples, but also include the regions without

diffraction intensity. Thus the first step of the refinement process is to take account into the background contribution, and the intensity of the background I_b can be described:

$$I_b = \sum_{j=1}^{n} B_j \, T_{j-1}$$

where B_j is the refineable quantity, T_{j-1} is angular (or time-of-flight) dependence and n is the number of background terms, which depends on the complexity of the background level.

2.4.2 Peak shape

The peak profiles in diffraction patterns collected from a sample are usually complicated. Thus it is important to describe the peak profiles of the diffraction patterns accurately, in order to obtain an accurate refinement result. Peak shape in a diffraction pattern is dependent on the following factors:

1. Instrumental factors. The influence of the instrument originates from the uncertainty in the wavelength of the incident beam.
2. Sample factors. In this thesis, the neutron or X-ray diffraction data are collected from polycrystalline powder samples, rather than from a perfect single crystal. Thus, the broadening of the diffracted peaks can be caused by the samples themselves, such as the particle size or internal strain. The Sherrer equation can describe the influence of the particle size on the peak shape.

$$d = \frac{K\lambda}{\beta cos\theta}$$

where d is the average size the ordered crystalline domains, K is the shape factor, λ is the X-ray wavelength, β is the line broadening at half the maximum intensity (FWHM) and θ is the Bragg angle.

3. Darwin width. Due to the uncertainty principle, the position of a photon implies an intrinsic ambiguity, which leads to Darwin width in the diffraction patterns. In practice, the broadening attributed to this effect can be neglected compared to the other experimental factors mentioned above.

The Pseudo-Voigt function is considered as an accurate description of the observed peak shapes, which consists of the Lorentzian (L) and Gaussian (G) components. The Lorentzian component describes the peak broadening from structural features, while the Gaussian component describes the peak broadening due to instrumental factors. Thus, the Pseudo-Voigt function is described as a linear combination of these two components, as shown in the following equation:

$$F(\Delta T) = \eta L(\Delta t, \Gamma) + (1 - \eta) G(\Delta t, \Gamma)$$

where ΔT is the deviation in the position of a reflection from the calculated position, Γ is a function of the FWHM and η is the mixing parameter.

In the data collected at the D2B facility, the diffraction is based on a constant wavelength profile. The contribution of the Gaussian component, Γ_G, can be described as follows:

$$\Gamma_G = \sqrt{Utan^2\theta + Vtan\theta + W + \frac{P}{cos^2\theta}}$$

where the *U*, *V* and *W* terms are related to the instrumental broadening and *P* is related to Scherrer broadening. The contribution of the Lorentzian component, Γ_L, can be described as follows:

$$\Gamma_L = \frac{X}{cos\theta} + Ytan\theta$$

where the *X* parameter is the contribution from Scherrer broadening and the *Y* parameter is the strain broadening contribution. All these parameters are allowed to be refined.

In the data collected at the POLARIS facility, the Gaussian component, σ^2, and Lorentzian component, γ, for time-of-flight experiments are described as:

$$\sigma^2 = {\sigma_0}^2 + {\sigma_1}^2 d^2 + {\sigma_2}^2 d^4$$

$$\gamma = \gamma_0 + (\gamma_1 + \gamma_{1e} cos\varphi\alpha) + (\gamma_2 + \gamma_{2e} cos\varphi\alpha) d^2 + \gamma_L$$

where σ_n are the Gaussian parameters for instrumental broadening and γ_n are the parameters for micro-strain and Scherrer broadening.

2.4.3 Fitting parameters

The fitting of the refinement can be statistically evaluated by three parameters: the reduced χ^2, the residual function, R_p and the weighted residual function, wR_p, which are defined by the following equations.

$$\chi^2 = \frac{R_{wp}}{R_e} = \frac{\sum_i w_i (y_{i,obs} - y_{i,cal})^2}{n_{obs} - n_{var}}$$

$$wR_p = 100 \times \sqrt{\frac{\sum_i w_i (y_{i,obs} - y_{i,cal})^2}{\sum_i w_i {y_{i,obs}}^2}}$$

$$R_p = 100 \times \frac{\sum_i |y_{i,obs} - y_{i,cal}|}{\sum_i y_{i,obs}}$$

where the *obs* numbers are those taken from observation and the *cal* numbers are those taken from calculations. The smaller values of these parameters suggest a better fit.

2.5 Bond valence sums

The bond valence sums (BVS) method is a procedure to calculate the oxidation state of an ion, which allows the estimation of the valence of an ion according to the bond lengths within its coordination sphere.

$$V_i = \sum_j v_{ij}$$

where V_i is the total valence of a particular ion and v_{ij} is the valence of a bond between two atoms *i* and *j*, which can be calculated using the following empirical equation:

$$v_{ij} = exp\left(\frac{r_0 - r_{ij}}{B}\right)$$

where r_0 is the value of bond length for unit bond valence, r_{ij} is the observed bond length between atoms *i* and *j* and *B* is an empirical constant. Usually the *b* constant can be calculated as 0.37.

Bond valence sums are actually the comparison of the bond lengths of an ion in a particular coordination environment with that of the same ion previously reported in the literature. The application of BVS method in low-temperature topochemistry should be cautious, because most of the reported bond lengths were derived from thermodynamically stable phases.

2.6 SQUID magnetometry

A Superconducting Quantum Interference Device (SQUID) was used to study the magnetic behaviours of the samples. The superconducting detection coils in this instrument, as shown in Figure 2.8, yield extremely high-accuracy measurements. As the position of the sample (DC magnetization) or time (AC magnetization) changes, a current is induced and detected by the superconducting ring. This electrical signal is then converted into magnetic data.

All the magnetization data in this thesis were collected using a Quantum Design MPMS XL SQUID magnetometer. ~ 50 mg of a powder sample was sealed in a capsule and suspended in a straw for low-temperature measurements. For high-temperature

measurements, the sample was sealed in a Pyrex glass tube and placed into a specific furnace equipped with the SQUID magnetometer.

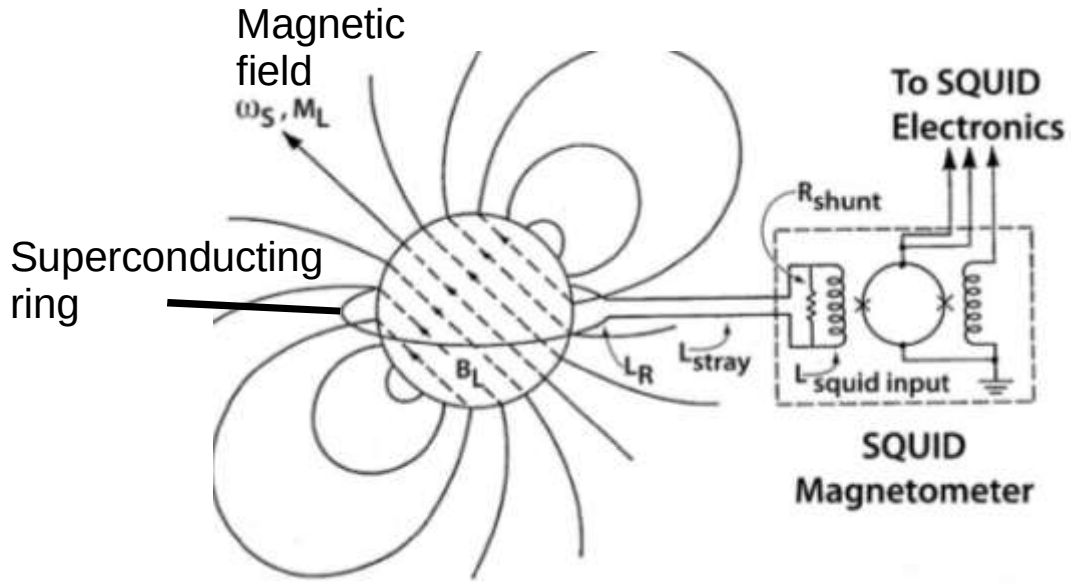

Figure 2.8 Diagram of SQUID instrument[60]

2.6.1 DC magnetization

In the DC magnetic measurements, a constant magnetic field is applied. The movement of the sample in the applied magnetic field induces a measurable current, which is related to the induced magnetic moment. The molar magnetic susceptibility can be described as follows:

$$\chi_m = \frac{M}{H}$$

where H is the applied field in units of Oersted (Oe), and M is the magnetic moment induced in the applied field.

1. Zero-field-cooled and field-cooled magnetization data. The sample is usually measured in the temperature range 5 < T/K < 300 at a constant applied field of 100 Oe. High-temperature magnetization data can usually be collected in the temperature

range 300 < T/K < 700 in a furnace at a constant applied field 1000 Oe. The divergence of the zero-field-cooled and field-cooled magnetization data suggests magnetic order. The zero-field-cooled and field-cooled magnetization data above the magnetic order temperature may obey the Curie-Weiss Law, as discussed below.

2. Field-dependent magnetization data. The magnetization data are recorded as a function of applied field at an appointed temperature. After field-cooling, the field-dependent magnetization data exhibit hysteresis in a ferromagnetic system. In a spin-glass system, the magnetization data is an 'off-centering' hysteresis loop. In an antiferromagnetic system, the magnetic moment, *M* and the applied field, *H* follow a linear relationship.

2.6.2 Curie-Weiss law

In the ferromagnetic/antiferromagnetic systems, the magnetic susceptibilities and the absolute temperature follow a specific relationship, the Curie-Weiss Law, which can be described by the following equation:

$$\chi = \frac{C}{T - \theta}$$

where χ is the magnetic susceptibility, C is the Curie constant and θ is the Weiss constant. Considering the effect of temperature independent paramagnetism, the Curie-Weiss law can be modified by introducing a further constant, K.

$$\chi = \frac{C}{T - \theta} + K$$

2.6.3 AC magnetization

In AC measurements, a small AC driven magnetic field is employed. A time-dependent moment in a sample will be caused and induce a measurable current. In the measurement, given a small AC field, the induced AC moment can be described as follows:

$$M_{AC} = \frac{dM}{dH} \cdot H_{AC}\sin(\omega t)$$

where H_{AC} is the amplitude of the driving field and ω is the driving frequency. When the high driving frequency is employed, the magnetization of the sample will lag behind the drive field, thus AC magnetic susceptibility measurement gives two quantities: the magnitude of the susceptibility, χ, and the phase shift, φ, which can be expressed as a real component χ' and an imaginary component χ''

$$\chi' = \chi \cos\varphi$$

$$\chi'' = \chi \sin\varphi$$

The real component is the slope of $M(H)$ curve, and the imaginary part is dissipative processes in the sample.

AC magnetization is usually employed to detect the presence of spin-glass behaviour in the sample. Evidence for the spin-glass behaviour present is the frequency dependent magnetic response (real component χ') of this phase. Thus AC susceptibility measurement is widely used in this thesis.

2.7 Second-harmonic generation

Second-harmonic generation (SHG) is a nonlinear optical process, which can be described as a conversion of photons into new photons with twice the energy (or doubling frequency) when they interact with a nonlinear material. The nonlinear optical effects can be written as:

$$P_i = \chi_{ij}E_j + \chi_{ijk}E_jE_k + \chi_{ijkl}E_jE_kE_l + ...$$

where χ_{ij} is the electric susceptibility, χ_{ijk} and χ_{ijkl} are the second-order and third-order nonlinear coefficient respectively.

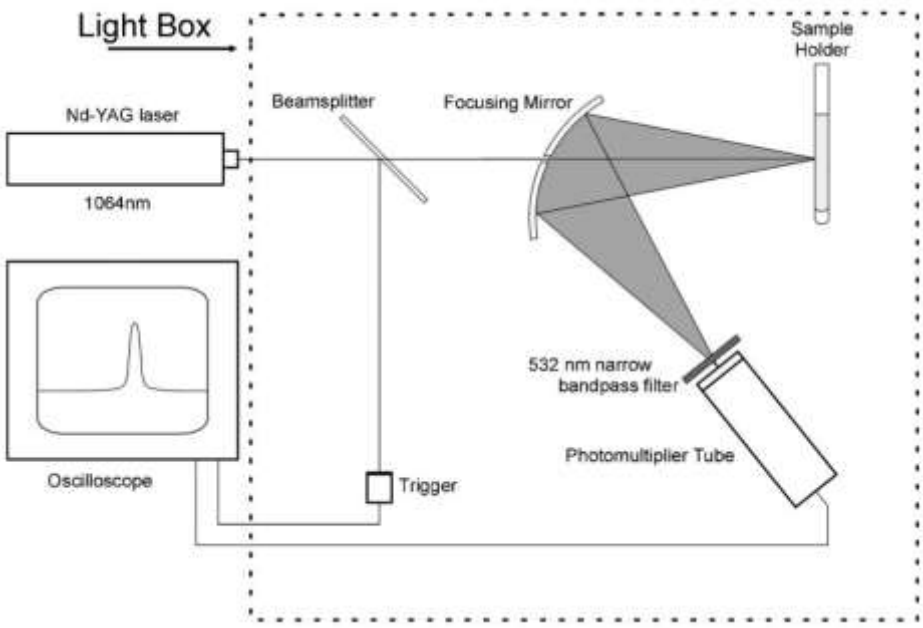

Figure 2.9 Diagram of a modified Kurtz–Powder Laser System[61]

Powder SHG measurement is usually used for examining the noncentrosymmetric structure of a new phase. Figure 2.9 shows a typical set-up for powder SHG measurements. Powder SHG measurements were performed on a modified Kurtz-NLO system[62,63] using a pulsed Nd:YAG laser with a wavelength of 1064 nm. About 50 mg of powder sample was placed in a fused silica tube. As the powder SHG efficiency has been shown to depend strongly on particle size,[61] the reported materials were ground and sieved into distinct particle size ranges (<20, 20–45, 45–63, 63–75, 75–90, >90 mm). Relevant comparisons with known SHG materials were made by grinding and sieving crystalline α-SiO_2 (non-phase-matchable) and $LiNbO_3$ (phase-matchable) into the same particle size ranges.

2.8 Pyro-current measurement

The pellet was prepared with silver paint electrodes of area 4 mm^2. Variable temperature dielectric constant measurements were performed using an Andeen Hagerling 2700 A high precision capacitance bridge and an Oxford Instruments helium flow cryostat with a custom probe. In addition, the pyro-current was measured on warming at 1 K/min once the electrodes had fully discharged at 10 K, having cooled the sample in an electric field of both ±230 V/mm from room temperature. This measurement was repeated under an external magnetic field of 2 T, applied perpendicular to the electric field in a Quantum Design PPMS. Ferroelectric switching was investigated at 78 K by employing the PUND method[79].

2.9 Resistance measurement

Resistance measurements were performed on a home-made system with an Oxford Instruments helium flow cryostat and a custom probe. The as-prepared pellets were cut into a sample bar (4 mm x 1.5 mm x 12 mm) and connected using copper wire with the four-probe method. Silver paste was used to make a good electrical connection between the copper wires and the sample bar. The sample was then placed into a Quantum Design PPMS, and the resistance measurements were carried out in the temperature range $5 < T/K < 300$.

2.10 Iodometric titrations

Iodometric titrations were carried out in order to determine the average oxidation states of B-site cations, particularly Fe and Co in this investigation. The measurements involved two steps, the standardisation of sodium thiosulphate solution and the determination of oxidation states of B-site cations.

The sodium thiosulphate solution was standardised through a titration based on the following reactions.

$$IO_3^-{}_{(aq)} + 5I^-{}_{(aq)} + 6H^+{}_{(aq)} \rightarrow 3I_{2\,(s)} + 3H_2O_{(l)}$$

$$I_{2\,(s)} + S_2O_3^{2-}{}_{(aq)} \rightarrow 2I^-{}_{(aq)} + S_4O_6^{2-}{}_{(aq)}$$

During the determination of oxidation states of B-site cations, about 40 mg of samples were weighed and dissolved along with an excess of potassium iodide (KI) in hydrochloric acid solution. The measurements were conducted by using the standardised sodium thiosulphate ($Na_2S_2O_3$) solution to reduce the iodine, which was the product of the redox reaction between the B-site cations and potassium iodide. Starch solution was added as a colour indicator during the titration and the titration terminates with an observable colour change in the solution. The reaction processes are as follows.

$$M^{n+}{}_{(aq)} + I^-{}_{(aq)} \rightarrow I_{2\,(s)} + M^{(n-1)+}{}_{(aq)}$$

$$I_{2\,(s)} + S_2O_3^{2-}{}_{(aq)} \rightarrow 2I^-{}_{(aq)} + S_4O_6^{2-}{}_{(aq)}$$

All the titration measurements were carried out under an inert argon atmosphere in order to avoid oxidation of iodide by oxygen in the air. The average oxidation states of the B-site cations were calculated according to the above reaction equations.

Chapter 3 Complex cation ordering in Ba_2YMO_5 (M = Co and Fe)

3.1 Introduction

Materials with cation-ordered perovskite structures have been intensively studied because they often exhibit significantly different physical properties compared to their disordered analogues. For example, cation ordered Sr_2FeMoO_6 exhibits a magnetoresistive behaviour, whereas the disordered phase does not.[8] In spite of the interest in the excellent physical behaviours that cation-ordered perovskite phases exhibit, it is very challenging to synthesize materials with complex cation ordering patterns. This is because at the high temperatures required for the synthesis of these materials entropy frustrates the formation of the cation-ordered phases. Thus a strong enthalpic motivation is needed to overcome this thermodynamic condition in order to prepare cation ordered phases. The conventional strategy adopted is to introduce cations with different charges and/or sizes into suitable lattices, and thus cation order can be achieved by the tendency to neutralize the local charge and/or minimize the local lattice strain. Typical cation ordering patterns adopted by perovskite phases are the rock salt, columnar, or layered arrangements[7] as shown in Figure 3.1a.

However, these charge and/or size requirements tend to limit the diversity of cation ordering patterns and restrict the chemical composition of materials. Thus novel strategies to prepare cation ordered phases are being attempted. Recently Turp et al.[23] utilized the preference some cations have for particular coordination numbers and geometries, to synthesize the anion-deficient perovskite $Ba_4CaFe_3O_{9.5}$ with a complex cation ordering pattern. In the structure of $Ba_4CaFe_3O_{9.5}$, as shown in Figure 3.1b, the large Ca^{2+} cations occupy octahedral sites and Fe^{3+} cations are located in the tetrahedral and pyramidal sites.

Interestingly, the complex cation ordering in $Ba_4CaFe_3O_{9.5}$ lifts the inversion symmetry of the host perovskite lattice to give rise to an acentric structure and the material exhibits second harmonic generation activity.

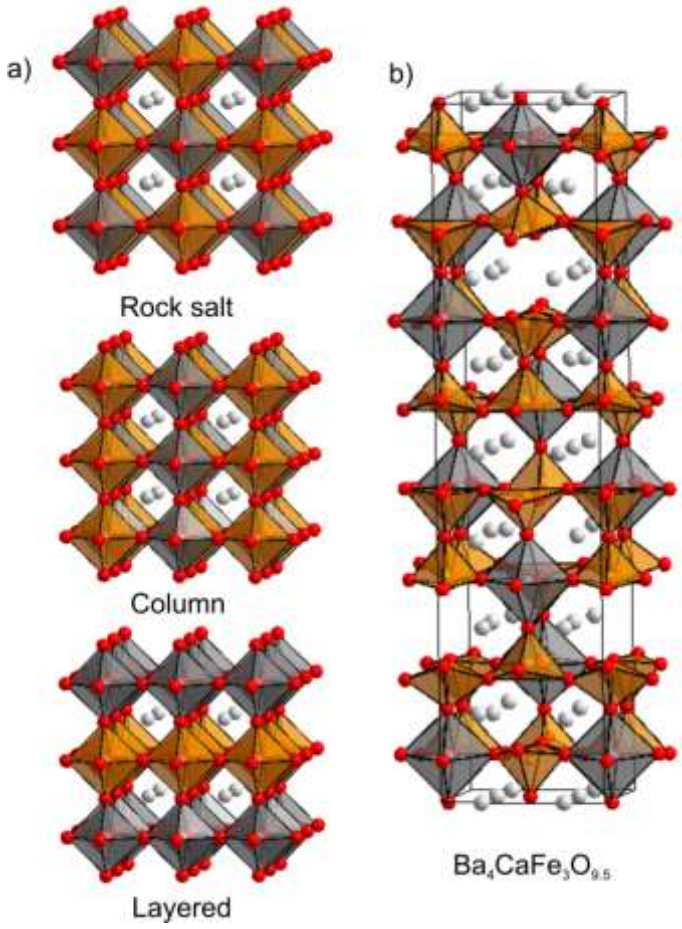

Figure 3.1 (a) Typical B-site cation ordering patterns: rock salt, column, and layered. (b) The complex cation ordered structure of $Ba_4CaFe_3O_{9.5}$.

The introduction of anion vacancies, combined with the size differences between B-site cations, encourages the segregation of cations which favour different coordination environments and the formation of complex cation ordering patterns. In this chapter, the cation and anion-vacancy ordered phases Ba_2YFeO_5 and Ba_2YCoO_5 are described and the structure and magnetic behaviours are discussed.

3.2 Experimental

Ba_2YFeO_5 was prepared via a high-temperature ceramic route. Suitable stoichiometric ratios of $BaCO_3$ (99.997%), Y_2O_3 (99.998%, dried at 900 ^oC) and Fe_2O_3 (99.99%) were ground together in an agate pestle and mortar and then heated in air at 1000 ^oC to decompose the carbonate. The resulting materials were then reground, pressed into 13 mm pellets and heated at 1425 ^oC for two periods of 40 hours under flowing argon. The formation of single phase was confirmed by X-ray powder diffraction.

Ba_2YCoO_5 was prepared via a citrate precursor method. Suitable ratios of $BaCO_3$ (99.997%), Y_2O_3 (99.998%, dried at 900 ^oC) and cobalt powder (99.99%) were dissolved in 150 mL of a 1:1 mixture of 6 M nitric acid and distilled water. A total of 3.3 mol equivalent of citric acid and 5 mL of analar ethylene glycol were added, and the solution was heated with constant stirring. The gel formed was subsequently ground into a powder, and heated to 850 ^oC at 1 ^oC/min in air. The resulting powder was then pressed into 13 mm pellets and heated at 965 ^oC for 4 periods of 40 hours under flowing argon. The formation of single phase was confirmed by X-ray powder diffraction.

Neutron powder diffraction data were collected on the instrument D2b at ILL, France (Ba_2YFeO_5) and GEM at ISIS, UK (Ba_2YCoO_5).

3.3 Results

3.3.1 Chemical and structural charaterization

X-ray powder diffraction data collected from Ba_2YFeO_5 could be indexed using a monoclinic unit cell (a = 7.31 Å, b = 6.12 Å, c = 7.52 Å and β = 117.6 ^{o}), suggesting that Ba_2YFeO_5 adopts a complicated cation ordered structure rather than a simple cubic

perovskite structure. Iodometric titrations performed on the Ba_2YFeO_5 sample indicated an average iron oxidation state of +3 (detailed in Table A3.1).

X-ray powder diffraction data collected from Ba_2YCoO_5 are similar to those collected from the Fe analogue, suggesting that Ba_2YCoO_5 adopts the same structure as the Fe analogue (Figure 3.2). Iodometric titrations performed on the Ba_2YCoO_5 sample indicated an average cobalt oxidation state of +3 (detailed in Table A3.2).

X-ray powder diffraction data collected from both Ba_2YFeO_5 and Ba_2YCoO_5 samples do not allow the positions of oxide ions to be determined accurately, as explained in chapter 2. In order to better understand the structures of Ba_2YMO_5 (M = Fe, Co) phases, neutron powder diffraction data were collected from both samples.

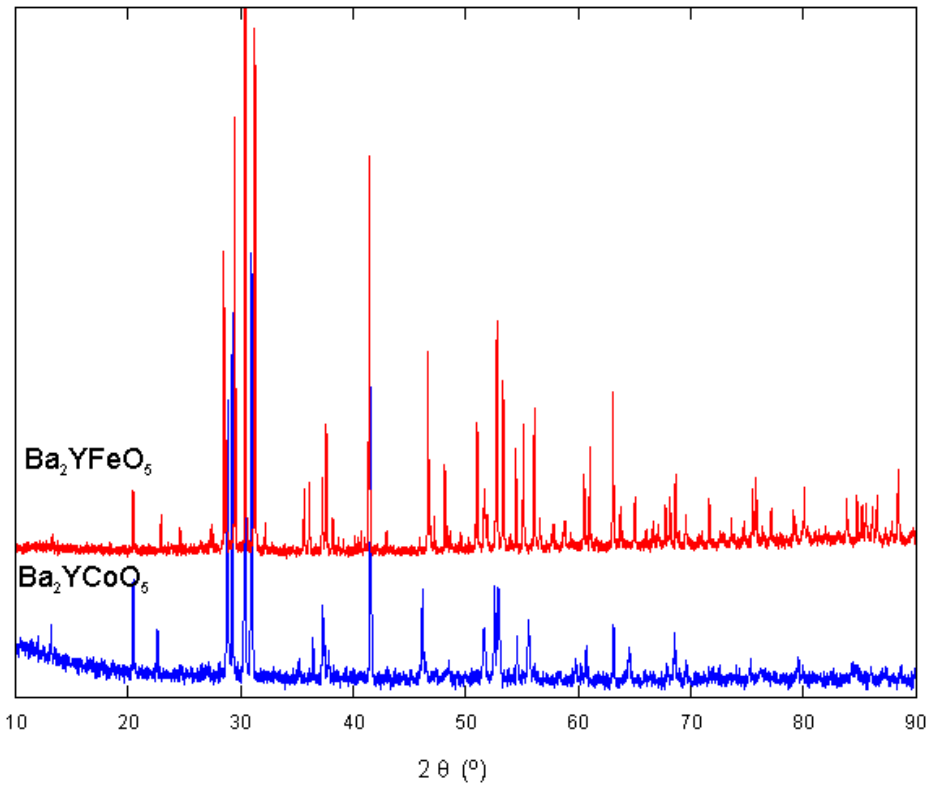

Figure 3.2 X-ray diffraction data collected from Ba_2YMO_5 (M = Fe and Co).

3.3.2 Structural refinements

3.3.2.1 Ba_2YFeO_5

In order to determine the structure of Ba_2YFeO_5, a series of structural models based on known cation-ordered $Ba_2MM'O_5$ phases were constructed and the simulation results of the constructed models were then compared with the neutron powder diffraction data collected from Ba_2YFeO_5.

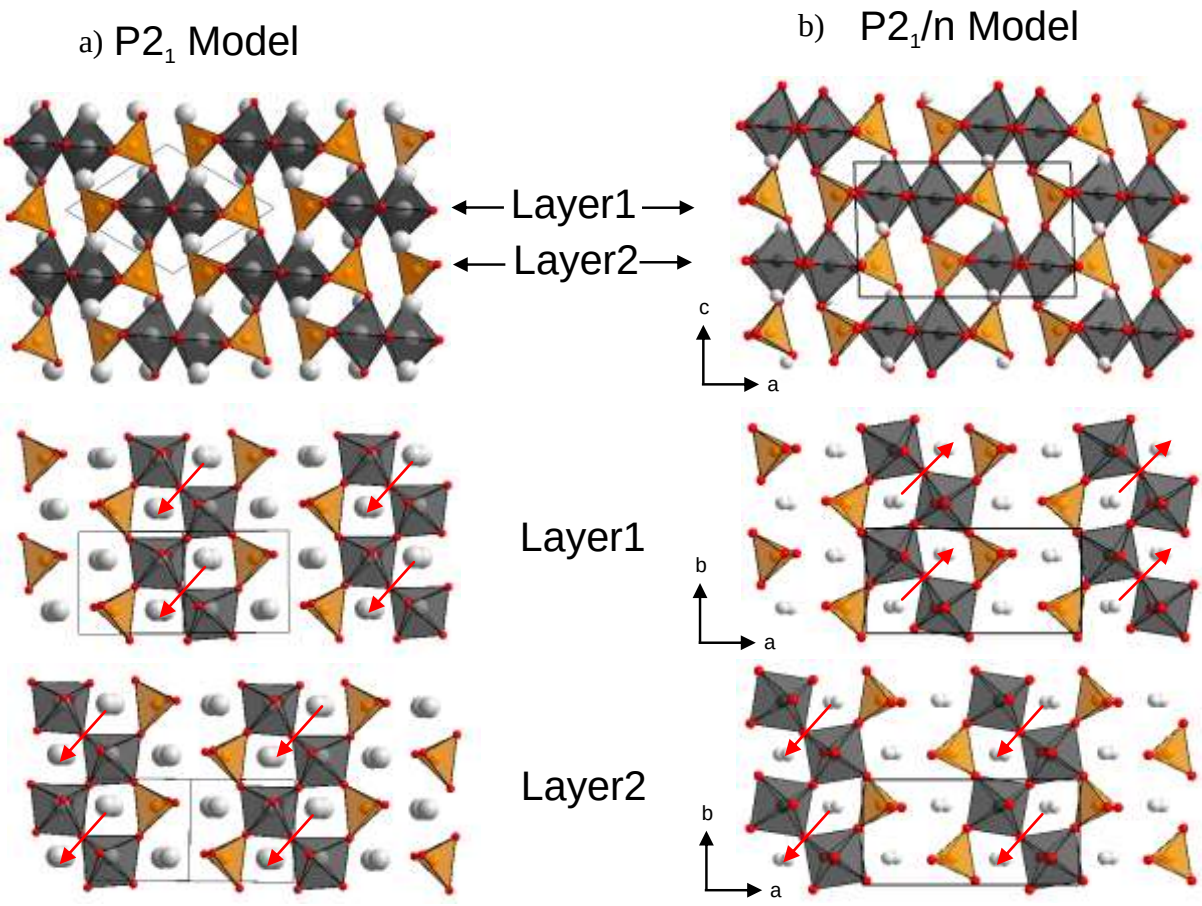

Figure 3.3 Structural models constructed based on *P2$_1$* and *P2$_1$/n* space groups. Grey octahedra represent YO_6, orange tetrahedra FeO_4, and grey spheres Ba^{2+}.

A model based on the structure of Ba_2NdAlO_5[64] (Figure 3.3a) was constructed in the *P2$_1$* space group with neodymium and aluminium replaced with yttrium and iron respectively. The simulation results of this *P2$_1$* model could account for majority of the diffraction features collected from Ba_2YFeO_5. Thus this *P2$_1$* model was then refined against the neutron

powder diffraction data collected from Ba_2YFeO_5 at room temperature. The result of refinement indicated that the majority of the observed diffraction features can be accounted for very well by this *P2₁* model, but some diffraction features with low intensity were not described, suggesting that Ba_2YFeO_5 shares a similar cation-ordered structure with the known Ba_2NdAlO_5 phase but has a subtly different arrangement of oxide ions. The additional features in the neutron diffraction data could be indexed using a larger unit cell which is related to the lattice parameters of a simple cubic perovskite structure by means of a $2\sqrt{2} \times \sqrt{2} \times 2$ expansion as shown in Figure 3.3b.

Thus another structural model, based on the cation ordering pattern of Ba_2NdAlO_5, was constructed in the larger cell determined from the Ba_2YFeO_5 neutron diffraction data, with *P2₁/n* space group symmetry. As shown in Figure 3.3b, it can be seen that the difference between *P2₁* and *P2₁/n* models lies in the twisting of YO_6 octahedra in the lattices. In the *P2₁* model all the octahedral chains twist in the same direction, while in the *P2₁/n* model the octahedral chains twist in opposite directions in adjacent layers. This slight difference cannot be detected by X-ray powder diffraction data, hence the smaller unit cell was observed for the X-ray diffraction data. This is why neutron powder diffraction data are necessary to solve the structure exactly. Refinement of the model with an expanded unit cell against neutron powder diffraction data collected from Ba_2YFeO_5 converged rapidly to give a good statistical fit (χ^2 = 2.81). Refinement of the yttrium and iron site fractional occupancies indicated no evidence of anti-site cation disorder. Observed calculated and difference plots from the refinement are shown in Figure 3.4. The refined structure of Ba_2YFeO_5 is shown in Figure 3.5. Full details of the refined structure of Ba_2YFeO_5 are listed in Table 3.1, with selected bond lengths in Table 3.2.

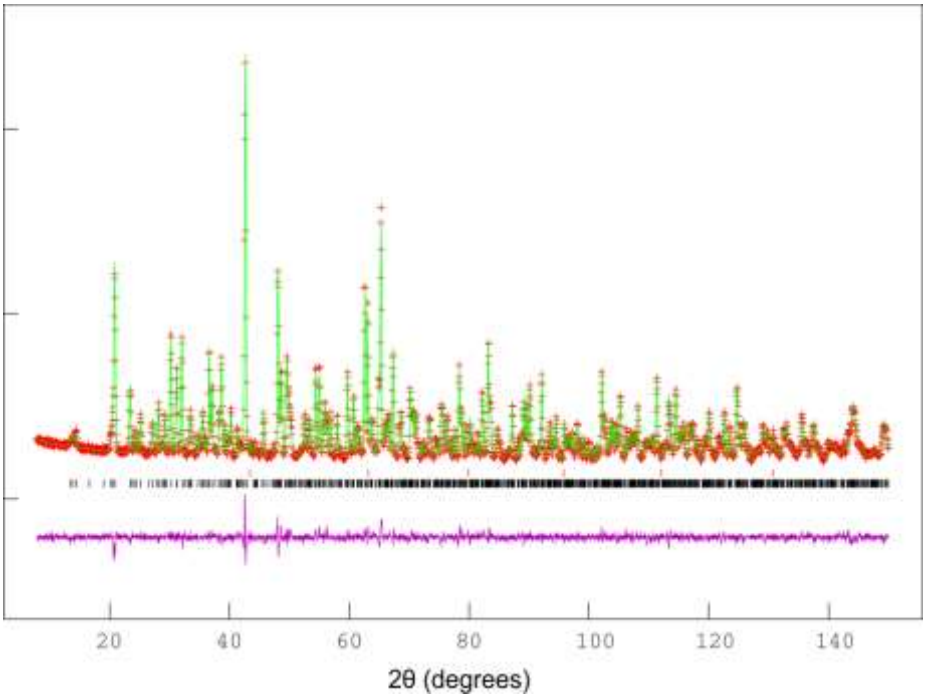

Figure 3.4 Observed, calculated and difference plots from the refinement of Ba_2YFeO_5 against neutron diffraction data. Lower tick marks indicate peak positions of the title phase; upper tick marks indicate peak positions from the vanadium sample holder.

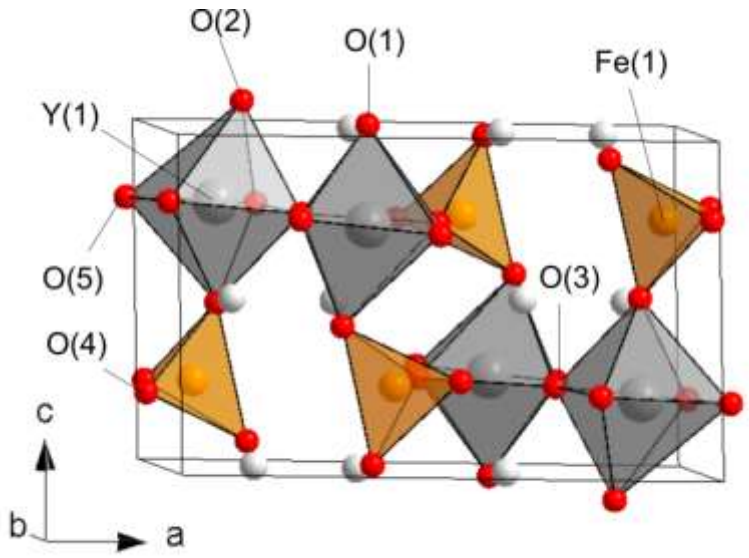

Figure 3.5 Atomic positions in the structure of Ba_2YFeO_5.

Atom	site	*x*	*y*	*z*	U_{iso} (Å^2)
Ba(1)	*4e*	0.1529(2)	0.2585(1)	0.0176(4)	0.0073(8)
Ba(2)	*4e*	0.1168(2)	0.2559(9)	0.5087(4)	0.0032(7)
Y(1)	*4e*	0.8697(2)	0.2497(8)	0.2297(3)	0.0035(5)
Fe(1)	*4e*	0.9157(1)	0.2369(4)	0.7570(2)	0.0017(4)
O(1)	*4e*	0.8710(2)	0.2598(7)	0.5252(4)	0.0087(7)
O(2)	*4e*	0.3194(2)	0.2377(9)	0.4319(4)	0.0101(8)
O(3)	*4e*	0.2285(3)	0.0445(7)	0.7530(5)	0.0064(8)
O(4)	*4e*	0.5201(3)	0.0409(6)	0.2829(4)	0.0071(8)
O(5)	*4e*	0.4822(3)	0.5381(7)	0.2707(5)	0.0097(9)
Ba_2YFeO_5 - Space group $P2_1/n$ a = 12.5860(1) Å, b = 6.08289(7) Å, c = 7.8070(1) Å, β = 92.247(1) ^{o} χ^2 = 2.81, wRp = 4.11%, Rp = 3.18%					

Table 3.1. Structural parameters refined against neutron powder diffraction data collected from Ba_2YFeO_5 at room temperature.

cation	anion	Bond (Å)	BVS
Y(1)	O(1)	2.307(4)	Y +3.10
	O(2)	2.387(4)	
	O(3)	2.182(6)	
	O(3)	2.187(5)	
	O(4)	2.254(6)	
	O(5)	2.265(5)	
Fe(1)	O(1)	1.878(3)	Fe +2.90
	O(2)	1.867(3)	
	O(4)	1.872(5)	
	O(5)	1.890(4)	

Table 3.2. Selected bond lengths from the refined structure of Ba_2YFeO_5.

3.3.2.2 Ba_2YCoO_5

Neutron powder diffraction data collected from Ba_2YCoO_5 could be readily indexed using a monoclinic unit cell (a = 12.39 Å, b = 6.11 Å, c = 7.87 Å, β = 91.6 °), directly analogous to the expanded cell of Ba_2YFeO_5, suggesting that Ba_2YCoO_5 and Ba_2YFeO_5 adopt similar structures. Thus a $P2_1/n$ structural model was constructed on the basis of the Ba_2YFeO_5 structure described above, in which iron was replaced with cobalt. The constructed model was then refined against the neutron powder diffraction data collected from Ba_2YCoO_5 at room temperature. During the refinements, the all atomic positional and displacement parameters were allowed to refine freely. Refinement of $P2_1/n$ model against neutron powder diffraction data collected from Ba_2YCoO_5 converged rapidly to give a good statistical fit (χ^2 = 2.48). Observed, calculated and difference plots from the refinement are shown in Figure 3.6 and Appendix A3.3. Refinement of the yttrium and cobalt site occupancies indicated no evidence of anti-site cation disorder. Full details of the refined structure of Ba_2YCoO_5 are listed in Table 3.3, with selected bond lengths in Table 3.4.

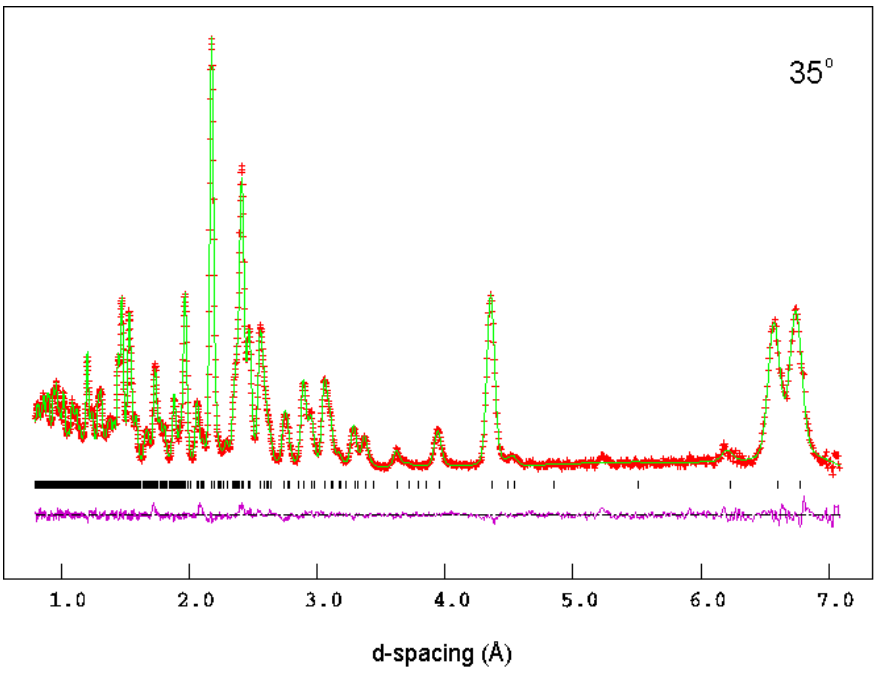

Figure 3.6 Observed, calculated and difference plots from the refinement of Ba_2YCoO_5 against neutron diffraction data.

Atom	site	*x*	*y*	*z*	U_{iso} (Å^2)
Ba(1)	*4e*	0.1400(1)	0.2550(6)	0.0064(2)	0.0059(3)
Ba(2)	*4e*	0.1159(2)	0.2499(6)	0.5051(3)	0.0059(3)
Y(1)	*4e*	0.8713(1)	0.2448(6)	0.2367(2)	0.0081(3)
Co(1)	*4e*	0.9070(3)	0.2351(16)	0.7520(6)	0.0183(15)
O(1)	*4e*	0.8675(1)	0.2543(6)	0.5256(3)	0.0152(3)
O(2)	*4e*	0.3272(1)	0.2393(6)	0.4416(2)	0.0152(3)
O(3)	*4e*	0.2316(2)	0.0396(4)	0.7555(4)	0.0096(6)
O(4)	*4e*	0.5089(2)	0.0255(4)	0.2724(4)	0.0152(3)
O(5)	*4e*	0.4824(2)	0.5287(4)	0.2656(4)	0.0152(3)
Ba_2YCoO_5 - Space group $P2_1/n$ a = 12.387(6) Å, b = 6.105(3) Å, c = 7.870(3) Å, β = 91.615(1) ^{o} χ^2 = 2.502, wRp = 2.32%, Rp = 2.09%					

Table 3.3 Structural parameters refined against neutron powder diffraction data collected from Ba_2YCoO_5 at room temperature.

Cation	Anion	Bond (Å)	BVS
Y(1)	O(1)	2.276(3)	Y +3.22
	O(2)	2.373(3)	
	O(3)	2.156(4)	
	O(3)	2.183(4)	
	O(4)	2.269(4)	
	O(5)	2.242(4)	
Co(1)	O(1)	1.838(5)	Co +2.57
	O(2)	1.820(5)	
	O(4)	1.935(8)	
	O(5)	1.863(9)	

Table 3.4 Selected bond lengths from the refined structure of Ba_2YCoO_5.

3.3.3 Magnetic behaviour

Ba_2YFeO_5. Zero-field-cooled and field-cooled magnetization data of Ba_2YFeO_5 were collected in an applied field of 100 Oe in the temperature range of 5 < T / K < 300. As shown in Figure 3.7, the data collected from Ba_2YFeO_5 can be fitted to the Curie – Weiss law ($\chi = C / (T - \theta)$), over the whole measured temperature range, to give values of C = 4.84(4) cm^3 K mol^{-1}; θ = -21.5(2) K, consistent with paramagnetic behaviour. Neutron diffraction data collected from Ba_2YFeO_5 at 5 K show no additional diffraction features compared to analogous room temperature data, inconsistent with magnetic order at low temperature.

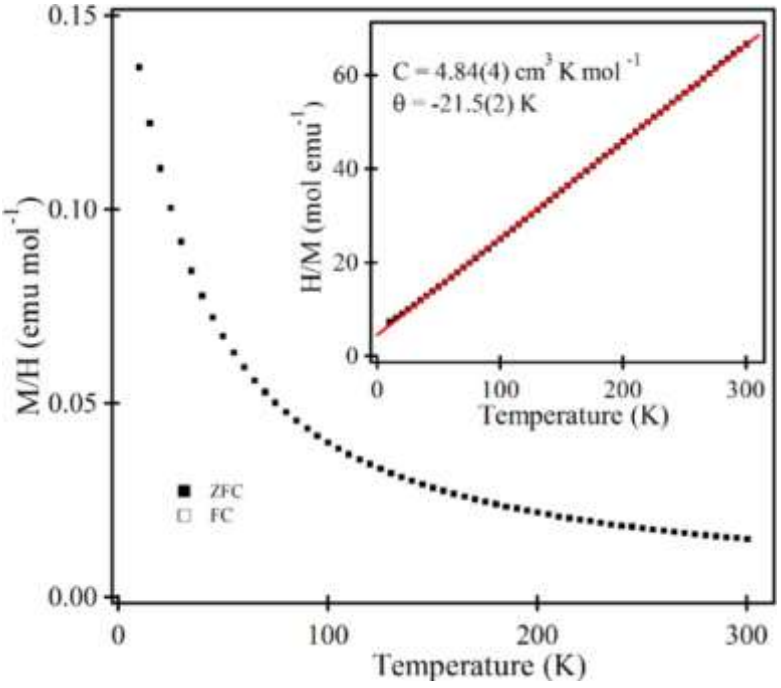

Figure 3.7 Zero-field-cooled and field-cooled magnetization data collected from Ba_2YFeO_5. Insets show fits of H/M to the Curie–Weiss law.

Ba_2YCoO_5. As shown in Figure 3.8, zero-field-cooled and field-cooled magnetization data collected from Ba_2YCoO_5 can be fitted to the Curie – Weiss law in the temperature range 40 < T/K < 300, to yield values of C = 2.632(2) cm^3 K mol^{-1} and θ = -34.8(1) K. Magnetization data collected from Ba_2YCoO_5 diverge below 10 K slightly, suggesting the onset of

magnetic order. Neutron powder diffraction data were collected from Ba_2YCoO_5 at 7 K. However, as shown in Figure 3.9, no obvious additional diffraction features can be observed compared to analogous room temperature data.

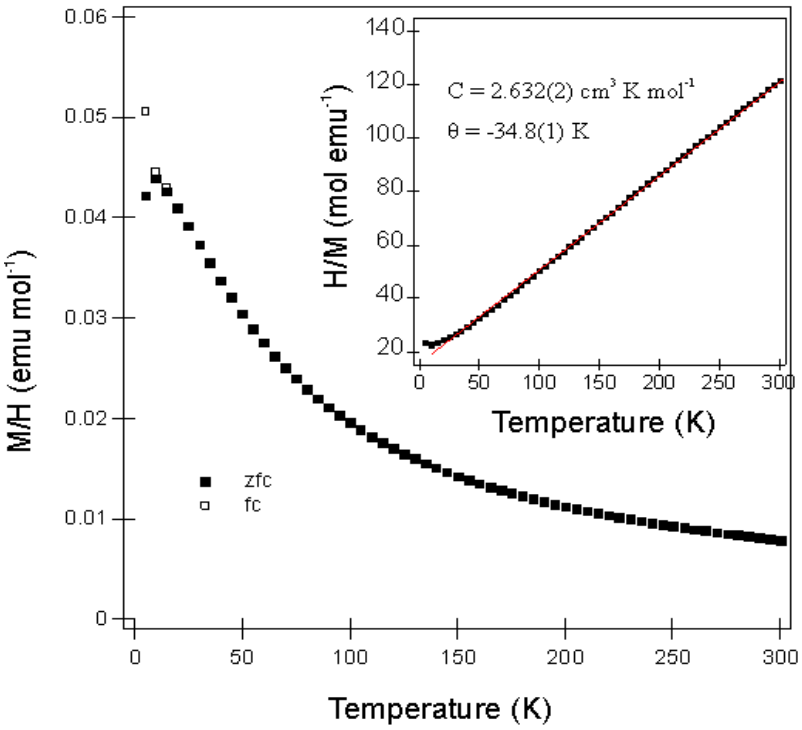

Figure 3.8 Zero-field-cooled and field-cooled magnetization data collected from Ba_2YCoO_5. Insets show fits of H/M to the Curie–Weiss law.

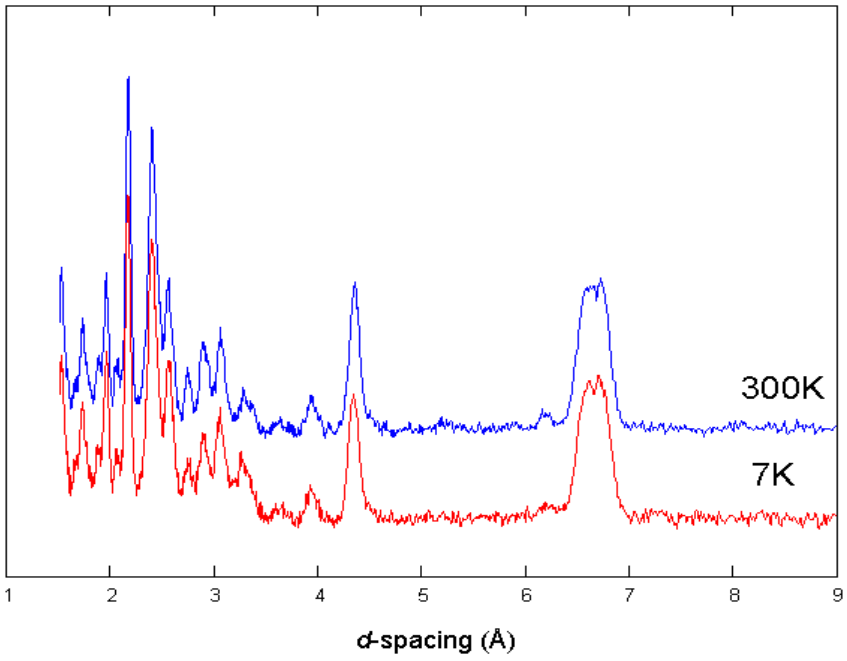

Figure 3.9 Comparison of neutron diffraction data collected from Ba_2YCoO_5 at 7 and 300 K.

3.4 Discussion

3.4.1 Cation and anion-vacancy ordering in Ba_2YMO_5 (M= Fe and Co)

The anion-deficient Ba_2YMO_5 (M = Fe, Co) perovskite phases described above adopt structures with complex cation and anion-vacancy ordered structures with a $2\sqrt{2} \times \sqrt{2} \times 2$ geometric unit cell expansion relative to a simple cubic perovskite phase.

The Ba_2YMO_5 (M = Fe, Co) phases adopt a complicated cation ordering pattern, in which Y^{3+} and Fe^{3+}/Co^{3+} cations are located in octahedral and tetrahedral sites respectively. Considering the size difference and coordination environments of two B-site cations in the crystal structures of Ba_2YFeO_5, the large Y^{3+} cations demonstrate a strong preference for the sites with coordination number of 6. Comparatively, the smaller Fe^{3+} cations can be located in the sites with lower coordination number. In addition, the d^5 'spherical' electronic configuration allows Fe^{3+} to be located in tetrahedral sites with no 'electronic' penalty. As a result, the complex cation ordered structure is constructed based on an extended network of YO_6 octahedra and FeO_4 tetrahedra. Thus the size difference between Y^{3+} and Fe^{3+}/Co^{3+} cations is considered as one of the important factors leading the cation ordering in the lattice of Ba_2YMO_5 (M = Fe, Co).

As shown in Figure 3.10, a large number of anion vacancies are observed in the lattice of Ba_2YMO_5 (M = Fe, Co), leading to the formation of two distinct transition metal coordination sites with different coordination number, a 6-coordinate octahedral site and a 4-coordinate tetrahedral site. All the Y^{3+} cations are located in the octahedral sites and Fe^{3+}/Co^{3+} cations occupy the tetrahedral sites. The overall structural framework is constructed based on the zigzag chains of the apex-linked YO_6 octahedra extending along *y* direction interspersed with MO_4 (M = Fe, Co) tetrahedra.

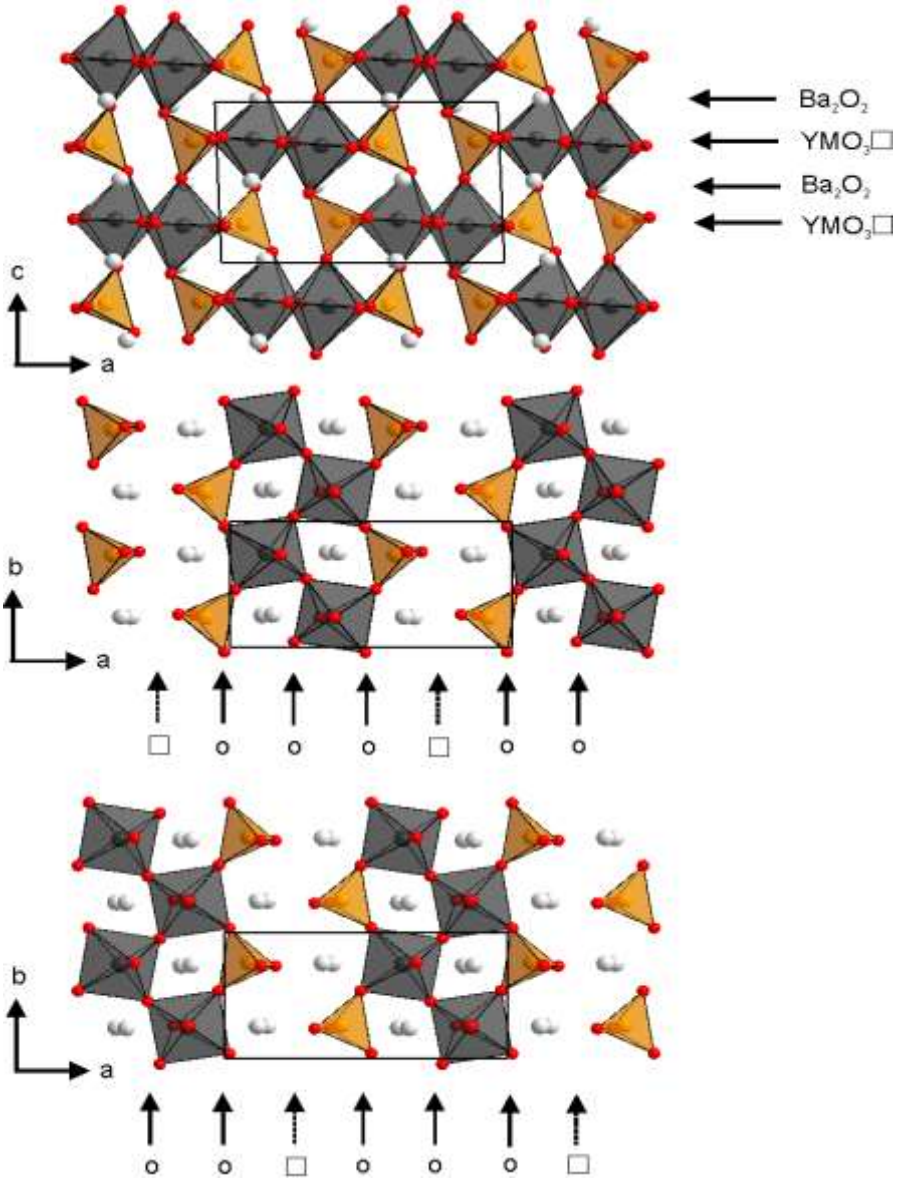

Figure 3.10 Refined of structure of Ba_2YMO_5. (a) View down the b-axis. (b) View down the c-axis showing the layer of polyhedra at z ~ 0.75. (c) View down the c-axis showing the layer of polyhedra at z ~ 0.25. Solid line indicates unit cell.

The anion vacancies present in the lattice of Ba_2YMO_5 (M = Fe, Co) are in an unusual arrangement. In order to clarify the arrangement of anion vacancies in the lattice, the structure of Ba_2YMO_5 (M = Fe, Co) can be described as a repeated stacking sequence of – Ba_2O_2 – YMO_3 – Ba_2O_2 – YMO_3 – in an analogy to the – AO – BO_2 – AO – BO_2 – stacking in the simple cubic perovskite structure, as shown in Figure 3.10. In each YMO_3 layer, the cyclic sequence of the anion vacancies distributed along *x*-axis follows – – O –

O – O – –. The anion vacancies are stacked in an ordered arrangement in the adjacent YMO_3 layers.

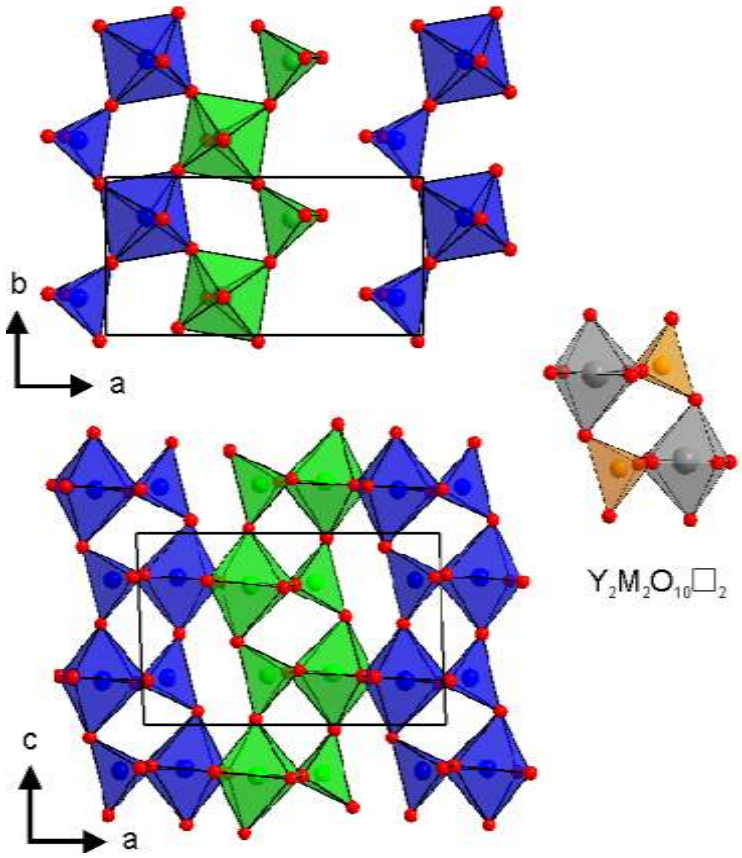

Figure 3.12 Structures of Ba_2YMO_5 (left) and $Ba_3YM_2O_{7.5}$ (right) are constructed from $Y_2M_2O_{10}$ $_2$ cation and anion-vacancy ordered units (middle). In the latter structure these units are combined with apex-linked dimers of MO_4 tetrahedra.

3.4.2 Bond network

In the structure of Ba_2YMO_5 (M = Fe, Co), $Y_2M_2O_{10}$ $_2$ basic building units can be observed as shown in Figure 3.12. Each $Y_2M_2O_{10}$ $_2$ building unit contains two YO_6 octahedra and two MO_4 tetrahedra connected in an anti-parallel arrangement to form a 'rock-salt' type cation-ordered unit as shown in Figure 3.12. Neighbouring $Y_2M_2O_{10}$ $_2$ units are connected to each other in the *yz*-plane through Y – O – Y bonds with YO_6 octahedra sharing apexes. The resulting structure of Ba_2YMO_5 (M = Fe and Co) is composed of the zigzag chains of YO_6 octahedra and isolated MO_4 tetrahedra along *y*-axis.

In the structure of Ba_2YMO_5 (M = Fe and Co), no M – O − M connections can be observed at the interface between $Y_2M_2O_{10}$ $_2$ units due to the mismatch between long Y − O and short M − O bond lengths. The recurrence of the $Y_2Mn_2O_{10}$ $_2$ units in the structures of Ba_2YMO_5 (M = Fe, Co) can be understood on the basis of secondary building units, indicating $Y_2M_2O_{10}$ $_2$ basic unit is a stable local structural configuration which actually can be seen as a rock-salt type cation ordering unit. The formation of this secondary building unit not only minimizes the local lattice stain due to the size difference of Y^{3+} and M^{3+} (M = Fe and Co) cations, but also localizes the anion vacancies in an appropriate manner, maintaining a 6-fold coordination of Y^{3+} and a 4-fold coordination of Fe^{3+}/Co^{3+}.

It should be noted that the Ba_2YMO_5 (M = Fe, Co) phases do not adopt the commonly observed brownmillerite structure, although they have the same stoichiometric composition of $A_2B_2O_5$. In order to understand the factors influencing the complex cation ordering in Ba_2YMO_5 (M = Fe and Co), several cation-ordered double perovskite structures are listed in Figure 3.11. The rock-salt type cation ordering is the most common in double perovskite structures, which can be induced by charge differences (e.g. Sr_2MoFeO_6) or size differences (e.g. Ba_2ErRuO_6[65]) between the two cations in the B sites. When anion vacancies are introduced into the lattice, 4-coordinate tetrahedral sites are formed, leading to different cation arrangements in the lattice. In the structure of Sr_2MnGaO_5, the introduction of anion vacancies leads to a layered arrangement of GaO_4 tetrahedra (Ga^{3+} CN4 = 0.47 Å) and MnO_6 octahedra (Mn^{3+} CN6 = 0.645 Å).[66] In the structure of Ba_2YMO_5 (M = Fe, Co), the large size difference between Y^{3+} (CN6 = 0.9 Å) and M^{3+} (Fe^{3+} CN4 = 0.49 Å), combined with the presence of anion vacancies in the lattice, limits the formation of M – O – M bond similar to the Ga – O – Ga bond in Sr_2MnGaO_5. Thus, the cation-ordered structure adopted by Ba_2YMO_5 (M = Fe, Co) is attributed to the combination of cation size difference between two B-site cations and the presence of anion vacancies in the lattice.

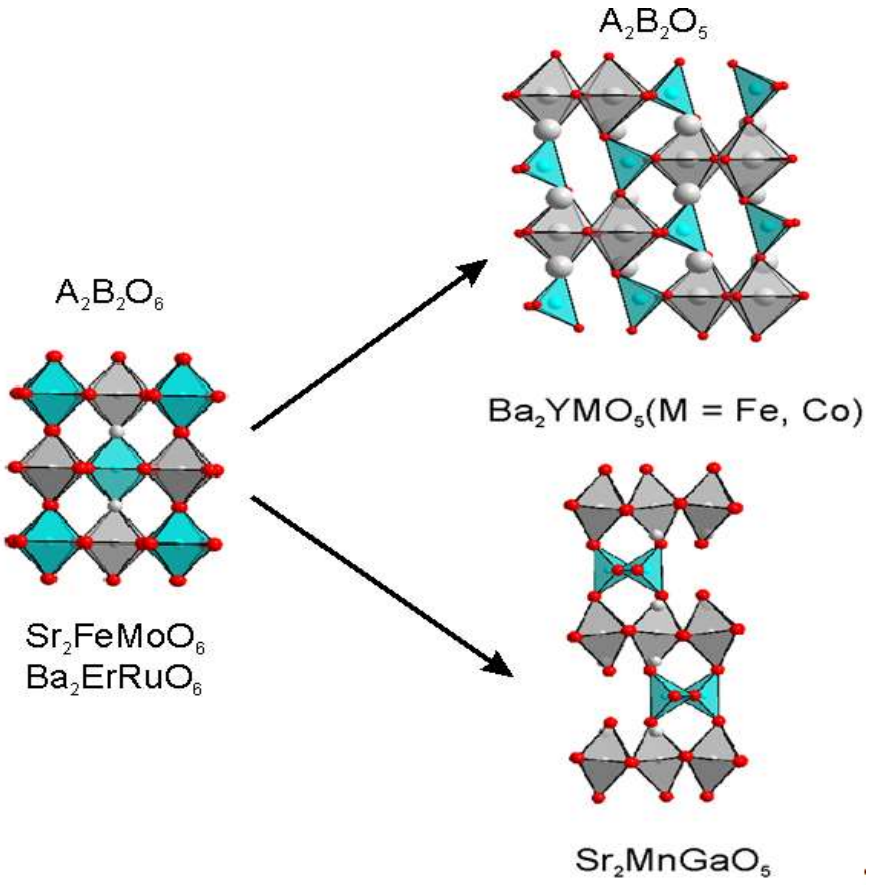

Figure 3.11 Relationship of structure and cation size and anion vacancies in double perovskites.

The presence of anion vacancies, combined with the particular lattice strain, leads to the stabilization of this kind of cation ordering pattern. Thus by analyzing the structures of these phases, it could be concluded that the particular cation ordering patterns can be designed by carefully selecting cations with different coordination preference and controlling the oxygen content.

3.4.3 Tetrahedral Co^{3+} centres in Ba_2YCoO_5

It should be noted the Co^{3+} cations in the structure of Ba_2YCoO_5 are located in the tetrahedral sites. Tetrahedral Co^{3+} centres are very rare in the extended oxides and octahedral Co^{3+} centres are common, because Co^{3+} adopts a d^6 electronic configuration which is stabilized by an octahedral ligand field. An example is Co_3O_4 which adopts a normal spinel structure consisting of CoO_4 tetrahedra and CoO_6 octahedra in a three

dimensional framework (Figure 3.13), in which all Co^{2+} centres are located in the tetrahedral sites (light blue) and Co^{3+} in the octahedral sites (dark blue), demonstrating the preference of Co^{3+} for octahedral coordination.

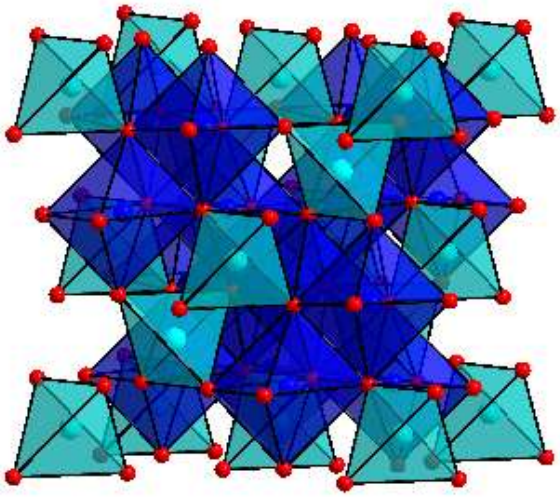

Figure 3.13 Structure of Co_3O_4.

The coordination environment of a transition metal is influenced by the structural framework in which it resides. For example, $ACoO_2$ (A = Li, Na, K and Rb) is a typical series of phases illustrating the effect of structural framework on the coordination number of transition metal centres. As shown in Figure 3.14, $LiCoO_2$[67] and $NaCoO_2$[68] adopt layered structures consisting of edge-sharing CoO_6 octahedra. The replacement of Li^+/Na^+ with larger K^+ in the 'A' sites leads to the formation of a new layered structure $KCoO_2$, consisting of edge-sharing CoO_5 pyramids.[69] In the structure of $RbCoO_2$[69], all the Co^{3+} centres were located in the apex-sharing CoO_4 tetrahedral sites. Thus an appropriate framework can stabilize the formation of tetrahedral Co^{3+} centres. In the structure of Ba_2YCoO_5, the size difference between Y^{3+} and Co^{3+} cations leads to a distance of 4.29 Å between cobalt centres (the average length of Co – O bonds in Ba_2YCoO_5 is 1.86 Å), thus limiting the Co – O – Co interactions and yielding Co^{3+} centres in the tetrahedral sites, as shown in Figure 3.14.

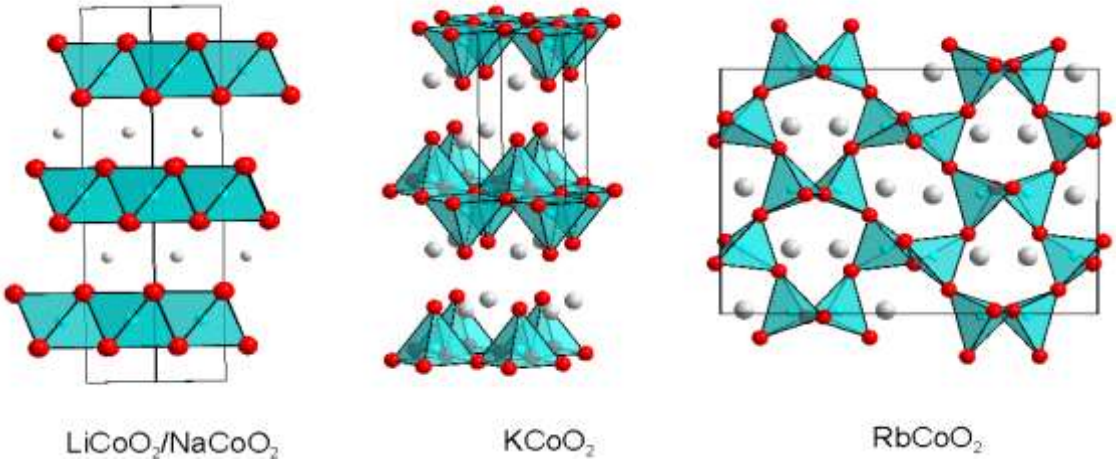

Face-sharing (CN = 6) | **Edge-sharing (CN = 5)** | **Corner-sharing (CN = 4)**

Figure 3.14 Structures of $ACoO_2$ (A = Li, Na, K and Rb).

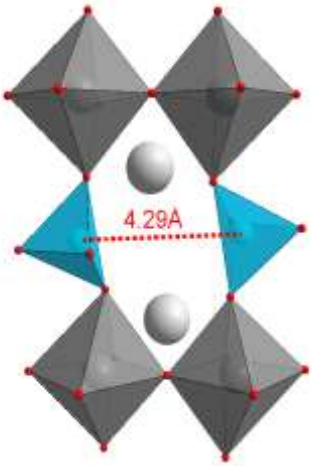

Figure 3.15 Illustration of Co^{3+} in tetrahedral sites.

In addition, the control of oxygen content in perovskite structures can facilitate to locate Co^{3+} centers in tetrahedral sites. For example, compared to the structure of the perfect stiochoimetric perovskite $LaCoO_3$, $Sr_2Co_2O_5$ adopts a brownmillerite structure, locating Co^{3+} centres in tetrahedral and octahedral sites.[70] In the structure of Ba_2YCoO_5, all the Y^{3+} centres are in the octahedral sites. The control of oxygen content in the lattice yields the formation of tetrahedral sites rather than pyramids or octahedral sites, which also limits the

Co – O – Co interactions. The presence of tetrahedral Co^{3+} centres in the structure of Ba_2YCoO_5 is therefore a consequence of these two factors.

3.4.4 Magnetism

Magnetization data collected from Ba_2YFeO_5 are consistent with paramagnetic behavior over the measured temperature range ($5 < T/K < 300$) with an observed moment approximately in line with that expected for a spin-only, S = 5/2, Fe^{3+} center ($\mu_{expected} = 5.91\ \mu_B$, $\mu_{observed} = 6.22\ \mu_B$).The lack of magnetic order is attributed to the absence of an extended Fe – O – Fe lattice in Ba_2YFeO_5.

Ba_2YCoO_5 adopts a similar structure to the Ba_2YFeO_5, in which the lack of long-range Co – O – Co interactions limits the long-range magnetic order. Although a divergence of the zero-field-cooled and field-cooled magnetization data was observed for Ba_2YCoO_5 at about 10 K, neutron powder diffraction data collected from Ba_2YCoO_5 at 7 K shows no additional diffraction feature compared to that collected at room temperature, indicating no magnetic order.

3.5 Conclusion

New complex cation and anion-vacancy ordered phases Ba_2YMO_5 (M = Fe and Co) were synthesized under flowing argon. The structures of Ba_2YMO_5 (M = Fe and Co) consist of YO_6 octahedra and MO_4 tetrahedra. The size difference between Y^{3+} and M^{3+} (M = Fe and Co) and the presence of anion vacancies in the lattice leads to the formation of a pseudo one-dimensional structure, which are constructed on the zigzag chains of YO_6 octahedra with tetrahedral M^{3+} (M = Fe and Co) centres in between.

Appendix

Mass (mg)	$x_{caculated}$	$x_{average}$
38.5	5.019	5.02(1)
39.1	5.021	
38.6	5.018	

Table A3.1 Iodometric titration results of Ba_2YFeO_x

Mass (mg)	$x_{caculated}$	$x_{average}$
39.5	4.986	5.01(2)
40.3	5.024	
38.6	5.012	

Table A3.2 Iodometric titration results of Ba_2YCoO_x

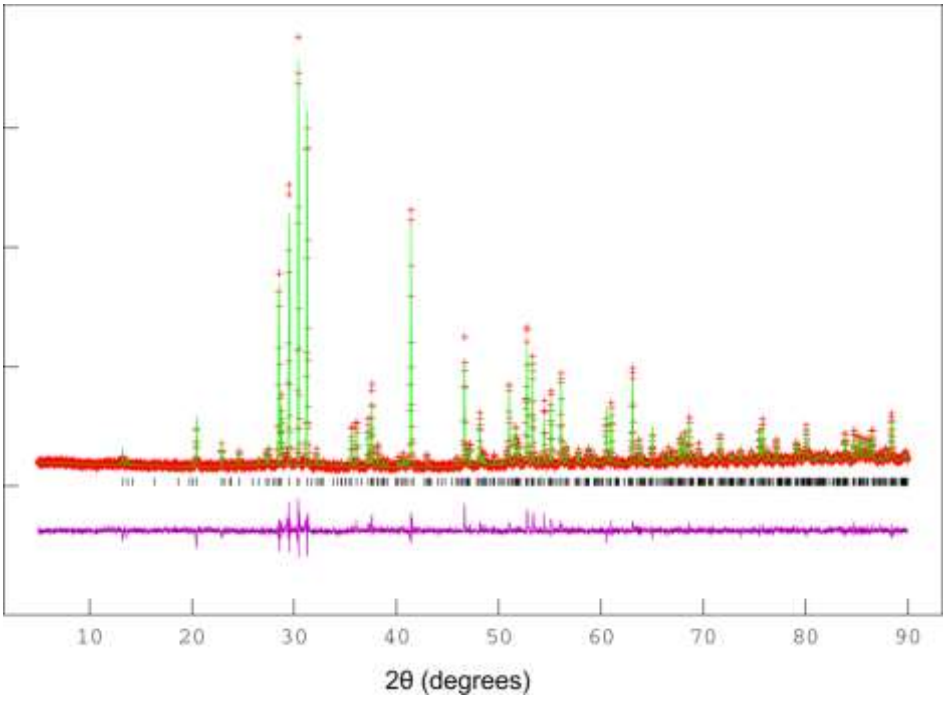

Figure A3.1 Observed, calculated and difference plots from the refinement of Ba_2YFeO_5 against X-ray diffraction data.

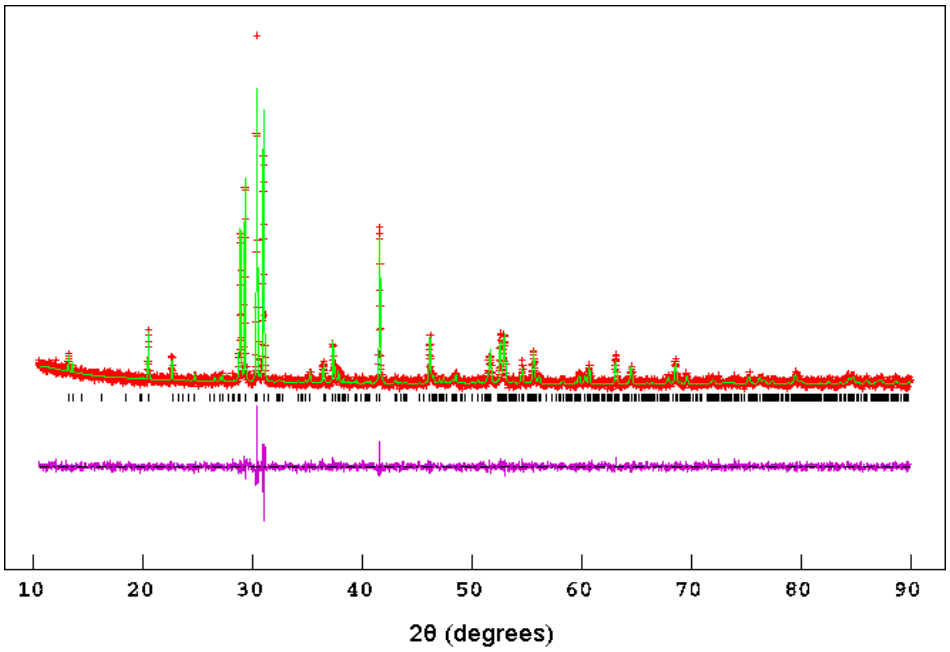

Figure A3.2 Observed, calculated and difference plots from the refinement of Ba_2YCoO_5 against X-ray diffraction data.

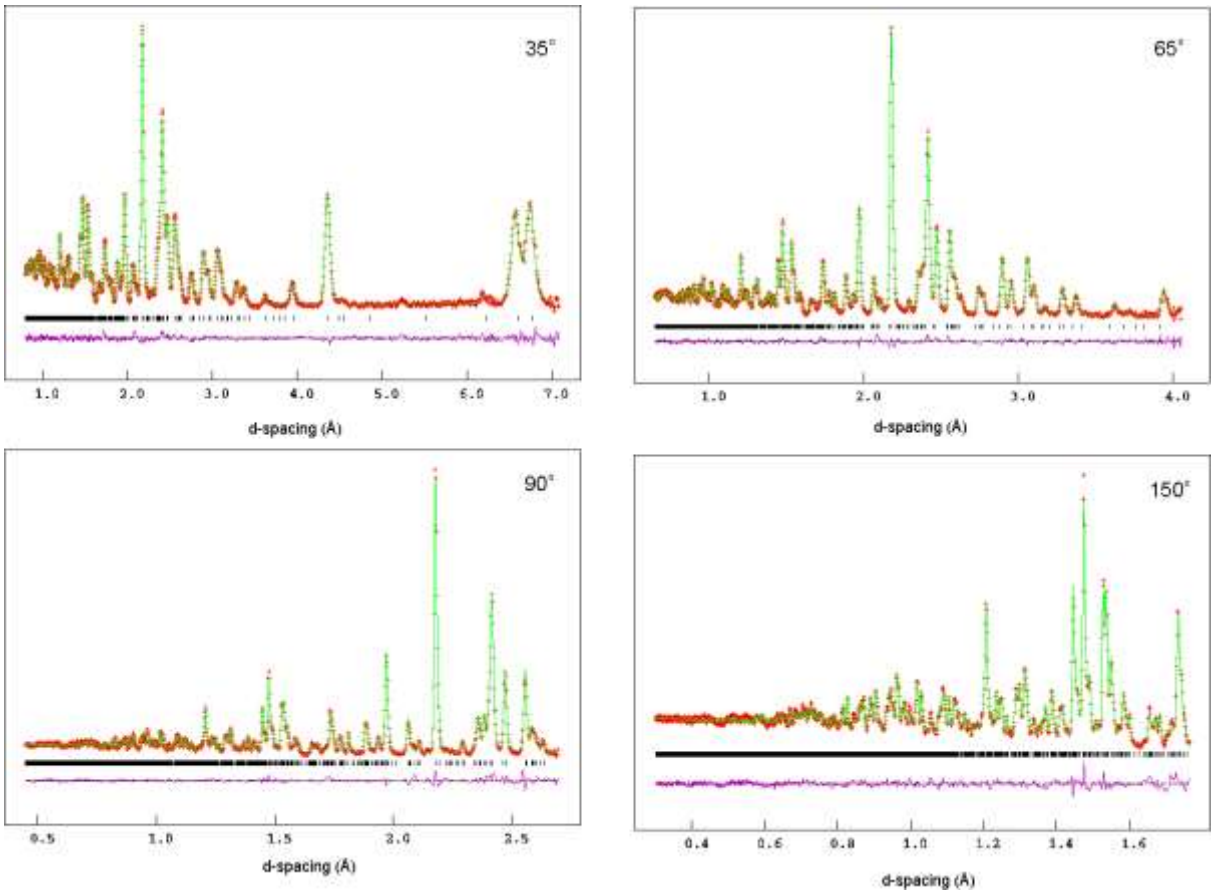

Figure A3.3 Observed, calculated and difference plots from the refinement of Ba_2YCoO_5 against neutron diffraction data.

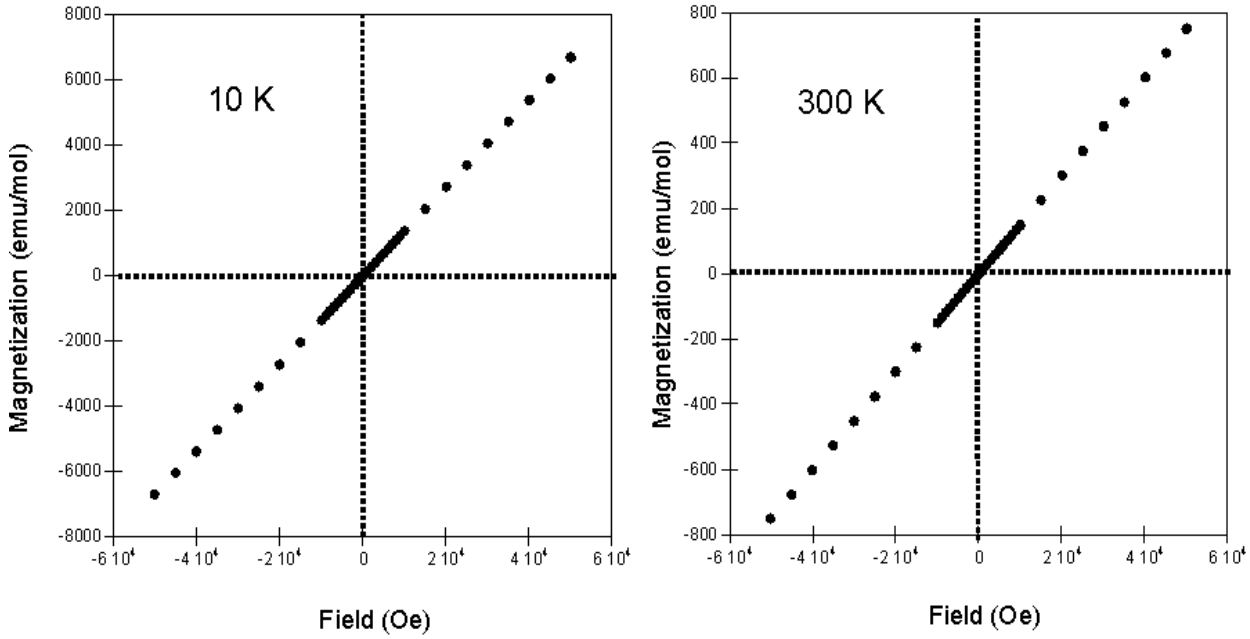

Figure A3.4 Magnetization-field isotherm collected at 5 K and 300 K from Ba_2YFeO_5.

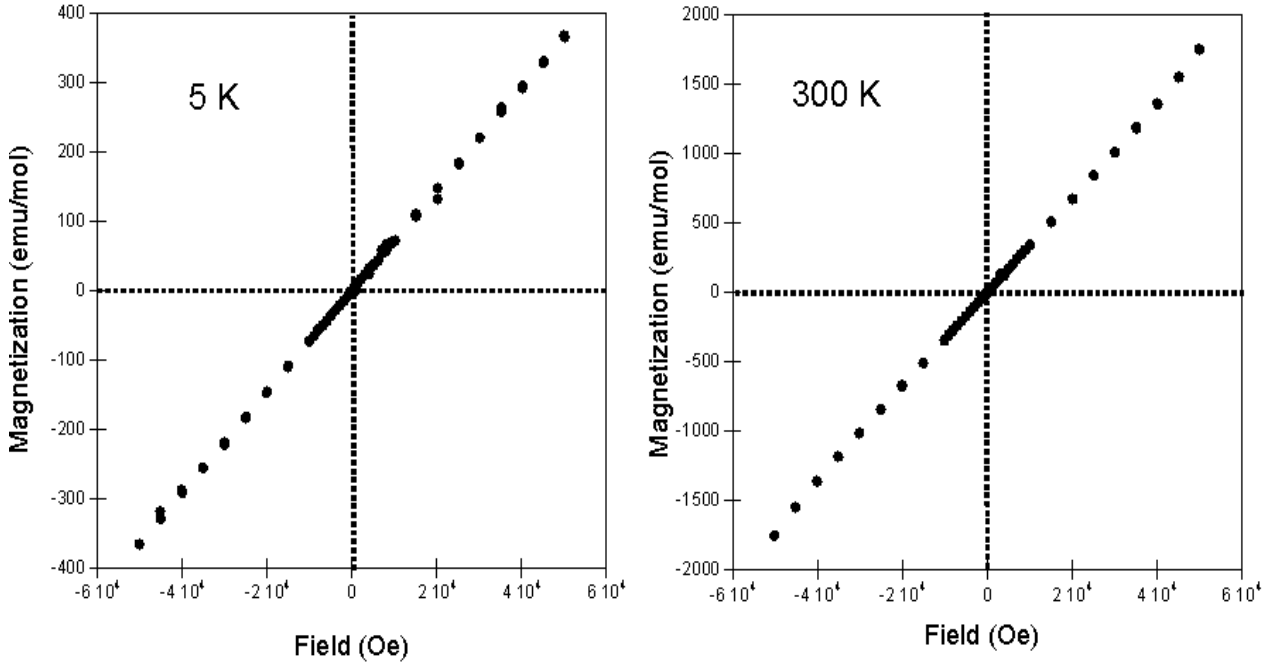

Figure A3.5 Magnetization-field isotherm collected at 5 K and 300 K from Ba_2YCoO_5.

Chapter 4 Complex cation ordering in $Ba_3YM_2O_{7.5}$ (M = Fe and Co)

4.1 Introduction

In chapter 3, the complex cation ordered phases Ba_2YFeO_5 and Ba_2YCoO_5 were described. Structural studies indicated that Ba_2YMO_5 (M= Fe, Co) phases consist of ordered arrays of YO_6 octahedra and FeO_4/CoO_4 tetrahedra. Complex cation order occurs as a function of the size difference and coordination preferences of cations. By appropriately selecting the cations and controlling the oxygen content, complex cation ordering patterns can be induced on the basis of anion-deficient perovskite lattices. In this chapter, the ratio of Y^{3+} and M^{3+} (M= Fe, Co) cations is adjusted in the lattice and the complex cation ordered $Ba_3YM_2O_{7.5}$ (M= Fe, Co) phases were synthesized. The structure and magnetic behaviours of $Ba_3YM_2O_{7.5}$ are discussed.

4.2 Experimental

$Ba_3YFe_2O_{7.5}$ was prepared via a high-temperature ceramic synthesis route. Suitable stoichiometric ratios of $BaCO_3$ (99.997%), Y_2O_3 (99.998%, dried at 900 ^oC) and Fe_2O_3 (99.99%) were ground together in an agate pestle and mortar and then heated in air at 1000 ^oC to decompose the carbonate. The resulting materials were then reground, pressed into 13 mm pellets and heated at 1425 ^oC for two periods of 40 hours under flowing argon. The formation of single phase was confirmed by X-ray powder diffraction.

$Ba_3YCo_2O_{7.5}$ was prepared via a citrate precursor method. Suitable ratios of $BaCO_3$ (99.997%), Y_2O_3 (99.998%, dried at 900 ^oC) and cobalt powder (99.99%) were dissolved in 150 mL of a 1:1 mixture of 6 M nitric acid and distilled water. A total of 3.3 mol equivalent of citric acid and 5 mL of analar ethylene glycol were added, and the solution was heated with constant stirring. The gel formed was subsequently ground into a fine powder, and heated to 850 ^oC at 1 ^oC/min in air. The resulting powder was then pressed into 13 mm pellets and heated at 900 ^oC for 4 periods of 40 hours under flowing argon. The formation of single phase was confirmed by X-ray powder diffraction.

Neutron powder diffraction data were collected on the instrument D2b at ILL ($Ba_3YFe_2O_{7.5}$), France and GEM at ISIS, UK ($Ba_3YCo_2O_{7.5}$).

4.3 Results

4.3.1 Chemical and structural characterization

$Ba_3YFe_2O_{7.5}$. X-ray powder diffraction data collected from $Ba_3YFe_2O_{7.5}$ could be readily indexed using a monoclinic cell (a = 8.02 Å, b = 5.99 Å, c = 18.46 Å, β = 91.2 ^{o}), related to the lattice parameters of a simple cubic perovskite structure by means of a $2 \times \sqrt{2} \times 3\sqrt{2}$ expansion as shown in Figure 4.1. Electron diffraction data confirm the expanded cell, as shown in Figure 4.2. Iodometric titrations performed on the $Ba_3YFe_2O_{7.5}$ sample indicated an average iron oxidation state of +3 (detailed in Table A4.1), confirming the stated composition.

$Ba_3YCo_2O_{7.5}$. X-ray powder diffraction data collected from $Ba_3YCo_2O_{7.5}$ could also be readily indexed using a monoclinic cell (a = 7.96 Å, b = 5.97 Å, c = 18.30 Å, β = 91.0 ^{o}), related to the lattice parameters of a simple cubic perovskite structure by means of a $2 \times \sqrt{2} \times 3\sqrt{2}$ expansion, suggesting that $Ba_3YCo_2O_{7.5}$ adopts a similar structure to the Fe analogue.

Iodometric titrations performed on the $Ba_3YCo_2O_{7.5}$ sample indicate an average cobalt oxidation state of +3 (detailed in Table A4.2), consistent with the stated composition.

It is really challenging to determine the positions of oxides present in the lattices of $Ba_3YM_2O_{7.5}$ (M = Fe and Co) using X-ray powder diffraction. Thus neutron powder diffraction data were collected from $Ba_3YM_2O_{7.5}$ in order to characterize the detailed structures.

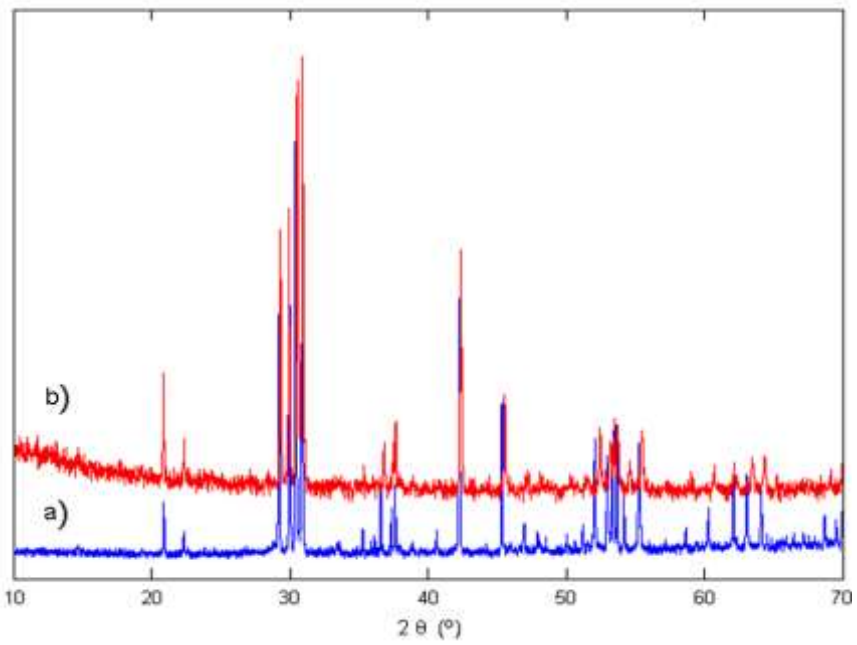

Figure 4.1 Powder X-ray diffraction data collected from $Ba_3YFe_2O_{7.5}$ (a) and $Ba_3YCo_2O_{7.5}$ (b).

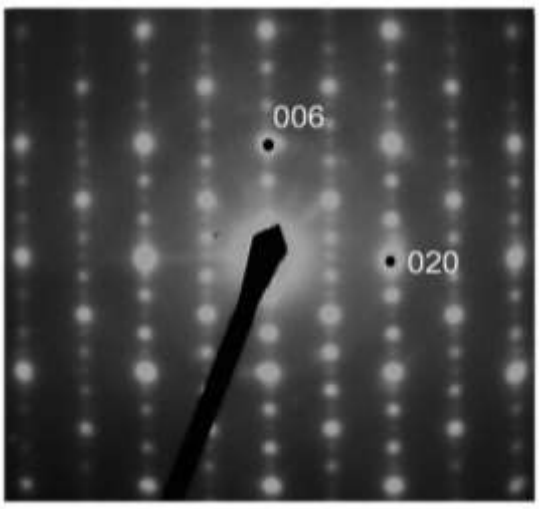

Figure 4.2. Electron diffraction data collected from [100] zone axes of $Ba_3YFe_2O_{7.5}$.

4.3.2 Structural refinements

4.3.2.1 $Ba_3YFe_2O_{7.5}$

Neutron powder diffraction data collected from $Ba_3YFe_2O_{7.5}$ could be readily indexed using a monoclinic cell (a = 8.02 Å, b = 5.99 Å, c = 18.46 Å, β = 91.2 ^{o}), confirming previous analysis using X-ray powder diffraction data. A series of structural models based on known cation-ordered $Ba_3MM'_2O_{7.5}$ phases were prepared. The simulation results of all the constructed models were compared with the neutron powder diffraction data collected from $Ba_3YFe_2O_{7.5}$. Two models seem account for the majority of the diffraction features. One model was based on the reported low-temperature, β-phase structure of $Ba_3ErGa_2O_{7.5}$ with *P2/c* space group symmetry, in which erbium and gallium are replaced with yttrium and iron respectively.[71] The other structural model was based on the high-temperature α-phase of $Ba_3ErGa_2O_{7.5}$ using a model adapted from the structure of $Sr_3YAl_2O_{7.5}$[72] reported by Wang et al., with *C2* space group symmetry, with strontium and aluminium replaced by barium and iron respectively. These two models are shown in Figure 4.3.

It can be clearly seen in Figure 4.3 that the *C2* and *P2/c* models adopt similar cation ordering patterns in which all the yttrium cations are located in octahedral sites and iron in tetrahedral sites. The difference between these two models lies in the twisting direction of YO_6 octahedra and MO_4 (M = Fe, Co) tetrahedra. This slight difference cannot be differentiated by X-ray powder diffraction data. This is why neutron powder diffraction data is necessary for solving the structures exactly.

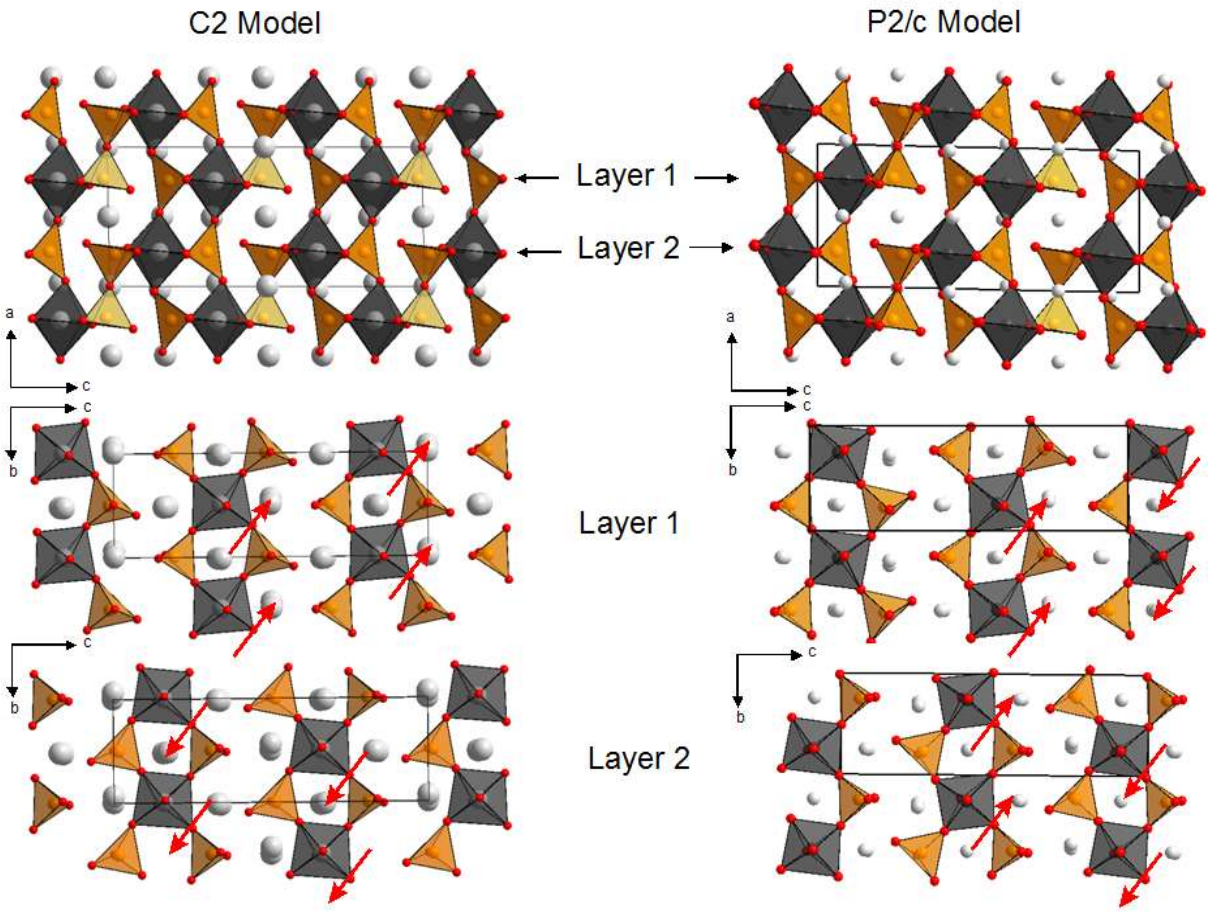

Figure 4.3 Structural models constructed based on *C2* and *P2/c* space groups. Grey octahedra represent YO_6, orange tetrahedra FeO_4, and grey spheres Ba^{2+}.

The two models were refined against the neutron powder diffraction collected from $Ba_3YFe_2O_{7.5}$. However, some diffraction features with low intensity could not be accounted for using the *C2* model due to the extinction conditions of the higher symmetry of this model. In contrast, refinement results showed the *P2/c* model accounted for all of the observed diffraction features well, indicating this is the structure adopted by $Ba_3YFe_2O_{7.5}$. Refinement of the *P2/c* model against neutron powder diffraction data collected from $Ba_3YFe_2O_{7.5}$ converged rapidly and yielded a good statistical fit (χ^2 = 3.28). Observed calculated and difference plots from the refinement are shown in Figure 4.4. Refinement of the yttrium and iron site fractional occupancies revealed no evidence of anti-site cation

disorder, indicating $Ba_3YFe_2O_{7.5}$ adopts a fully cation ordered structure. Full details of the refined structure of $Ba_3YFe_2O_{7.5}$ are given in Table 4.1, with selected bond lengths in Table 4.2. Figure 4.5 shows the refined structure of $Ba_3YFe_2O_{7.5}$.

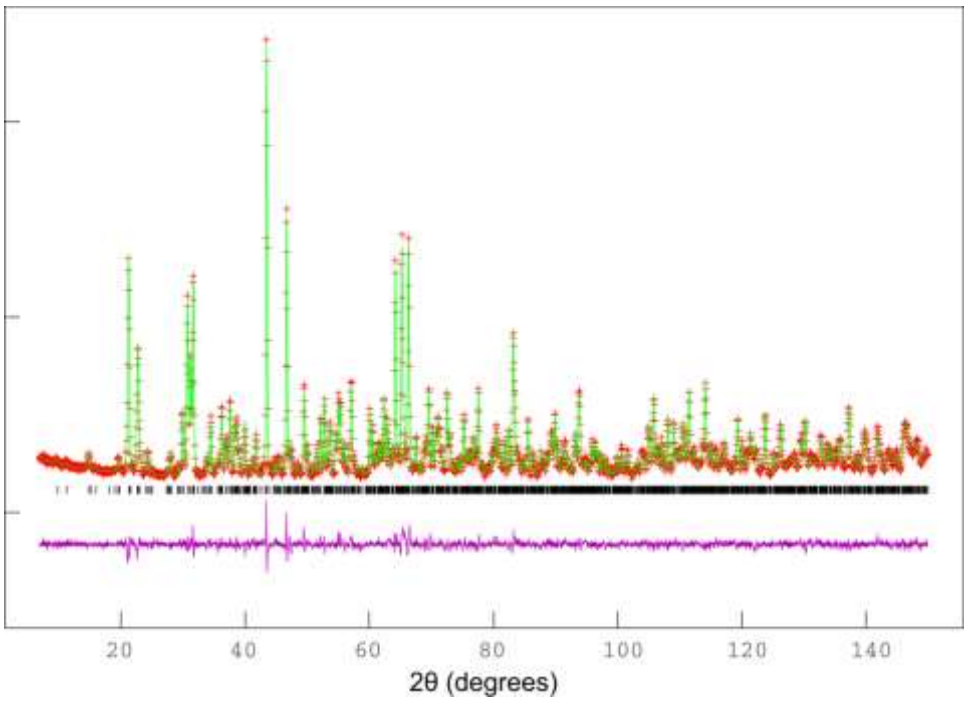

Figure 4.4 Observed, calculated and difference plots from the refinement of $Ba_3YFe_2O_{7.5}$ against neutron diffraction data.

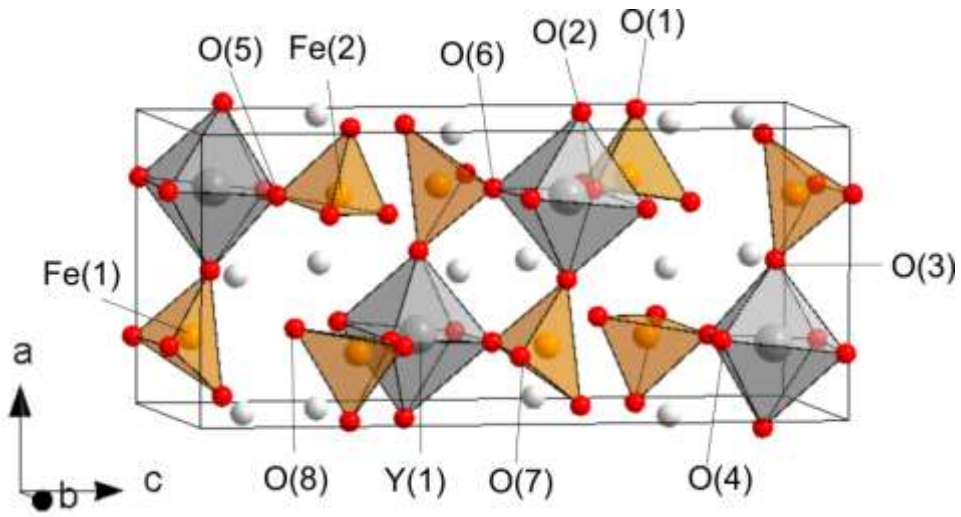

Figure 4.5 Atomic positions in the structure of $Ba_3YFe_2O_{7.5}$.

Atom	Site	*x*	*y*	*z*	U_{iso} (Å^2)
Ba(1)	*2e*	0	0.2824(16)	¼	0.0057(5)
Ba(2)	*2f*	½	0.3233(13)	¼	0.0057(5)
Ba(3)	*4g*	0.0267(5)	0.7529(15)	0.0886(2)	0.0057(5)
Ba(4)	*4g*	0.4960(7)	0.2505(13)	0.5780(3)	0.0057(5)
Y(1)	*4g*	0.2453(5)	0.2542(11)	0.4091(1)	0.0044(7)
Fe(1)	*4g*	0.2464(3)	0.2522(7)	0.0594(1)	0.0020(5)
Fe(2)	*4g*	0.2293(3)	0.7720(6)	0.2649(1)	0.0046(7)
O(1)	*2e*	0	0.7983(16)	¼	0.0190(23)
O(2)	*4g*	0.0410(5)	0.7647(11)	0.6095(2)	0.0093(4)
O(3)	*4g*	0.4709(5)	0.2480(13)	0.0892(2)	0.0093(4)
O(4)	*4g*	0.2744(7)	0.0500(8)	0.3074(2)	0.0093(4)
O(5)	*4g*	0.2498(7)	0.5548(8)	0.3385(3)	0.0093(4)
O(6)	*4g*	0.2369(9)	0.4896(9)	0.5002(3)	0.0093(4)
O(7)	*4g*	0.2299(9)	0.0149(9)	0.9935(3)	0.0093(4)
O(8)	*4g*	0.3065(7)	0.3365(1)	0.6788(3)	0.0205(14)
$Ba_3YFe_2O_{7.5}$ Space group - *P2/c* *a* = 8.0234(1) Å, *b* = 5.98935(8) Å, *c* = 18.4565(2) Å, *β* = 91.225(1) °; χ^2 = 3.28, wRp = 4.54 %, Rp = 3.53 %					

Table 4.1. Structural parameters refined against neutron powder diffraction data collected from $Ba_3YFe_2O_{7.5}$ at room temperature.

Cation	Anion	Bond(Å)	BVS
Y(1)	O(2)	2.318(6)	Y +3.15
	O(3)	2.277(6)	
	O(4)	2.257(6)	
	O(5)	2.223(7)	
	O(6)	2.196(7)	
	O(7)	2.247(7)	
Fe(1)	O(2)	1.910(5)	Fe +2.82
	O(3)	1.872(5)	
	O(6)	1.894(7)	
	O(7)	1.874(6)	
Fe(2)	O(1)	1.861(3)	Fe +3.01
	O(4)	1.873(6)	
	O(5)	1.885(6)	
	O(8)	1.837(6)	

Table 4.2. Selected bond lengths from the refined structure of $Ba_3YFe_2O_{7.5}$.[73]

4.3.2.2 $Ba_3YCo_2O_{7.5}$

Neutron powder diffraction data collected from $Ba_3YCo_2O_{7.5}$ could also be readily indexed using a monoclinic cell (a = 7.96 Å, b = 5.97 Å, c = 18.30 Å, β = 91.0 ^{o}), suggesting that $Ba_3YCo_2O_{7.5}$ adopts a similar structure to $Ba_3YFe_2O_{7.5}$. Thus *C2* and *P2/c* models were constructed, analogous to those described for $Ba_3YFe_2O_{7.5}$, by substituting the Fe with Co based on the structure of $Ba_3YFe_2O_{7.5}$. Refinement of the *P2/c* model against neutron powder diffraction data collected from $Ba_3YCo_2O_{7.5}$ converged rapidly and yielded a better statistical fit (χ^2 = 1.93) than the value obtained from the refinement of *C2* model (χ^2 = 4.21), indicating $Ba_3YCo_2O_{7.5}$ adopts the same structure as the Fe analogue. Refinement of the yttrium and cobalt site occupancies revealed no evidence of anti-site cation disorder. Observed calculated and difference plots from the refinement are shown in Figure 4.6. Full details of the refined structure of $Ba_3YCo_2O_{7.5}$ are given in Table 4.3, with selected bond lengths in Table 4.4.

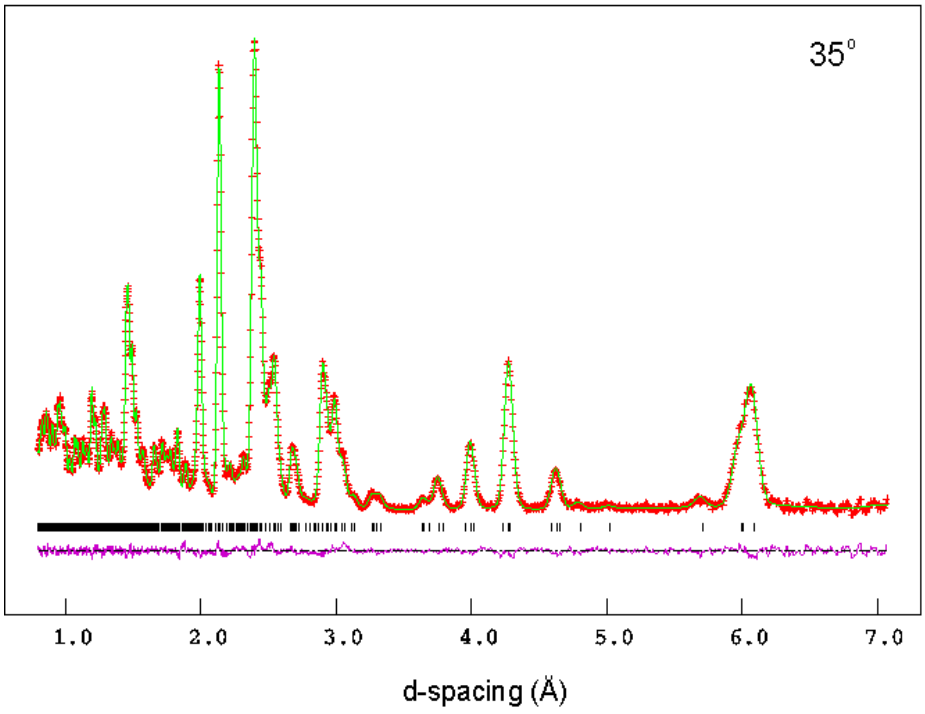

Figure 4.6 Observed, calculated and difference plots from the refinement of $Ba_3YCo_2O_{7.5}$ against neutron diffraction data.

Atom	Site	*x*	*y*	*z*	U_{iso} (Å^2)
Ba(1)	*2e*	0	0.2898(6)	¼	0.0074(2)
Ba(2)	*2f*	½	0.3207(5)	¼	0.0074(2)
Ba(3)	*4g*	0.0179(2)	0.7515(6)	0.0882(1)	0.0074(2)
Ba(4)	*4g*	0.5033(3)	0.2515(5)	0.5764(1)	0.0074(2)
Y(1)	*4g*	0.2458(2)	0.2498(3)	0.41095(8)	0.0040(2)
Co(1)	*4g*	0.2457(5)	0.2619(10)	0.0647(2)	0.0032(8)
Co(2)	*4g*	0.2291(5)	0.7730(8)	0.2622(2)	0.0090(11)
O(1)	*2e*	0	0.8002(6)	¼	0.0214(10)
O(2)	*4g*	0.0428(2)	0.7670(4)	0.6066(1)	0.0103(2)
O(3)	*4g*	0.4680(2)	0.2487(5)	0.0909(1)	0.0103(2)
O(4)	*4g*	0.2751(3)	0.0376(4)	0.3114(1)	0.0103(2)
O(5)	*4g*	0.2516(3)	0.5379(4)	0.3351(1)	0.0103(2)
O(6)	*4g*	0.2363(4)	0.4899(4)	0.4999(1)	0.0103(2)
O(7)	*4g*	0.2364(4)	0.0122(3)	0.9950(1)	0.0103(2)
O(8)	*4g*	0.2999(3)	0.3543(4)	0.6806(1)	0.0186(6)
$Ba_3YCo_2O_{7.5}$ Space group – *P2/c* *a* = 7.966(3) Å, *b* = 5.973(2) Å, *c* = 18.298(7) Å, *β* = 90.994(1) °; χ^2 = 1.907, wRp = 1.75 %, Rp = 1.71 %					

Table 4.3 Structural parameters refined against neutron powder diffraction data collected from $Ba_3YCo_2O_{7.5}$ at room temperature.

Cation	Anion	Bond(Å)	BVS
Y(1)	O(2)	2.319(2)	Y +3.32
	O(3)	2.281(2)	
	O(4)	2.235(3)	
	O(5)	2.212(3)	
	O(6)	2.172(3)	
	O(7)	2.197(2)	
Co(1)	O(2)	1.807(4)	Co +2.53
	O(3)	1.831(4)	
	O(6)	1.898(6)	
	O(7)	1.963(6)	
Co(2)	O(1)	1.841(4)	Co +2.68
	O(4)	1.853(5)	
	O(5)	1.943(5)	
	O(8)	1.776(4)	

Table 4.4. Selected bond lengths from the refined structure of $Ba_3YCo_2O_{7.5}$.

4.3.3 Magnetism

$Ba_3YFe_2O_{7.5}$. Zero-field-cooled and field-cooled magnetization data collected from $Ba_3YFe_2O_{7.5}$ in an applied field of 100 Oe in the temperature range 5 < T/K < 300 are shown in Figure 4.7. The data can be readily fitted to the Curie-Weiss law over the whole temperature range to give values of C = 5.05 (3) cm^3 K mol^{-1} and θ = - 36.6(2) K, indicating that $Ba_3YFe_2O_{7.5}$ exhibits paramagnetic behaviour. Neutron diffraction data collected from $Ba_3YFe_2O_{7.5}$ at 5 K exhibit no additional diffraction features relative to analogous data collected at room temperature, indicating the absence of magnetic order.

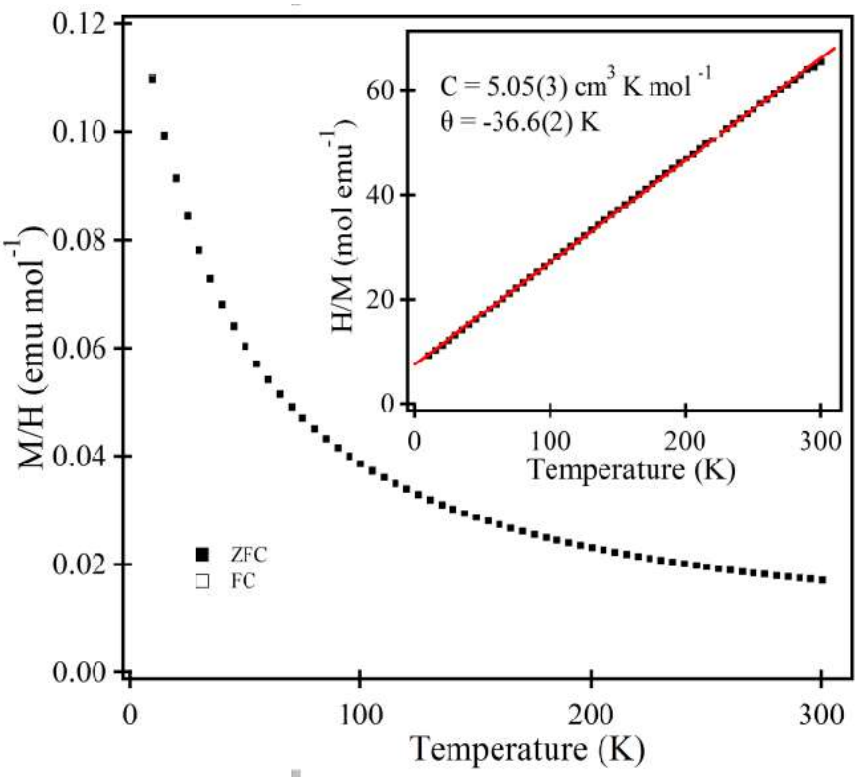

Figure 4.7 Zero-field-cooled and field-cooled magnetization data collected from $Ba_3YFe_2O_{7.5}$. Insets show fits of H/M to the Curie–Weiss law.

$Ba_3YCo_2O_{7.5}$. Zero-field-cooled and field-cooled magnetization data collected from $Ba_3YCo_2O_{7.5}$ in an applied field of 100 Oe in the temperature range 5 < T/K < 300 are shown in Figure 4.8. The data can be readily fitted to the Curie - Weiss law in the

temperature range 65 < T/K < 300, to yield values of C = 5.949(9) cm^3 K mol^{-1} and θ = -65.0(3) K. The zero-field-cooled and field-cooled data diverge below 20 K, suggesting the onset of magnetic order at this temperature.

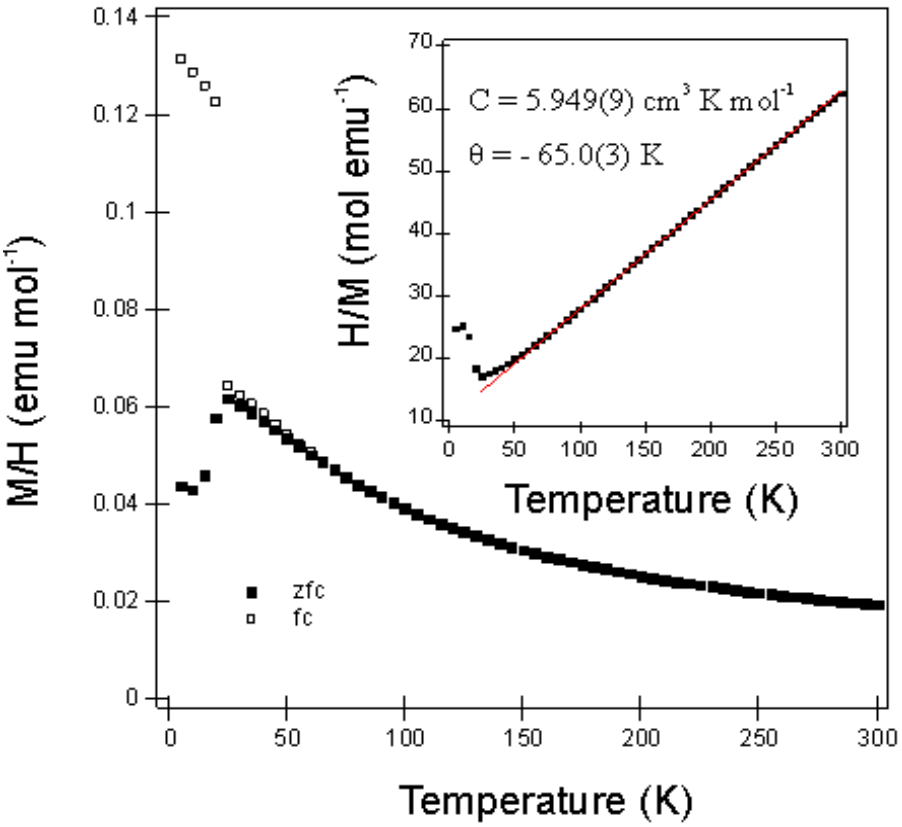

Figure 4.8 Zero-field-cooled and field-cooled magnetization data collected from $Ba_3YCo_2O_{7.5}$. Insets show fits of H/M to the Curie–Weiss law.

In order to determine the magnetic structure of $Ba_3YCo_2O_{7.5}$, neutron powder diffraction data were collected from $Ba_3YCo_2O_{7.5}$ at 7 K. As shown in Figure 4.9, the data exhibit additional diffraction features compared to the analogous data collected at room temperature. These additional diffraction features can be indexed using the crystallographic unit cell. The intensities of the additional diffraction features can be described using an antiferromagnetic model in which the magnetic moments of the cobalt centres in the rock-salt type $Y_2Co_2O_5$ units are aligned along *a*-axis. Thus a magnetic model was constructed and refined against

the neutron powder diffraction collected $Ba_3YCo_2O_{7.5}$ at 7 K, as shown in Figure 4.10. The refined results indicate an ordered moment of 1.64(3) per cobalt centre.

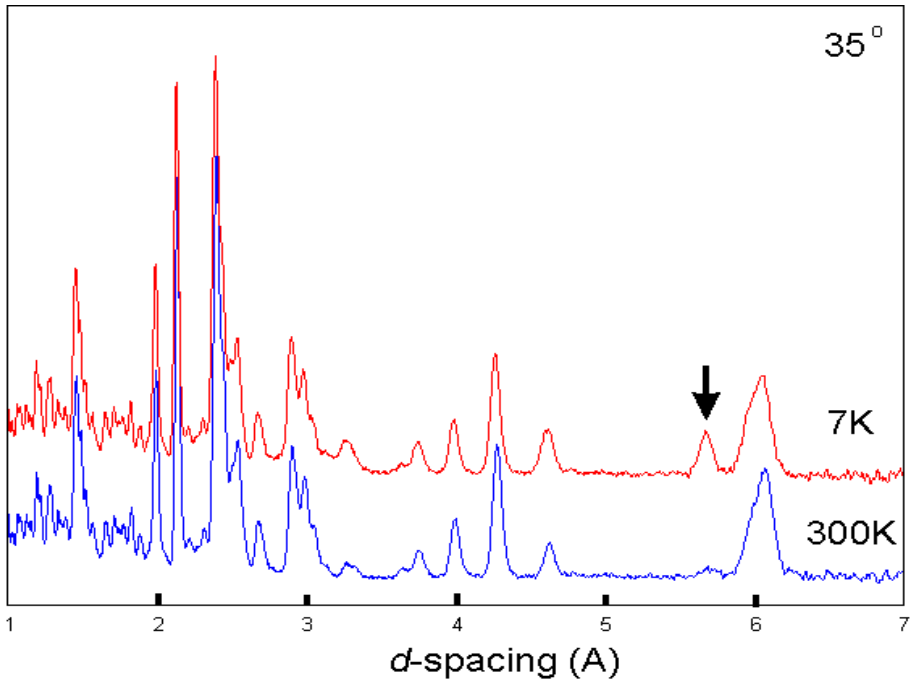

Figure 4.9 Comparison of neutron diffraction data collected from $Ba_3YCo_2O_{7.5}$ at 7 and 300 K. Arrow marks additional diffraction reflections.

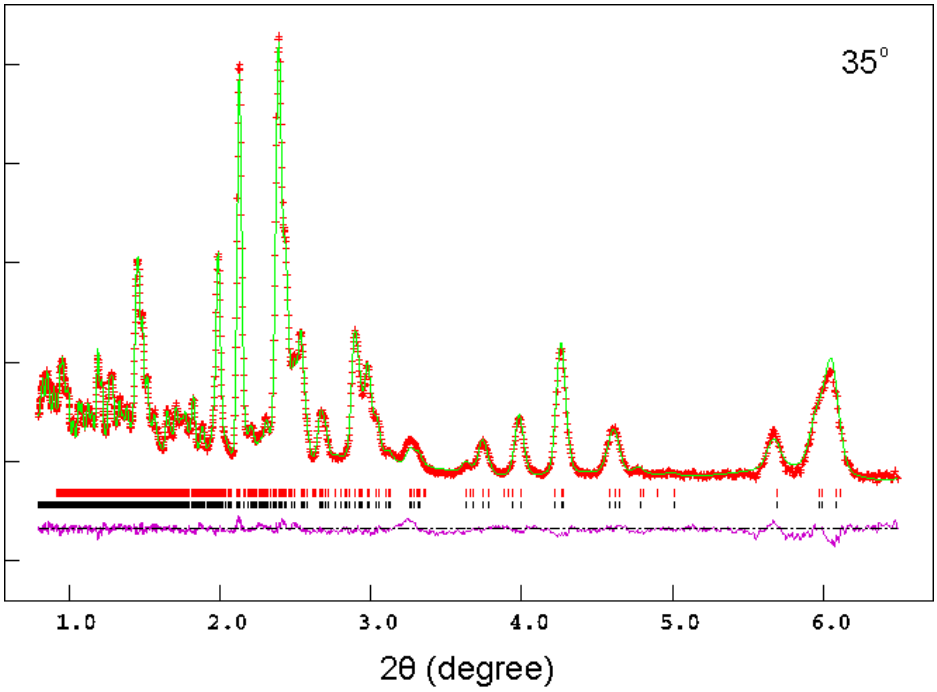

Figure 4.10 Observed calculated and difference plots from the refinement of $Ba_3YCo_2O_{7.5}$ against neutron diffraction data collected at 7 K. The red tick marks correspond to the magnetic unit cell.

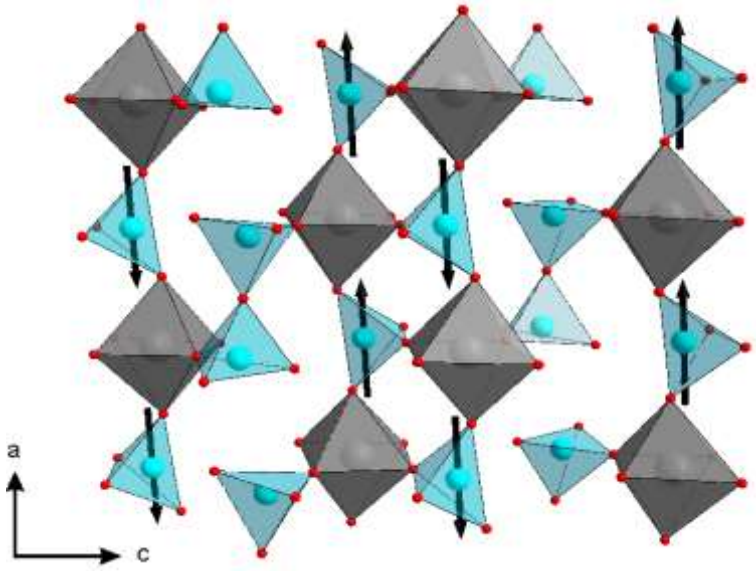

Figure 4.11 The refined magnetic model of $Ba_3YCo_2O_{7.5}$.

In order to confirm the magnetic structure adopted by $Ba_3YCo_2O_{7.5}$ at low temperature, an antiferromagnetic model was introduced into the cobalt centres in Co_2O_7 dimers and then refined against the neutron powder diffraction data collected from $Ba_3YCo_2O_{7.5}$ at 7 K. The results gave the magnetic ordered moment in Co_2O_7 dimers to be zero within error. Figure 4.11 shows the refined magnetic model. Table 4.5 lists the refined results of the magnetic model.

atom	x	y	z	$M_x(\mu_B)$	$M_y(\mu_B)$	$M_z(\mu_B)$
Co(1)	0.7544	0.7420	0.9355	1.64(3)	0	0
Co(2)	0.2456	0.2580	0.0645	-1.64(3)	0	0
Co(3)	0.7544	0.2580	0.4355	1.64(3)	0	0
Co(4)	0.2456	0.7420	0.5645	-1.64(3)	0	0
Co(5)	0.2291	0.7731	0.2622	0	0	0
Co(6)	0.7709	0.7731	0.2378	0	0	0
Co(5)	0.7709	0.2269	0.7378	0	0	0
Co(6)	0.2291	0.2269	0.7622	0	0	0
$Ba_3YCo_2O_{7.5}$ -Space group-*P1* a = 7.957 Å, b = 5.959 Å, c = 18.251 Å, V= 592.422 Å^3						

Table 4.5 Structural parameters from the ferromagnetic refinement of $Ba_3YCo_2O_{7.5}$ against neutron diffraction data collected at 7 K.

4.4 Discussion

4.4.1 Cation and anion-vacancy ordering in $Ba_3YM_2O_{7.5}$ (M = Fe and Co)

The anion-deficient $Ba_3YM_2O_{7.5}$ (M = Fe, Co) perovskite phases described above adopt structures with complex cation and anion-vacancy ordered structures with a $3\sqrt{2} \times \sqrt{2} \times 2$ geometric unit cell expansion compared to a simple cubic perovskite phase.

Similar to the structure of Ba_2YMO_5 (M = Fe, Co) described in Chapter 3, the $Ba_3YM_2O_{7.5}$ (M = Fe, Co) phases also adopt a complex cation-ordered structure, in which Y^{3+} cations occupy the octahedral sites and Fe^{3+}/Co^{3+} cations are located in the tetrahedral sites. The different coordination geometries of Y^{3+} and M^{3+} (M = Fe, Co) centres encourage the segregation of cations, leading to the observed cation ordered structures. As shown in Figure 4.12, the anion vacancies in $Ba_3YM_2O_{7.5}$ (M = Fe, Co) adopt an ordered arrangement, which can be described as a repeated stacking sequence of $– Ba_3O_3 – YM_2O_5 – Ba_3O_2 – YM_2O_5 –$ in an analogy to the $– AO – BO_2 – AO – BO_2 –$ stacking in the simple cubic perovskite structure. The anion vacancies in Ba_3O_2 layers are introduced by an ordered arrangement of M_2O_7 (M = Fe, Co) dimers. Further inspecting the structures of $Ba_3YM_2O_{7.5}$ (M = Fe, Co), the oxide ions occupy half of the positions between MO_4 tetrahedra in an ordered manner. In each YM_2O_5 (M = Fe, Co) layer, the cyclic sequence of the anion vacancies distributed along *z*-axis follows an $– O – O_2 – O_2 – O – O_2 – O_2 – O –$ arrangement. This ordered arrangement of anion vacancies encourages the segregation of Y^{3+} and M^{3+} (M = Fe, Co) cations in the lattice. Also, the presence of M^{3+} (M = Fe, Co) cations localizes the anion vacancies in the lattice to yield an anion-vacancy ordered and cation ordered structure.

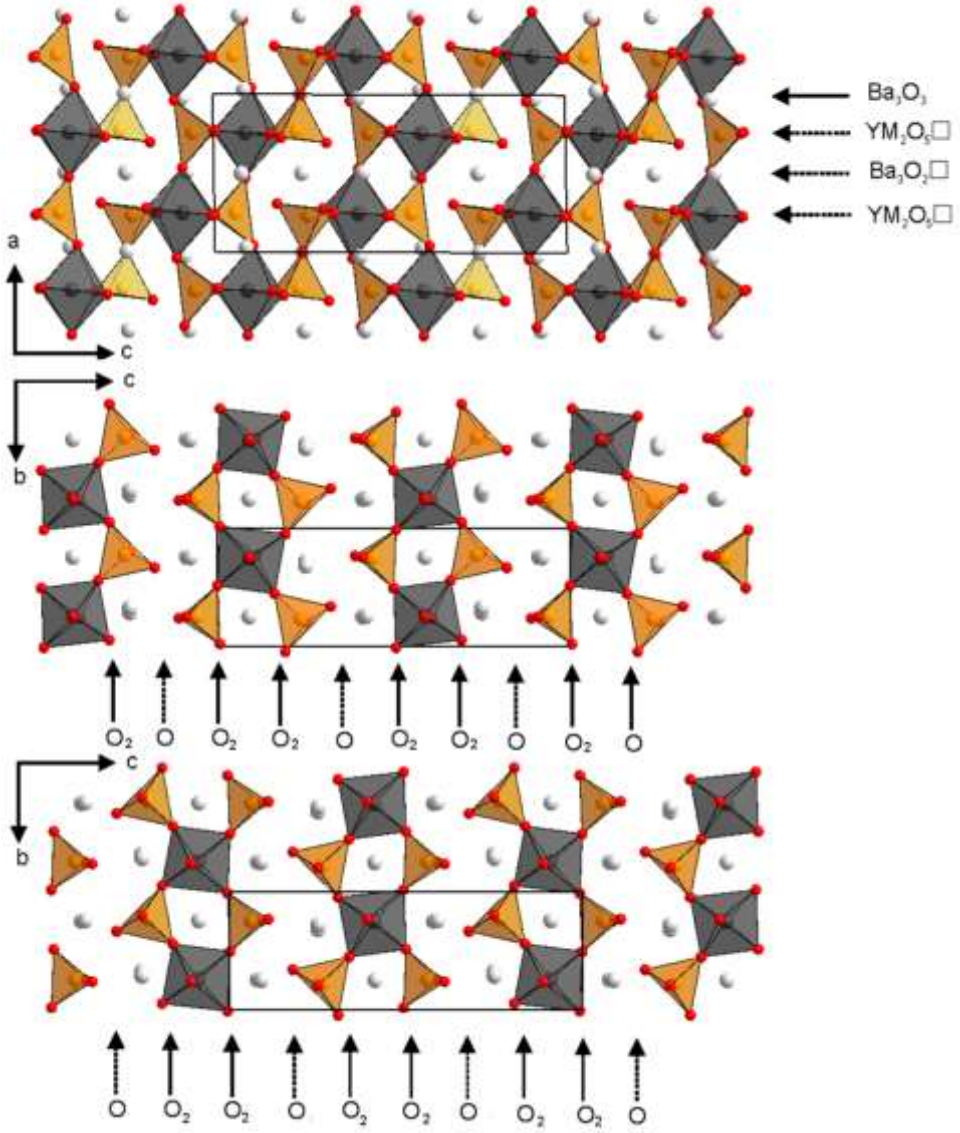

Figure 4.12 Refined structure of $Ba_3YM_2O_{7.5}$ (M = Fe and Co). (a) View down the b-axis. (b) View down the a-axis showing the layer of polyhedra at x~0.75. (c) View down the a-axis showing the layer of polyhedra at x~0.25. Solid line indicates unit cell.

4.4.2 Bond network

The structures of $Ba_3YM_2O_{7.5}$ (M = Fe, Co) can be divided up into different basic units. As shown in Figure 4.13, two YO_6 octahedra and two MO_4 tetrahedra (M = Fe and Co) are connected to each other in an anti-parallel arrangement to form a simple $Y_2M_2O_{10}$ 2 building unit (blue unit), which can actually be described as a rock-salt type cation ordered

unit. The $Y_2M_2O_{10}\square_2$ units can also be observed in the lattice of Ba_2YMO_5 (M = Fe and Co) as discussed in Chapter 3.

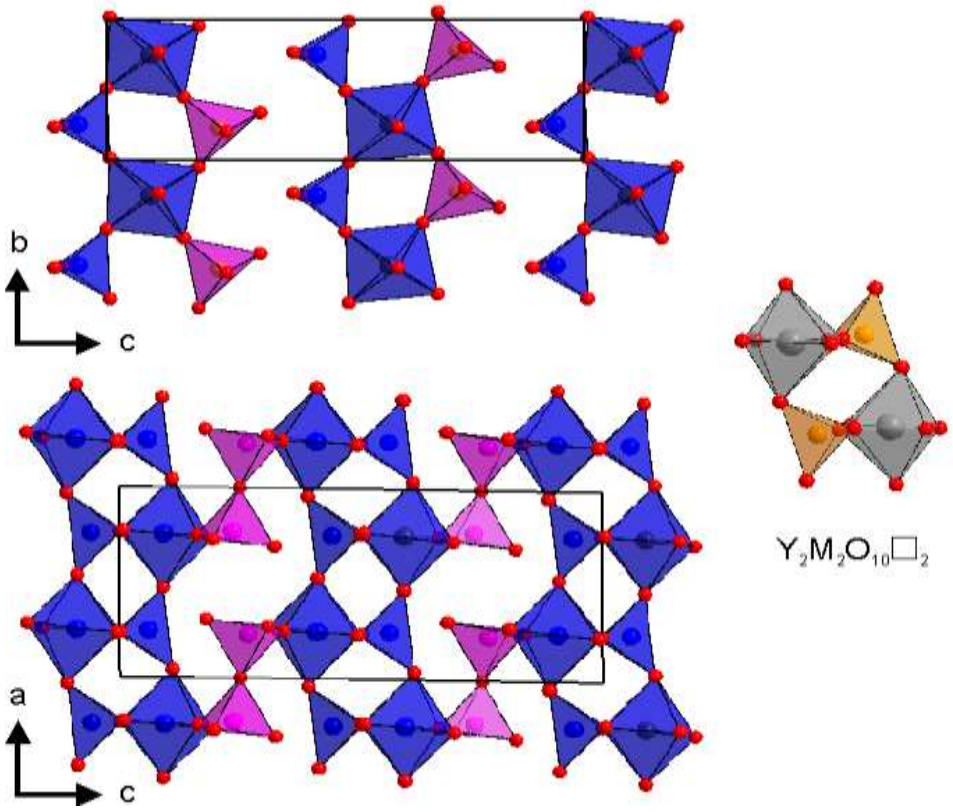

Figure 4.13 Structure of $Ba_3YM_2O_{7.5}$ (M = Fe and Co) constructed based on $Y_2M_2O_{10}\square_2$ sub-units and M_2O_7 dimers.

The extra M^{3+} (M = Fe and Co) cations are present in the form of M_2O_7 (M = Fe and Co) dimers which are very common in anion-deficient hexagonal perovskite structures.[74,75] The neighbouring $Y_2M_2O_{10}\square_2$ (M = Fe and Co) units are related by a (0, ½, ½) stacking vector and connected by the M_2O_7 dimers via a chain of Y – O – M – O – M – O – Y bonds. This separated arrangement of $Y_2M_2O_{10}\square_2$ (M = Fe and Co) units inter-connected with the layers of M_2O_7 dimers not only minimizes the local strain arising from the size difference of Y^{3+} and M^{3+} (M = Fe and Co) cations (Y^{3+} CN6 = 0.90 Å; Fe^{3+} CN4 = 0.49 Å)[73], but also localizes the anion vacancies in the MO_4 (M = Fe, Co) tetrahedra, whilst maintaining the six-coordinate environment of yttrium centres.

4.4.3 Relationship of cation ordering and anion vacancies in perovskite structure.

In order to understand the factors inducing the cation ordering in $Ba_3YM_2O_{7.5}$, a series of triple perovskite phases with different cation ordering patterns are listed in Figure 4.14. A disordered arrangement of cations is common in perovskite structures such as $Ba_3CoTi_2O_9$ as shown in Figure 4.14a. When oxygen vacancies are introduced in the lattice of perovskite structures, tetrahedral sites are formed in the lattice, driving the segregation of cations which have special preferences for particular coordination environment and the formation of complex cation ordering. For example, Si^{4+} and Ga^{3+} can be located in the tetrahedral sites. A complex cation ordering is achieved in the lattice of $Sr_3MgSi_2O_8$ (Figure 4.14b), in which Mg^{2+} and Si^{4+} cations are in octahedral and tetrahedral sites respectively.[76] In contrast, a layered cation ordering is observed in the lattice of $Ca_{2.5}Sr_{0.5}Mn_2GaO_8$ in which $Mn^{3+/4+}$ and Ga^{3+} cations are in octahedral and tetrahedral sites respectively (Figure 4.14c).[20] It should be noted the size difference between Mg^{2+} and Si^{4+} ($r(Mg^{2+})/r(Si^{4+}) = 2.77$) in $Sr_3MgSi_2O_8$ is much bigger than that between $Mn^{3+/4+}$ and Ga^{3+} ($r(Mn^{3+})/r(Ga^{3+}) = 1.37$; $r(Mn^{4+})/r(Ga^{3+}) = 1.13$) in $Ca_{2.5}Sr_{0.5}Mn_2GaO_8$, suggesting that the complex cation ordering can be induced by controlling not only the oxygen content of the composition but also the size difference between the pair of cations in the lattice.

When the oxygen content decreases further, complex cation ordering is achieved in $A_3B_3O_{7.5}$ family. For example, complex cation ordering is observed in $Ba_3YFe_2O_{7.5}$, in which YO_6 octahedra and FeO_4 tetrahedra are connected in a rock-salt type arrangement and Fe_2O_7 dimers are also observed. It should be noted that the complex cation ordered structure of $Ba_3YFe_2O_{7.5}$ is quite different from the layered structure adopted by $Ca_{2.5}Sr_{0.5}Mn_2GaO_8$ (Figure 4.14c) or another type of complex cation ordered structure adopted by

$Ba_3DyAl_2O_{7.5}$[77] (Figure 4.14d). This is attributed to an 'appropriate' size difference between Y^{3+} and Fe^{3+} in $Ba_3YFe_2O_{7.5}$.

Firstly, the large size difference between Y^{3+} and Fe^{3+} prevents the long range Fe – O – Fe interactions due to the difference in lengths of Y – O and Fe – O bonds. Thus the layered structure similar to $Ca_{2.5}Sr_{0.5}Mn_2GaO_8$ cannot be constructed in $Ba_3YFe_2O_{7.5}$. Secondly, the size difference between Dy^{3+} and Al^{3+} cations ($r(Dy^{3+})/r(Al^{3+})$ = 2.34) is much larger than that between Y^{3+} and Fe^{3+}($r(Y^{3+})/r(Fe^{3+})$ = 1.84), as shown in Figure 4.14d, e. Thus the rock-salt type basic units similar to the $Y_2Fe_2O_{10}$ $_2$ units in $Ba_3YFe_2O_{7.5}$ cannot be constructed in $Ba_3DyAl_2O_{7.5}$.

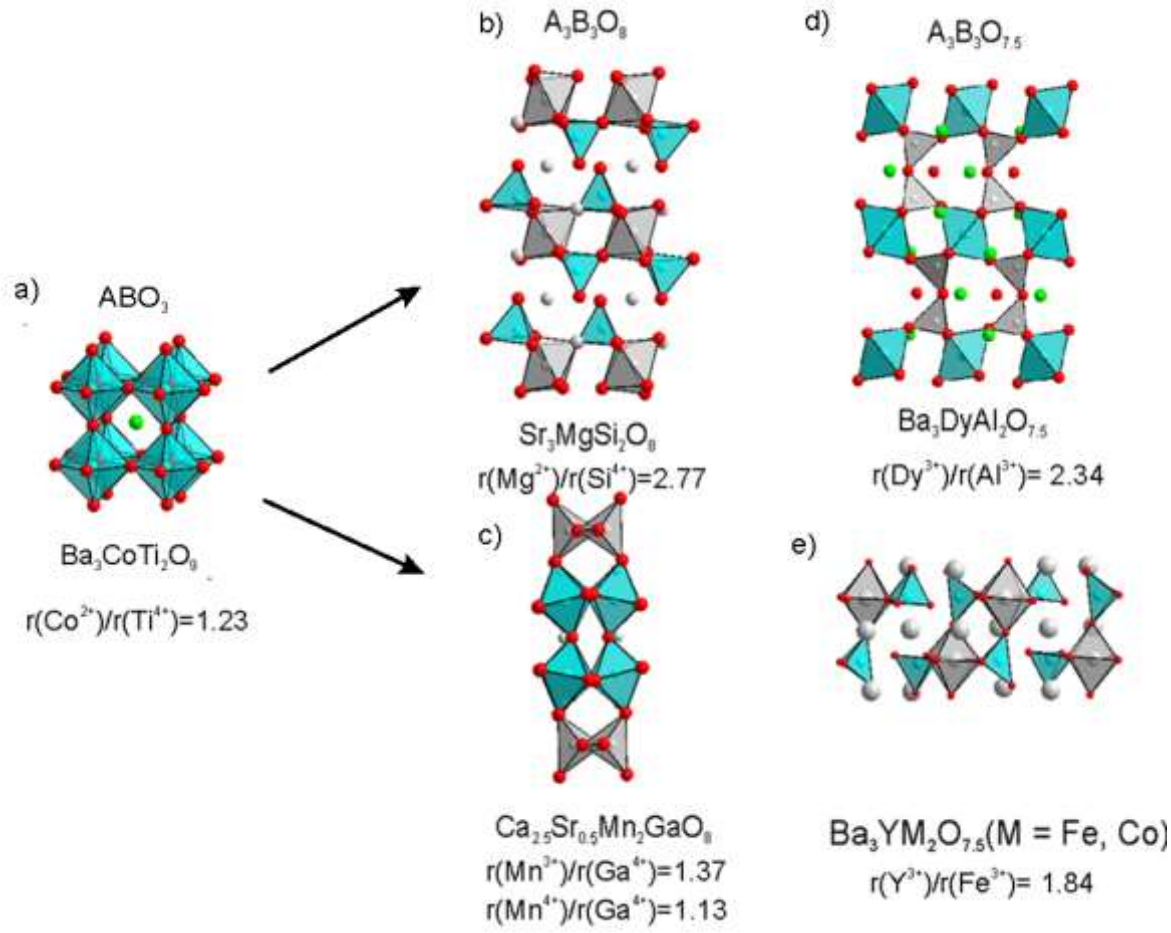

Figure 4.14 Relationship of structures and cation size and anion vacancies in triple perovskite structures.

By analyzing these complex cation ordered structures, it can be concluded that the the combination of cation size difference between pair of cations and anion vacancies leads to the complex cation ordering in the structure of $Ba_3YM_2O_{7.5}$ (M = Fe, Co). Thus diverse B-site cation ordering schemes can be achieved by appropriately selecting B-site cations and controlling the anion vacancies.

4.4.4 Magnetism

Magnetization data collected from $Ba_3YFe_2O_{7.5}$ indicate paramagnetic behaviour. Despite doubling the number of iron centers in each formula unit compared to Ba_2YFeO_5, the molar susceptibility of $Ba_3YFe_2O_{7.5}$ (C = 5.05(3) cm^3 K mol^{-1}) is similar to that of Ba_2YFeO_5 (C = 4.84(4) cm^3 K mol^{-1}), suggesting that the coupled iron centers in the Fe_2O_7 dimers only make a modest contribution to the susceptibility of $Ba_3YFe_2O_{7.5}$. This means the majority of the magnetic response coming from the iron centers in the $Y_2Fe_2O_{10}\square_2$ slabs, thus explaining why Ba_2YFeO_5 and $Ba_3YFe_2O_{7.5}$ have very similar magnetic susceptibilities. Although the pairs of iron centres in the Fe_2O_7 dimers are coupled through Fe – O – Fe interactions, the interactions between the dimers are blocked by YO_6 octahedra and anion vacancies, which limit the long-range magnetic order in the lattice.

Magnetization data collected from $Ba_3YCo_2O_{7.5}$ indicate paramagnetic behaviour above 45 K. Below this temperature zero-field-cooled and field-cooled data collected from $Ba_3YCo_2O_{7.5}$ diverge significantly. Neutron powder diffraction data collected from $Ba_3YCo_2O_{7.5}$ at 7 K indicate that $Ba_3YCo_2O_{7.5}$ adopts an antiferromagnetic order. The observed Curie constant (C = 5.949(9) cm^3 K mol^{-1}) is consistent with the expected value for spin-only Co^{3+} centres (S = 2, C_{exp} = 6 cm^3 K mol^{-1}), indicating a strong interaction between Co^{3+} centres through the superexchange of Co – O – Y – O – Co compared to the

observed magnetic behaviour of $Ba_3YFe_2O_{7.5}$. This could be attributed to a stronger Co^{3+} - O covalent interaction than the Fe^{3+} - O bond.

4.5 Conclusion

Complex cation ordering is achieved in the anion-deficient perovskite $Ba_3YM_2O_{7.5}$ (M = Fe, Co) phases. The structures of $Ba_3YM_2O_{7.5}$ (M = Fe, Co) consist of YO_6 octahedra and MO_4 tetrahedra. Structural analysis indicates this complex cation ordering is attributed to the size difference between Y^{3+} and M^{3+} cations and the presence of anion vacancies in the lattice. Complex cation ordering can be induced by carefully selecting the cations with different sizes and electronic configurations, and controlling the oxygen content in the lattice.

Appendix

Mass (mg)	$x_{caculated}$	$x_{average}$
39.7	7.501	7.50(1)
37.0	7.496	
38.8	7.507	

Table A4.1 Iodometric titration results of Ba_3YFe_2Ox.

Mass (mg)	$x_{caculated}$	$x_{average}$
38.9	7.503	7.50(1)
38.5	7.505	
39.0	7.495	

Table A4.2 Iodometric titration results of Ba_3YCo_2Ox.

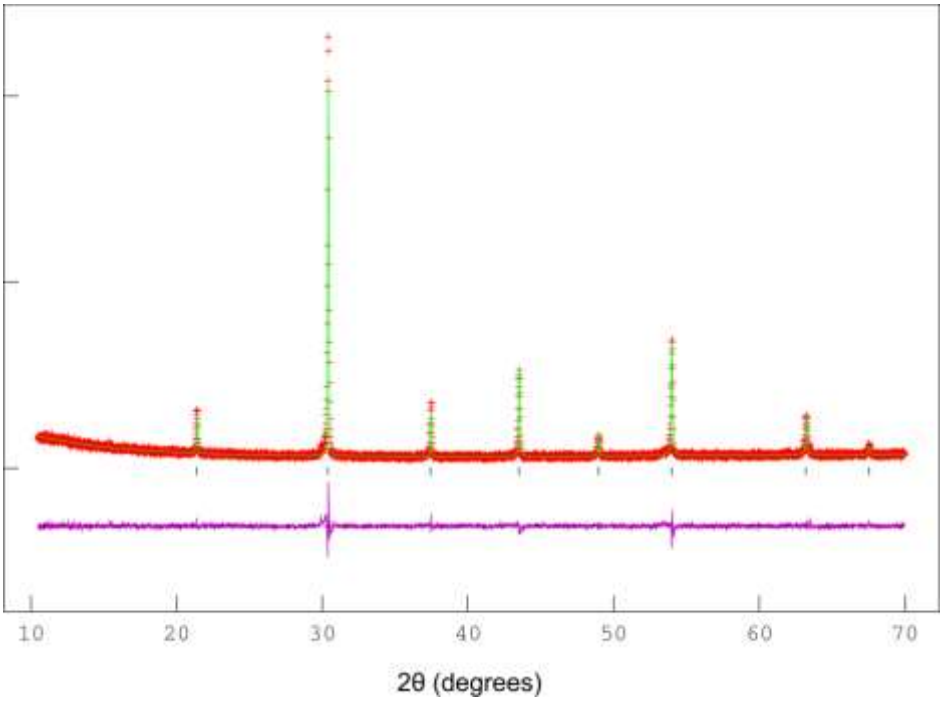

Figure A4.1 Observed, calculated and difference plots from the refinement of $Ba_4YFe_3O_{10}$ against X-ray diffraction data.

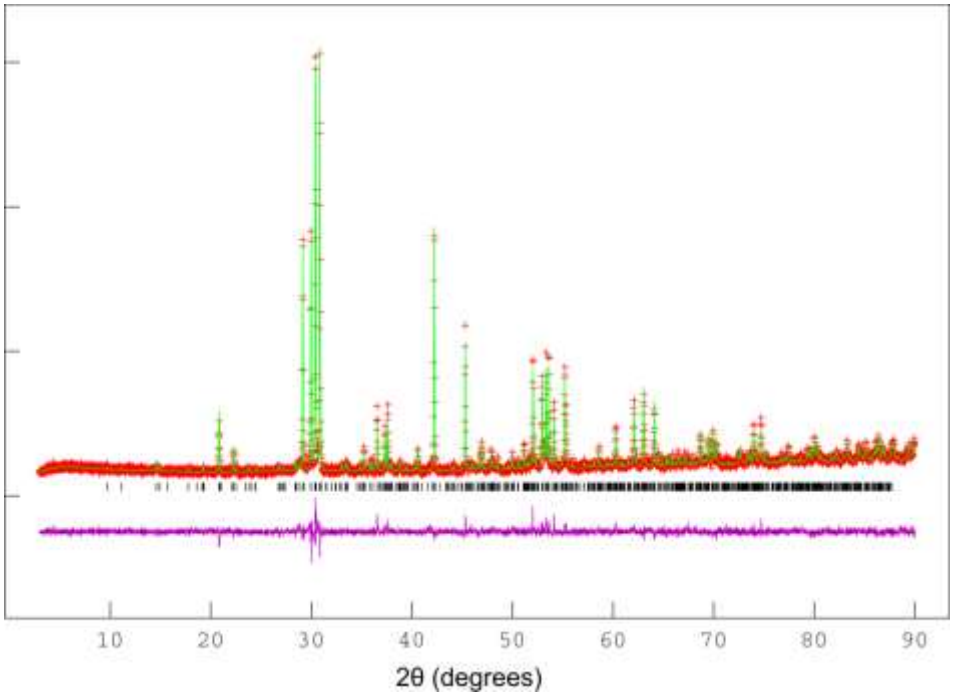

Figure A4.2 Observed, calculated and difference plots from the refinement of $Ba_3YFe_2O_{7.5}$ against X-ray diffraction data.

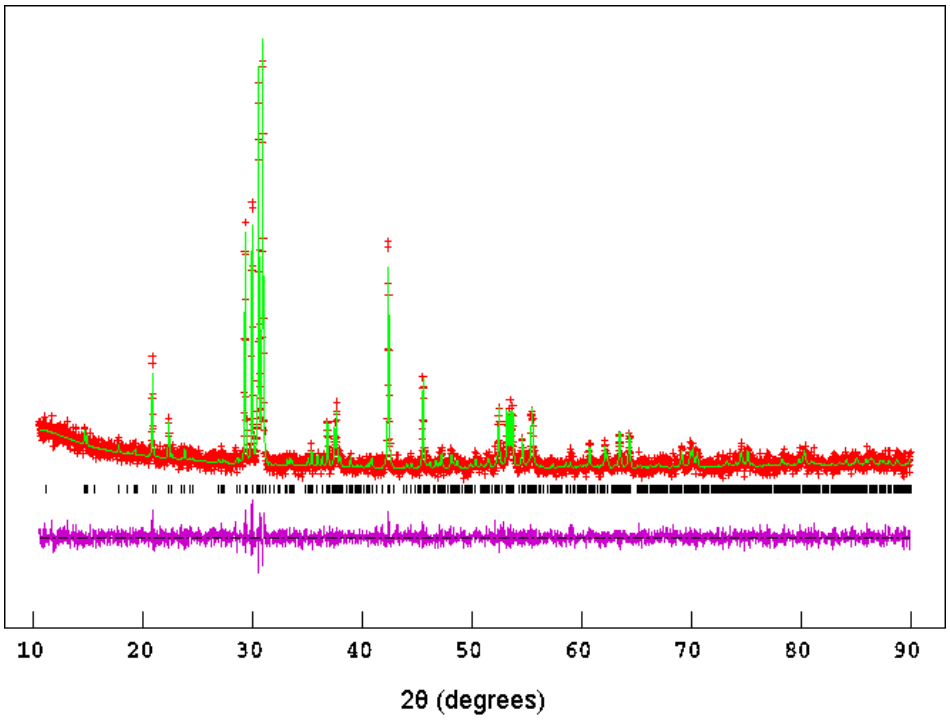

Figure A4.3 Observed, calculated and difference plots from the refinement of $Ba_3YCo_2O_{7.5}$ against X-ray diffraction data.

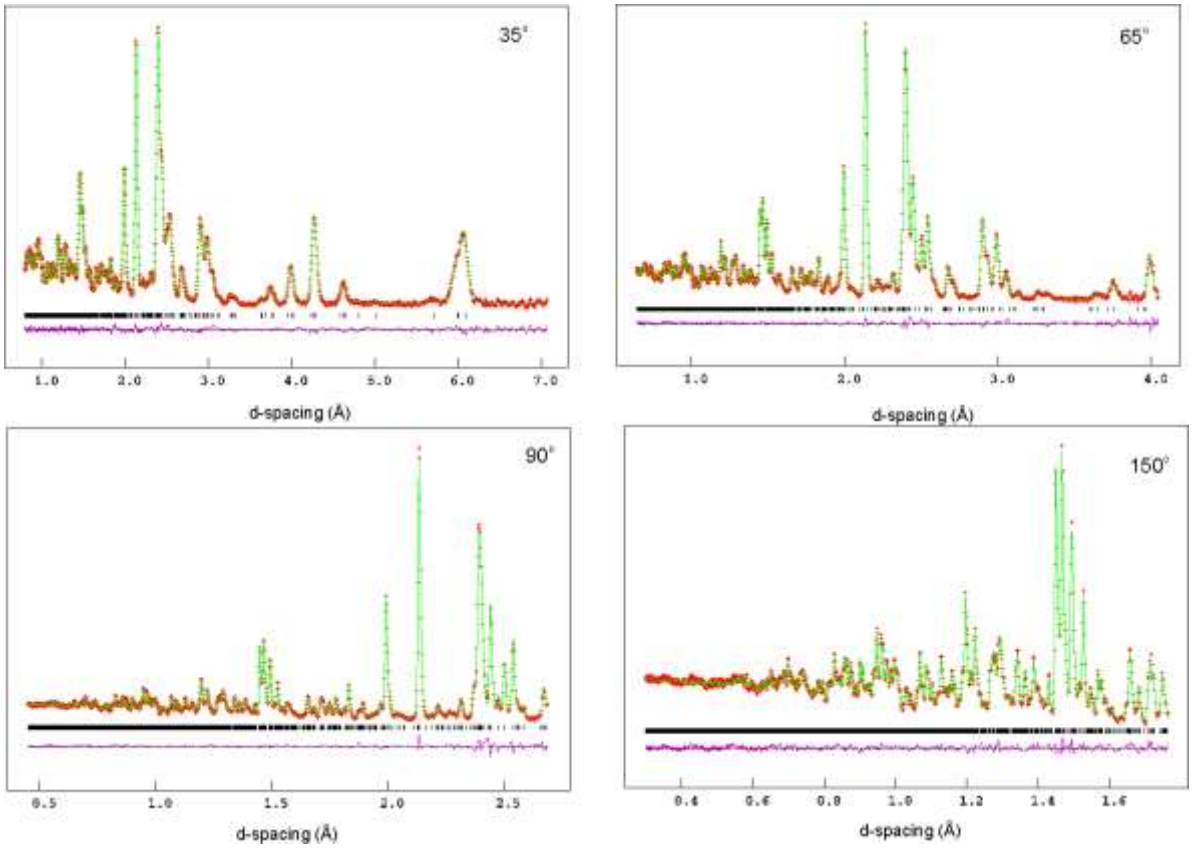

Figure A4.4 Observed, calculated and difference plots from the refinement of $Ba_3YCo_2O_{7.5}$ against neutron diffraction data.

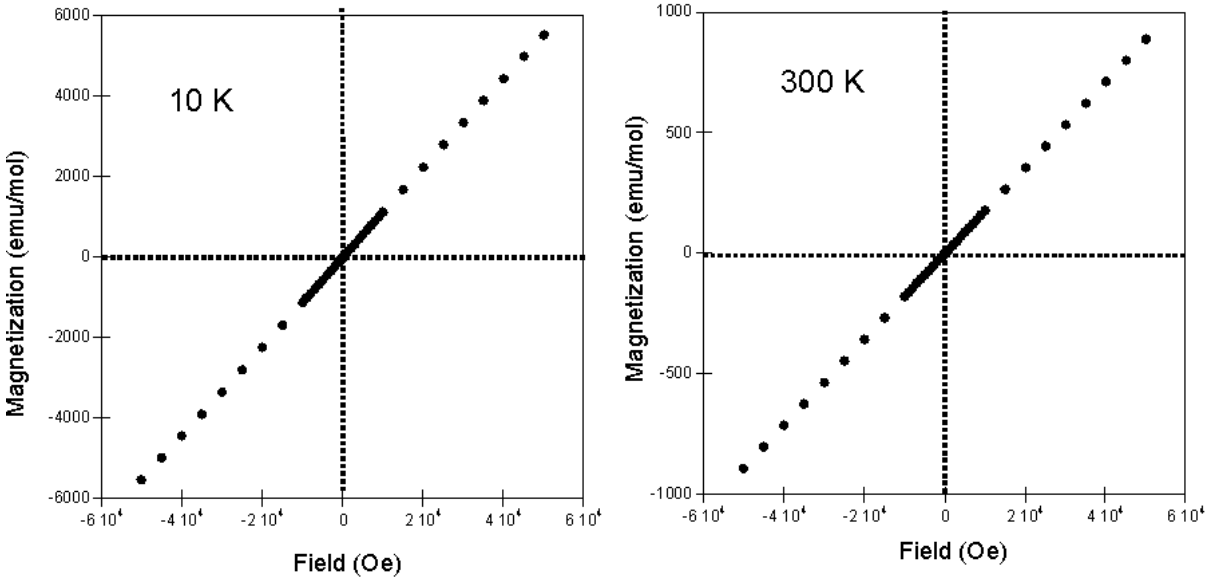

Figure A4.5 Magnetization-field isotherm collected at 10 K and 300 K from $Ba_3YFe_2O_{7.5}$.

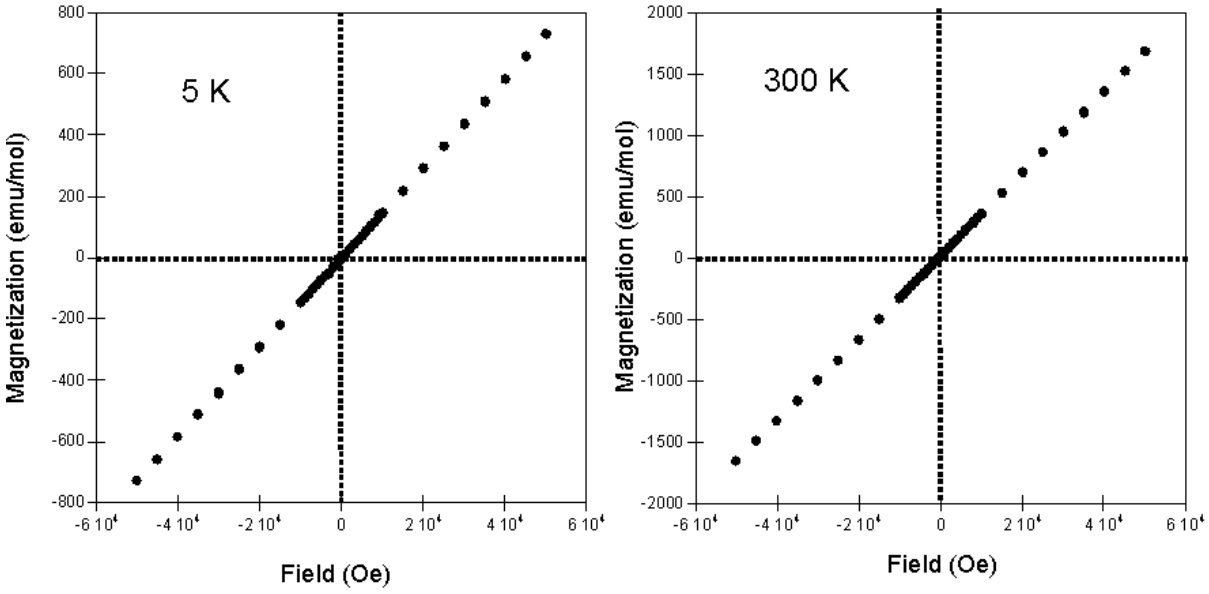

Figure A4.6 Magnetization-field isotherm collected at 5 K and 300 K from $Ba_3YCo_2O_{7.5}$.

Atom	Site	*x*	*y*	*z*	U_{iso} (Å^2)
Ba(1)	*2e*	0	0.2897(6)	¼	0.0075(2)
Ba(2)	*2f*	½	0.3209(6)	¼	0.0075(2)
Ba(3)	*4g*	0.0180(2)	0.7513(6)	0.0882(1)	0.0075(2)
Ba(4)	*4g*	0.5033(3)	0.2515(5)	0.5765(1)	0.0075(2)
Y(1)	*4g*	0.2458(2)	0.2499(3)	0.41094(8)	0.0040(2)
Co(1)	*4g*	0.2454(5)	0.2620(11)	0.0647(2)	0.0030(8)
Co(2)	*4g*	0.2290(5)	0.7729(8)	0.2622(2)	0.0090(11)
O(1)	*2e*	0	0.8002(6)	¼	0.0214(10)
O(2)	*4g*	0.0428(2)	0.7671(4)	0.60661(9)	0.0103(2)
O(3)	*4g*	0.4680(2)	0.2487(5)	0.0909(1)	0.0103(2)
O(4)	*4g*	0.2751(3)	0.0376(4)	0.3114(1)	0.0103(2)
O(5)	*4g*	0.2515(3)	0.5379(4)	0.3351(1)	0.0103(2)
O(6)	*4g*	0.2363(4)	0.4899(4)	0.4999(1)	0.0103(2)
O(7)	*4g*	0.2364(4)	0.0122(3)	0.9950(1)	0.0103(2)
O(8)	*4g*	0.2999(3)	0.3543(4)	0.6806(1)	0.0186(6)
$Ba_3YCo_2O_{7.5}$ Space group - *P2/c* *a* = 7.957(3) Å, *b* = 5.959(2) Å, *c* = 18.251(7) Å, *β* = 90.989(1) °; χ^2 = 2.405, wRp = 2.04 %, Rp = 1.98 %					

Table A4.3 Structural parameters refined against neutron powder diffraction data collected from $Ba_3YCo_2O_{7.5}$ at 7 K.

Chapter 5 Topochemical oxidation of Ba_2YFeO_5

5.1 Introduction

Topochemical oxidation has been widely applied in synthesizing new transition-metal oxides. Topochemical oxidation allows the oxidation state and spin state of transition metals to be adjusted, whilst maintaining the arrangement of cations in the host lattice. The resulting products of topochemical oxidation can exhibit interesting physical and electronic behaviours. For example, topochemical oxidation of $BaFeO_{2.5}$ under ozone leads to the formation of $BaFeO_3$, as shown in Figure 5.1. The new cubic $BaFeO_3$ phase exhibits ferromagnetic behaviour[34], in contrast to the thermodynamically more stable hexagonal $BaFeO_3$ phase which does not.

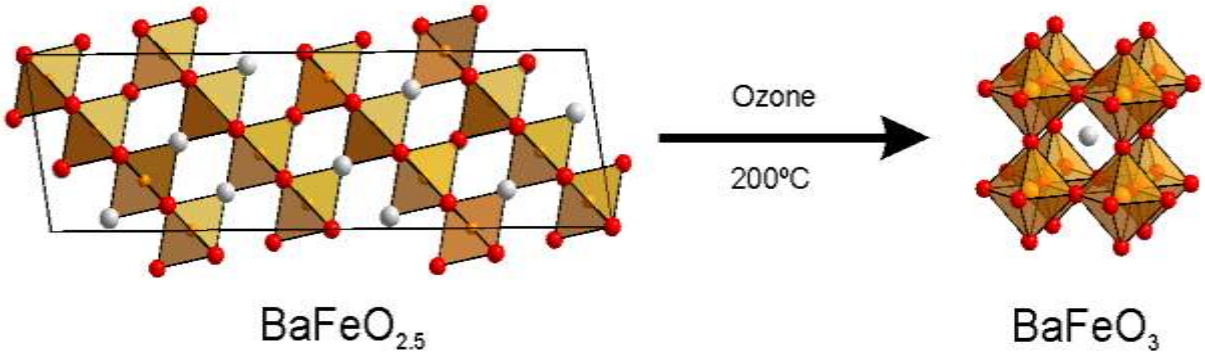

Figure 5.1 Topochemical oxidation of $BaFeO_{2.5}$ to $BaFeO_3$.

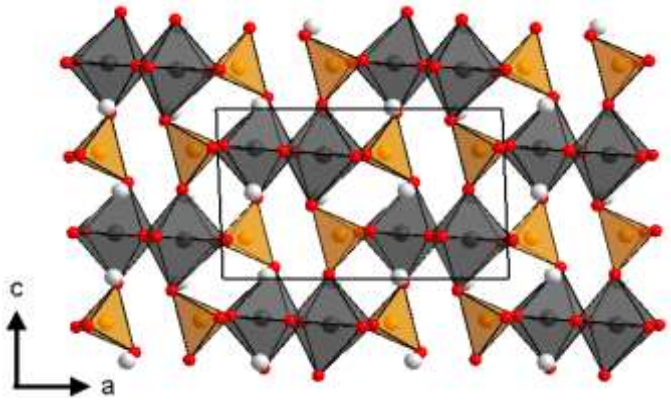

Figure 5.2 Structure of Ba_2YFeO_5.

As discussed in Chapter 3, Ba_2YFeO_5 adopts a cation ordered and anion-vacancy ordered structure. The presence of a large number of anion vacancies in the lattice (Figure 5.2) allows modifications to be made by topochemical oxidation processes. Thus this chapter focuses on the topochemical oxidation of Ba_2YFeO_5. The structure, magnetic and electronic behaviours of the oxidized sample will be discussed.

5.2 Experimental

$Ba_2YFeO_{5.5}$ was prepared via a low-temperature oxidation of the cation ordered perovskite Ba_2YFeO_5. The as-prepared Ba_2YFeO_5 sample (Chapter 3) was placed into a high pressure vessel and heated at 410 ^oC for 24 h under 80 bar oxygen to form $Ba_2YFeO_{5.5}$, as described in Chapter 2.

5.3 Results

5.3.1 Characterization of $Ba_2YFeO_{5.5}$.

X-ray powder diffraction data collected from both Ba_2YFeO_5 and $Ba_2YFeO_{5.5}$ are shown in Figure 5.3. It can be clearly observed that the data collected from the oxidized sample is different from that collected from the as-prepared Ba_2YFeO_5 sample, suggesting an oxidation reaction has occurred. The data collected from $Ba_2YFeO_{5.5}$ can be readily indexed using an orthorhombic unit cell (a = 12.13 Å, b = 6.06 Å, c = 8.09 Å). Iodometric titrations performed on the oxidized sample indicated an average iron oxidation state of Fe^{4+} (detailed in Table A5.1), consistent with the stated composition.

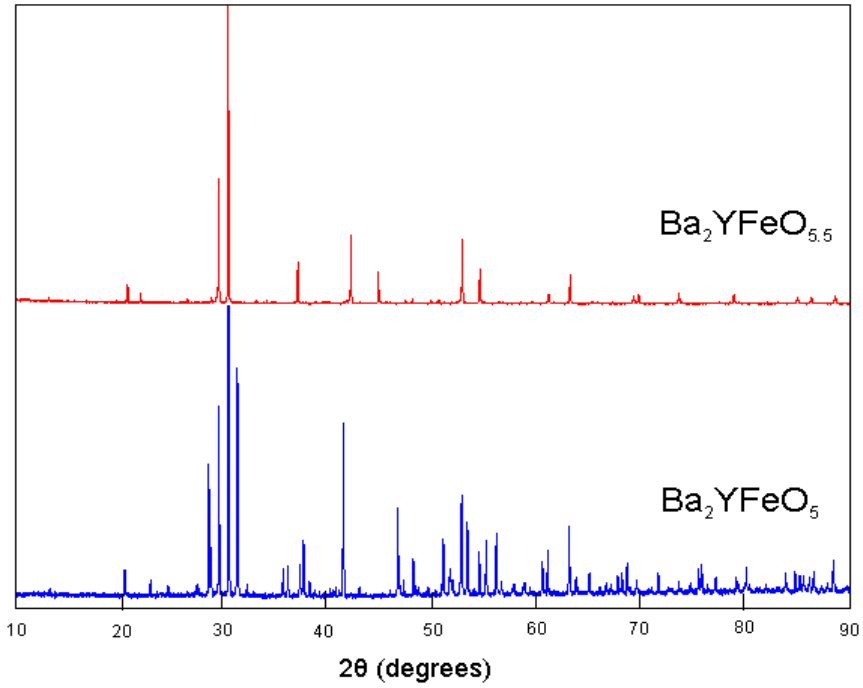

Figure 5.3. X-ray powder diffraction data collected from Ba_2YFeO_5 and $Ba_2YFeO_{5.5}$.

5.3.2 Room temperature structural refinement

Neutron powder diffraction data collected from $Ba_2YFeO_{5.5}$ at room temperature could be readily indexed using an orthorhombic unit cell (a = 12.13 Å, b = 6.06 Å, c = 8.09 Å) with extinction conditions consistent with $Pb2_1m$ (No. 26)[78] space group symmetry. Considering that $Ba_2YFeO_{5.5}$ was synthesized via the low-temperature oxidation of the cation ordered Ba_2YFeO_5 phase, it is assumed that $Ba_2YFeO_{5.5}$ shares a similar cation ordering pattern to Ba_2YFeO_5. Thus a structural model with a composition of Ba_2YFeO_6 was constructed on the basis of the cation ordered structure of Ba_2YFeO_5 with additional oxide ions inserted into all the anion vacancies of the lattice to form a 'perovskite' phase with complete oxygen stoichiometry. This model was then refined against the neutron powder diffraction data collected from $Ba_2YFeO_{5.5}$. During the refinement, the atomic positions and the fractional occupancies of cations and oxide anions were allowed to refine. Refinement of the

constructed model against neutron powder diffraction data collected from $Ba_2YFeO_{5.5}$ converged rapidly to give a good visual and statistical fit (χ^2 = 5.886). Observed calculated and difference plots from the refinement are shown in Figure 5.4.

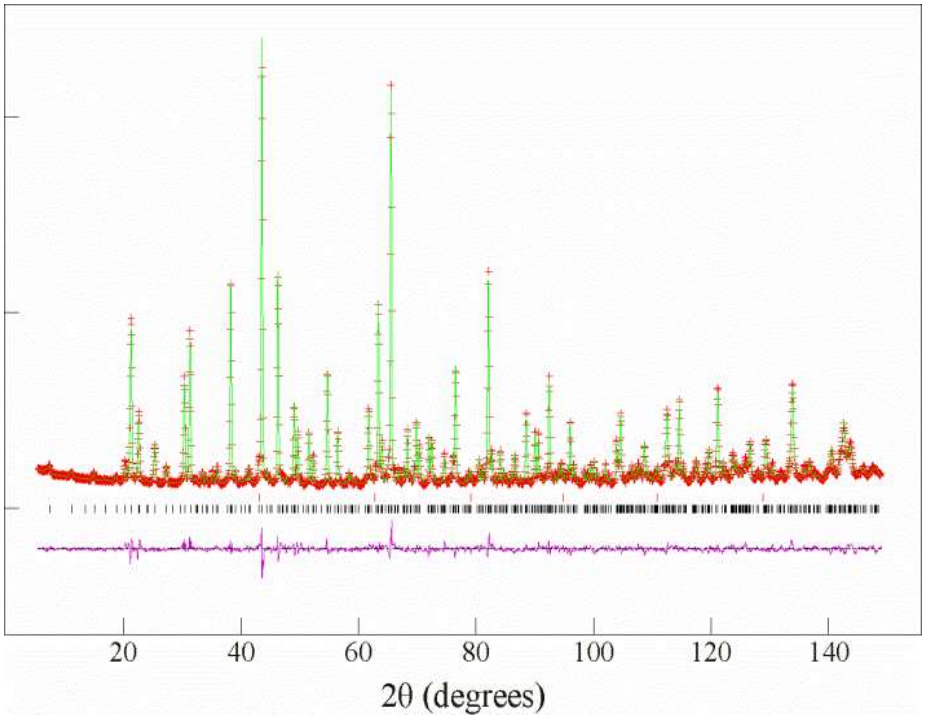

Figure 5.4 Observed, calculated and difference plots from the structural refinement of $Ba_2YFeO_{5.5}$ against neutron powder diffraction data collected at room temperature. The red tick marks indicate peak positions of the vanadium sample holder.

Refinement of the yttrium and iron site occupancies revealed no evidence of anti-site disorder, indicating the cation order of the parent Ba_2YFeO_5 phase is retained in the oxidized phase. Refinement of the atomic positions and fractional occupancies of the oxide ions indicated the additional oxide ions are inserted into the vacancies in alternate layers of the lattice to form an anion-vacancy ordered arrangement (Figure 5.5) and to yield a new phase with composition $Ba_2YFeO_{5.5}$, consistent with the results of iodometric titration. Full details of the refined structure of $Ba_2YFeO_{5.5}$ are listed in Table 5.1, with selected bond lengths in Table 5.2. Figure 5.5 gives a picture of the refined structure of $Ba_2YFeO_{5.5}$. It can be seen that the insertion of the oxide ions leads to a new structure consisting of six-

coordinate yttrium centres, with iron in five-coordinate (blue polyhedra) and four-coordinate (orange polyhedra) sites.

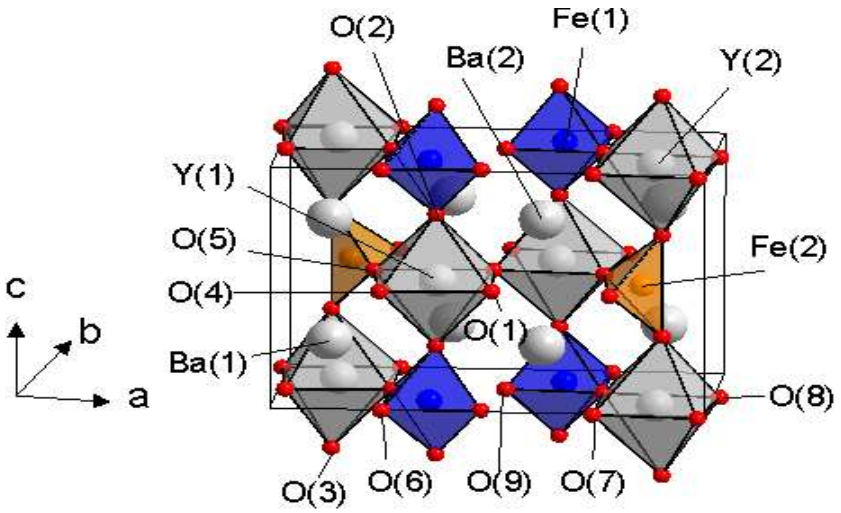

Figure 5.5 Atomic positions of refined structure of $Ba_2YFeO_{5.5}$.

Atom	site	x	y	z	U_{iso} ($Å^2$)
Ba(1)	4c	0.1264(6)	0.2310(22)	0.2471(8)	0.0150(6)
Ba(2)	4c	0.3852(6)	0.7392(22)	0.2376(7)	0.0150(6)
Y(1)	2b	0.3743(4)	0.2439(18)	½	0.0069(6)
Y(2)	2a	0.1249(4)	0.7311(21)	0	0.0069(6)
Fe(1)	2a	0.3566(4)	0.2337(18)	0	0.0070(11)
Fe(2)	2b	0.1548(5)	0.7203(16)	½	0.0116(12)
O(1)	2b	0.5086(13)	0.0090(24)	½	0.0190(17)
O(2)	4c	0.3697(5)	0.2567(14)	0.2259(8)	0.0139(7)
O(3)	4c	0.1089(5)	0.7202(19)	0.2890(7)	0.0139(7)
O(4)	2b	0.2526(11)	0.9570(21)	½	0.0139(7)
O(5)	2b	0.7818(8)	0.9539(18)	½	0.0139(7)
O(6)	2a	0.2553(12)	0.9913(24)	0	0.0139(7)
O(7)	2a	0.7424(10)	0.9785(22)	0	0.0139(7)
O(8)	2a	0.9855(10)	0.9404(22)	0	0.0190(17)
O(9)	2a	0.4836(8)	0.0375(16)	0	0.0123(21)
$Ba_2YFeO_{5.5}$ -space group $Pb2_1m$. a = 12.1320(2) Å, b = 6.0606(1) Å, c =8.0956(1) Å, V= 595.257(2) $Å^3$ χ^2 = 5.886, wRp = 5.34 %, Rp = 4.15 %					

Table 5.1 The refined structure of $Ba_2YFeO_{5.5}$ at room temperature.

cation	anion	Bond (Å)	BVS
Y(1)	O(1)	2.164(17)	Y +3.48
	O(1)	2.145(17)	
	O(2)	2 × 2.221(6)	
	O(4)	2.282(12)	
	O(5)	2.281(16)	
Y(2)	O(3)	2 × 2.349(6)	Y +3.08
	O(6)	2.234(17)	
	O(7)	2.222(16)	
	O(8)	2.213(17)	
	O(8)	2.114(15)	
Fe(1)	O(2)	2 × 1.841(7)	Fe +3.73
	O(6)	1.915(17)	
	O(7)	1.909(16)	
	O(9)	1.946(12)	
Fe(2)	O(3)	2 × 1.797(6)	Fe +3.69
	O(4)	1.862(15)	
	O(5)	1.788(14)	

Table 5.2 Selected bond lengths from the refined structure of $Ba_2YFeO_{5.5}$ at room temperature.

5.3.3 Second-harmonic generation

The insertion of oxide ions into the structural lattice of Ba_2YFeO_5 leads to a breaking of inversion symmetry of the host lattice, yielding a noncentrosymmetric structure (space group, *Pb2₁m* (No. 26)[77-78]). In order to confirm this feature, powder second-harmonic generation (SHG) measurements were performed as described in Chapter 2. The measurements indicated that the material has phase-matchable SHG response with an intensity of approximately 1 × SiO_2 as shown in Figure 5.6, confirming a noncentrosymmetric structure adopted by $Ba_2YFeO_{5.5}$.

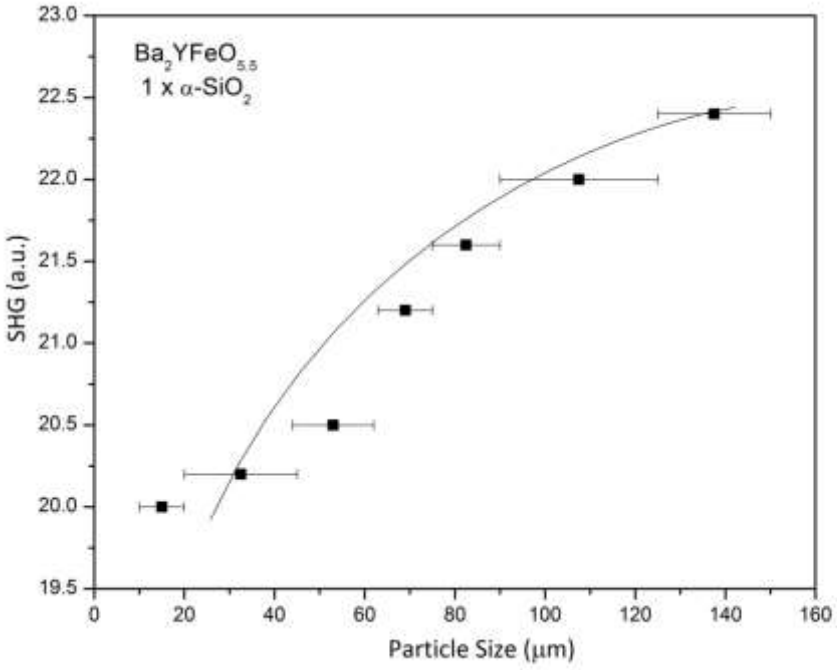

Figure 5.6 SHG intensity vs particle size data for $Ba_2YFeO_{5.5}$. The curve is drawn to guide the eye and is not a fit to the data.

5.3.4 Magnetic characterization

Zero-field-cooled and field-cooled DC magnetization data collected from $Ba_2YFeO_{5.5}$ in an applied field of 100 Oe in the temperature range of 5 < T/K < 300 are shown in Figure 5.7. The data collected in the range 40 < T/K < 300 can be fitted to the Curie-Weiss law ($\chi = C/(T-\theta)$), giving a Curie constant of 2.54 cm^3 K mol^{-1} and a Weiss constant θ = 14.7 K. Below 25 K the zero-field-cooled and field-cooled data diverge, consistent with the onset of magnetic order.

Magnetization field isotherms collected at 20 and 5 K exhibit hysteresis and indicate saturated moments of 1.45 and 1.27 μ_B per formula unit respectively in an applied field of 5 T, as shown in Figure 5.8. The hysteresis loop collected from $Ba_2YFeO_{5.5}$ at low temperature exhibits irregular shape, which motivated the collection of AC susceptibility data.

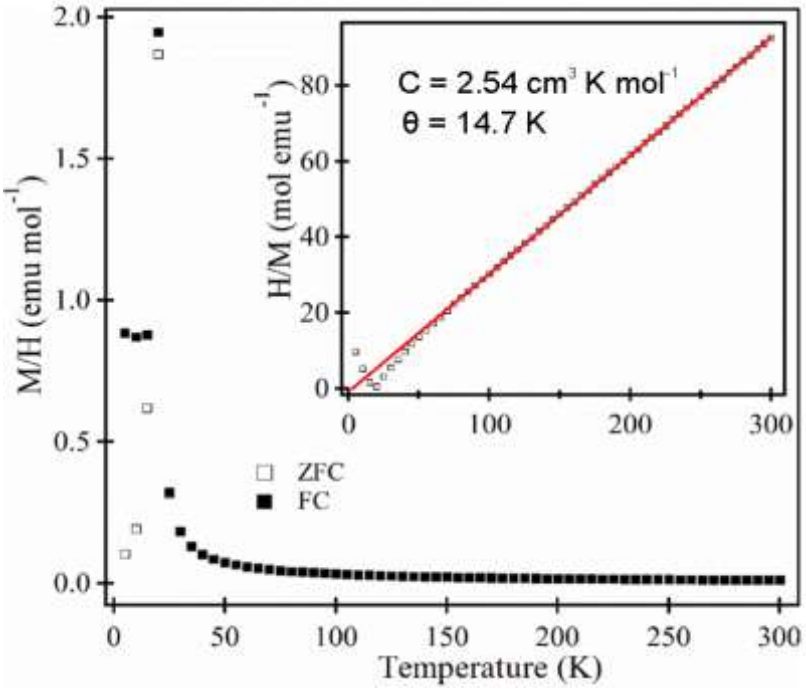

Figure 5.7 Zero-field-cooled and field-cooled magnetization data collected from $Ba_2YFeO_{5.5}$ in the temperature range 5 < T (K) < 300. Inset shows a fit to the Curie-Weiss law.

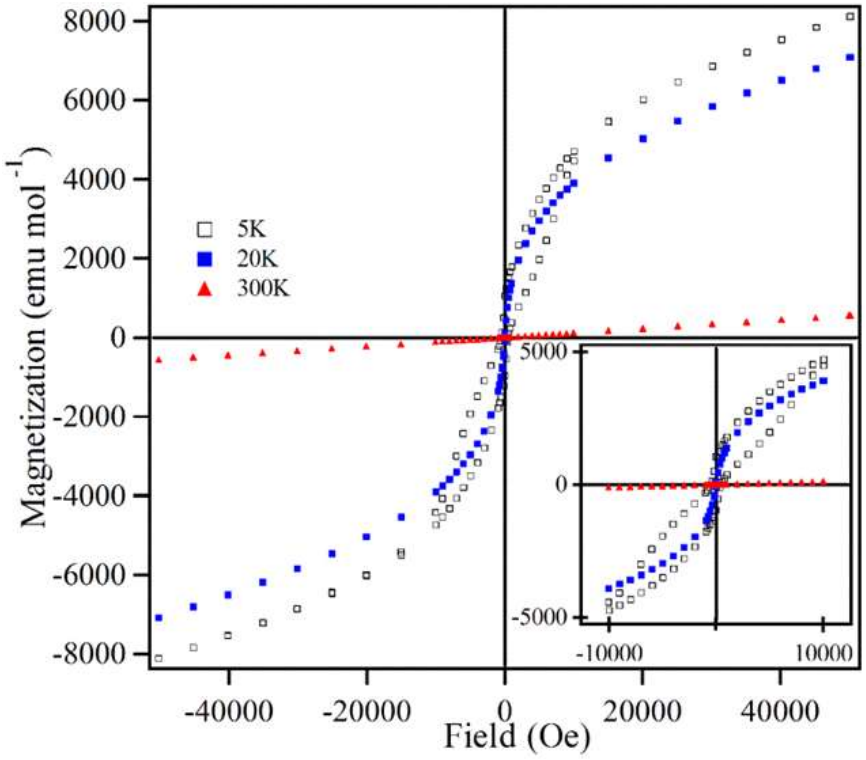

Figure 5.8 Magnetization-field isotherms collected from $Ba_2YFeO_{5.5}$ at 5, 20 and 300 K, inset shows expended region around zero applied field.

AC susceptibility measurements were conducted to determine the frequency dependence of the magnetic response. AC susceptibility data were collected at frequencies of 1, 10, 100 and 1000 Hz in the temperature of 10 < T/K < 30 to detect any spin-glass behaviour. As shown in Figure 5.9, a sharp frequency-independent peak was observed at T ~ 20 K in the real part of the magnetic response, inconsistent with spin-glass behaviour.

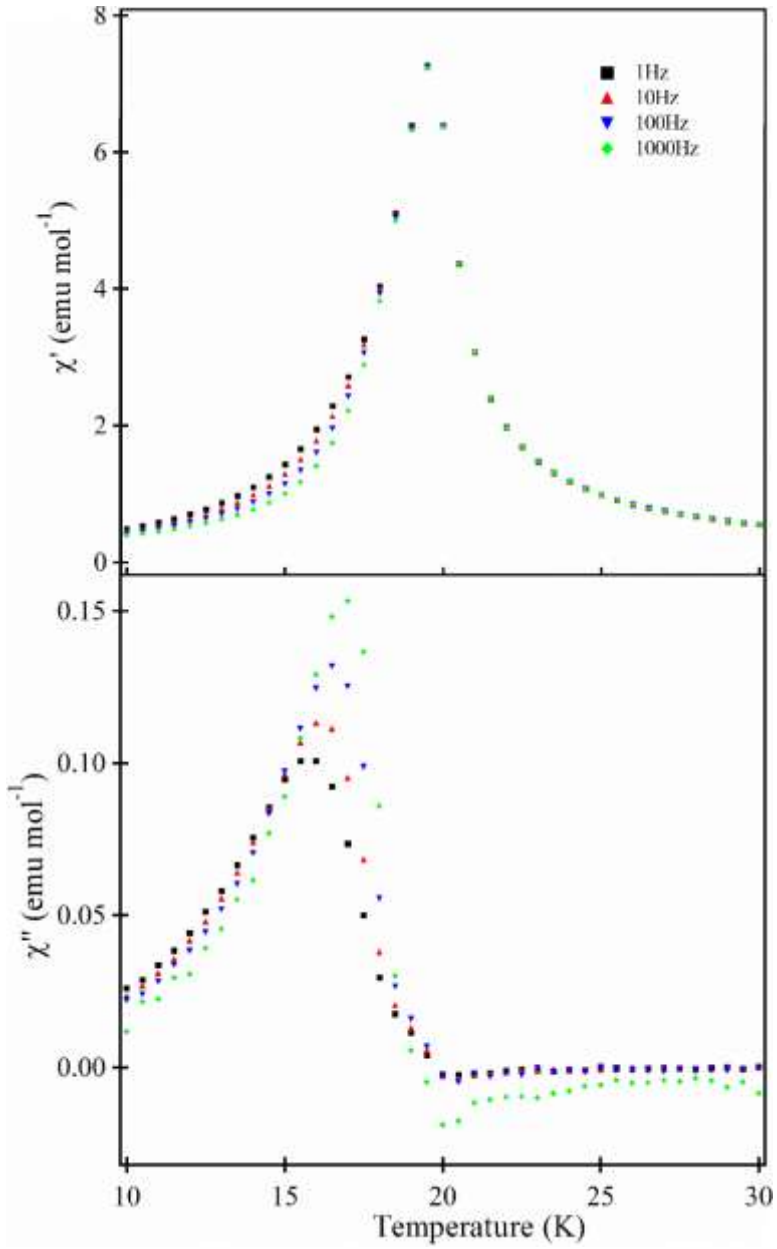

Figure 5.9 Real part and imaginary part of the ac susceptibility as a function of temperature (10 < T/K <30) at frequencies of 1, 10, 100 and 1000 Hz for $Ba_2YFeO_{5.5}$.

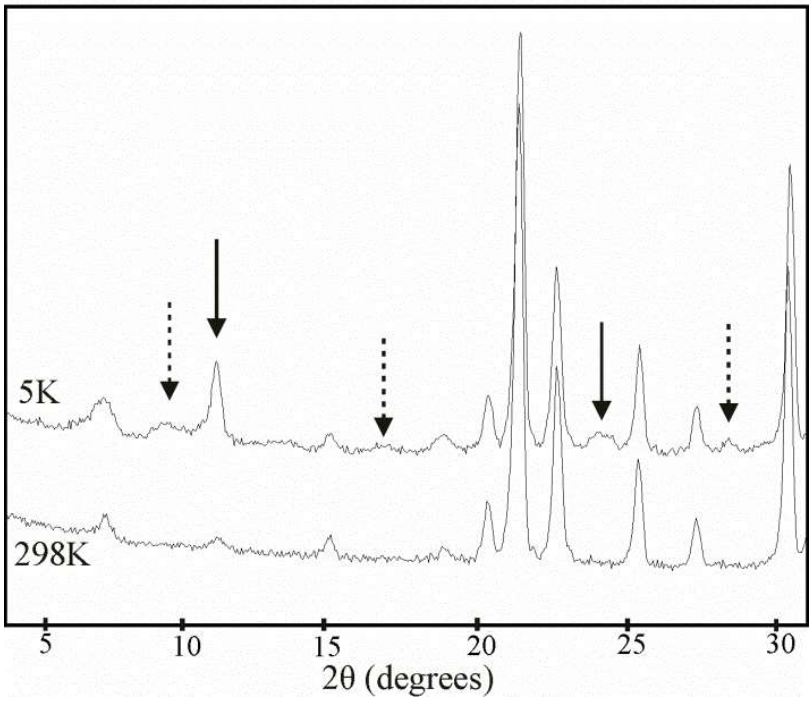

Figure 5.10 Neutron diffraction data collected from $Ba_2YFeO_{5.5}$ at 5 K and 300 K. Arrows mark the positions of additional diffraction features which appear on cooling, indicative of magnetic order.

In order to determine the magnetic order present in $Ba_2YFeO_{5.5}$, neutron powder diffraction data were collected at low temperature. Neutron powder diffraction data collected from $Ba_2YFeO_{5.5}$ at 5 K exhibit additional diffraction features compared to the room temperature data as shown in Figure 5.10, indicating magnetic order. These additional diffraction features consist of two components, the sharp peaks (bold arrows) and broad peaks (dotted arrows). The strong sharp diffraction features can be indexed using a crystallographic cell, and the intensities are accounted for using a ferromagnetic model of spins located on pyramidal sites aligned along *a*-axis. The weak broad diffraction features can be indexed using a $1 \times 1 \times 2$ expansion relative to the crystallographic cell, and the intensities are accounted for using an antiferromagnetic model of spins located on tetrahedral sites aligned along *b*-axis. The constructed magnetic models are shown in Figure 5.12. Refinement of these two magnetic models against the neutron diffraction data collected at 5 K gives a good fit (Figure 5.11), and yields ordered moments of 3.9(2) μ_B and

3.6(4) μ_B per iron centre for the cations in pyramidal (ferromagnetic) and tetrahedral (antiferromagnetic) sites respectively.

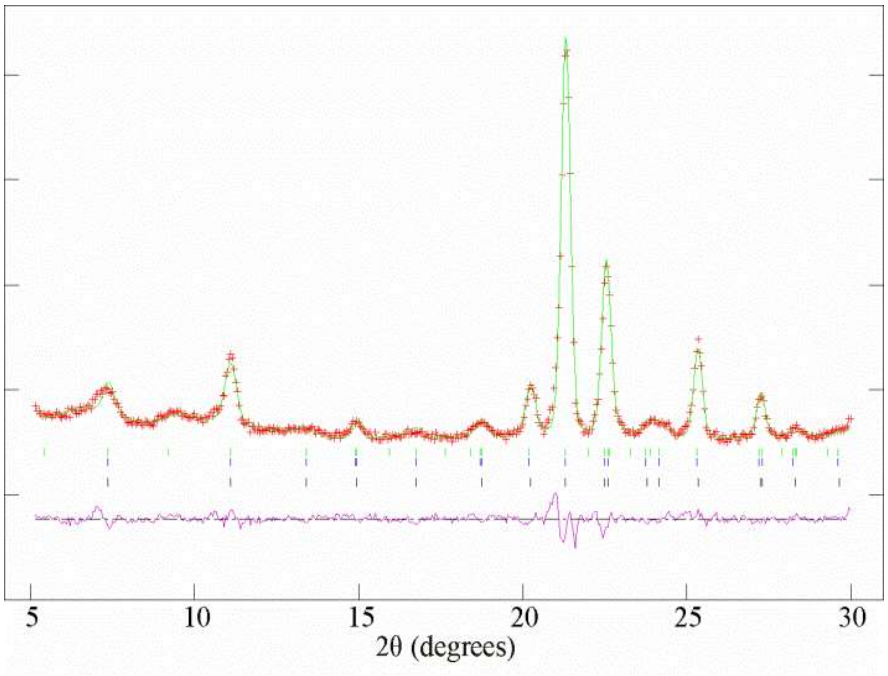

Figure 5.11 Observed, calculated and difference plots from the structural and magnetic refinement of $Ba_2YFeO_{5.5}$ against data collected at 5 K. Lower tick marks indicate allowed structural peak positions, and middle and upper tick marks indicated allowed magnetic peak positions.

In order to confirm the complex magnetic structure adopted by $Ba_2YFeO_{5.5}$ at low temperature, modifications were made into two magnetic models. Iron centres in tetrahedral sites were introduced into the ferromagnetic model and iron centres in pyramidal sites were introduced into the antiferromagnetic model. The magnetic moment on each iron centre was set to be 4 μ_B, and two models were then refined against the neutron powder diffraction data collected from $Ba_2YFeO_{5.5}$ at 5 K. The refinement results indicated antiferromagnetic in the pyramidal centres and ferromagnetic in the tetrahedral centres to be zero, within error, consistent with the previous results.

Figure 5.12 shows a representation of the refined magnetic structure. Full details of the refined magnetic models are given in Table 5.3 and 5.4. As shown in Figure 5.12, the ordered magnetic structure of $Ba_2YFeO_{5.5}$ can be described as a combination of

ferromagnetic order of the FeO_5 (blue centres) layers inter-leaved with antiferromagnetic order of the FeO_4 (orange centres) layers. Table 5.3 and 5.4 list the refined magnetic models.

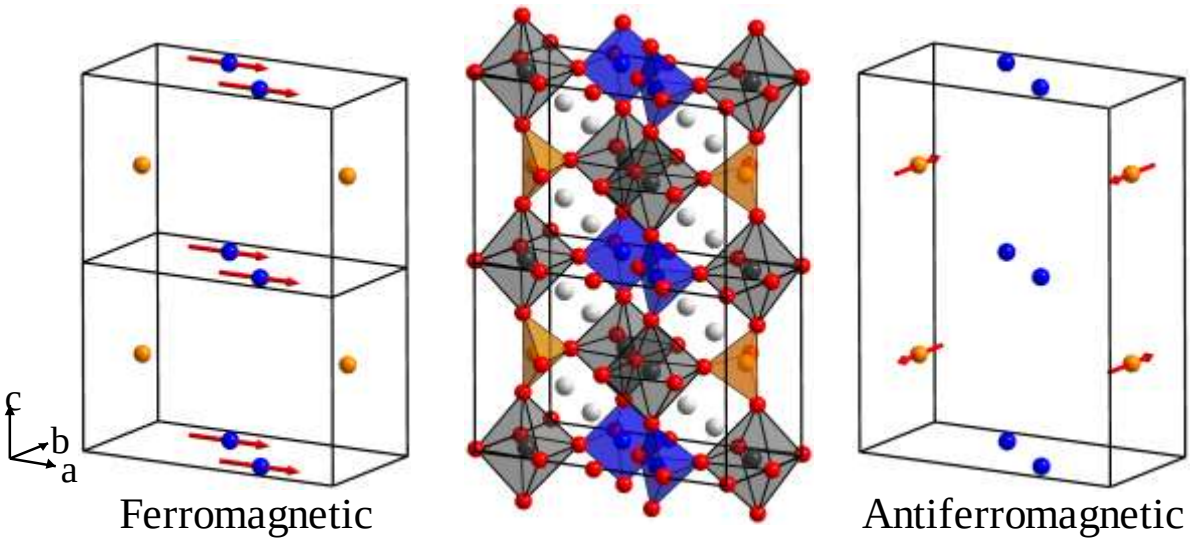

Figure 5.12 Magnetic structure of $Ba_2YFeO_{5.5}$ refined against neutron diffraction data collected at 5 K.

Atom	x	y	z	$M_x(\mu_B)$	$M_y(\mu_B)$	$M_z(\mu_B)$
Fe(1)	0.3588	0.2333	0	0	0	0
Fe(2)	0.6439	0.7288	0	0	0	0
Fe(3)	0.1545	0.7220	¼	0	-3.62(41)	0
Fe(4)	0.8507	0.2124	¼	0	3.62(41)	0
Fe(5)	0.3588	0.2333	½	0	0	0
Fe(6)	0.6439	0.7288	½	0	0	0
Fe(7)	0.1545	0.7220	¾	0	3.62(41)	0
Fe(8)	0.8507	0.2124	¾	0	-3.62(41)	0
$Ba_2YFeO_{5.5}$ -Space group-*P1* *a* = 12.0932 Å, *b* = 6.0410 Å, *c* = 16.1832 Å, V = 1182.264 $Å^3$						

Table 5.3 Structural parameters from the antiferromagnetic refinement of $Ba_2YFeO_{5.5}$ against neutron diffraction data collected at 5 K.

atom	x	y	z	$M_x(\mu_B)$	$M_y(\mu_B)$	$M_z(\mu_B)$
Fe(1)	0.3588	0.2333	0	3.91(23)	0	0
Fe(2)	0.6439	0.7288	0	3.91(23)	0	0
Fe(3)	0.1545	0.7220	½	0	0	0
Fe(4)	0.8507	0.2124	½	0	0	0
$Ba_2YFeO_{5.5}$ -Space group-*P1* *a* = 12.0932 Å, *b* = 6.0410 Å, *c* = 8.0916 Å, V = 591.132 $Å^3$						

Table 5.4 Structural parameters from the ferromagnetic refinement of $Ba_2YFeO_{5.5}$ against neutron diffraction data collected at 5 K.

5.3.5 Polar behaviours of $Ba_2YFeO_{5.5}$

$Ba_2YFeO_{5.5}$ adopts a polar noncentrosymmetric structure with space group of $Pb2_1m$ (No. 26)[77], indicating that the insertion of oxide ions breaks the inversion symmetry of the host lattice. In addition, magnetization data and neutron powder diffraction data at low temperature indicate that $Ba_2YFeO_{5.5}$ adopts a combination of ferromagnetic and antiferromagnetic behaviours at low temperature. The structure and magnetic properties motivate an interest in two questions: a) Is the polarization of the material switchable in an applied electric field, allowing the material to exhibit ferroelectric behaviour? ; b) Are the magnetic and electric behaviours coupled at low temperature, yielding a multiferroic material?

In order to examine these questions, a series of experiments were carried out. Figure 5.13 shows a plot of the pyroelectric current as a function of temperature. Initially, the sample was cooled from room temperature to 5 K in an opposite applied electric field. No changes in the pyrocurrent could be observed in the intrinsic region below 100 K, indicating neither change in electric polarization nor entry into a pyroelectric phase occurred at low temperature. Above 100 K, an extrinsic pyrocurrent evolved due to the thermal relaxation of charge, which is trapped at grain boundaries within the sample.

The pyrocurrent was also measured under an applied magnetic field in order to investigate any coupling between the polarization and the magnetic ordering below 20 K. As shown in the lower inset of Figure 5.13, a dependence of pyroelectric current on magnetic field could not be observed. However, the possibility of ferroelectricity cannot be excluded if the ferroelectric transition temperature is above 100 K. Thus ferroelectric hysteresis was measured using a PUND method[79] at 78 K. As shown in the upper inset of Figure 5.13, no hysteresis loop can be observed, consistent with the absence of ferroelectricity.

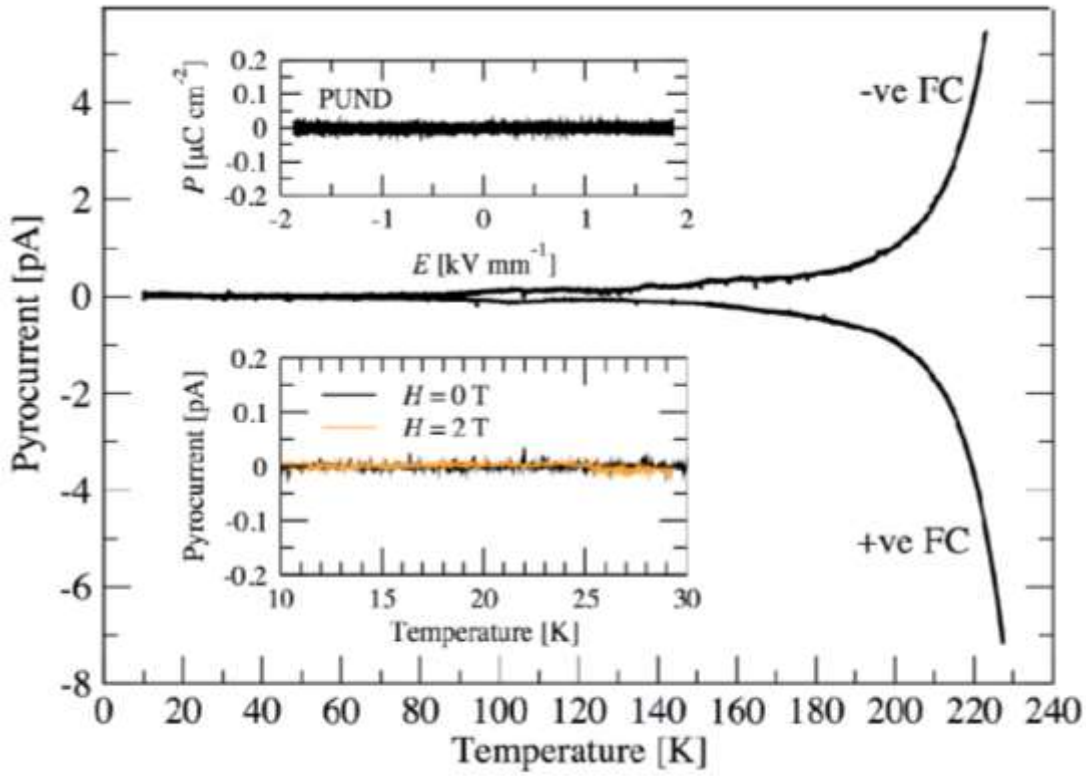

Figure 5.13 The pyrocurrent measured under opposite poling fields. The lower inset shows detail around the magnetic ordering temperature with and without an applied 2 T magnetic field. Results of a PUND ferroelectric hysteresis measurement at 78 K are given in the upper inset.

In addition, the dielectric behaviour of $Ba_2YFeO_{5.5}$ was measured at low temperature in order to confirm the absence of ferroelectricity. The real component of the dielectric constant and loss tangent were measured as a function of temperature between 10 and 240 K. As shown in Figure 5.14, a drop in ε_r' and tan δ can be observed at 210 K. The sample bar

for dielectric behaviours was prepared by oxidizing the pellets which were synthesized in a solid-state reaction. Thus the dielectric behaviour could be rationalized on the basis of Maxwell-Wagner relaxation induced by polycrystalline samples, where charge becomes trapped at interfaces in an electrically inhomogeneous material to give rise to Debye-like relaxation processes under an AC measuring voltage.[80,81]

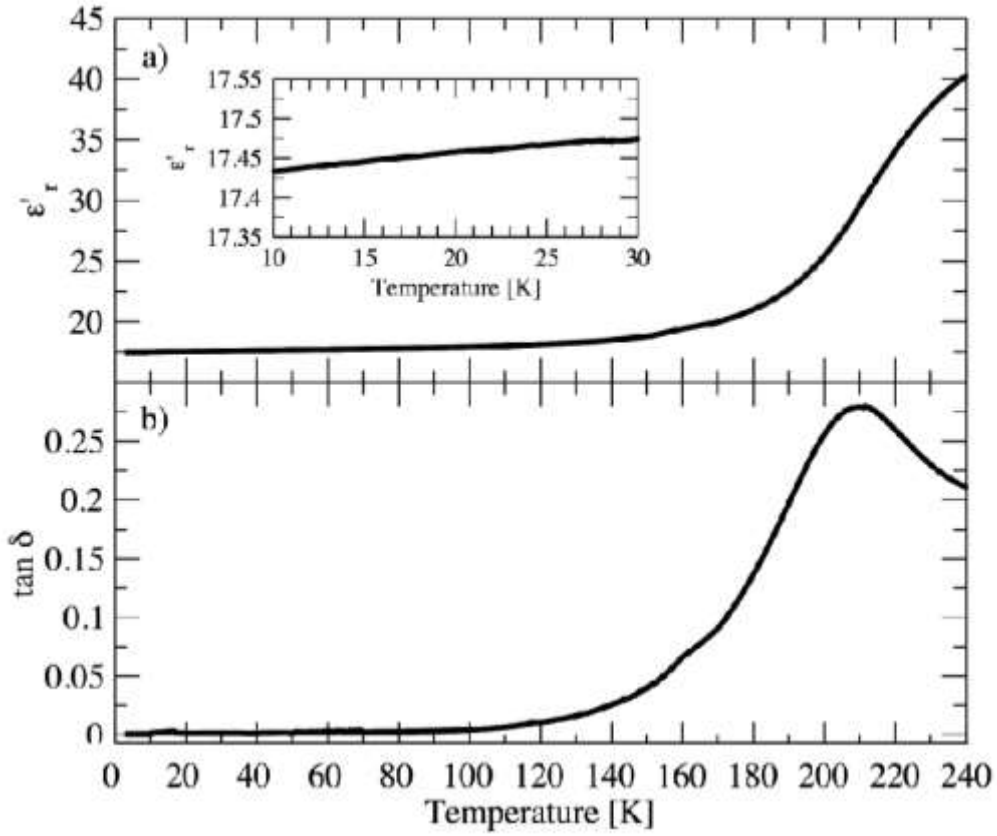

Figure 5.14 (a) and (b) The temperature dependence of the real component of the dielectric constant and the loss tangent, measured at 10 kHz.

In summary, the sample behaves intrinsically below 100 K, once the resistivity of the material is sufficiently large to prevent the movement of charge, and thus charge trapping. The details at low temperature are given in the inset of Figure 5.14a, which shows no evidence for an electric transition upon magnetic ordering at 20 K.

The lack of switchable polarization limits the $Ba_2YFeO_{5.5}$ material to exhibit pyroelectric behaviour only. In principle, a transition could be observed at high temperature due to a noncentrosymmetric-centrosymmetric structural transition. However, attempts to measure an undistorted centrosymmetric $Ba_2YFeO_{5.5}$ phase was limited by the decomposition of the phase at higher temperature. Thus the transition to paraelectric phase cannot be observed in the temperature-dependent pyroelectric current curve.

5.4 Discussion

The oxidation of Ba_2YFeO_5 was carried out under 80 oxygen pressure at 410 ^oC and leads to the formation of a new $Ba_2YFeO_{5.5}$ phase, consisting of YO_6 octahedra, FeO_5 pyramids and FeO_4 tetrahedra, as shown in Figure 5.15. Structural analysis indicated the product phase $Ba_2YFeO_{5.5}$ adopts a cation ordered structure which is identical to the Ba_2YFeO_5 host structure. In addition, the inserted oxide ions are located in the $Ba_2YFeO_{5.5}$ lattice in an ordered arrangement. More importantly, the insertion of oxide ions into the structure breaks the inversion symmetry of host structure to form a noncentrosymmetric structure with space group $Pb2_1m$. This polar structural feature allows the oxidized material to exhibit second harmonic generation activity and pyroelectric behaviour.

5.4.1 Anion-vacancy order

The insertion of oxide ions into the structural lattice of Ba_2YFeO_5 leads to the formation of $Ba_2YFeO_{5.5}$, in which the inserted oxide ions arranged in an ordered manner. The oxide ions are inserted into half the vacant anion sites within the cation-ordered Ba_2YFeO_5 framework. As shown in Figure 5.15, the structure changes from a Ba_2O_2 - $YFeO_3$ - Ba_2O_2 - $YFeO_3$ stacking sequence of Ba_2YFeO_5 into a Ba_2O_2 - $YFeO_4$ - Ba_2O_2 - $YFeO_3$ stacking sequence of $Ba_2YFeO_{5.5}$. As a result, there are two distinct types of iron centre: a set of

FeO_4 centres in the $YFeO_3$ layers of the material which basically retain the arrangement present in Ba_2YFeO_5, and a new set of FeO_5 centres in the $YFeO_4$ layers of the material, as shown in Figure 5.15.

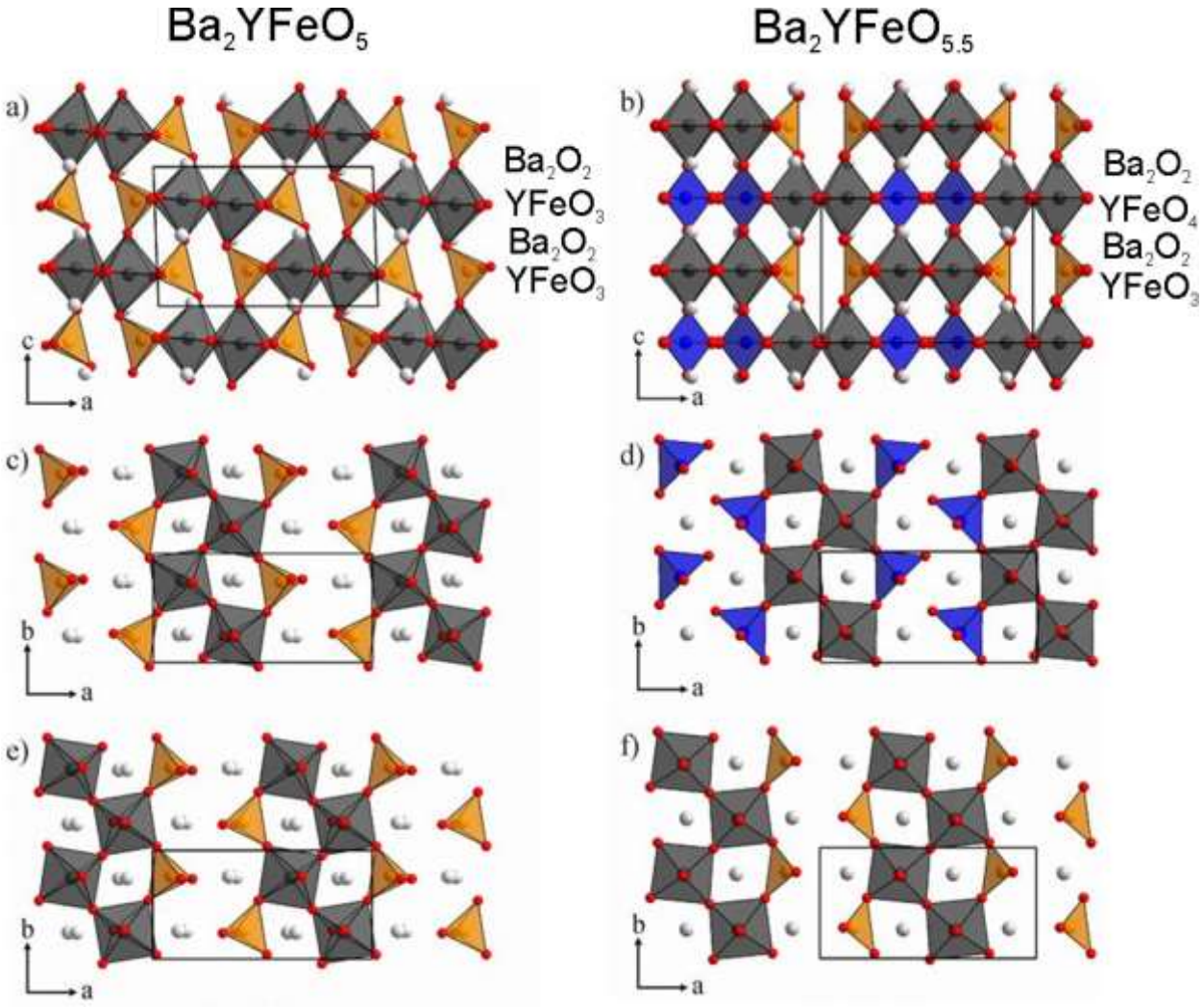

Figure 5.15 The structures of Ba_2YFeO_5 and $Ba_2YFeO_{5.5}$. (a, b) view down the b-axis of Ba_2YFeO_5 and $Ba_2YFeO_{5.5}$. (c, d) View down the c-axis showing polyhedra at z ~ 0.75 for Ba_2YFeO_5 and z ~ 0 for $Ba_2YFeO_{5.5}$. (e, f) View down the c-axis showing polyhedra at z ~ 0.25 for Ba_2YFeO_5 and z ~ 0.5 for $Ba_2YFeO_{5.5}$ respectively. Solid lines indicate the respective unit cells. Grey octahedra represent YO_6 units, orange tetrahedra FeO_4 units, blue square-based pyramids FeO_5 units, grey spheres Ba^{2+} cations.

The ordered arrangement of the inserted oxide ions in the structure of $Ba_2YFeO_{5.5}$ is unusual compared to the products of other reactions in topochemical anion-insertion. The topochemical oxidation reactions of $A_2B_2O_5$ brownmillerite phases show a similar process to the oxidation reaction of Ba_2YFeO_5 discussed in this chapter.

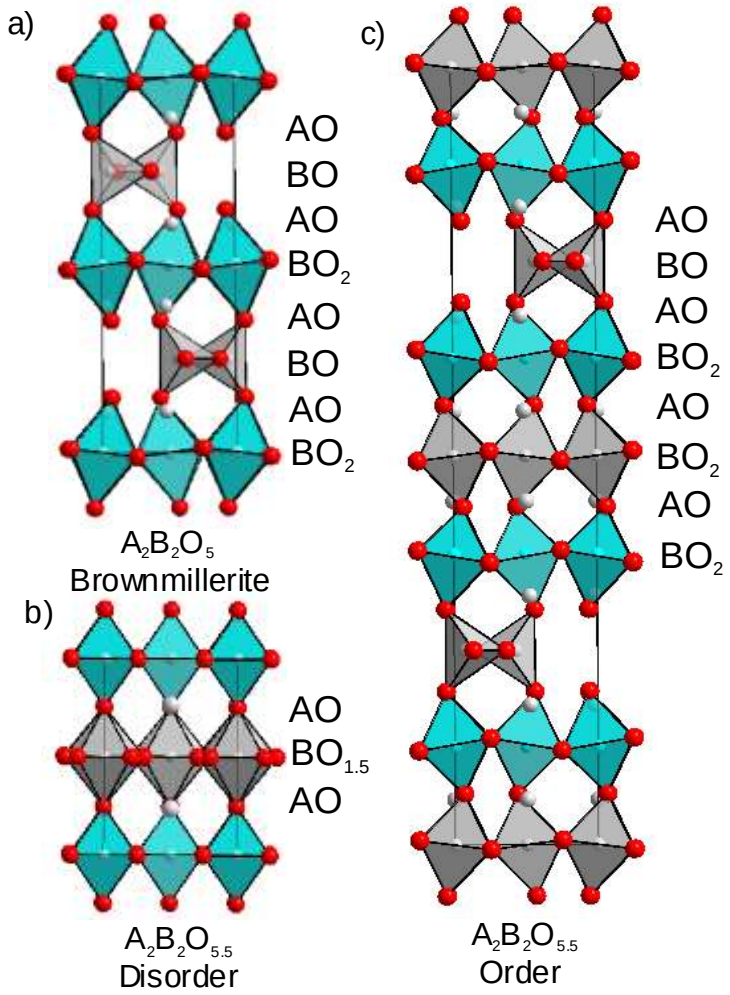

Figure 5.16 The arrangement of anion vacancies of the oxidized brownmillerite phases.

Brownmillerite phases adopt a layered structure with a stacking sequence of – AO – BO – AO –BO_2 – AO – BO – AO – BO_2 –, as shown in Figure 5.16a. The oxidation of a brownmillerite phase under oxygen at low temperature retains the arrangement of cations within the host phase, thus this oxidation reaction can also be considered as a topochemical reaction. It should be noted that this oxidation reaction can lead to the formation of two different types of structure. For example, the oxidation of Sr_2MnGaO_5 to $Sr_2MnGaO_{5.5}$ inserts oxide ions into the phase in a disordered manner and yields a staking sequence of – AO – $BO_{1.5}$ – AO – $BO_{1.5}$ –, as shown in Figure 5.16b. In contrast, the oxidation of Ca_2MnAlO_5 to $Ca_2MnAlO_{5.5}$ inserts oxide ions into the host in an ordered manner to give a

stacking sequence of – AO – BO – AO – BO_2 – AO – BO_2 – AO – BO_2 –[82], as shown in Figure 5.16c. Structural investigations have indicated that the ordered arrangement of the inserted oxide ions into the lattice of Ca_2MnAlO_5 could be induced by the tendency to minimize the internal strain in the product phase.

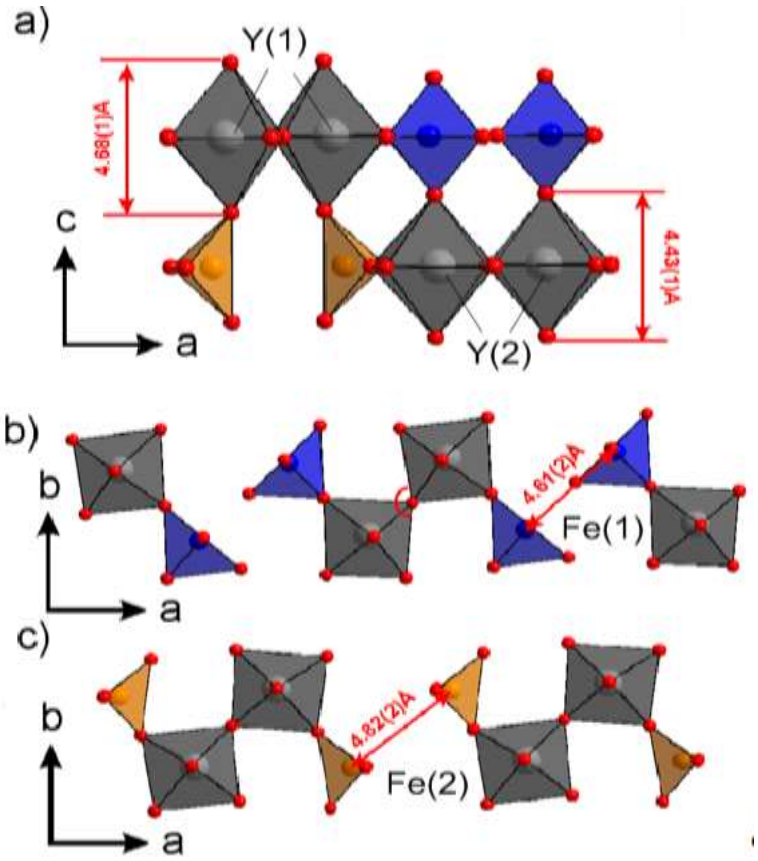

Figure 5.17 Structural distortions in $Ba_2YFeO_{5.5}$.

The anion insertion into the Ca_2MnAlO_5 brownmillerite structure seems similar to the topochemical oxidation process in this chapter, suggesting lattice strain could also be driving the ordered insertion of oxide ions into $Ba_2YFeO_{5.5}$. Close inspection of the structure of $Ba_2YFeO_{5.5}$ reveals that the bond valence sums (BVS) of the Y(2) centres give a value of +3.08, almost identical to the value of yttrium centres in Ba_2YFeO_5 (+3.10), suggesting that $Y(2)O_6$ octahedra underwent only a slight distortion, maintaining the environment of yttrium centres in Ba_2YFeO_5. Comparatively, the $Y(1)O_6$ octahedra underwent an obvious distortion in *c* direction, giving an increased BVS value of +3.48. As

shown in Figure 5.17a, the distance between the two oxide ions at the apex positions in the $Y(1)O_6$ octahedra is 4.68(1) Å, 5.3% bigger than that in the $Y(2)O_6$ octahedra. In addition, the insertion of oxide ions into the lattice leads to the different distances between the Fe(1) centres (4.61 Å) and Fe(2) centres (4.82 Å), as shown in Figure 5.17b and c. Considering that the structure is constructed of zigzag chains of the YO_6 octahedra, when the oxide ions are inserted into the ~ (1/4, 0, 1/4) vacant positions in the host lattice, the lattice strain induces a cooperative tilting in the zigzag chains of YO_6 octahedra so that the oxide ions could not be inserted into the 'vacant' position in the adjacent layers. Thus the ordered arrangement of inserted oxide ions in the alternate layers would minimize the internal strain.

It could also be considered that the charge disproportionation of Fe^{4+} as observed in other phases would lead to the $Fe^{3+}O_4$ and $Fe^{5+}O_5$ centres, thus yielding the ordered arrangement of anion vacancies in $Ba_2YFeO_{5.5}$. Previous studies on Mössbauer spectroscopy and neutron diffraction data[83,84] indicated charge disproportionation of the Fe^{4+} centres into Fe^{3+} and Fe^{5+} centres in the structure of $CaFeO_3$ due to the electronic instability of Fe^{4+} cations in octahedral sites. Based on this assumption, the $Fe(1)O_4$ and $Fe(2)O_5$ centres were analyzed using bond valence sums. The analyses give the similar values for two centres (FeO_5 = Fe+3.73; FeO_4 = Fe+3.69) at room temperature and remain equal even at 5 K. Thus there is no evidence to support the charge disproportionation of Fe^{4+} cations.

5.4.2 Symmetry breaking in $Ba_2YFeO_{5.5}$

$Ba_2YFeO_{5.5}$ adopts a polar noncentrosymmetric structure, which allows this material to exhibit second-harmonic generation activity and pyroelectric behaviour. The insertion of oxide ions into the host lattice of Ba_2YFeO_5 leads to a breaking of inversion symmetry. In this case, the noncentrosymmetric structure was achieved without involving SOJT cations

(such as Ti^{4+} cations or 'lone-pair' cations like Bi^{3+}) in the lattice which is the conventional strategy to achieve noncentrosymmetric structures as discussed in Chapter 1. The symmetry breaking in $Ba_2YFeO_{5.5}$ is driven by a combination of two factors: a) electronic instability; b) lattice strain.

a) Electronic instability. Close inspection of the structure of $Ba_2YFeO_{5.5}$ reveals that the 'bond' length (grey) of Fe(1) – O(9) is 2.67 Å, much larger than average Fe - O bond length of 1.89 Å, as shown in Figure 5.18. As a result, the coordination environment of the Fe(1) centres is '5+1'-coordinate pyramid rather than 6-coordinate octahedra.

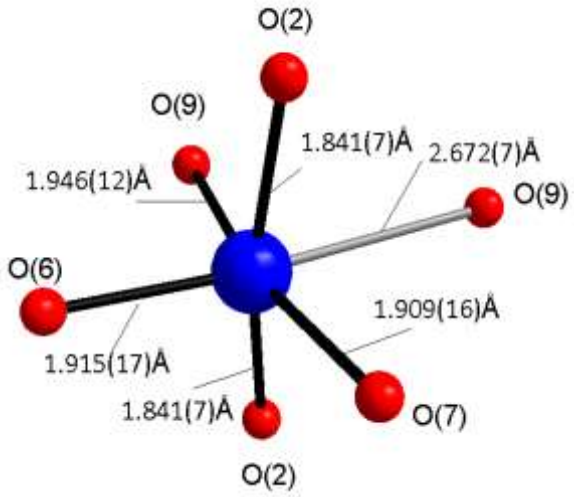

Figure 5.18 Coordination environment of Fe(1) centre.

Iodometric titration results and neutron diffraction data of $Ba_2YFeO_{5.5}$ confirmed an average oxidation state of Fe^{4+}, which has a degenerate $t_{2g}^3 e_g^1$ electronic configuration and is not stable in an octahedral ligand field with respect to a local distorted coordination. In order to stabilize the d^4 electronic configuration, the $d_{x^2-y^2}$ orbital would be lifted with respect to the d_{z^2} orbital. Thus a primary Jahn-Teller distortion is observed, which 'pushes' one of the coordinated oxide ions far away

from the iron centre. As a result, Fe^{4+} cations is stabilized in the 5-coordinate pyramidal sites, which adopt a $(d_{xz}, d_{yz})^2(d_{xy})^1(d_z^2)^1(d_{x^2-y^2})^0$ electronic configuration as shown in Figure 5.19. Thus the electronic instability could be considered as one of main factors driving a breaking of inversion symmetry.

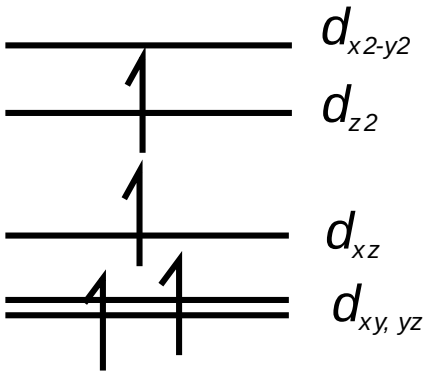

Figure 5.19 Electronic configuration of Fe^{4+} in square pyramidal sites.

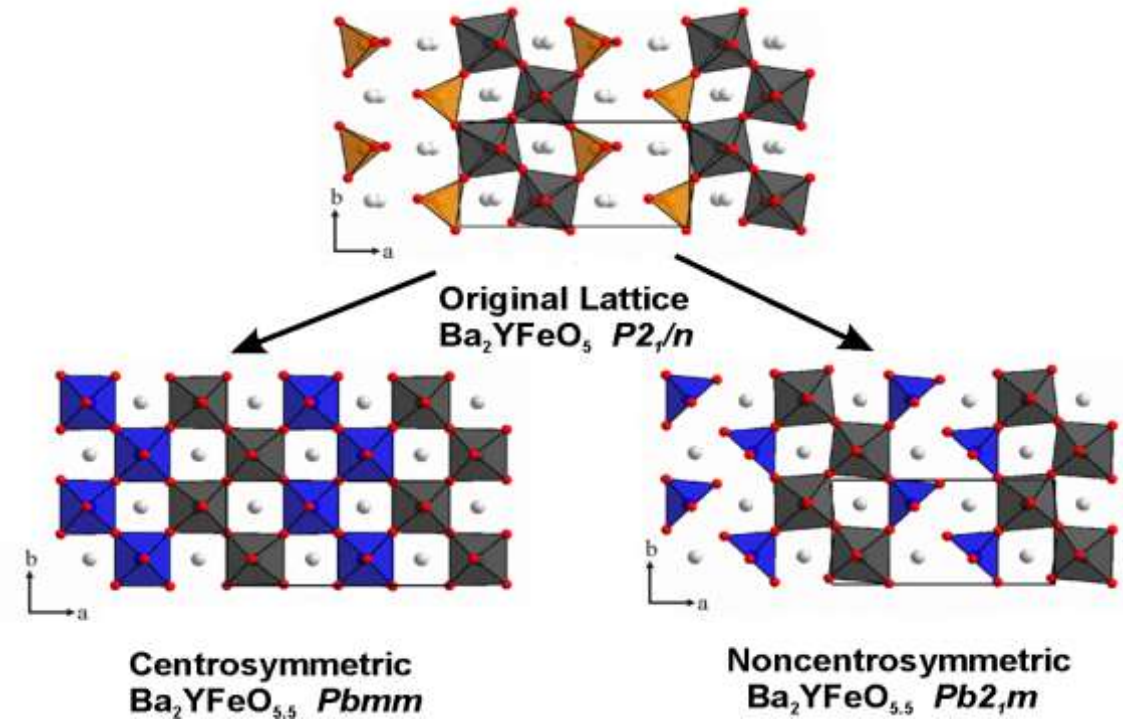

Figure 5.20 The $YFeO_3$ layers in Ba_2YFeO_5 (top) and the $YFeO_4$ layers in the hypothetical, undistorted centrosymmetric (middle) and distorted non-centrosymmetric (bottom) structures of $Ba_2YFeO_{5.5}$.

It should be noted that on the basis of this Jahn-Teller distortion the point symmetry of MO_6 octahedra could also descend from O_h (*m-3m*) to D_{4h} (*mmm*) like the hypothetical *Pbmm* structure as shown in Figure 5.20, which could also yield a lifting of the degeneracy among the *d* orbitals in the octahedral field. However, the hypothetical *Pbmm* structure would retain the inversion symmetry of lattice, leading to a centrosymmetric structure. This suggests that other factors should be considered in the symmetry breaking of oxide insertion into $Ba_2YFeO_{5.5}$.

b) Lattice Strain. Ba_2YFeO_5 adopts a complicated cation ordering pattern, consisting of YO_6 octahedra and Fe^{3+} tetrahedra as described in Chapter 3. The presence of anion vacancies in the lattice, combined with the size difference between Y^{3+} and Fe^{3+}, leads to a structure with low structural symmetry ($P2_1/n$). The structure of Ba_2YFeO_5 is constructed based on the YO_6 zigzag chains with the FeO_4 tetrahedra in between to form a pseudo one-dimensional framework, as shown in Figure 5.20. This kind of structure adopts different extension along *x*, *y* and/or *z* directions to form a low-dimensional lattice. This anisotropic nature of the low-dimensional lattice would provide an opportunity to construct noncentrosymmetric structures. For example, some low-dimensional chalcophosphates have already been proven to be promising candidates for ferroelectricity, piezoelectricity and second harmonic generation (SHG).[85,86]

Ba_2YFeO_5 has a centrosymmetric structure. However, the presence of anion vacancies in the lattice allows a modification to be conducted in the structure. Thus the symmetry breaking of $Ba_2YFeO_{5.5}$ can be considered as a two-step process: 1) the formation of the low-symmetry host lattice; 2) the modification through the insertion of oxide ions.

$Ba_2YFeO_{5.5}$ underwent an unusual distortion in the topochemical oxidation. As a result, all the FeO_5 units are twisted in the same direction, yielding a net polarization along *y*-axis as shown in Figure 5.21. Thus the formation of the polar structure is based on the lattice strain arising from the structural distortion. It is believed that the lattice strain, based on a large Ba^{2+} cations in the A sites and two cations (Y^{3+} and Fe^{4+}) with large size difference in the B sites, providing another driving force for the symmetry breaking and NCS arrangement of polyhedra.

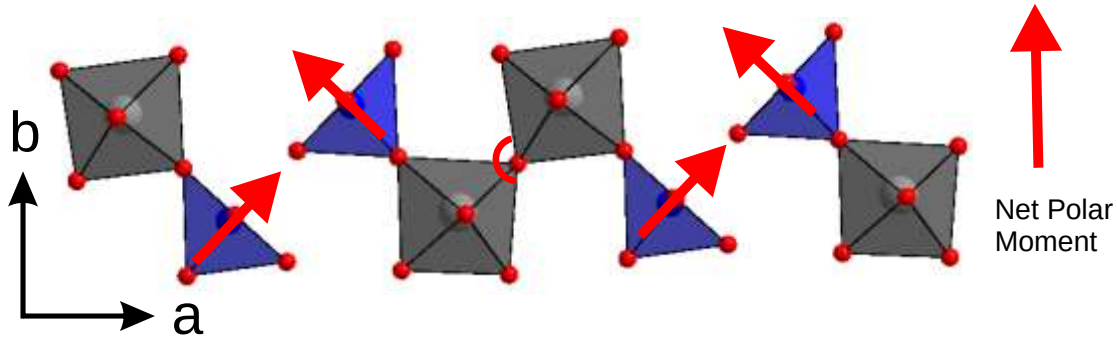

Figure 5.21 Illustration of net polar moment in $Ba_2YFeO_{5.5}$.

To sum up, the symmetry breaking in $Ba_2YFeO_{5.5}$ lattice is attributed to a combined effect of Jahn-Teller instability of the Fe^{4+} centres and lattice stain, which directs the system to adopt a distorted structure and form an NCS phase.

5.4.3 Magnetic behaviours

As discussed above, magnetization data collected from $Ba_2YFeO_{5.5}$ can be fitted to the Curie-Weiss law in the temperature range 40 < T/K <300 to give a Curie constant of C = 2.54 cm^3 K mol^{-1}, consistent with an observed moment approximately in line with that expected for a spin-only, S = 2, Fe^{4+} centre ($C_{expected}$ = 3 cm^3 K mol^{-1}). When the temperature is lower than 20 K, the magnetic order is observed. As shown in Figure 5.12, the FeO_5 centres exhibit a ferromagnetic order paralleled to *x*-axis, whilst the FeO_4 centres adopt an antiferromagnetic order paralleled to *y*-axis. Thus $Ba_2YFeO_{5.5}$ adopts an unusual

two-component magnetic structure, consisting of ferromagnetic and antiferromagnetic layers. The ferromagnetic interactions between FeO_5 centres can be rationalized on the basis of the Goodenough – Kanamori rules. The Fe^{4+} centres with square pyramidal coordination environments adopt a $(d_{xz}, d_{yz})^2(d_{xy})^1(d_z^2)^1(d_{x^2-y^2})^0$ electronic configuration, as shown in Figure 5.18. Thus the superexchange between neighbouring FeO_5 centres $Fe(d_z^2)^1$-O*2p*-$Fe(d_{x^2-y^2})^0$ leads to a ferromagnetic coupling (Figure 5.22), consistent with the refined magnetic structure.

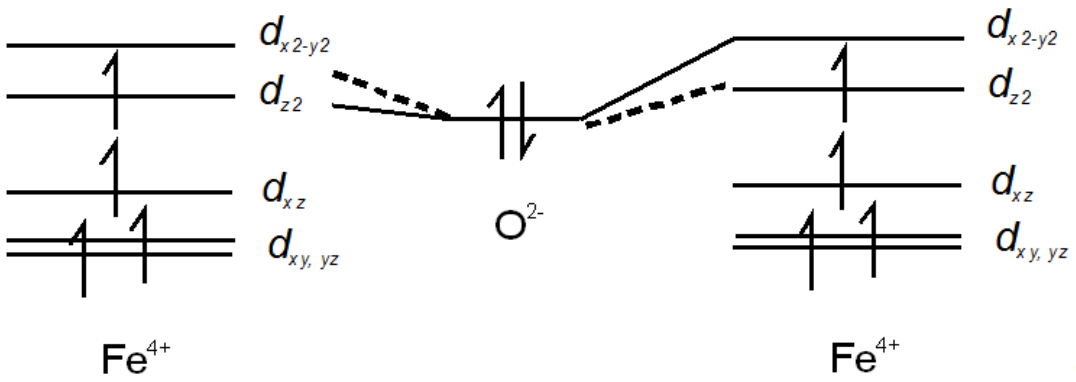

Figure 5.22 Graph of Fe^{4+} - O - Fe^{4+} superexchange in the square pyramidal sites.

The additional magnetic diffraction features assigned to the ferromagnetic and antiferromagnetic order in neutron powder diffraction data collected from $Ba_2YFeO_{5.5}$ at 5 K have different peak shapes. The diffraction peaks assigned to the antiferromagnetic order of FeO_4 centres are significantly broader than those assigned to the ferromagnetic order of FeO_5 centres. This difference could be caused by the absence of an extended Fe – O – Fe bond network connecting the FeO_4 centres. It should be noted that the refinement of the magnetic models against the neutron diffraction data collected at 5 K indicates an ordered moment of 3.6(4) μ_B along *y*-axis per iron centre for the cations in the tetrahedral sites, which is slightly smaller than the expected value for d^4 Fe^{4+} centers (4 μ_B). This difference

in the magnitude of magnetic moment could be attributed to covalency between Fe^{4+} and the surrounding oxide ions.

5.5 Conclusion

$Ba_2YFeO_{5.5}$ adopts an anion-vacancy ordered structure, consisting of YO_6 octahedra, FeO_4 tetrahedra and FeO_5 pyramids. The insertion of oxides into Ba_2YFeO_5 breaks the inversion symmetry of the host lattice. This symmetry breaking in $Ba_2YFeO_{5.5}$ could be attributed to the combination of electronic instability and lattice strain. The polar structure allows this material to exhibit the second-harmonic generation activity and pyroelectric behaviour. Magnetization data indicated that $Ba_2YFeO_{5.5}$ adopted a combined state of ferromagnetic and antiferromagnetic order at low temperature.

Appendix

Mass of sample(mg)	$x_{caculated}$	$x_{average}$
38.3	5.502	5.50(1)
39.5	5.498	
38.5	5.502	

Table A5.1 Results of iodometric titrations performed on the oxidized sample Ba_2YFeO_x

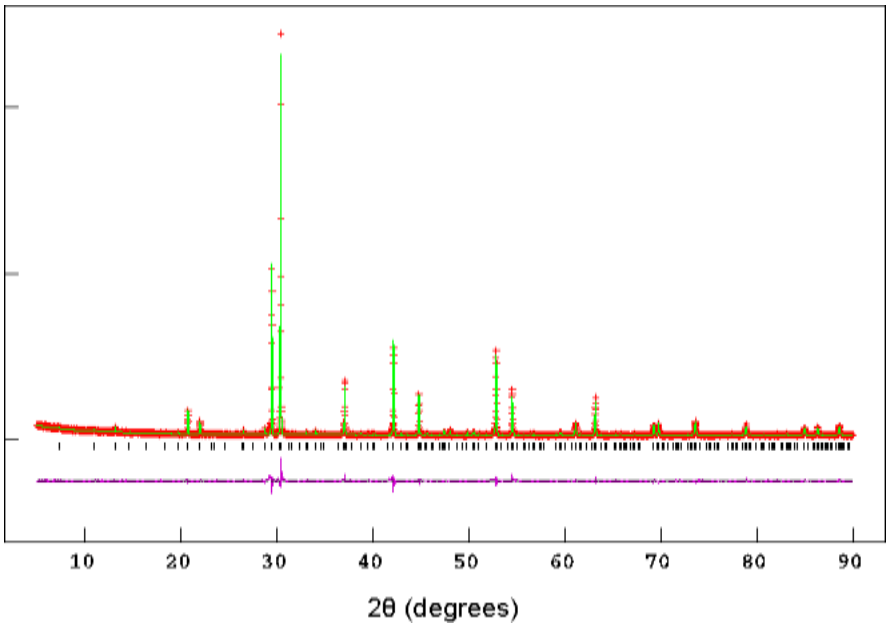

Figure A5.1. Observed, calculated and difference plots from the structural refinement of $Ba_2YFeO_{5.5}$ against X-ray powder diffraction data collected at room temperature.

Atom	site	x	y	z	U_{iso} (Å^2)
Ba(1)	4c	0.1278(6)	0.2311(25)	0.2429(7)	0.0053(6)
Ba(2)	4c	0.3873(6)	0.7430(21)	0.2339(6)	0.0053(6)
Y(1)	2b	0.3739(5)	0.2465(18)	½	0.0007(6)
Y(2)	2a	0.1261(5)	0.7285(22)	0	0.0007(6)
Fe(1)	2a	0.3587(4)	0.2342(19)	0	0.0049(11)
Fe(2)	2b	0.1547(4)	0.7225(15)	½	0.0044(11)
O(1)	2b	0.5134(11)	0.0212(21)	½	0.0073(16)
O(2)	4c	0.3732(5)	0.2547(16)	0.2242(8)	0.0072(7)
O(3)	4c	0.1090(5)	0.7258(21)	0.2875(7)	0.0072(7)
O(4)	2b	0.2501(12)	0.9537(21)	½	0.0072(7)
O(5)	2b	0.7849(8)	0.9499(18)	½	0.0072(7)
O(6)	2a	0.2508(12)	0.9945(22)	0	0.0073(16)
O(7)	2a	0.7344(9)	0.9820(21)	0	0.0072(7)
O(8)	2a	0.9821(11)	0.9393(22)	0	0.0072(7)
O(9)	2a	0.4823(7)	0.0385(15)	0	0.0068(19)
$Ba_2YFeO_{5.5}$ -space group *Pb2$_1$m*. *a* = 12.0937(2) Å, *b* = 6.0410(1) Å, *c* = 8.0919(1) Å, V= 591.189(2) Å^3 χ^2 = 6.853, wRp = 5.94 %, Rp = 4.62 %					

Table A5.2 Refined structure of $Ba_2YFeO_{5.5}$ at 5 K.

Chapter 6 Fluorination reaction of Ba_2YCoO_5

6.1 Introduction

Chapter 5 described how the insertion of oxide ions into the lattice of Ba_2YFeO_5 leads to the formation of $Ba_2YFeO_{5.5}$ which exhibits second-harmonic generation activity and pyroelectric behaviour. In addition to the insertion of oxide ions, fluoride ions can also be inserted into a perovskite lattice with anion vacancies. For example, $Sr_2Mn_2O_5F$ was prepared via a fluorination reaction of $Sr_2Mn_2O_5$[87] as shown in Figure 6.1.

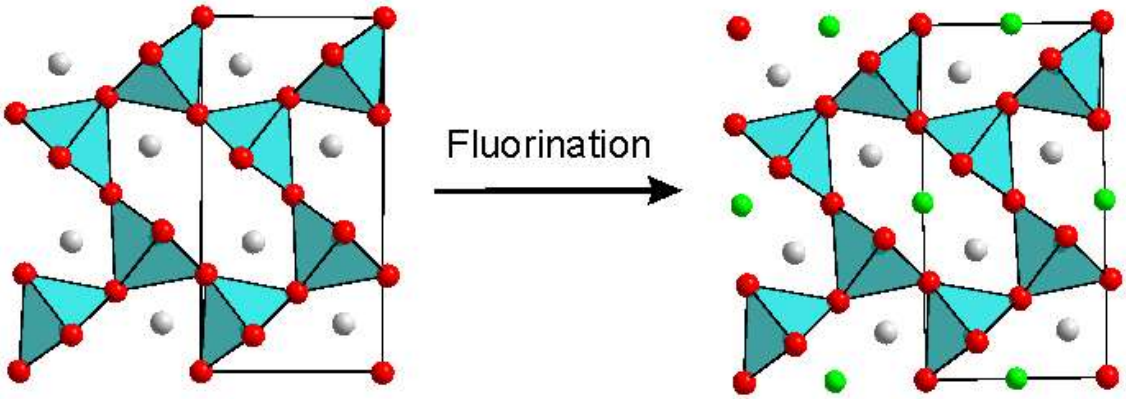

Figure 6.1 Fluorination reaction of $Sr_2Mn_2O_5$ to $Sr_2Mn_2O_5F$.

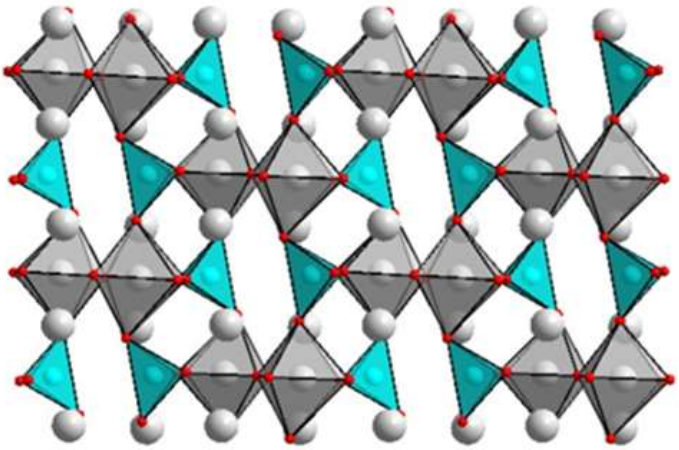

Figure 6.2 Structure of Ba_2YCoO_5.

In common with Ba_2YFeO_5, Ba_2YCoO_5 also has anion vacancies in the structure, as shown in Figure 6.2. In this chapter, the fluorination of Ba_2YCoO_5 was carried out, leading to the formation of $Ba_2YCoO_5F_{0.42}$. The structure and magnetic behaviour of $Ba_2YCoO_5F_{0.42}$ are discussed. The insertion of anions like oxide ions and fluoride ions into the lattice of Ba_2YMO_5 (M = Fe and Co) is analyzed.

6.2 Experimental

Initially, attempts to oxidize Ba_2YCoO_5 were carried out under flowing oxygen at 400 and 450 ^oC and under 100 bar oxygen pressure at 250 ^oC, as detailed in Table 6.1. X-ray powder diffraction data collected from the final products indicated no oxidation reaction occurred. Ba_2YCoO_5 was then heated at 500 ^oC under flowing oxygen or 270 ^oC under 100 bar oxygen pressure. X-ray powder diffraction data collected from the products of these materials indicated the decomposition of Ba_2YCoO_5 and the formation of the Co^{4+}-containing phase Ba_2CoO_4. Thus it is concluded that Ba_2YCoO_5 could not be topochemically oxidized by oxide ions insertion by this route.

Reactions	Temperature/^oC	Results
O_2 flow	400, 450	No reaction
O_2 flow	500	Decomposed to Ba_2CoO_4
100 bar O_2	250	No reaction
100 bar O_2	270	Decomposed to Ba_2CoO_4
CuF_2, O_2 flow	250	No reaction
CuF_2, O_2 flow	275	New phase

Table 6.1 Topochemical reaction of Ba_2YCoO_5 carried out under different conditions.

Fluorination of Ba_2YCoO_5 was carried out using CuF_2 as a solid fluorinating agent. The mixture of as-prepared Ba_2YCoO_5 and CuF_2 was heated under flowing oxygen at different

temperatures. X-ray powder diffraction data collected from the products of these materials indicated a reaction occurred at 275 ^{o}C. A sample for neutron powder diffraction analysis was prepared by grinding together a 1: 0.625 molar ratio of Ba_2YCoO_5: CuF_2 in an agate mortar and pestle and then heating the mixture at 275 ^{o}C under flowing oxygen for two periods of 12 h. During the reaction, CuF_2 is converted into CuO according to the following reaction.

$$MO_x + CuF_2 \xrightarrow{O_2} MO_xF_y + CuO$$

As a result, the fluorinated sample was contaminated by CuO impurity. In order to avoid the complications related to CuO impurity, samples for magnetic and optical measurements were prepared in the 'separated' reactions, as shown in Figure 6.3. Excess CuF_2 was heated at 500 ^{o}C under flowing oxygen to form F_2 gas. The resulting mixture of O_2/F_2 gases was then passed over a sample of Ba_2YCoO_5 which was held at 275 ^{o}C. A diagram of the reaction apparatus is shown in Figure 6.3.

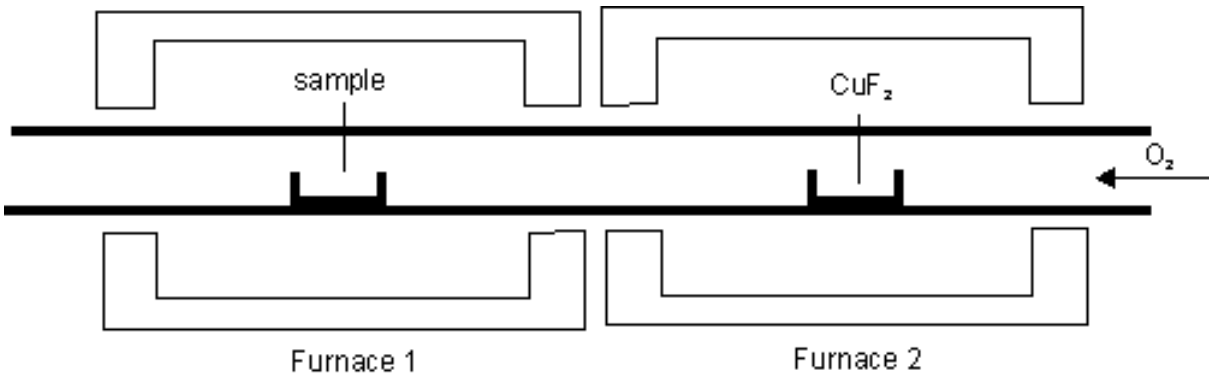

Figure 6.3 Fluorination reaction system.

6.3 Results

6.3.1 Characterization of $Ba_2YCoO_5F_{0.42}$

X-ray powder diffraction data were collected from both the as-prepared Ba_2YCoO_5 sample and the fluorinated sample. As shown in Figure 6.4, the two sets are different, indicating a

fluorination reaction has occurred. During the fluorination, both the insertion of fluoride ions and the exchange between oxide ions and fluoride ions could occur in the same time.[88] Thus the fluorinated sample is initially regarded as having a composition of '$Ba_2YCoO_xF_y$'.

6.3.2 Structural Refinement

X-ray powder diffraction data collected from $Ba_2YCoO_xF_y$ can be indexed using an orthorhombic unit cell (a = 12.33 Å, b = 6.09 Å, c = 7.95 Å). Neutron powder diffraction data were collected from $Ba_2YCoO_xF_y$ to determine the structure exactly.

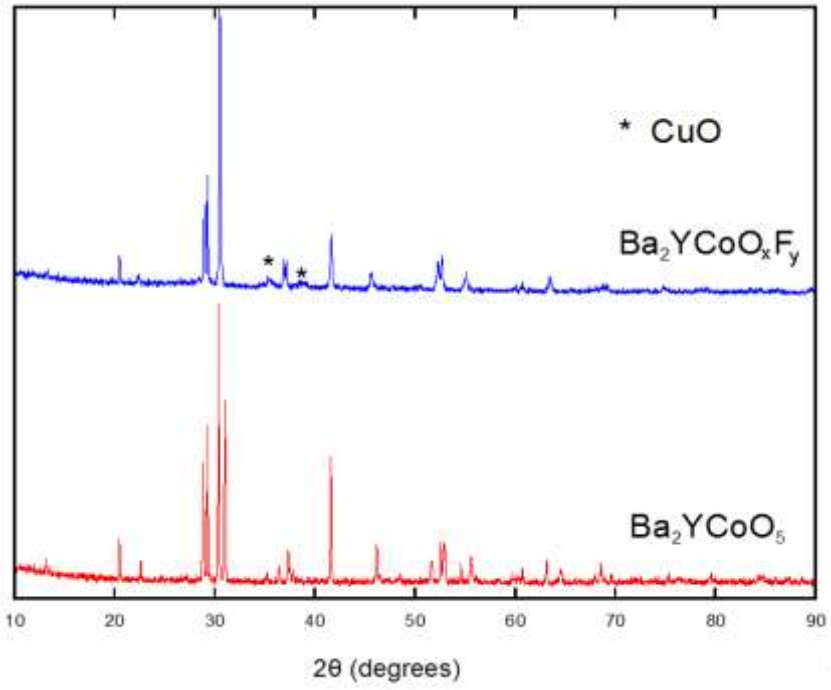

Figure 6.4 X-ray powder diffraction data collected from Ba_2YCoO_5 and $Ba_2YCoO_xF_y$.

Neutron powder diffraction data collected from $Ba_2YCoO_xF_y$ at room temperature could be readily indexed using the same unit cell, confirming the result of X-ray powder diffraction measurements. The first structural model was constructed based on the $Ba_2YFeO_{5.5}$ structure with space group of $Pb2_1m$. The iron sites in the lattice were replaced by cobalt and all the

anion vacancies were filled with additional anions, giving a stiochiometric formula of $Ba_2YCoO_xF_y$ ($x + y = 6$). This model was then refined against the neutron powder diffraction data collected from $Ba_2YCoO_xF_y$ phase at room temperature. Given the similarity of the neutron scattering lengths of oxygen and fluorine, no attempt was made to distinguish between two anion types at the first stage of refinement. During the refinement, the atomic positions and the fractional occupancies of cations and anions were allowed to be refined. However, refinement of this model against neutron powder diffraction data collected from $Ba_2YCoO_xF_y$ gave a bad visual and statistical fit ($\chi^2 = 10.50$), suggesting that $Ba_2YCoO_xF_y$ adopts a different structure from $Ba_2YFeO_{5.5}$.

Since the fluorination reaction occurred at a low temperature, the ordered arrangement of the cations in the host lattice is assumed to be retained in the fluorinated phase. Thus, another two structural models can be constructed in space group of *Pbn2₁* (No.33, noncentrosymmetric) and *Pbnm* (No. 62, centrosymmetric) respectively with the arrangement of cations in the Ba_2YCoO_5 structure (*P2₁/n*). The two structural models were initially refined against the neutron diffraction data collected from $Ba_2YCoO_xF_y$ at room temperature. During the refinement, the atomic positions and the fractional occupancies of cations, oxides and fluorides were allowed to be refined. Both models give good visual and statistical fit (*Pbn2₁* $\chi^2 = 3.08$; *Pbnm* $\chi^2 = 3.06$).

Close inspection of two structural models reveals that the differences between two models lie in the slight difference in the arrangement of the anions. As shown in Figure 6.5, there is an anion site in the *Pbnm* model at the *4e* positions of (*x*, *y*, 1/4) due to the presence of mirror plane along *z* direction. In contrast, the analogous anion site in the *Pbn2₁* model are at a *4a* positions of (*x*, *y*, *z*), allowing the anions to move along the *z* direction, thus yielding a noncentrosymmetric structure. That means the polar structure (*Pbn2₁*) would be

'converted' into centrosymmetric structure (*Pbnm*) when the position of this anion site is at (*x*, *y*, ¼). The neutron diffraction data locate the anion position very close to (*x*, *y*, ¼) and the fitting statistics for the two models are equivalent. Thus the two structural models cannot be differentiated by the analysis of neutron powder diffraction data.

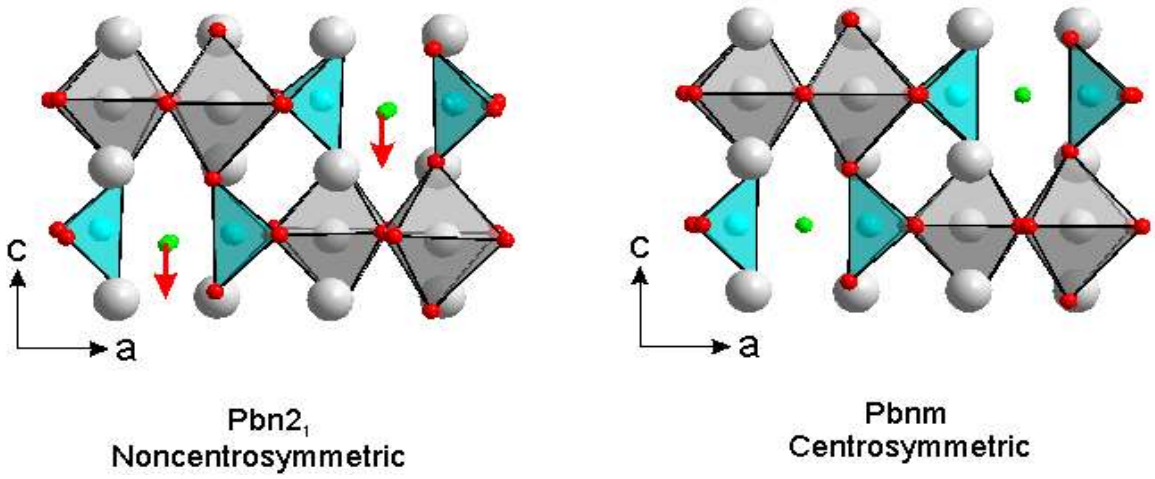

Figure 6.5 Structural models constructed based on *Pbn2$_1$* and *Pbnm* space group.

SHG measurements were conducted to examine if the material exhibits a SHG response. SHG measurements performed on a $Ba_2YCoO_xF_y$ sample exhibited no detectable SHG activity, therefore no evidence is observed to support that $Ba_2YCoO_xF_y$ adopts the polar structure (*Pbn2$_1$*), thus the centrosymmetric *Pbnm* space group would be preferred.

Refinement of yttrium and cobalt site occupancies revealed no evidence of anti-site cation disorder, indicating that the cation order in the host lattice was retained in the fluorination reaction. Refinement of the fractional occupancies of the anions indicated a sample stoichiometry of $Ba_2YCoO_xF_y$, $x + y = 5.42(2)$. During the iodometric titration of this material, the cobalt present is reduced from a mixture of Co^{3+}/Co^{4+} to Co^{2+}, taking up 4.95(2) x 10^{20} electrons per gram. This result combined with the result of neutron powder diffraction analysis gives a composition of $Ba_2YCoO_5F_{0.42(1)}$. Based on the composition of the fluorinated phase, it is believed that the fluoride ions are inserted into the vacant

positions in the host lattice of Ba_2YCoO_5. Observed calculated and difference plots from the refinement are shown in Figure 6.6. Full details of the refined structure of $Ba_2YCoO_5F_{0.42}$ are listed in Table 6.2, with selected bond lengths in Table 6.3. Figure 6.7 gives a picture of the refined structure of $Ba_2YCoO_5F_{0.42}$.

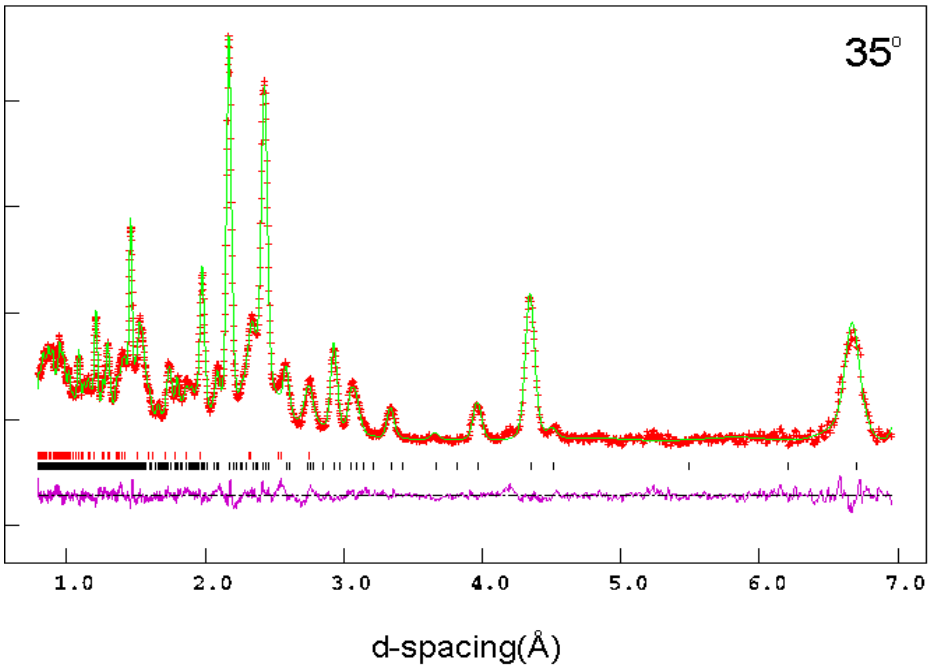

Figure 6.6 Observed, calculated and difference plots from the structural refinement of $Ba_2YCoO_5F_{0.42}$ against neutron powder diffraction data collected at room temperature. The red tick marks indicate the peaks position of CuO impurities.

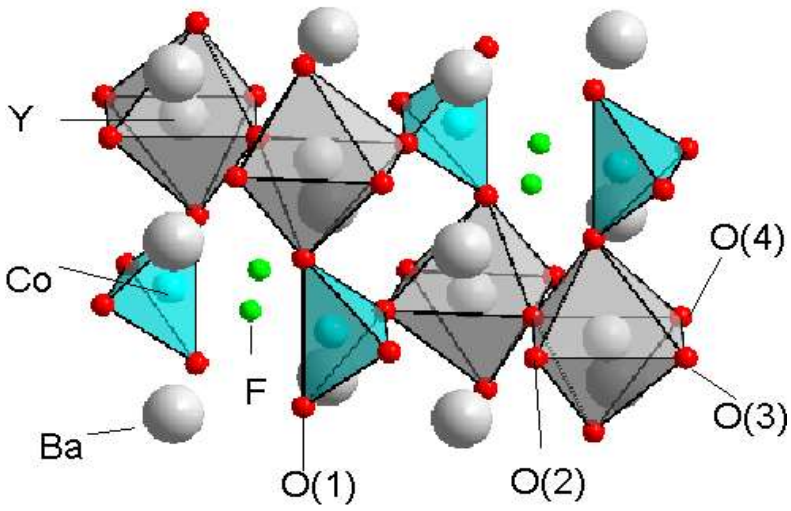

Figure 6.7 Refined structure of $Ba_2YCoO_5F_{0.42}$.

Atom	site	*x*	*y*	*z*	fraction	U_{iso} (Å^2)
Ba(1)	*4e*	0.1248(3)	0.2508(17)	0.9981(3)	1	0.0092(6)
Y(1)	*4e*	0.8724(2)	0.2439(17)	¼	1	0.0156(9)
Co(1)	*4e*	0.8989(7)	0.247(6)	¾	1	0.0172(29)
O(1)	*4e*	0.2431(2)	0.0116(21)	¾	1	0.0253(7)
O(2)	*4e*	0.3531(2)	0.2391(14)	0.4652(3)	1	0.0253(7)
O(3)	*4e*	0.5005(7)	0.0140 (18)	¼	1	0.0253(7)
O(4)	*4e*	0.4862(5)	0.5065(12)	¼	1	0.0253(7)
F(1)	*4e*	0.249(3)	0.007(7)	¼	0.42(1)	0.036(6)
$Ba_2YCoO_5F_{0.42}$- Space group *Pbnm* *a* = 12.3138(15) Å, *b* = 6.0804(7) Å, *c* = 7.8951(9) Å, V = 591.1(2) Å^3						
CuO- Space group *C2/c* *a* = 4.656(3), *b* = 3.419(2), *c* = 5.120(3), *β* = 99.3(2)^o						
χ^2 = 3.067, wRp = 3.23 %, Rp = 2.88 %						

Table 6.2 Structural parameters refined against neutron powder diffraction data collected from $Ba_2YCoO_5F_{0.42}$ at room temperature.

cation	anion	Bond (Å)	BVS
Y(1)	O(1)	2 × 2.263(2)	Y +3.45
	O(2)	2.195(13)	
	O(2)	2.091(14)	
	O(3)	2.262(10)	
	O(4)	2.269(13)	
Co(1)	O(1)	2 × 1.792(4)	Co +2.82
	O(3)	1.879(31)	
	O(4)	1.918(30)	
	F(1)	2.369(54)	
	F(1)	2.400(55)	

Table 6.3 Selected bond lengths of cations from the refined structure of $Ba_2YCoO_5F_{0.42}$.

The oxide/fluoride distributions in some oxyfluoride phases can be determined by a detailed analysis of the local anion bonding polyhedra by means of bond valence sums (BVS).[88-90] In order to confirm the positions of fluoride ions, bond valence sums of anions were calculated. Each fluoride ion is surrounded by four barium and two cobalt cations, as shown in Figure 6.8.

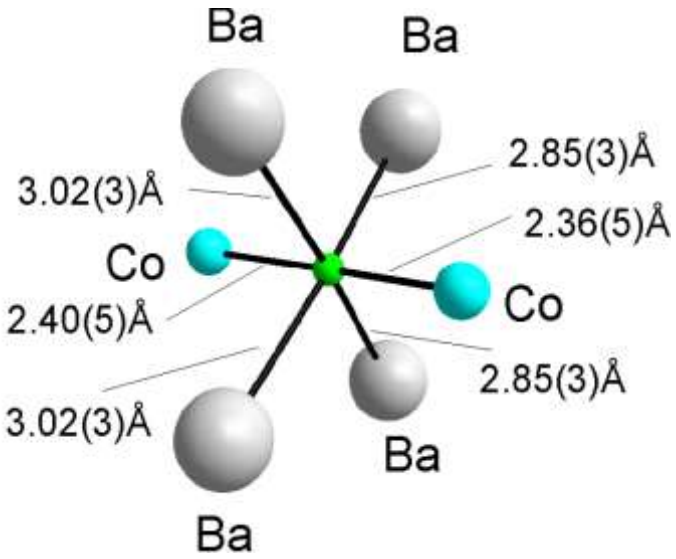

Figure 6.8 Coordination environment of fluoride ions in $Ba_2YCoO_5F_{0.42}$.

It can be seen in Table 6.4 that the four anion sites present in $Ba_2YCoO_5F_{0.42}$ which are retained from the structure of Ba_2YCoO_5 (O(1) – O(4)) have similar BVS values to the analogous anion sites in the host Ba_2YCoO_5. If the 'vacant' positions in Ba_2YCoO_5 were occupied by an oxide ion rather than a fluoride ion, the BVS calculated would be -1.02, which is much smaller than the value calculated for the oxide ions in other positions (-1.78 ~ -2.17). In contrast, the BVS calculated using a fluoride ion in this position gives a reasonable value of -0.79. Thus it can be concluded that $Ba_2YCoO_5F_{0.42}$ is formed by the simple topochemical insertion of fluoride ions into Ba_2YCoO_5, with all the added fluoride ions located in a partially filled site at (~ 0.25, 0, ¼).

$Ba_2YCoO_5F_{0.42}$				Ba_2YCoO_5	
anion	cation	Bond (Å)	BVS	anion	BVS
O(1)	Ba(1)	2 × 3.356(4)	O-1.83	O(1)	O-1.78
	Ba(1)	2 × 2.996(13)			
	Y(1)	2.263(2)		O(2)	O-1.69
	Co(1)	1.792(4)			
O(2)	Ba(1)	2 × 3.012(11)	O-2.17	O(3)	O-2.18
	Ba(1)	2 × 2.83(1)			
	Y(1)	2.195(13)			
	Y(1)	2.091(14)			
O(3)	Ba(1)	2 × 3.033(8)	O-1.85	O(4)	O-1.74
	Ba(1)	2 × 2.834(8)			
	Y(1)	2.262(10)			
	Co(1)	1.879(31)			
O(4)	Ba(1)	2 × 2.868(9)	O-1.78	O(5)	O-1.92
	Ba(1)	2 × 2.983(10)			
	Y(1)	2.269(13)			
	Co(1)	1.918(30)			
F	Ba(1)	2 × 3.02(3)	F-0.79 (O-1.02)*		
	Ba(1)	2 × 2.85(3)			
	Co(1)	2.36(5)			
	Co(1)	2.40(5)			

Table 6.4 Selected bond lengths of anions from the refined structure of $Ba_2YCoO_5F_{0.42}$ and Ba_2YCoO_5.

6.3.3 Magnetic characterization

Zero-field-cooled and field-cooled DC magnetization data collected from $Ba_2YCoO_5F_{0.42}$ in an applied field of 100 Oe in the temperature range of 5 < T/K < 300 are shown in Figure 6.9. The data collected can be fitted to the Curie-Weiss law ($\chi = C/(T - \theta)$) in the range 45 < T/K < 300 to give a Curie constant of 2.989(3) cm^3 K mol^{-1} and a Weiss constant θ = -42.7(2) K, broadly in agreement with a value of C = 3.57 cm^3 K mol^{-1} expected for the spin-only moment of a combination of Co^{3+} and Co^{4+} centres in the stated ratio. Below 30 K the zero-field-cooled and field-cooled data diverge, consistent with the onset of magnetic order. Magnetization field isotherms collected at room temperature and 5 K are linear, as shown in Figure 6.10.

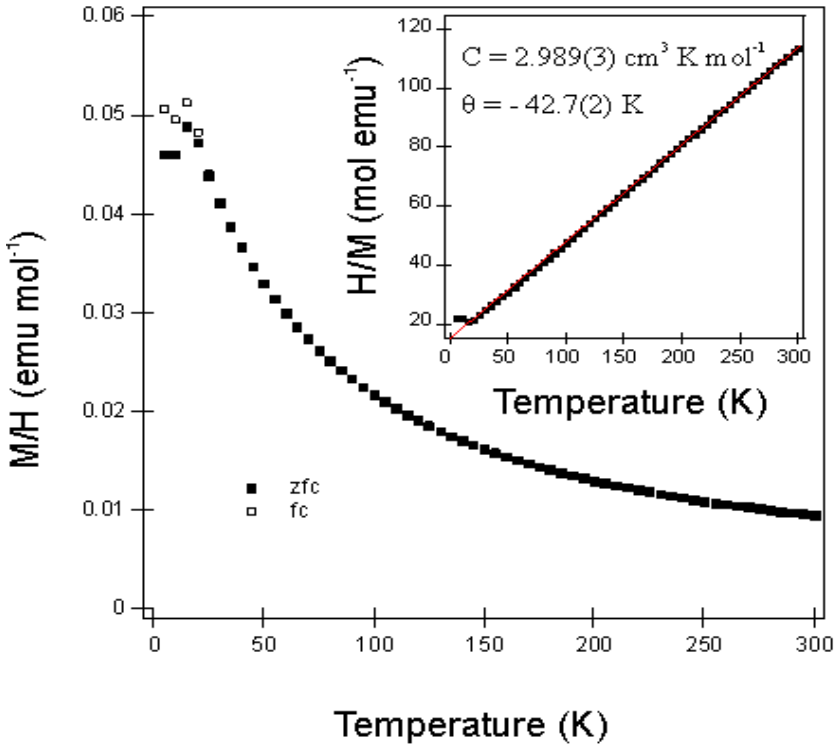

Figure 6.9 Zero-field-cooled and field-cooled magnetization data collected from $Ba_2YCoO_5F_{0.42}$ in the temperature range 5 < T (K) < 300. Inset shows a fit to the Curie-Weiss law.

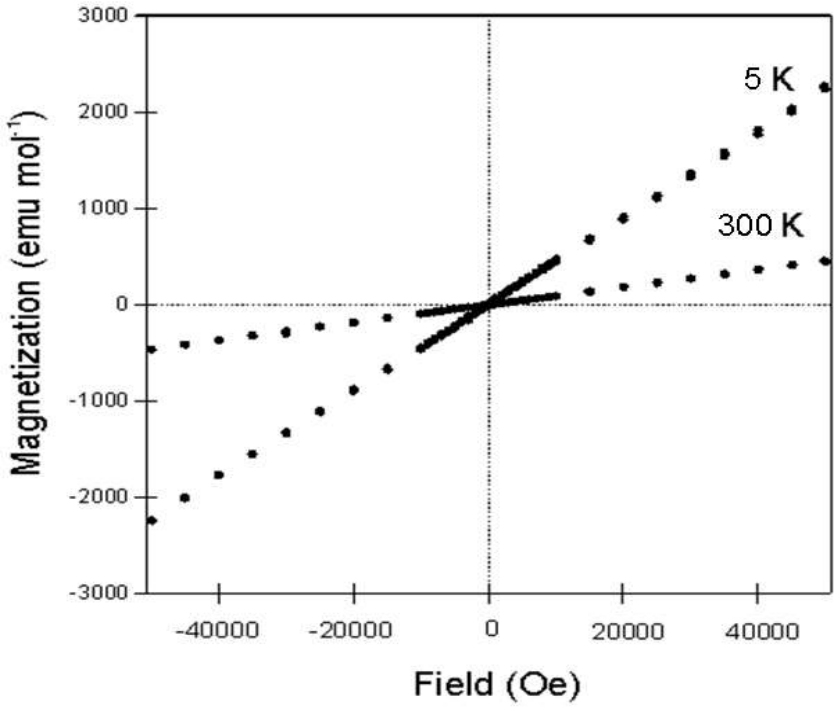

Figure 6.10 Magnetization-field isotherms collected from $Ba_2YCoO_5F_{0.42}$ at 5 and 300 K.

In order to determine the magnetic structure at low temperature, neutron powder diffraction data were collected from $Ba_2YCoO_5F_{0.42}$ sample at 7 K. As shown in Figure 6.11, the data at 7 K exhibit additional diffraction features compared to the analogous data collected at room temperature, confirming magnetic order at low temperature. These additional diffraction features can be indexed using the crystallographic unit cell. The intensities of these additional diffraction features can be accounted for using an antiferromagnetic model, in which the magnetic moments of cobalt centres are aligned along *c*-axis, as shown in Figure 6.13. Thus a magnetic model was constructed and refined against the neutron powder diffraction data collected from $Ba_2YCoO_5F_{0.42}$ at 7 K, giving an ordered moment of 0.95(8) μ_B per cobalt centre.

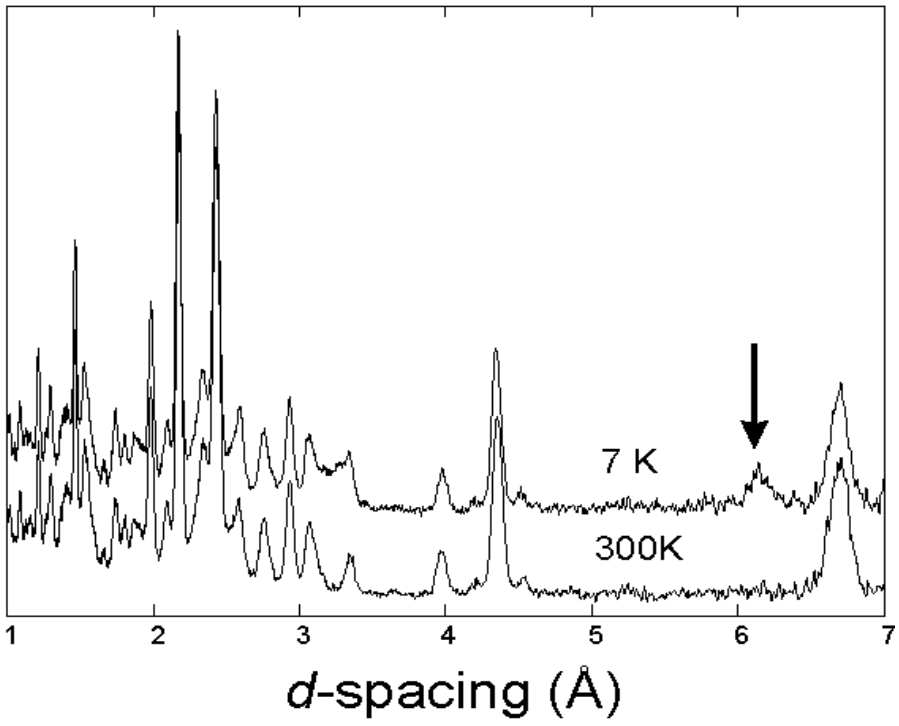

Figure 6.11 Neutron diffraction data collected from $Ba_2YCoO_5F_{0.42}$ at 7 K and 300 K. Arrows mark the positions of additional diffraction features which appear on cooling, indicative of magnetic order.

Figure 6.12 shows the refinement of nuclear and magnetic models against the neutron powder diffraction data collected from $Ba_2YCoO_5F_{0.42}$ at 7 K. It should be noted the

additional scattering is observed at ~3.28 Å in the Bank 35^{o} data, which is assigned to the diffraction features from accidentally frozen nitrogen in the cryostat. The refined magnetic model is shown in Figure 6.13.

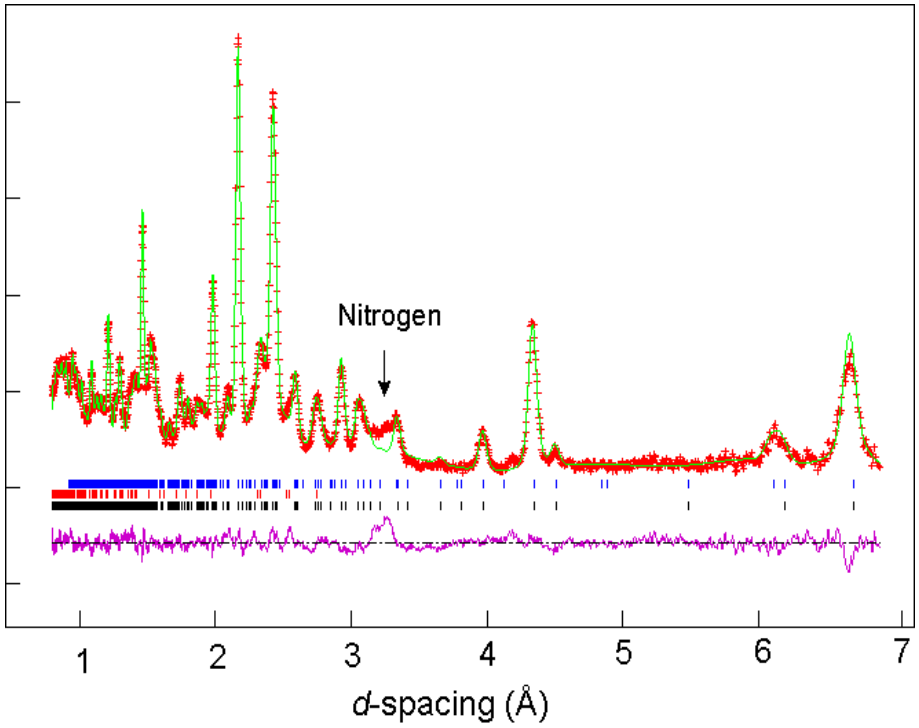

Figure 6.12 Observed, calculated and difference plots from the structural and magnetic refinement of $Ba_2YCoO_5F_{0.42}$ against data collected at 7 K. Lower tick marks indicated allowed structural peak positions from main phase, and middle marks indicated allowed peak positions from CuO impurity and upper tick marks indicated allowed magnetic peak positions.

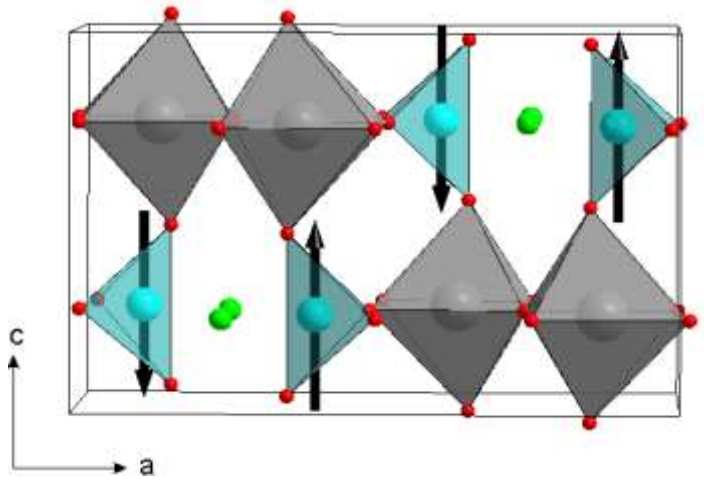

Figure 6.13 Magnetic structure of $Ba_2YCoO_5F_{0.42}$ refined against neutron diffraction data collected at 7 K.

atom	x	y	z	$M_x(\mu_B)$	$M_y(\mu_B)$	$M_z(\mu_B)$
Co(1)	0.3891	0.2477	0.2391	0.95(8)	0	0
Co(2)	0.6109	0.7523	0.7391	-0.95(8)	0	0
Co(3)	0.1109	0.7477	0.2391	-0.95(8)	0	0
Co(4)	0.8891	0.2523	0.7391	0.95(8)	0	0
$Ba_2YCoO_5F_{0.42}$ -Space group-*P1* *a* = 12.3114 Å, *b* = 6.0709 Å, *c* = 7.9147 Å, *V* = 591.1 Å^3						

Table 6.5 Structural parameters from the ferromagnetic refinement of $Ba_2YCoO_5F_{0.42}$ against neutron diffraction data collected at 7 K.

6.4 Discussion

Reaction of Ba_2YCoO_5 with CuF_2 under flowing oxygen results in the topochemical insertion of fluoride ions into the lattice and the formation of $Ba_2YCoO_5F_{0.42}$. The fluorinated phase retains the arrangement of cations observed in the host phase and the insertion of fluoride ions leads to only modest changes in the host structure. The fluoride ions in the lattice of $Ba_2YCoO_5F_{0.42}$ are inserted into the vacant sites of Ba_2YCoO_5 in a disordered arrangement.

6.4.1 Disordered arrangement of fluoride ions

Close inspection of the structure of $Ba_2YCoO_5F_{0.42}$ reveals that the insertion of fluoride ions into the structural lattice of Ba_2YCoO_5 leads to an unusual arrangement of anions in $Ba_2YCoO_5F_{0.42}$. The oxide ions retain the ordered arrangement of the host lattice, and the fluoride ions are inserted into ~ 40 % vacant anion sites within the cation-ordered Ba_2YCoO_5 framework in a disordered arrangement. As shown in Figure 6.14, the structure changes from a Ba_2O_2 - $YCoO_3$ - Ba_2O_2 - $YCoO_3$ stacking sequence in Ba_2YCoO_5 into a Ba_2O_2 - $YCoO_{3}F_{0.4}$ $_{0.6}$ - Ba_2O_2 - $YCoO_{3}F_{0.4}$ $_{0.6}$ stacking sequence in $Ba_2YCoO_5F_{0.42}$, as shown in Figure 6.14.

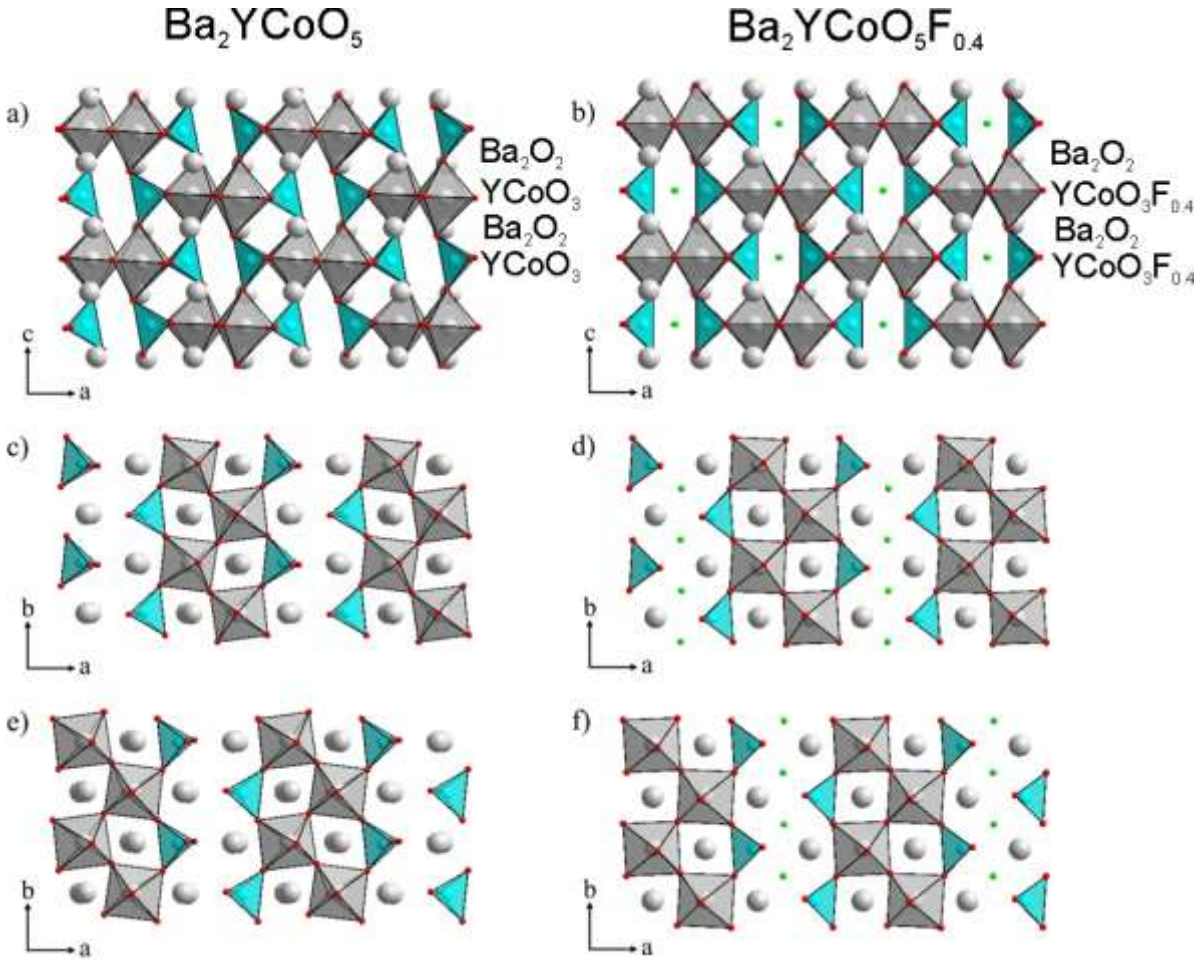

Figure 6.14. The structures of Ba_2YCoO_5 and $Ba_2YCoO_5F_{0.42}$. (a, b) view down the b-axis of Ba_2YCoO_5 and $Ba_2YCoO_5F_{0.42}$. (c, d) View down the c-axis showing polyhedra at z ~ 0.75 for Ba_2YCoO_5 and z ~ 0 for $Ba_2YCoO_5F_{0.42}$. (e, f) View down the c-axis showing polyhedra at z ~ 0.25 for Ba_2YCoO_5 and z ~ 0.5 for $Ba_2YCoO_5F_{0.42}$ respectively. Solid lines indicate the respective unit cells. Grey octahedra represent YO_6 units, blue tetrahedra CoO_4 units, grey spheres Ba^{2+} cations, green spheres F^- anions.

As discussed in Chapter 3, Ba_2YCoO_5 and Ba_2YFeO_5 adopt similar structures. The insertion of oxide ions into Ba_2YFeO_5 leads to an ordered arrangement of oxide ions in $Ba_2YFeO_{5.5}$. In contrast, the inserted fluoride ions in the lattice of $Ba_2YCoO_5F_{0.42}$ adopt a disordered arrangement. As discussed in Chapter 5, the ordered arrangement of inserted oxide ions in $Ba_2YFeO_{5.5}$ could be attributed to the combined effect of lattice strain and a local Jahn-Teller instability. Thus, these two factors are also considered in the insertion of fluoride ions into the lattice of Ba_2YCoO_5.

Lattice strain. Considering the changes of structures between Ba_2YCoO_5 and $Ba_2YCoO_5F_{0.42}$, the largest structural effect of fluorination is a general contraction of the YO_6 octahedra and CoO_4 tetrahedra, which can be observed in the linkages parallel to the *z*-axis, where the angle between oxide ions which connect the YO_6 octahedra and CoO_4 tetrahedra change from 165.11(7)^o in Ba_2YCoO_5 to 180^o in $Ba_2YCoO_5F_{0.42}$, as shown in Figure 6.15. As described in Chapter 5, the insertion of oxide ions into Ba_2YFeO_5 leads to a dramatic distortion in YO_6 octahedra, which help stabilize the formation of $Ba_2YFeO_{5.5}$. In contrast, only a modest structural change is observed on the insertion of fluoride ions into Ba_2YCoO_5.

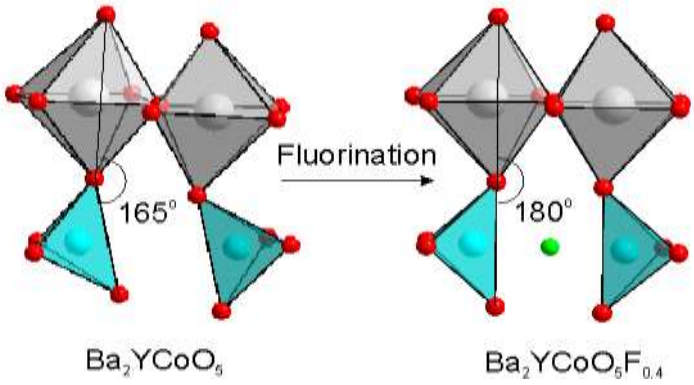

Figure 6.15 Structural change of Ba_2YCoO_5 in the fluorination reaction.

Previous studies indicated that Sr – F bonds, rather than Ru – F bonds, were formed when the fluoride ions were inserted into the layered structure of $Sr_3Ru_2O_7$.[35] It should be noted that the bond lengths of the Co – F bonds in $Ba_2YCoO_5F_{0.42}$ are much longer than the Co – O bonds, as shown in Figure 6.16, suggesting only a weak interaction between cobalt and fluoride. The long Co – F bond suggests that the Co – F interaction is not the primary factor to locate the fluoride ions in the lattice. The cobalt centres in $Ba_2YCoO_5F_{0.42}$ would be considered to be retained in the tetrahedral coordination geometry, similar to the cobalt centres in the host phase. In contrast, the oxide ion insertion in Ba_2YFeO_5 leads to the

formation of 5-coordinate iron centres. Thus the insertion of fluoride ions into Ba_2YCoO_5 has a different structural consequence from the insertion of oxide ions into Ba_2YFeO_5.

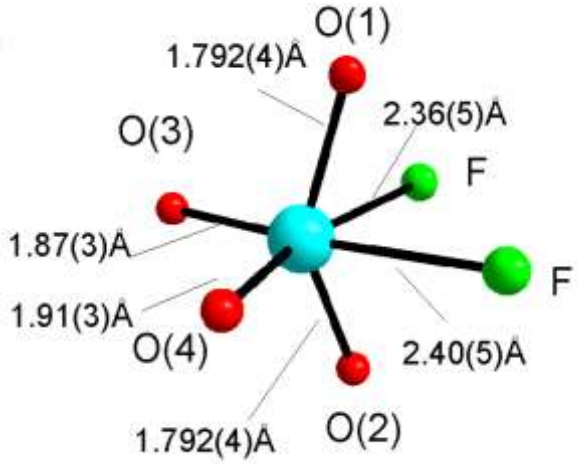

Figure 6.16 Coordination environment of cobalt in $Ba_2YCoO_5F_{0.42}$.

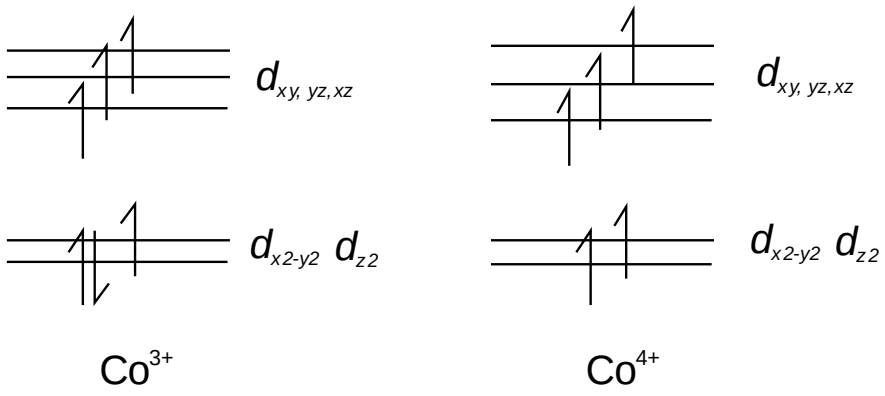

Figure 6.17 Electronic configurations of Co^{3+} and Co^{4+} centres in tetrahedral sites.

Electronic factors. As discussed in the Chapter 5, Fe^{4+} centres are located in square pyramidal and tetrahedral sites in $Ba_2YFeO_{5.5}$. The Jahn-Teller distortion is observed in $Ba_2YFeO_{5.5}$, which induces the formation of the '5+1' coordinate Fe^{4+} centres in the lattice and results in the ordered arrangement of the inserted oxide ions. In contrast, the Co^{3+} and Co^{4+} cations present in $Ba_2YCoO_5F_{0.42}$ adopt d^6 and d^5 electronic configurations respectively, as shown in Figure 6.17. The lack of Jahn-Teller cations could be a factor leading to the disordered arrangement of the inserted fluoride ions in $Ba_2YCoO_5F_{0.42}$.

It should be mentioned that a disordered arrangement of inserted anions is common in the products of topochemical oxidation. For example, fluoride ions and oxide ions can be inserted into the brownmillerite phase Sr_2GaMnO_5, leading to the formation of Sr_2GaMnO_5F and $Sr_2GaMnO_{5.5}$, in which the inserted fluoride ions or oxide ions adopt a disordered arrangement. By comparing the arrangement of anions within $Ba_2YFeO_{5.5}$ and $Ba_2YCoO_5F_{0.42}$, it can be speculated that lattice strain and electronic considerations are the primary factors leading to the ordered arrangement of inserted oxides in $Ba_2YFeO_{5.5}$ and the disordered arrangement of inserted fluoride ions in $Ba_2YCoO_5F_{0.42}$.

6.4.2 Anion insertion into Ba_2YMO_5 (M = Co and Fe)

In Chapter 5, the insertion of oxide ions into Ba_2YFeO_5 leads to the formation of $Ba_2YFeO_{5.5}$. Thus the oxidation of Ba_2YCoO_5 was initially attempted under oxygen atmosphere (ambient pressure or high pressure). X-ray powder diffraction data indicated that no reaction occurred under flowing oxygen below 500 ^oC or 100 bar of oxygen below 250 ^oC, as shown in Table 6.1. The decomposition of Ba_2YCoO_5 and the formation of Ba_2CoO_4 were observed when the temperature was raised up to 500 ^oC under flowing oxygen or 270 ^oC under 100 bar oxygen pressure. In contrast, Ba_2YCoO_5 can be fluorinated using CuF_2 as a fluorinating agent under flowing oxygen to form $Ba_2YCoO_5F_{0.42}$. However, the fluorination of Ba_2YFeO_5 cannot be achieved under ambient or high-pressure oxygen environment. Thus the insertion of oxide ions can only occur in the Ba_2YFeO_5, while the insertion of fluoride ions can only occurs in the Co analogue. The selective anion-insertion reaction observed in Ba_2YMO_5 (M = Fe and Co) is unusual, which motivates the interest to understand the reason for the different oxidative reactions in the two phases.

In the case of oxide ion insertion into Ba_2YFeO_5, the increase in lattice strain, combined with a local electronic instability of Fe^{4+} centres, results in an ordered arrangement of oxide ions. These two features limit the formation of a long range Fe – O – Fe network (Figure 6.18) and lead to the formation of 5-coordinate FeO_5 pyramids. If the insertion of oxide ions could also be achieved in Ba_2YCoO_5, a dramatic structural change would also be observed in the lattice of $Ba_2YCoO_{5.5}$, due to the lack of the local Jahn-Teller distortion, which would require a dramatic contraction of the host lattice to accommodate the extended Co – O – Co network. The dramatic distortions could not be stabilized in $Ba_2YCoO_{5.5}$, which could explain why the oxide ions cannot be inserted into Ba_2YCoO_5.

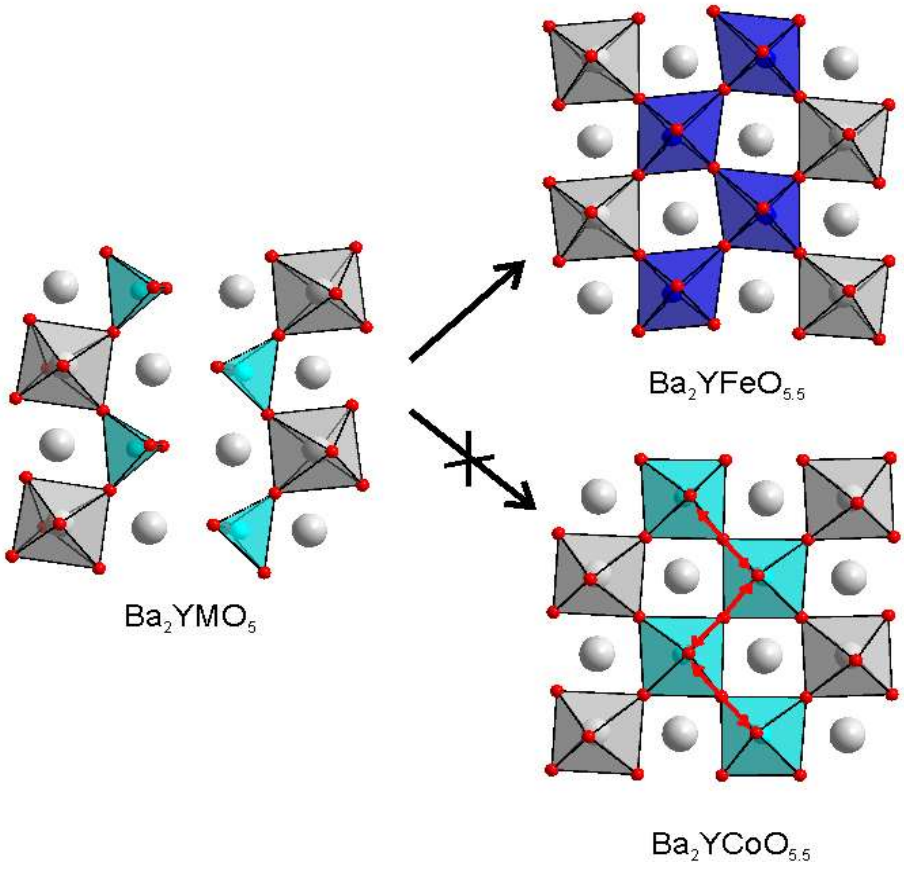

Figure 6.18 Illustration of oxide insertion into the lattice of Ba_2YFeO_5 and Ba_2YCoO_5.

The size difference between Co^{4+} (CN6 = 0.53 Å) and Fe^{4+} (CN6 = 0.585 Å) can be considered as another factor influencing the processes of anion insertion into the lattice of

Ba_2YMO_5 (M = Fe, Co). Topochemical oxidation allows the structural lattices of the host phases to be retained. However, the insertion of anions into the host lattice would lead to a contraction in the metal – anion bonds, which would build up an internal strain in the lattice. The stabilization of the product of topochemical oxidation requires a way to release the internal strain arising from the change of metal – anion bonds.

For example, the insertion of oxide ions into Ba_2YFeO_5 leads to a change from Fe^{3+} to Fe^{4+} and shorter Fe – O bonds. As discussed in Chapter 3 and 5, the rock-salt type basic units ($Y_2Fe_2O_{10}$ and $Y_2Fe_2O_{11}$) are observed in the lattice of Ba_2YFeO_5 and $Ba_2YFeO_{5.5}$. The size difference between the two B-site cations (Y and Fe) is an important factor leading to the formation of the rock-salt type basic unit. An increase in size difference between the pair of B-site cations would lead to the destabilization of the rock-salt type basic unit. For example, this rock-salt type basic unit is not observed in the lattice of $Ba_3DyAl_2O_{7.5}$ due to the large size difference between Dy^{3+} and Al^{3+} ($r(Dy^{3+})/r(Al^{3+}) = 2.34$) compared to that between Y^{3+} and Fe^{3+} ($r(Y^{3+})/r(Fe^{3+}) = 1.84$). In order to release the strain arising from the change from Fe^{3+} to Fe^{4+} in the topochemical oxidation and retain the framework of Ba_2YFeO_5 based on the rock-salt type basic units, $Ba_2YFeO_{5.5}$ undergoes a dramatic distortion in the YO_6 octahedra to accommodate the shrinking of the Fe – O bonds. In contrast, if Ba_2YCoO_5 would be oxidized to $Ba_2YCoO_{5.5}$, the formation of the smaller Co^{4+} cations (Co^{4+} CN6 = 0.53 Å, Fe^{4+} CN6 = 0.585 Å) would lead to an even larger built-up of strain in the lattice which cannot be released by a simple distortion. This could explain why the topochemical oxidation of Ba_2YCoO_5 is not achieved and the decomposition of Ba_2YCoO_5 and formation of Ba_2CoO_4 in the oxidation reaction. Thus the ratio of Co^{4+}/Co^{3+} cations is restricted to a small range in order to stabilize the structure. The insertion of fluoride ions into the lattice of Ba_2YCoO_5 yields a comparatively small ratio of Co^{4+}/Co^{3+} cations and only a slight structural distortion.

Figure 19a and b show the comparison of the structures of Ba_2YCoO_5 and $Ba_2YCoO_5F_{0.42}$, and the geometry around the 'vacant' anion site at (0.25, 0, 0.25) in Ba_2YCoO_5 and the geometry around the fluoride ion in $Ba_2YCoO_5F_{0.42}$. It can be seen that the two sites have very similar coordination environments and almost identical BVS values, indicating that the insertion of fluoride ions into the lattice of Ba_2YCoO_5 only causes a very small disturbance to the host structure. This could explain why the anion insertion in the lattice of Ba_2YCoO_5 could be achieved by the fluorination reaction.

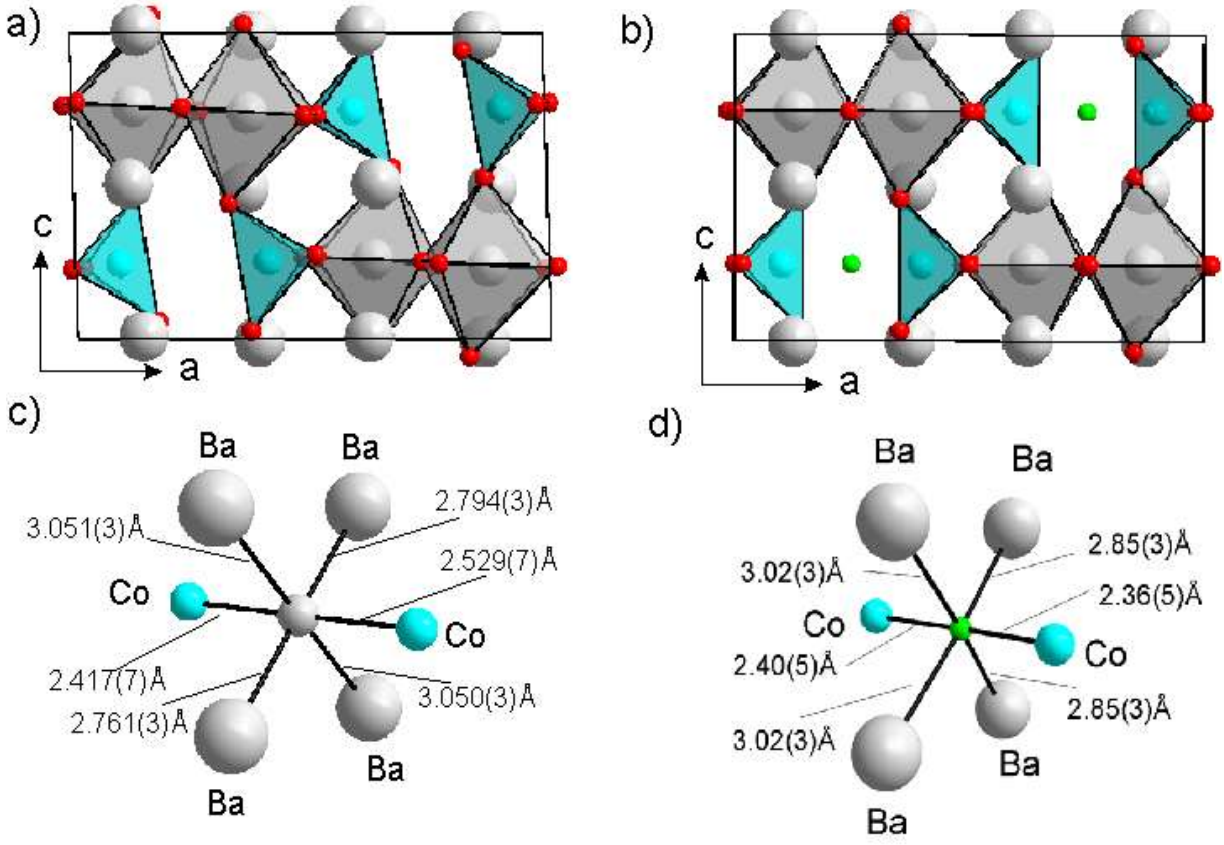

BVS = F -0.80 BVS = F -0.79

Figure 6.19 A comparison of the structures of a) Ba_2YCoO_5 and b) $Ba_2YCoO_5F_{0.42}$. c) The 'vacant' anion site in Ba_2YCoO_5 and d) the local coordination polyhedron of fluoride ions in $Ba_2YCoO_5F_{0.42}$.

The fluorination reaction of Ba_2YFeO_5 has been attempted at 400 ^oC under flowing oxygen. It is really surprising that the fluorination reaction of Ba_2YFeO_5 cannot be achieved. Although it is unclear why Ba_2YFeO_5 and Ba_2YCoO_5 can accommodate different anions in

the processes of anion insertion, it could be speculated that the different electronic configurations and sizes of Fe^{4+} and Co^{4+} could be the main factors leading to the different processes of anion insertion.

6.4.3 Centrosymmetric structure in $Ba_2YCoO_5F_{0.42}$

Compared with the noncentrosymmetric $Ba_2YFeO_{5.5}$ structure, the insertion of fluoride ions into the lattice of Ba_2YCoO_5 leads to the formation of a centroysmmetric $Ba_2YCoO_5F_{0.42}$ phase, although two host phases (Ba_2YCoO_5 and Ba_2YFeO_5) share a similar structural lattice and cation ordering pattern. As discussed in Chapter 5, the symmetry breaking in $Ba_2YFeO_{5.5}$ is attributed to the combined effect of lattice strain and local electronic instability of Fe^{4+} cations. Thus the difference between these two processes of anion insertion (the insertion of oxide ions into Ba_2YFeO_5 and the insertion of fluoride ions into Ba_2YCoO_5) could be led by the lack of strong Jahn – Teller active cations in $Ba_2YCoO_5F_{0.42}$ (d^6 Co^{3+} and d^5 Co^{4+}). The absence of local distortion in cobalt centres of $Ba_2YCoO_5F_{0.42}$ limits the cooperative distortions in the lattice, which are considered as an important factor stabilizing the noncentrosymmetric structure of $Ba_2YFeO_{5.5}$ as discussed in Chapter 5. Thus it could be a main reason leading to a centrosymmetric structure being adopted by $Ba_2YCoO_5F_{0.42}$.

6.4.4 Magnetic behaviour

Magnetization data collected from $Ba_2YCoO_5F_{0.42}$ can be fitted to the Curie-Weiss law in the temperature range $40 < T/K < 300$ to give a Curie constant of $C = 2.989(3)$ cm^3 K mol^{-1}, consistent with the expected value for a combination of spin-only Co^{4+} ($S = 5/2$) and Co^{3+} ($S = 2$) centres ($C_{expected} = 3.57$ cm^3 K mol^{-1}). However, it should be noted that the magnetic moment extracted from the neutron powder diffraction data collected from $Ba_2YCoO_5F_{0.42}$

at 7 K (0.95(8) μ_B along *x* direction) is significantly smaller than expected (d^6 Co^{3+} and d^5 Co^{4+}), which could be attributed to a magnetic disorder in the *y* or *z* directions.

When the temperature is lower than 20 K, the magnetic order is observed. As shown in Figure 6.13, the CoO_4 centres exhibit an antiferromagnetic order paralleled to *z*-axis. According to the Goodenough – Kanamori rules, the superexchange between Co^{3+} – Co^{3+}, Co^{3+} – Co^{4+} or Co^{4+} – Co^{4+} interactions would lead to antiferromagnetic order, consistent with the observed magnetic behaviour.

It should be noted that $Ba_2YCoO_5F_{0.42}$ exhibits an antiferromagnetic order at 7 K whereas Ba_2YCoO_5 does not, confirmed by neutron powder diffraction collected from both samples at 7 K. This could be explained by the observed slight structural change between the two phases. As listed in Table 6.7, the average angle of Y – O – Co interactions in $Ba_2YCoO_5F_{0.42}$ (160.2°) is larger than the value in Ba_2YCoO_5 (156.2°), which could lead to a stronger superexchange interaction in $Ba_2YCoO_5F_{0.42}$.

$Ba_2YCoO_5F_{0.42}$		Ba_2YCoO_5	
Bond	Angle (°)	Bond	Angle (°)
Y(1)-O(2)-Co(1)	154.4(3)	Y(1)-O(2)-Co(1)	133.1(4)
		Y(1)-O(1)-Co(1)	162.7(2)
Y(1)-O(4)-Co(1)	163.8(1)	Y(1)-O(5)-Co(1)	155.7(4)
Y(1)-O(3)-Co(1)	177.1(2)	Y(1)-O(4)-Co(1)	173.5(1)
Average	160.2		156.2

Table 6.7 The Y – O – Co bond angle in the structures of $Ba_2YCoO_5F_{0.42}$ and Ba_2YCoO_5.

6.5 Conclusion

Fluorination reaction of Ba_2YCoO_5 was carried out using CuF_2 as a fluorine agent under flowing oxygen, leading to the formation of $Ba_2YCoO_5F_{0.42}$. Compared with the ordered arrangement of the inserted oxide ions in the lattice of $Ba_2YFeO_{5.5}$, the fluoride ions are

inserted into the vacant sites of Ba_2YCoO_5 in a disordered manner. The selective fluorination of Ba_2YCoO_5 in the presence of oxygen is rationalized on the basis of the lack of local electronic instability and size difference between Co^{4+} and Fe^{4+} cations.

Appendix

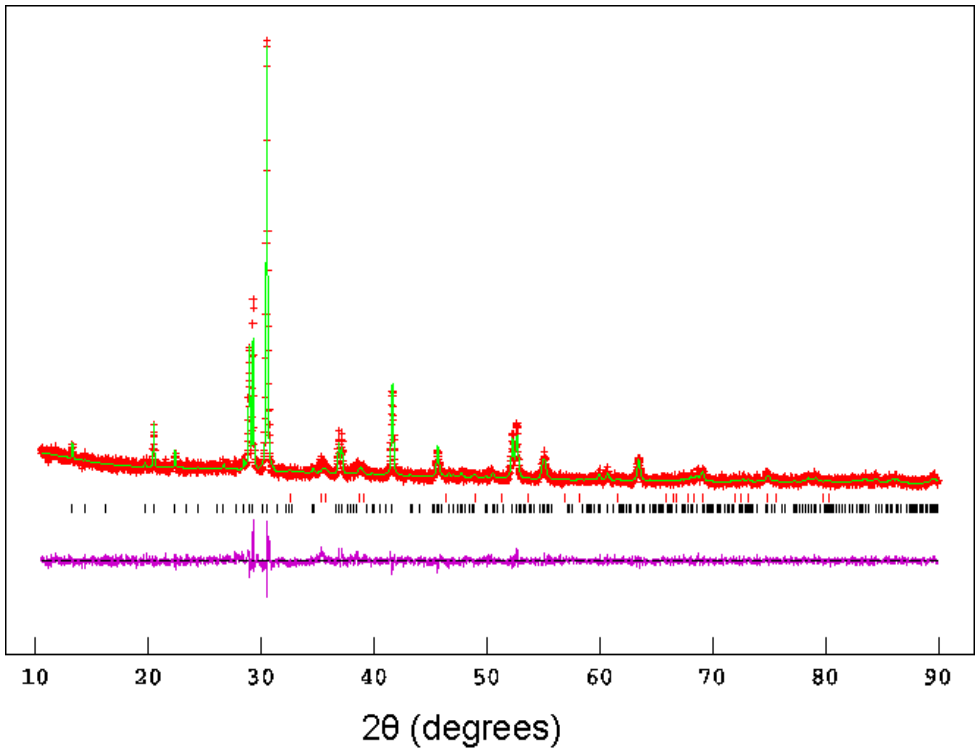

Figure A6.1 Observed, calculated and difference plots from the structural refinement of $Ba_2YCoO_5F_{0.4}$ against X-ray powder diffraction data collected at room temperature.

Atom	site	*x*	*y*	*z*	fraction	U_{iso} (Å^2)
Ba(1)	8d	0.1252(3)	0.2510(15)	0.9964(4)	1	0.0139(5)
Y(1)	4c	0.8741(2)	0.2421(13)	¼	1	0.0169(10)
Co(1)	4c	0.8961(6)	0.251(4)	¾	1	0.0024(21)
O(1)	4c	0.2447(9)	0.0125(20)	¾	1	0.0232(6)
O(2)	8d	0.3519(2)	0.2309(10)	0.4662(3)	1	0.0232(6)
O(3)	4c	0.5017(5)	0.0067(15)	¼	1	0.0232(6)
O(4)	4c	0.4837(5)	0.5086(13)	¼	1	0.0232(6)
F(1)	4c	0.251(3)	0.026(5)	¼	0.42	0.047(8)
$Ba_2YCoO_5F_{0.42}$ -space group *Pbnm* *a* = 12.3347(15) Å, *b* = 6.0917(7) Å, *c* = 7.9084(9) Å, V = 594.2(2) Å^3 χ^2 = 3.318, wRp = 3.40 %, Rp = 3.02 %						

Table A6.1 The refined structure of $Ba_2YCoO_5F_{0.42}$ at 7 K.

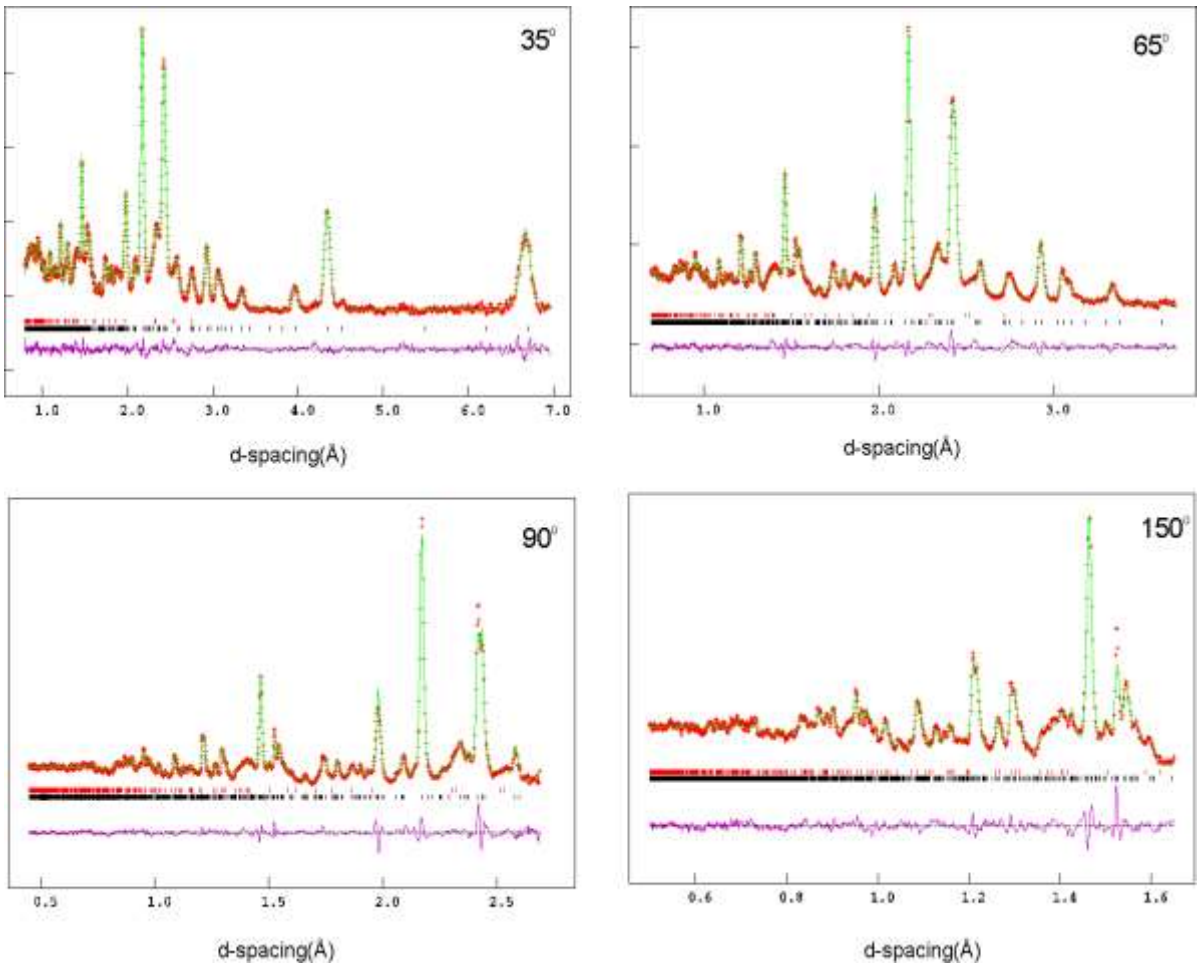

Figure A6.2 Observed, calculated and difference plots from the structural refinement of $Ba_2YCoO_5F_{0.42}$ against neutron powder diffraction data collected at room temperature. The red tick marks indicate the peaks position of CuO impurities.

Chapter 7 Structure and magnetism of the six-layered $LaCa_2Fe_2GaO_8$ phase

7.1 Introduction

In the Chapters 3 - 6, complex cation and anion-vacancy ordering patterns have been achieved in several anion-deficient perovskites. The brownmillerite structures, with a stoichiometric composition of $A_2B_2O_5$, are a common class of anion-vacancy ordered perovskite structures, consisting of alternating layers of octahedra and tetrahedra. Three common variants (*I2mb*, *Pnma* and *Imma*) can be adopted, which are related to the different arrangements of the chains of tetrahedra.[27]

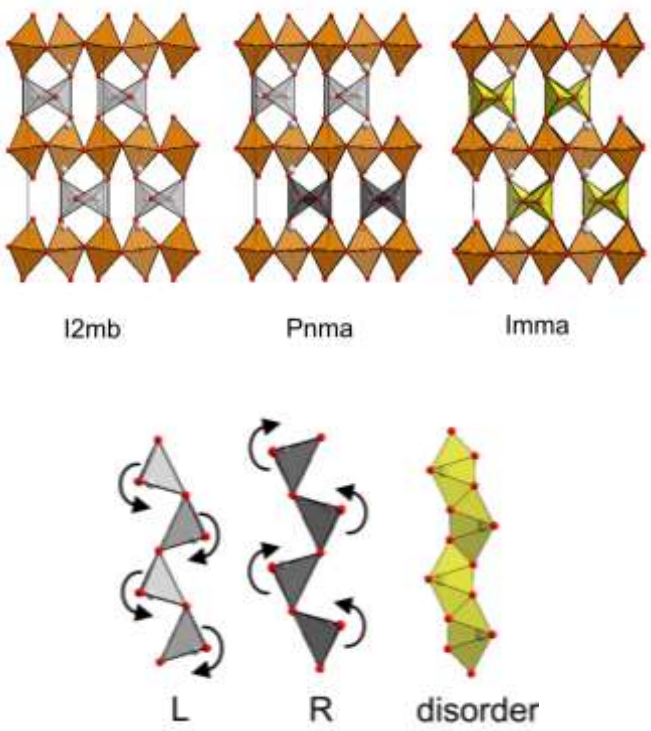

Figure 7.1 Twisting distortion of octahedra leads to eclipsed tetrahedral chains. (top) Twisting distortion of tetrahedral chains (bottom).

In the brownmillerite structure with the *I2mb* space group symmetry, all the chains of tetrahedra twist in the same direction, as shown in Figure 7.1. In the *Pnma* variant, the tetrahedra in adjacent layers twist in opposite directions. In the *Imma* variant, the twisting of chains of tetrahedra is disordered.

A 'triple-layer' structure related to the brownmillerite structure with a stoichoimetric composition of $A_3B_3O_8$ can be formed by carefully controlling the oxygen content of the phases. Compared to the brownmillerite family of structures, triple layer structures adopt an OOTOOT stacking sequence of BO_6 octahedra (O) and BO_4 tetrahedra (T), as shown in Figure 7.2. In common with the brownmillerite structures, three variants (*$P2_1ma$*, *Pbma* and *Imma*) could be constructed based on the different arrangements of the chains of tetrahedra in the lattices. As shown in Figure 7.1, the triple-layer phase $LaCa_2Fe_3O_8$ adopts the structure with space group *$P2_1ma$*, in which all the tetrahedra twist in the same direction, similar to that in *I2mb* brownmillerite structure.[27] When the chains of tetrahedra twist in a disordered manner, similar to that in *Imma* brownmillerite structure, the triple layer structure can be described in space group *Pmma* as reported for $LaSr_2Fe_3O_8$.[91]

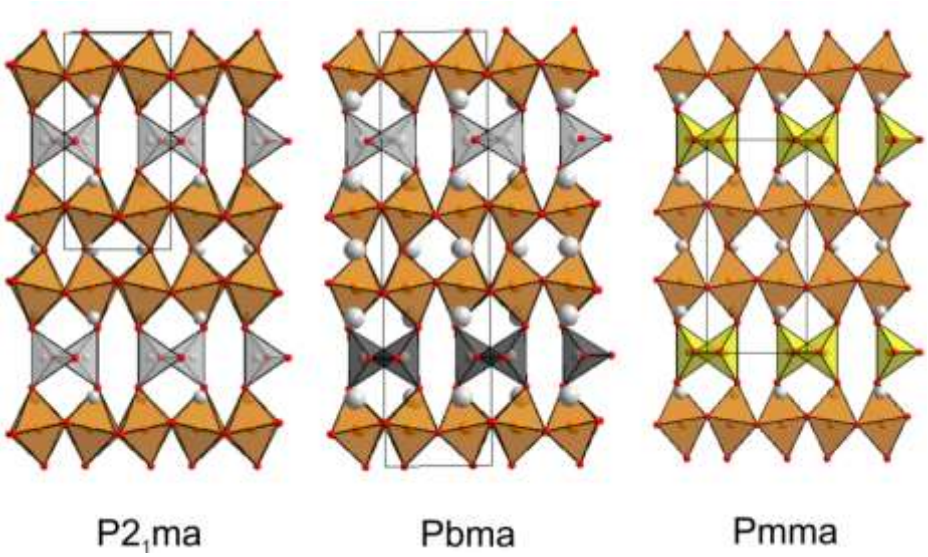

Figure 7.2 Three variants of triple-layer structure.

In this chapter, $LaCa_2Fe_2GaO_8$ was synthesized, which is the first example of triple layer phase with the *Pbma* space group in which the twist direction of tetrahedral chains alternates between adjacent tetrahedral layers, in a manner directly analogous to the *Pnma* brownmillerite structural variant. The structure and magnetic behaviour of $LaCa_2Fe_2GaO_8$ is described in this chapter.

7.2 Experimental

Samples of $LaCa_2Fe_2GaO_8$ were prepared via a standard ceramic synthesis route. Suitable stoichiometric ratios of La_2O_3 (99.999 %, dried at 900 ^oC), $SrCO_3$ (99.994 %), Ga_2O_3 (99.999 %) and Fe_2O_3 (99.99 %) were ground together in an agate pestle and mortar and then heated at 1000 ^oC in air to decompose the carbonate. The resulting powders were then reground, pressed into 13mm diameter pellets and heated at 1300 ^oC for two periods of 40 h under flowing argon.

7.3 Results

7.3.1 Characterization of $LaCa_2Fe_2GaO_8$

X-ray powder diffraction data were collected from $LaCa_2Fe_2GaO_8$ in order to confirm that a single phase was synthesized. As shown in Figure 7.3, the majority of the diffraction features can be readily indexed using an orthorhombic unit cell with lattice parameters of a = 5.48 Å, b = 11.34 Å and c = 5.60 Å, which is related to the lattice parameters of a simple cubic perovskite structure by means of a $\sqrt{2} \times 3 \times \sqrt{2}$ expansion. This suggests that $LaCa_2Fe_2GaO_8$ adopts a 'triple layer' structure as discussed in the introduction. However, close inspection of the X-ray powder diffraction data collected from $LaCa_2Fe_2GaO_8$ reveals

that some diffraction peaks with low intensity can only be indexed by a doubling of *b* lattice parameter, e.g. (061) and (151) as shown in the inset of Figure 7.3. Thus the $LaCa_2Fe_2GaO_8$ phase discussed in this chapter must have a unit cell with a $\sqrt{2} \times 6 \times \sqrt{2}$ expansion relative to a perovskite structure, rather than a $\sqrt{2} \times 3 \times \sqrt{2}$ expansion previously observed for triple layer materials. This suggests that $LaCa_2Fe_2GaO_8$ adopts a new variant of the triple layer structure.

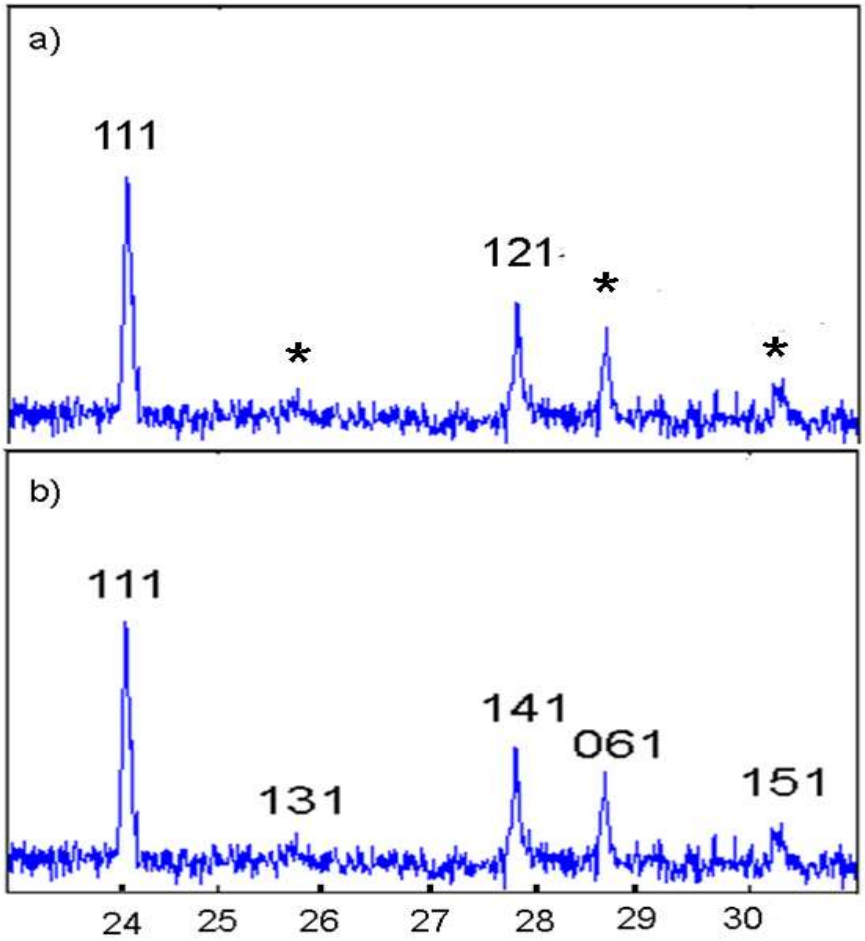

Figure 7.3 X-ray powder diffraction data collected from $LaCa_2Fe_2GaO_8$ indexed by cells with a $\sqrt{2} \times 3 \times \sqrt{2}$ expansion (* shows the unindexed diffraction features) (a) and a $\sqrt{2} \times 6 \times \sqrt{2}$ expansion (b).

Iodiometric titrations were carried out in order to determine the oxidation state of iron in $LaCa_2Fe_2GaO_8$. The results indicated an average iron oxidation state of Fe^{3+} (detailed in Table A7.1), confirming the composition of $LaCa_2Fe_2GaO_8$.

7.3.2 Structural refinement

Magnetization data discussed below indicate that $LaCa_2Fe_2GaO_8$ adopts a magnetically ordered state at room temperature and that the magnetic order-disorder transition temperature occurs at T ~ 550 K. Thus neutron powder diffraction data were collected from $LaCa_2Fe_2GaO_8$ at 600 K to analyze the nuclear structure. As in the analysis above, $LaCa_2Fe_2GaO_8$ adopts a 'triple-layer' structure similar to that of $LaCa_2Fe_3O_8$ (*Pm2₁a*) and $LaSr_2Fe_3O_8$ (*Pmma*), with a further doubling of the *b* lattice parameter. Thus, structural models based on the OOTOOT' stacking sequence of octahedral and tetrahedral layers were constructed.

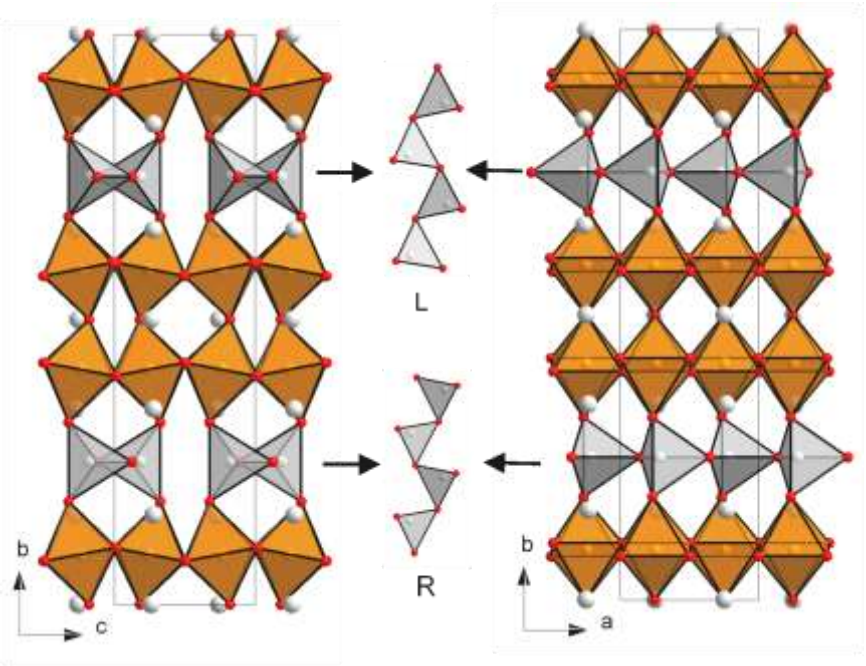

Figure 7.4 The *Pbma* structural models of $LaCa_2Fe_2GaO_8$.

Three models were constructed in space groups of *P2₁ma*, *Pbma* and *Pmma* (Figure 7.2) corresponding to the three different possible twisting arrangements of the chains of tetrahedra as shown in Figure 7.2. The *P2₁ma* and *Pmma* models were constructed based on the structures of $LaCa_2Fe_3O_8$[92] and $LaSr_2Fe_3O_8$[93] respectively by substituting the iron in the

tetrahedral sites with gallium, as shown in Figure 7.2. The *Pbma* model was constructed in a unit cell with approximately a $\sqrt{2} \times 6 \times \sqrt{2}$ expansion relative to a simple cubic perovskite unit cell, as shown in Figure 7.4. Compared to the $P2_1ma$ and *Pmma* structural models, the twisting direction of tetrahedra in *Pbma* model alternates between adjacent tetrahedral layers.

The three constructed models were then refined against the neutron powder diffraction data collected from $LaCa_2Fe_2GaO_8$ at 600 ^oC. During the refinement, the La/Ca and Ga/Fe ratios were variable within the constraint of overall composition. The anisotropic displacement factors of all atoms were refined along with the atomic positions and the fractional occupancies of cations and oxide ions. Figure 7.5 shows the observed calculated and difference plots from the structural refinements of the three different models. It can be seen that the majority of the diffraction features can be accounted for by these models. Close inspections reveal that some diffraction features cannot be accounted for using either $P2_1ma$ model or *Pmma* model (e.g. peaks at around 26.5^o, 31^o and 37.5^o), but the features can be described well by the *Pbma* model with a unit cell with a $\sqrt{2} \times 6 \times \sqrt{2}$ cell expansion.

Table 7.1 lists the fitting statistics for the refinements of three models against neutron powder diffraction data. It can be clearly seen that the *Pbma* model gives the best statistical fit.

Space group	χ^2	wRp (%)	Rp (%)
Pbma	**5.72**	**5.30**	**3.98**
$P2_1ma$	6.32	5.56	4.20
Pmma	7.30	5.97	4.35

Table 7.1 Fitting statistics for the refinements of the models against neutron powder diffraction data collected from $LaCa_2Fe_2GaO_8$ at 600 K.

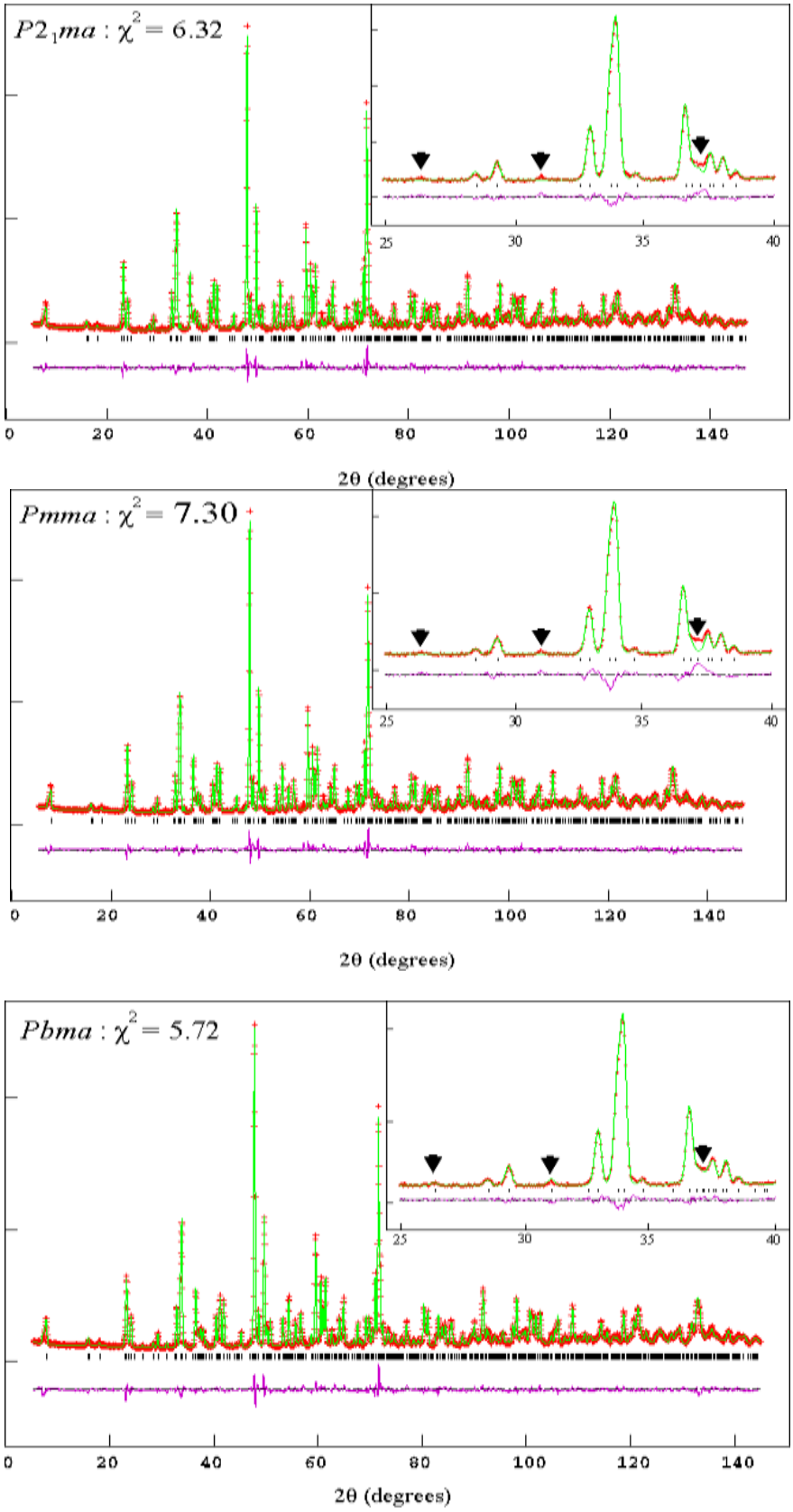

Figure 7.5 Observed calculated and difference plots from the structural refinements of the 'triple-layer' *$P2_1ma$*, *Pmma* and *Pbma* models against neutron powder diffraction data collected at 600 K. Arrows in the insets indicate the positions of diffraction reflections which cannot be accounted for.

In order to determine if the chains of tetrahedra in $LaCa_2Fe_2GaO_8$ are partially disordered, a modification was made to the *Pbma* structural model. Additional oxygen atomic positions were inserted into the tetrahedral layers to form the 'disordered' arrangement of oxide ions. As shown in Figure 7.6, the insertion of these additional oxides leads to a superposition of left and right-handed tetrahedral chains. The fractional occupancies of the oxide ions at these two positions in the tetrahedral layers were initially set to be 50 %, corresponding to a disordered arrangement of the chains of tetrahedra with different twist directions.

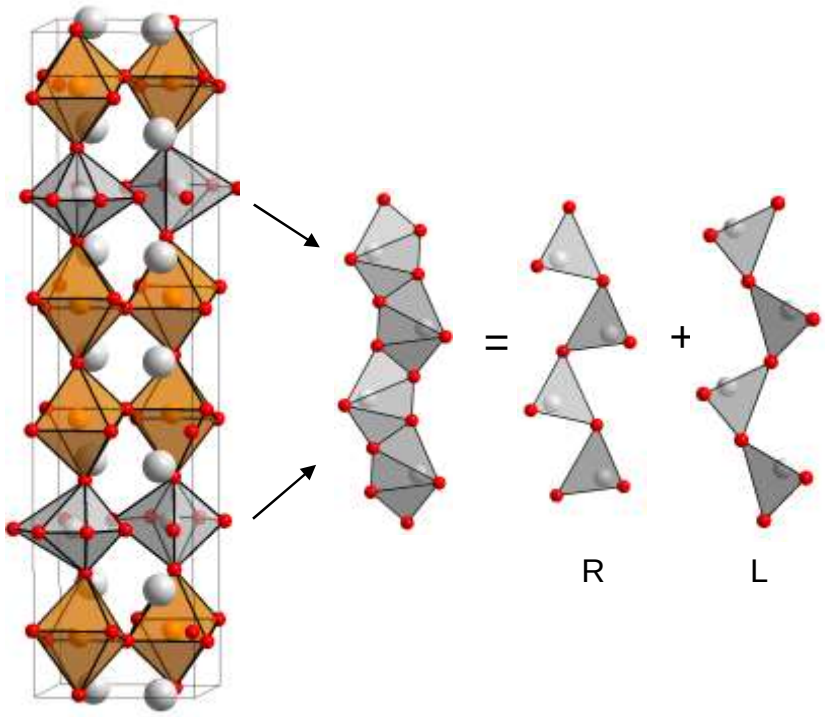

Figure 7.6 The insertion of oxide ions into the *Pbma* structural model for examining the anion-vacancy ordering in the lattice.

The modified structural model was then refined against the neutron powder diffraction data collected from $LaCa_2Fe_2GaO_8$ at 600 K. In the refinement, the fractional occupancies of oxide ions in the tetrahedral layers were allowed to vary within the constraint of overall composition. The refinement yields one set of occupancies to be unity and the other to be zero within error, confirming the ordered arrangement of the chains of tetrahedra with different twist directions in the adjacent tetrahedral layers of the *Pbma* structure adopted by

$LaCa_2Fe_2GaO_8$. Full details of the refined structure of $LaCa_2Fe_2GaO_8$ are listed in Table 7.2 and 7.3, with selected bond lengths in Table 7.4.

As shown in Table 7.2 and 7.4, the refinement of the fractional occupancies of cations on the A and B sites based on the *Pbma* structural model indicated a partially disordered cation arrangement, which exhibits a strong preference for locating Fe^{3+} cations on the octahedral sites and Ga^{3+} cations on the tetrahedral sites, and a preference for locating the La^{3+} cations on the 12-coordinate sites and Ca^{2+} cations on the 8-coordinate sites.

Atom	site	*x*	*y*	*z*	fraction	U_{equiv} (Å^2)
La/Ca(1)	*4c*	¼	0	0.7412(6)	0.74(1)/0.26(1)	0.0072
La/Ca(2)	*8e*	0.2568(14)	0.1568(1)	0.7254(7)	0.13(1)/0.87(1)	0.0174
Fe/Ga(1)	*4d*	0.2802(16)	¼	0.1828(6)	0.28(3)/0.72(3)	0.0235
Fe/Ga(2)	*8e*	0.2547(7)	0.0866(1)	0.2384(4)	0.86(1)/0.14(1)	0.0102
O(1)	*4c*	¼	0	0.1795(7)	1	0.0118
O(2)	*4d*	0.6476(10)	¼	0.1254(9)	1	0.0125
O(3)	*8e*	0.2294(13)	0.1801(1)	0.3249(5)	1	0.0174
O(4)	*8e*	0.0100(19)	0.0991(1)	0.9880(11)	1	0.0195
O(5)	*8e*	0.9981(14)	0.0758(1)	0.4954(10)	1	0.0108
$LaCa_2Fe_2GaO_8$ -space group *Pbma*. *a* = 5.4787(1) Å, *b* = 22.6780(4) Å, *c* = 5.6007(1) Å, V = 695.84(3) Å^3 χ^2 = 5.723, wRp = 5.30 %, Rp = 3.98 %						

Table 7.2 Refined structure of $LaCa_2Fe_2GaO_8$ at 600 K.

Atom	U_{11}(Å^2)	U_{22}(Å^2)	U_{33}(Å^2)	U_{12}(Å^2)	U_{13}(Å^2)	U_{23}(Å^2)
La/Ca(1)	0.006(1)	0.005(1)	0.009(2)	0	0	0
La/Ca(2)	0.006(1)	0.036(2)	0.011(1)	-0.012(3)	0.001(1)	0.002(1)
Fe/Ga(1)	0.003(1)	0.062(4)	0.003(1)	0.005(2)	0	0
Fe/Ga(2)	0.010(1)	0.007(1)	0.014(1)	0.007(1)	0.001(1)	-0.003(1)
O(1)	0.003(1)	0.024(3)	0.008(2)	0	0	0.001(1)
O(2)	0.007(2)	0.010(2)	0.020(3)	0.002(2)	0	0
O(3)	0.015(1)	0.031(3)	0.006(1)	0.011(2)	-0.002(1)	-0.005(2)
O(4)	0.011(2)	0.022(2)	0.024(2)	-0.013(1)	-0.002(1)	-0.001(1)
O(5)	0.009(1)	0.006(1)	0.017(1)	0.007(1)	0.009(2)	0.009(4)

Table 7.3 Anisotropic thermal parameters refined with *Pbma* model against neutron powder diffraction data collected from $LaCa_2Fe_2GaO_8$ at 600 K.

Cation	Anion	bond (Å)	BVS
La/Ca(1)	O(1)	2 × 2.775(1)	La+2.68/Ca+1.54
	O(1)	2.455(5)	
	O(1)	3.146(5)	
	O(4)	2 × 3.063(6)	
	O(4)	2 × 2.948(6)	
	O(5)	2 × 2.561(6)	
	O(5)	2 × 2.599(6)	
La/Ca(2)	O(2)	2.350(4)	La+3.28/Ca+1.88
	O(3)	2.657(10)	
	O(3)	2.309(5)	
	O(3)	2.951(10)	
	O(4)	2.493(9)	
	O(4)	2.388(9)	
	O(5)	2.579(7)	
	O(5)	2.654(7)	
Fe/Ga(1)	O(1)	1.992(2)	Fe+3.08/Ga+2.85
	O(3)	2.179(3)	
	O(4)	1.909(9)	
	O(4)	1.961(9)	
	O(5)	2.015(7)	
	O(5)	2.027(7)	
Fe/Ga(2)	O(2)	2.038(10)	Fe+3.02/Ga+2.79
	O(2)	1.873(7)	
	O(3)	2 × 1.795(3)	

Table 7.4: Selected bond lengths from the refined structure of $LaCa_2Fe_2GaO_8$ at 600 K.

7.3.3 Magnetic characterization

Zero-field-cooled and field-cooled magnetisation data were collected from $LaCa_2Fe_2GaO_8$ in the temperature range 300 < T/K < 650 in an applied magnetic field of 1000 Oe, as shown in Figure 7.7. The data diverge below 550 K, suggesting the onset of magnetic order. Further cooling leads to a significant divergence at about 470 K, which could be caused by further magnetic ordering transition.

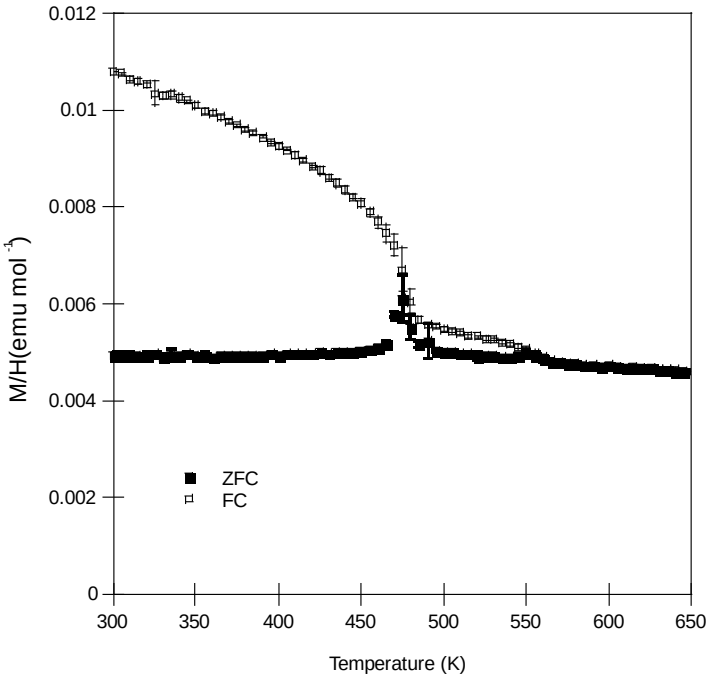

Figure 7.7 Zero-field-cooled and field-cooled magnetization data collected from $LaCa_2Fe_2GaO_8$ in the temperature range 300 < T (K) < 650. The anomaly at T ≈ 550 K is assigned to the onset of magnetic order.

In order to study the magnetic structure of $LaCa_2Fe_2GaO_8$, neutron powder diffraction data were collected at room temperature, 510 K and 600 K respectively. As shown in Figure 7.8, the data collected at 510 K show broad additional diffraction features compared to the neutron powder diffraction data collected at 600 K, confirming the onset of magnetic order. These additional diffraction features are significantly sharpened in the neutron powder diffraction data collected at room temperature.

The additional diffraction features can be indexed using the crystallographic unit cell. The intensities of the additional diffraction features are consistent with the simulation result of a G-type antiferromagnetically ordered arrangement of iron spins lying parallel to the *z*-axis. Thus a magnetic model was constructed, as shown in Figure 7.10, and refined against the neutron powder diffraction data collected from $LaCa_2Fe_2GaO_8$ at room temperature. Figure 7.9 shows the observed, calculated and difference plots from the structural and magnetic refinement of $LaCa_2Fe_2GaO_8$ against data collected at room temperature. The refinement

results give an ordered magnetic moments of 3.30(3) μ_B per iron for the cations on the octahedral sites and 2.92(15) μ_B per iron for the cations on the tetrahedral sites.

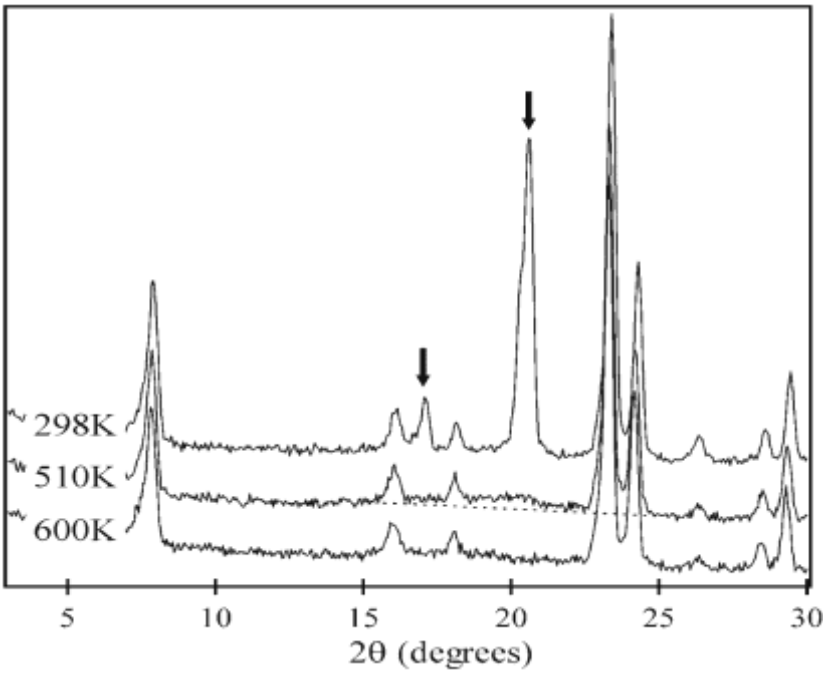

Figure 7.8 Neutron diffraction data collected from $LaCa_2Fe_2GaO_8$ at 298 K, 510 K and 600 K. Arrows mark the positions of additional diffraction features, indicative of magnetic order.

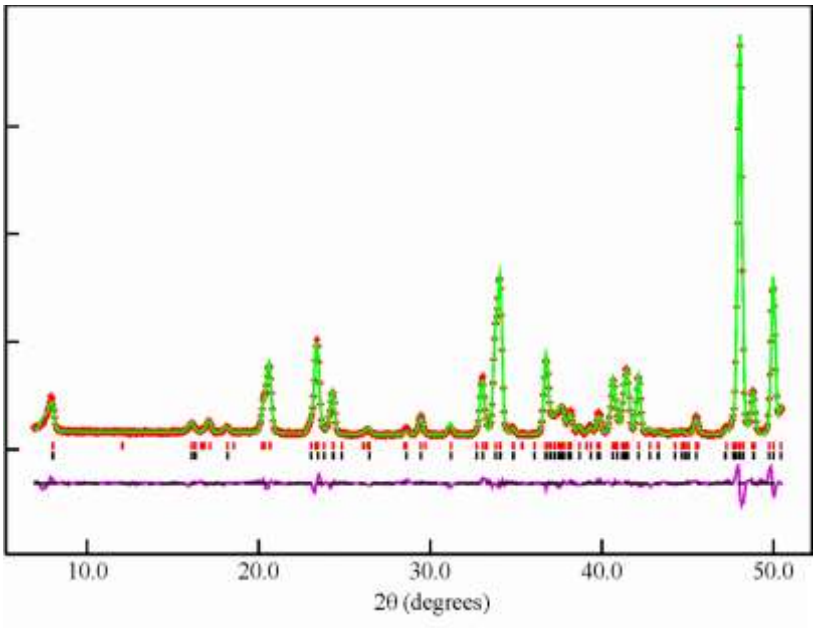

Figure 7.9 Observed, calculated and difference plots from the structural and magnetic refinement of $LaCa_2Fe_2GaO_8$ against data collected at 298 K. Lower tick marks indicate allowed structural peak positions, upper tick marks indicated allowed magnetic peak positions.

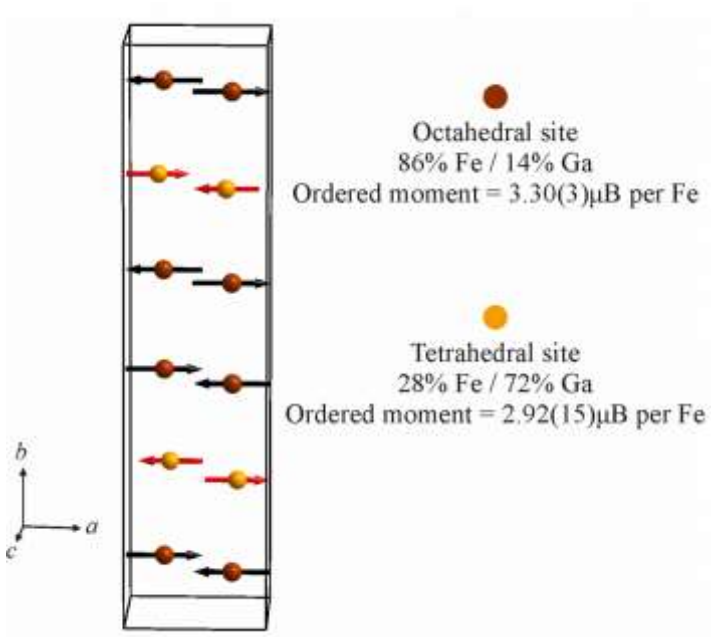

Figure 7.10 The magnetic structure of $LaCa_2Fe_2GaO_8$ refined against neutron diffraction data collected at room temperature.

7.4 Discussion

$LaCa_2Fe_2GaO_8$ was synthesized via a high-temperature solid state reaction. Structural analysis indicate that $LaCa_2Fe_2GaO_8$ adopts an anion-vacancy ordered, six-layer structure consisting of $(Fe/Ga)O_6$ octahedra and $(Fe/Ga)O_4$ tetrahedra in a stacking sequence of OOT_LOOT_R arrangement (a = 5.4784(1) Å, b = 22.6780(4) Å, c = 5.6007(1) Å, space group *Pbma*). The chains of tetrahedra in adjacent layers adopt a – L – R – L – R – arrangement, related to that of the four-layer *Pnma* type brownmillerite structure. In addition, the structure exhibits a preference for locating Fe^{3+} and Ga^{3+} cations in the octahedral and tetrahedral sites, respectively.

7.4.1 Arrangement of tetrahedral chains

The differences between the structure adopted by $LaCa_2Fe_2GaO_8$ and the structures adopted by $LaCa_2Fe_3O_8$ (*P2₁ma*) or $LaSr_2Fe_3O_8$ (*Pmma*) lie in the different arrangements of the tetrahedral chains in adjacent tetrahedral layers. For example, all the tetrahedra in the

structure of *P2₁ma* member twist in the same direction, while the tetrahedral chains in *Pmma* member twist in a disordered manner.

These three members of 'triple' layered structures can be considered as the extension of brownmillerite structures due to the same components (tetrahedral and octahedral layers) and similar stacking arrangement. The six-layer layer structure adopted by $LaCa_2Fe_2GaO_8$ can also be rationalized by considering three factors discussed in Chapter 1, pricinply dipole cancelation, disruption of additional oxides and electronic factors. The average oxidation of iron in $LaCa_2Fe_2GaO_8$ is Fe^{3+}, which has a d^5 electronic configuration. Thus the influences of charge ordering or a local Jahn-Teller distortion observed in $La_xBa_{1-x}MnO_{2.5}$ and $La_xCa_{1-x}MnO_{2.5}$ phases should be excluded when the arrangement of the chains of tetrahedra is considered in $LaCa_2Fe_2GaO_8$. Since not many 'triple' layered examples were reported, the twist angle of the tetrahedra in the chains, φ and tetrahedral layer separation, l (Figure 7.11) were only measured in three iron-containing phases.

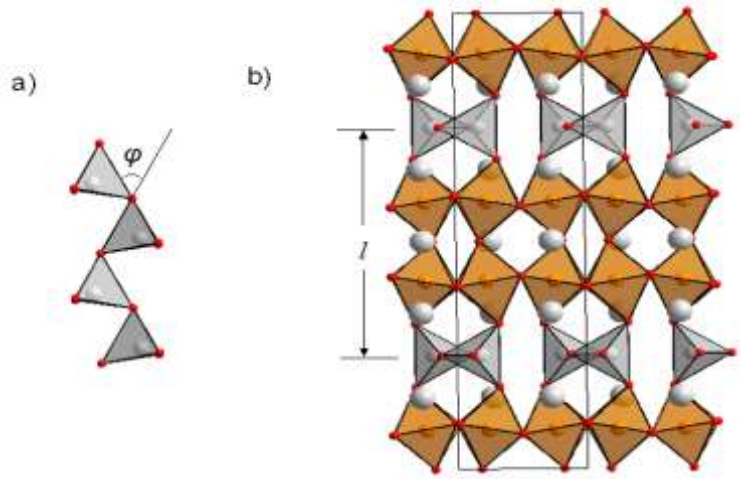

Figure 7.11 Tetrahedral chain twist angle, φ (a), tetrahedral layer separation, l of the 'triple' layer structure (b).

Compared with the structural change in the brownmillerite structures, a similar structural change can be observed in variants of the 'triple' layer structure, as shown in Figure 7.12. As reported previously, $LaCa_2Fe_3O_8$ (φ = 43.1°, l = 11.31 Å) adopts a *P2₁ma* triple layer

structure in which all the tetrahedral chains are twisted in the same direction,[92] in a manner analogous to the *I2mb* brownmillerite structural variant. In the structure of $LaCa_2Fe_2GaO_8$, the chain distortion angle φ is increased to 53.1°, which indicates an increase in the dipole moment of the tetrahedral chains. Thus $LaCa_2Fe_2GaO_8$ adopts a *Pbma* structure, in which the cooperative twisting manner of the tetrahedral chains between adjacent layers compensates the increased chain dipole. In the structure of $LaSr_2Fe_3O_8$,[93] the large Sr^{2+} cations on the A sites lead to an increase in the tetrahedral layer separation (l = 11.31 Å) and a disordered arrangement of tetrahedral chains which is described as *Pmma* space group.

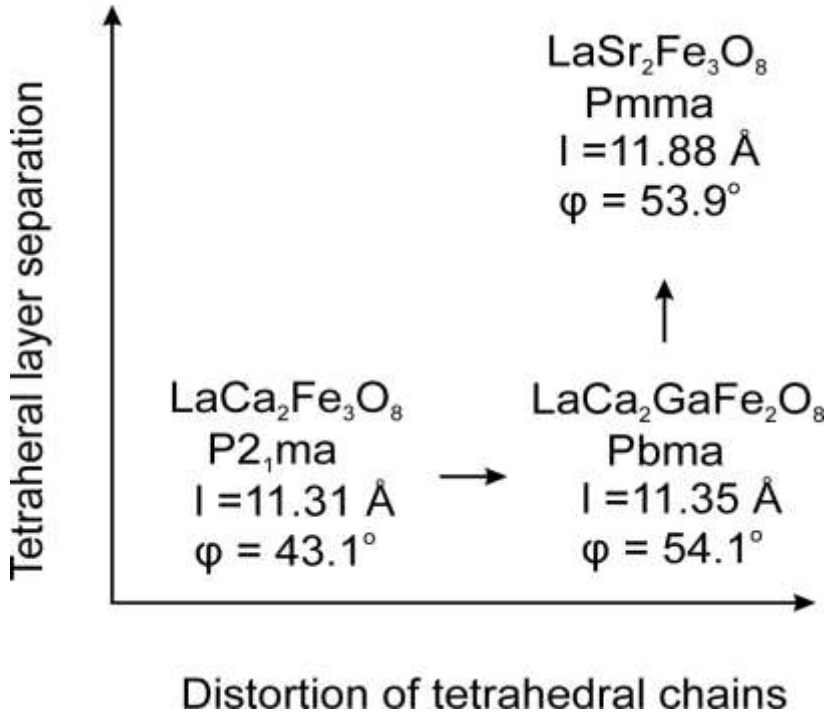

Figure 7.12 Variation in triple layer structural variant as a function of tetrahedral chain twist angle, φ, and tetrahedral layer separation, l, for iron containing $A_3B_3O_8$ phases.

However, it should be noted that this rationalization cannot be applied to all known triple-layer phases. The manganese containing triple-layer phases $Ca_{2.5}Sr_{0.5}Mn_2GaO_8$ (φ = 57.7 °, l = 11.37 Å)[20] and $Ca_{2.5}Sr_{0.5}Ga_{1.2}Mn_{0.8}O_8$ (φ = 57.6 °, l = 11.38 Å)[94] exhibit a larger distortion in the chains of tetrahedra than $LaCa_2Fe_2GaO_8$, and thus would be expected to adopt a *Pmma* type structure. However, the two phases adopt the *P2₁ma* type triple-layer structures,

inconsistent with the theory of dipole cancellation. This could be led by the local electronic factors, such as the Jahn-Teller distortion of Mn^{3+} cations or local Mn^{3+}/Mn^{4+} charge ordering in the two phases, indicating that the electronic factors should also be considered in determining the structural variant adopted by a particular phase.

7.4.2 Preparation conditions

Goosen et al.[95] reported that '$LaCa_2Fe_2GaO_8$' adopted a triple-layer structure with the *P2₁ma* space group symmetry in which all the tetrahedra twist in the same direction, as shown in Figure 7.2, inconsistent with the result discussed in this chapter. The structural analysis reveals that $LaCa_2Fe_2GaO_8$ in this chapter adopts a new six-layer structure with the *Pbma* space group symmetry. It should be noted that Goosen et al. prepared their '$LaCa_2Fe_2GaO_8$' sample at 1050 ^oC in air from a citrate-gel precursor. The $LaCa_2Fe_2GaO_8$ sample described in this chapter was synthesized at 1300 ^oC under an argon flow in a ceramic method. Thus the differences in synthesis conditions could be the reason leading to the different phases.

Structural characterization indicated that the lattice parameters of the sample described in this chapter (a = 5.4784(1) Å, b = 22.6780(4) Å, c = 5.6007(1) Å) are obviously larger than those of the Goosen's sample (a = 5.4467(6) Å, b = 11.2674(8) Å, c = 5.548(4) Å) in all three directions, confirming the formation of two different phases. Considering the conditions employed to prepare these two samples, the sample described in this chapter was synthesized in an argon flow. In addition, the high synthesis temperature (1300 ^oC) in argon leads to a 'reducing' environment. Thus the sample in this chapter can be described exactly as a formula of $LaCa_2Fe_2GaO_8$, confirmed by iodometric titrations. In contrast, Goosen et al. prepared their sample at 1050 ^oC in air. Thus it could be speculated that Goosen's

$LaCa_2Fe_2GaO_8$ sample could be slightly 'oxidized' to be a $LaCa_2Fe_2GaO_{8+x}$ phase. The extra oxide ions are considered to be located in the vacant anion sites within the tetrahedral layers, which would not only lead to a disruption of the twisting patterns of tetrahedral chains, but also make the octahedral and tetrahedral sites more similar, reducing the driving force to locate Fe^{3+} on the octahedral sites and Ga^{3+} on the tetrahedral sites. The fractional occupancies of the Fe^{3+}/Ga^{3+} cations on the octahedral sites of $LaCa_2Fe_2GaO_8$ described in this chapter is 0.86(1)/0.14(1), while the value of Goosen's sample was reported to be 0.66(2)/0.34(2), which is a good support to this idea. Thus the cation and anion arrangement in an anion-deficient perovskite structure is sensitive to the oxygen concentration in the lattice. The control of the synthesis temperature and oxygen concentrations in the structures provides a possibility to give rise to the formation of different structures.

7.4.3 Cation disorder

The structural analysis above indicate a partially disordered cation arrangement in the structure of $LaCa_2Fe_2GaO_8$ which nevertheless exhibits a strong preference for locating Fe^{3+} on the octahedral sites and Ga^{3+} on the tetrahedral sites. This is different to the structure of Sr_2MnGaO_5, in which all the Mn^{3+} cations are located in the octahedral sites and Ga^{3+} cations are located in tetrahedral sites[96]. This partial cation disorder could be caused by the d^5 electronic configuration of Fe^{3+} cations, indicating Fe^{3+} can be located in different coordination environments, like octahedra or tetrahedra. Although in many cases d^{10} Ga^{3+} cations favour to be located in 4-coordinate tetrahedral sites, the high temperature brings entropy leading to a partially disordered arrangement on the B sites, which is observed in the brownmillerite $Ca_2Fe_{1.44}Ga_{0.56}O_5$ phase.

The ordering of La^{3+} and Ca^{2+} cations in the A sites of perovskite structures is very rare. Due to the similar ionic sizes of La^{3+} and Ca^{2+} cations (La^{3+} CN = 12 , 1.36 Å; Ca^{2+} CN = 12, 1.34 Å), the La^{3+} and Ca^{2+} cations tend to adopt disordered arrangement in perovskite ($La_xCa_{1-x}CoO_3$[97]). However, in the six-layer $LaCa_2Fe_2GaO_8$ structure, the fractional occupancies of La^{3+} and Ca^{2+} cations in *4c* and *8d* positions indicate that La^{3+} cations favour to occupy the 12-coordinate sites (74 % La and 26 % Ca) while Ca^{2+} cations prefer to occupy the 8-coordinated sites (87 % Ca and 13 % La). The separation of La^{3+} and Ca^{2+} cations could be attributed to the presence of a large amount of anion vacancies in the lattice and thus the higher charged La^{3+} cations are favourably located in coordination environment with CN = 12, while the lower charged Ca^{2+} cations prefer to be located in coordination environment with CN = 8. A similar segregation of La^{3+}/Ca^{2+} cations in A sites is observed in a Ruddlesden-Popper phase $LaCa_2Mn_2O_7$, which exhibits a strong preference for locating Ca^{2+} in the 9-coordinate sites and La^{2+} in the 12-coordinate sites.[98]

7.4.4 Magnetism

The $LaCa_2Fe_2GaO_8$ phase undergoes two magnetic ordering transitions in the measured temperature range. As shown in Figure 7.1, the transitions occur at ~ 470 ^oC and 550 ^oC. The neutron powder diffraction data collected at 510 ^oC exhibit additional weak and broad features, indicating a short-range magnetic order. When the temperature is lowered to room temperature, these additional features are enhanced and sharpened. The refinement of the constructed magnetic model against the neutron powder diffraction data collected at room temperature gives a G-type antiferromagnetic order with ordered moments of 3.30(3) μ_B and 2.92(15) μ_B per iron centre for the octahedral and tetrahedral cation sites parallel with *z* axis. The ordered magnetic moments refined for the two Fe centres are significantly smaller than

5 μ_B (Fe^{3+} S = 5/2), which could be attributed to the local disordered canting from the magnetic moments. The magnetic coupling between the Fe centres in the *xz* plane is much stronger than that between the double layers of Fe centres parallel with the *y* axis. Thus below 470 K $LaCa_2Fe_2GaO_8$ is considered to adopt a three-dimensional antiferromagnetically order state.

The observed long-range magnetic order below 550 K is consistent with the presence of an extended Fe – O – Fe network in $LaCa_2Fe_2GaO_8$. However the magnetic ordering temperature is smaller than typically observed for Fe^{3+} cubic perovskite $LnFeO_3$ (Ln = lanthanide) phases (750 K)[99], indicating that the presence of Ga^{3+} centers in the B-cation sites of the lattice and anion vacancies in the framework disrupts the magnetic coupling between iron centres in $LaCa_2Fe_2GaO_8$.

7.5 Conclusion

In this chapter, a novel anion-deficient phase $LaCa_2Fe_2GaO_8$ was synthesized. $LaCa_2Fe_2GaO_8$ adopts a novel triple layer structure (a = 5.4784(1) Å, b = 22.6780(4) Å, c = 5.6007(1) Å, space group *Pbma*), consisting of an OOT_LOOT_R stacking of layers of $(Fe/Ga)O_6$ octahedra (O) and $(Fe/Ga)O_4$ tetrahedra (T). In this novel structure, the twisting directions of the chains of tetrahedra alternate in the adjacent tetrahedral layers, related to the *Pnma*-type brownmillerite structure. Magnetization data and neutron powder diffraction data indicate that $LaCa_2Fe_2GaO_8$ adopts a G-type antiferromagnetic order at room temperature.

Appendix

Mass (mg)	$x_{caculated}$	$x_{average}$
38.7	8.021	8.01(1)
39.2	8.015	
38.5	8.005	

Table A7.1 Iodometric titration results of $LaCa_2Fe_2GaO_x$

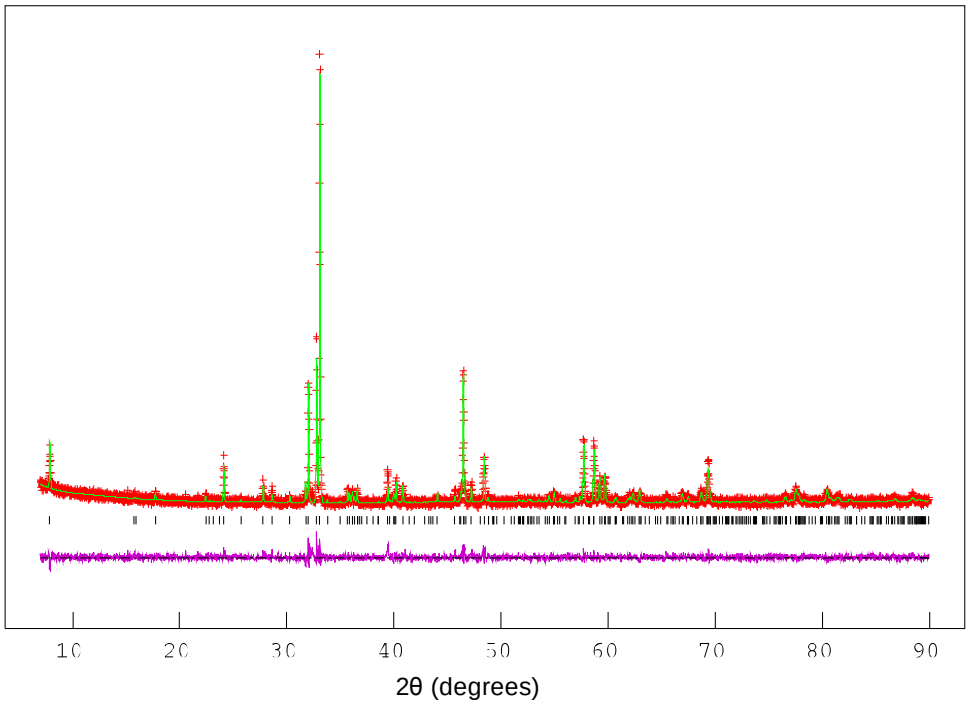

Figure A7.1. Observed, calculated and difference plots from the structural refinement of $LaCa_2Fe_2GaO_8$ (*Pbma* model) against X-ray powder diffraction data collected room temperature.

Atom	site	*x*	*y*	*z*	fraction	U_{equiv}(Å^2)
La/Ca(1)	*2a*	0.6080(7)	0	0.2582(5)	0.68(2)/0.32(2)	0.0063
La/Ca(2)	*4c*	0.5829(1)	0.3164(1)	0.2821(4)	0.15(5)/0.85(5)	0.0145
Fe/Ga(1)	*2b*	0.06751(5)	½	0.1859(6)	0.28(1)/0.72(1)	0.0193
Fe/Ga(2)	*4c*	0.09576(7)	0.1734(1)	0.2394(3)	0.86(2)/0.14(2)	0.0133
O(1)	*4c*	-0.1614(3)	0.1987(8)	0.01631(9)	1	0.0171
O(2)	*4c*	-0.1381(6)	0.1514(8)	0.5054(14)	1	0.0116
O(3)	*2b*	-0.7968(3)	½	-0.1271(19)	1	0.0090
O(4)	*2a*	0.09089(7)	0	0.1777(8)	1	0.0080
O(5)	*4c*	0.1014(6)	0.3610(9)	0.3245(35)	1	0.0279
$LaCa_2Fe_2GaO_8$ -space group *P2$_1$ma*. *a* = 5.4782(2) Å, *b* = 11.3385(1) Å, *c* = 5.6005(6) Å, V = 347.8726(5) Å^3 χ^2 = 6.327, wRp = 5.56%, Rp = 4.20 %						

Table A7.2 Refined *P2$_1$ma* structure of $LaCa_2Fe_2GaO_8$ at 600 K.

Atom	U_{11}(Å^2)	U_{22}(Å^2)	U_{33}(Å^2)	U_{12}(Å^2)	U_{13}(Å^2)	U_{23}(Å^2)
La/Ca(1)	0.001(1)	0.011(1)	0.004(2)	0	-0.003(2)	0
La/Ca(2)	0.001(1)	0.012(1)	0.009(1)	-0.002(2)	0.001(1)	-0.003(1)
Fe/Ga(1)	0.090(5)	0.008(2)	0.014(2)	0	-0.001(1)	0
Fe/Ga(2)	0.010(1)	0.012(1)	0.009(1)	-0.002(2)	0.001(1)	-0.003(1)
O(1)	0.012(2)	0.026(2)	0.007(2)	0.011(3)	0.001(1)	0.0040(2)
O(2)	0.011(2)	0.017(2)	0.007(2)	0	0.006(1)	0
O(3)	0.011(3)	0.015(3)	0.006(2)	0	0.011(2)	0
O(4)	0.009(3)	0.010(2)	0.005(2)	0	0.001(1)	0
O(5)	0.074(4)	0.003(1)	0.016(2)	0.005(4)	0.019(4)	0.001(1)

Table A7.3 Anisotropic thermal parameters refined with *P2$_1$ma* model against neutron powder diffraction data collected from $LaCa_2Fe_2GaO_8$ at 600 K.

Atom	site	*x*	*y*	*z*	fraction	U_{equiv}(Å^2)
La/Ca(1)	*2f*	¼	½	0.7422(3)	0.79(1)/0.21(1)	0.0061
La/Ca(2)	*4k*	¼	0.1863(1)	0.7220(28)	0.10(5)/0.89(5)	0.0160
Fe/Ga(1)	*4i*	0.2007(5)	0	0.1833(17)	0.15(2)/0.35(2)	0.0046
Fe/Ga(2)	*4k*	¼	0.3270(9)	0.2377(6)	0.70(3)/0.30(3)	0.0104
O(1)	*4g*	0	0.3011(9)	0	1	0.0193
O(2)	*4h*	0	0.3482(4)	½	1	0.0132
O(3)	*2f*	¼	½	0.1778(23)	1	0.0107
O(4)	*8l*	0.2570(7)	0.1388(4)	0.3232(14)	0.5	0.0268
O(5)	*4i*	0.1458(5)	0	0.8743(9)	0.5	0.0105
$LaCa_2Fe_2GaO_8$ -space group *Pmma*. *a* = 5.4783(5) Å, *b* = 11.3391(1) Å, *c* = 5.6008(1) Å, V = 347.9160(4) Å^3 χ^2 = 7.301, wRp = 5.97%, Rp = 4.35 %						

Table A7.4 Refined *Pmma* structure of $LaCa_2Fe_2GaO_8$ at 600 K.

Atom	U_{11}(Å^2)	U_{22}(Å^2)	U_{33}(Å^2)	U_{12}(Å^2)	U_{13}(Å^2)	U_{23}(Å^2)
La/Ca(1)	0.011(1)	0.009(1)	0.009(2)	0	0	0
La/Ca(2)	0.029(2)	0.009(1)	0.007(2)	0	0	0.004(1)
Fe/Ga(1)	0.001(1)	0.014(2)	0.010(2)	0	-0.002(1)	0
Fe/Ga(2)	0.002(1)	0.009(1)	0.005(1)	0	0	0.001(1)
O(1)	0.025(2)	0.018(1)	0.018(2)	0	-0.014(1)	0
O(2)	0.011(2)	0.012(1)	0.017(1)	0	0.009(1)	0
O(3)	0.022(3)	0.012(2)	0.005(2)	0	0	0
O(4)	0.051(4)	0.013(2)	0.018(2)	-0.004(2)	-0.038(6)	0.001(1)
O(5)	0.012(3)	0.020(3)	0.006(3)	0	0.002(2)	0

Table A7.5 Anisotropic thermal parameters refined with *Pmma* model against neutron powder diffraction data collected from $LaCa_2Fe_2GaO_8$ at 600 K.

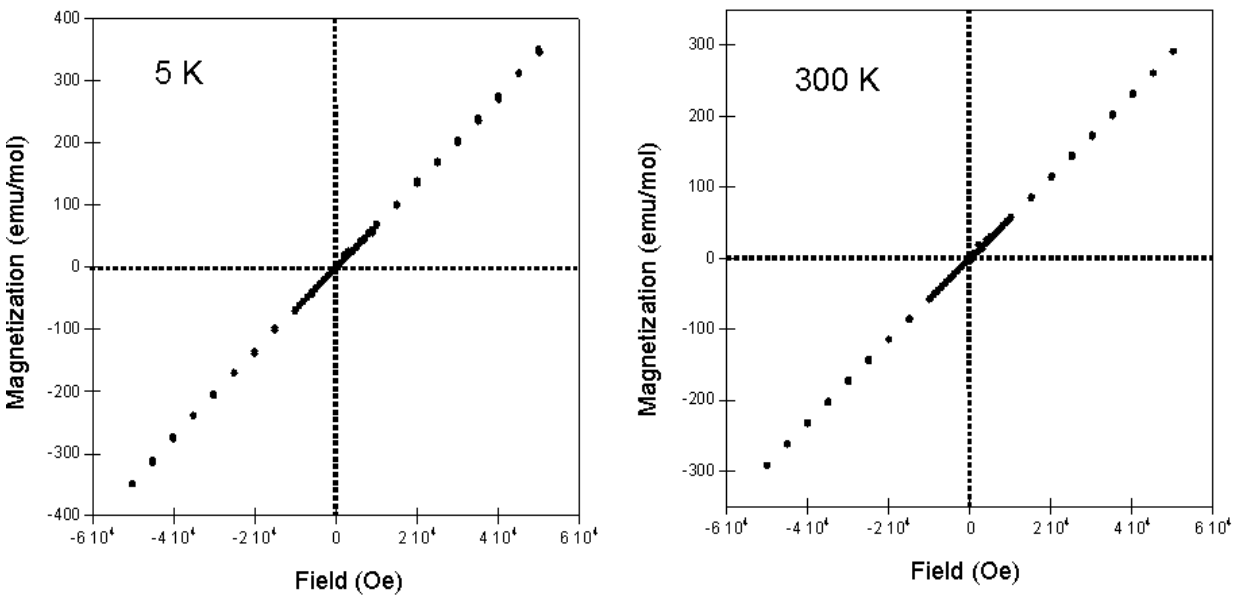

Figure A7.2. Magnetization-field isotherm collected at 5 K and 300 K from $LaCa_2Fe_2GaO_8$.

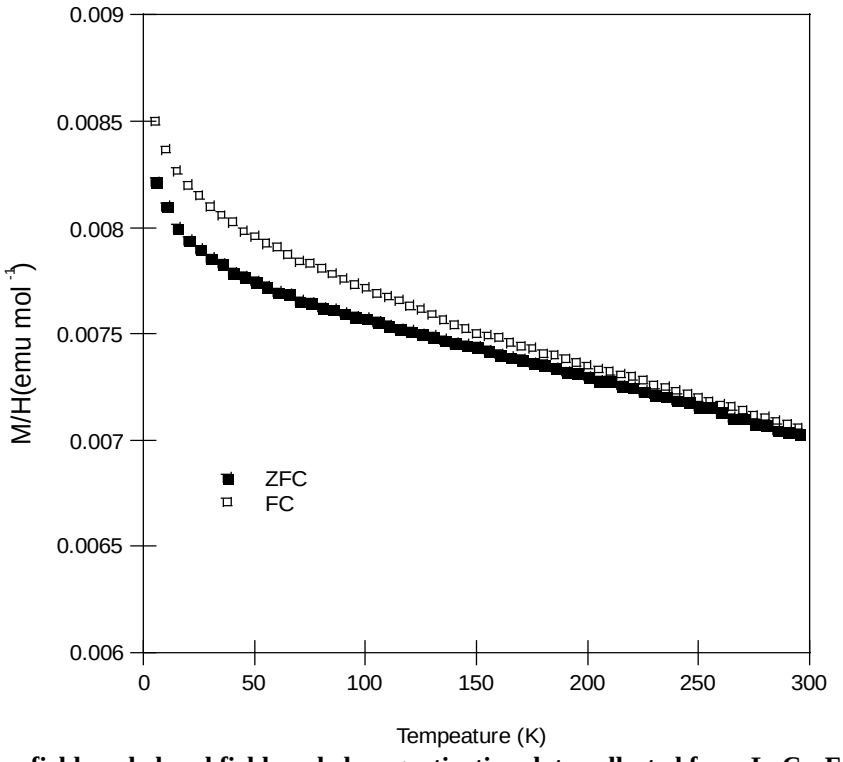

Figure 7.7 Zero-field-cooled and field-cooled magnetization data collected from $LaCa_2Fe_2GaO_8$ in the temperature range 5 < T (K) < 300.

Atom	site	*x*	*y*	*z*	fraction	U_{iso} (Å^2)
La/Ca(1)	*4c*	¼	0	0.7412(6)	0.74/0.26	0.0053(2)
La/Ca(2)	*8e*	0.2568(2)	0.1568(11)	0.7254(3)	0.13/0.87	0.0058(3)
Fe/Ga(1)	*4d*	0.2802(1)	¼	0.1828(5)	0.28/0.72	0.0145(4)
Fe/Ga(2)	*8e*	0.2547(4)	0.0866(11)	0.2384(2)	0.86/0.14	0.0054(1)
O(1)	*4c*	¼	0	0.1795(3)	1	0.0062(4)
O(2)	*4d*	0.6476(6)	¼	0.1254(1)	1	0.0099(1)
O(3)	*8e*	0.2294(3)	0.1801(2)	0.3249(1)	1	0.0114(3)
O(4)	*8e*	0.0100(1)	0.0991(2)	0.9880(5)	1	0.0062(4)
O(5)	*8e*	0.9981(5)	0.0758(2)	0.4954(4)	1	0.0062(4)
$LaCa_2Fe_2GaO_8$ -space group *Pbma*. *a* = 5.4625(1) Å, *b* = 22.5826(5) Å, *c* = 5.5858 (1) Å, V = 695.05(9) Å^3 χ^2 = 9.637 wRp = 5.82 %, Rp = 4.39 %						

Table A7.6 Refined *Pbma* Structure of $LaCa_2Fe_2GaO_8$ at room temperature.

Atom	*x*	*y*	*z*	fraction	$M_x(\mu_B)$
Fe(1)	0.2530	0.0862	0.2433	0.86	3.30(3)
Fe(2)	0.7530	0.0862	0.7567	0.86	-3.30(3)
Fe(3)	0.2945	¼	0.1833	0.28	-2.92(15)
Fe(4)	0.7945	¼	0.8167	0.28	2.92(15)
Fe(5)	0.2530	0.4138	0.2433	0.86	3.30(3)
Fe(6)	0.7530	0.4138	0.7567	0.86	-3.30(3)
Fe(7)	0.2470	0.5862	0.2433	0.86	-3.30(3)
Fe(8)	0.7470	0.5862	0.7567	0.86	3.30(3)
Fe(9)	0.2055	¾	0.1833	0.28	2.92(15)
Fe(10)	0.7055	¾	0.8167	0.28	-2.92(15)
Fe(11)	0.2470	0.9138	0.2433	0.86	-3.30(3)
Fe(12)	0.7470	0.9138	0.7567	0.86	3.30(3)
$LaCa_2Fe_2GaO_8$, Space group-*P1*, *a* = 5.4625 Å, *b* = 22.5826 Å, *c* = 5.5858 Å					

Table A7.7. Structural parameters from the magnetic refinement of $LaCa_2FeGa_2O_8$ against neutron diffraction data collected at room temperature.

Chapter 8 Structure, magnetism and conductivity of $La_xSr_{2-x}CoGaO_{5+\delta}$ ($0.5 < x < 1.0$)

8.1 Introduction

The spin state adopted by transition metal cations depends on the relative energy of the ligand-field splitting (Δ) and the pairing/exchange energy (P). For example, in an octahedral coordination environment *d*-orbitals are split into e_g and t_{2g} sets, yielding the gap Δ between e_g and t_{2g} sets as shown in Figure 8.1.

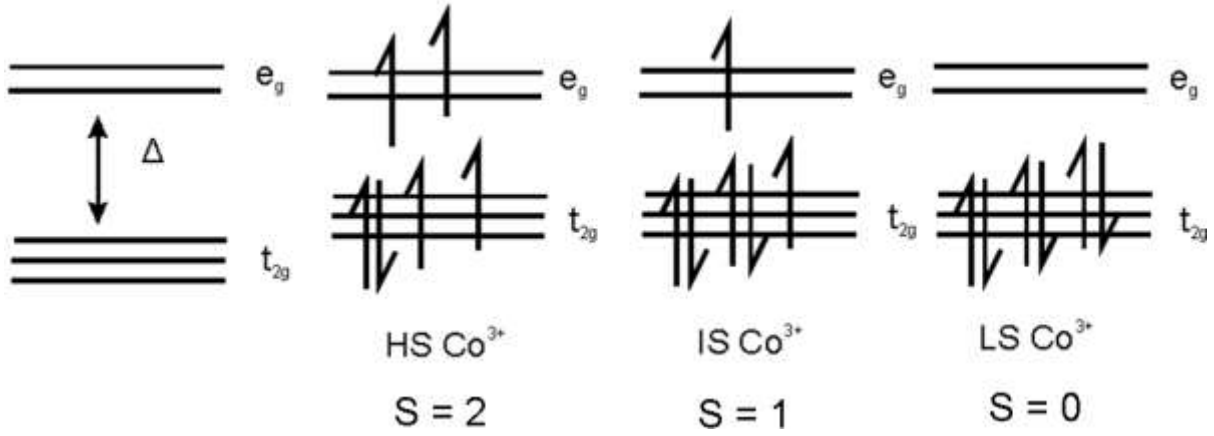

Figure 8.1 Crystal field splitting and Co^{3+} spin state in the octahedral sites.

High spin states (HS), in which S is maximized, will be preferred when the ligand-field splitting (Δ) is small. In contrast, low spin state (LS), in which S is minimized, will be preferred when the ligand-field splitting (Δ) is large. For example, Co^{3+} has a high spin, $t_{2g}^4e_g^2$ electronic configuration (S = 2) in weak ligand fields and a low spin, $t_{2g}^6e_g^0$ electronic configuration (S = 0) in strong ligand fields as shown in Figure 8.1.

In addition, some other factors can also influence the arrangement of electrons. For example, the intermediate spin state ($t_{2g}^5e_g^1$, S = 1) of Co^{3+} can be stabilized in $LaCoO_3$ by the presence of itinerant electrons or a dynamic Jahn-Teller distortion. Thus the spin states adopted by transition metal cations are determined by the combination of these factors.

By carefully selecting the number and identity of coordinating ligands, the size of Δ can be tuned so that small external disturbances, like changes of temperature or pressure, can bring about a change of spin state, as observed in the following two examples.

1. **Physical pressure.** A change of Co^{3+} spin state can be induced in $BiCoO_3$ by applied pressure as shown in Figure 8.2. The Co^{3+} centres in $BiCoO_3$ adopt HS state (S = 2) at ambient pressure.[100] When the applied pressure is above 3 GPa, a change of Co^{3+} spin state from HS to IS or LS occurs, which is confirmed by the observation of a dramatic change in electrical resistivity.

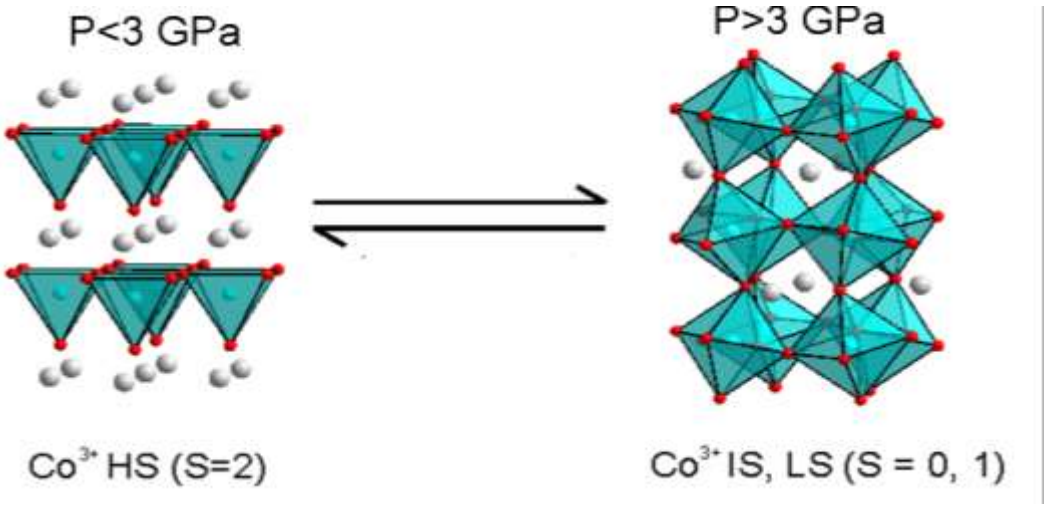

Figure 8.2 Co^{3+} spin-state transition of $BiCoO_3$ under applied pressure.

2. **Chemical pressure.** The Co^{3+} spin state in $LaCoO_3$ can be modulated by applied chemical pressure via the substitution of A-site cations with different sizes. For example, partial substitution of La^{3+} with Sm^{3+} leads to the formation of $La_{1-x}Sm_xCoO_3$. As the levels of substitution increase, the LS state becomes more stable and thus the LS - HS transition temperature shifts to higher temperatures due to the enhanced chemical pressure.[101] Similar behaviours can also be observed in Pr-doped $LaCoO_3$ samples.[102]

The change of spin state is an interesting physical phenomenon, especially when such transitions respond sensitively to external stimuli, suggesting that the change of external environment (e.g. temperature or pressure) can lead to a change in the magnetic behaviour of the materials. Thus the change of external environment can be detected by a magnetic signal, which makes the materials with these properties good candidates for sensing applications.

In this chapter, a series of anion-deficient $La_xSr_{2-x}CoGaO_{5+\delta}$ phases, which adopt brownmillerite structures, were synthesized. A change of Co^{3+} spin state was observed to occur when the x value in $La_xSr_{2-x}CoGaO_{5+\delta}$ increases. This is rationalized on the basis of the applied chemical pressure.

Composition	Synthesis Temperature (℃)
$La_{0.5}Sr_{1.5}CoGaO_{5.01}$	1100
$La_{0.6}Sr_{1.4}CoGaO_{5.02}$	1150
$La_{0.7}Sr_{1.3}CoGaO_{5.05}$	1175
$La_{0.8}Sr_{1.2}CoGaO_{5.09}$	1250
$La_{0.9}Sr_{1.1}CoGaO_{5.13}$	1275
$LaSrCoGaO_{5.18}$	1275

Table 8.1. Synthesis temperatures of $La_xSr_{2-x}CoGaO_{5+\delta}$.

8.2 Experimental

Samples in the compositional range $La_xSr_{2-x}CoGaO_{5+\delta}$ ($0 < x < 1$) were prepared via a standard ceramic synthesis route. Suitable stoichiometric ratios of La_2O_3 (99.999 %, dried at 900 ^oC), $SrCO_3$ (99.99 %), Ga_2O_3 (99.999 %) and Co_3O_4 (99.9985 %) were ground together in an agate pestle and mortar and then heated at 1000 ^oC in air for 12 h to decompose the carbonate. The resulting powders were then reground, pressed into 13 mm diameter pellets and heated for two periods of 40 h under 40 cm^3/min flowing argon at the temperatures as

listed in Table 8.1. In addition, a further set of samples of composition $La_{0.7}Sr_{1.3-y}Ca_yCoGaO_{5+\delta}$ ($0 < y < 0.2$) were prepared via the same method, with partial substitution of $CaCO_3$ (99.99 %) for $SrCO_3$.

8.3 Results

8.3.1 Characterization of $La_xSr_{2-x}CoGaO_{5+\delta}$ ($0 < x < 1$)

X-ray powder diffraction data were collected from $La_xSr_{2-x}CoGaO_{5+\delta}$ ($0 < x < 1$) samples in order to determine if single phases were synthesized. As shown in Figure 8.3 and 8.4, the majority of the diffraction peaks from the $La_xSr_{2-x}CoGaO_{5+\delta}$ ($0 < x < 1$) samples could be indexed using body-centred orthorhombic unit cells that have a $\sqrt{2}a_p \times 4a_p \times \sqrt{2}a_p$ geometric expansion relative to a simple cubic perovskite cell, suggesting brownmillerite-type structures are adopted.

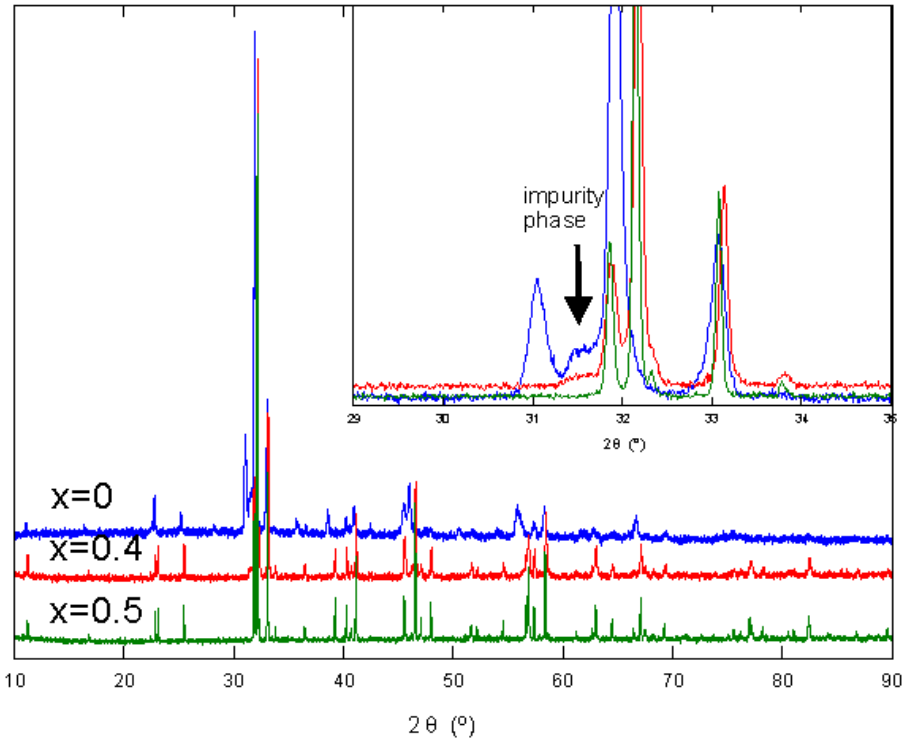

Figure 8.3 X-ray powder diffraction data collected from $La_xSr_{2-x}CoGaO_{5+\delta}$ (x = 0, 0.4, 0.5) samples.

However, in the X-ray diffraction data collected from $La_xSr_{2-x}CoGaO_{5+\delta}$ ($0 < x < 0.5$) samples some additional peaks can be observed (e.g. at 31.5°). Attempts to index all the diffraction features using expanded unit cells lead to a failure, suggesting that these additional diffraction features come from impurity phases. As shown in Figure 8.3, the increase in La/Sr ratio leads to a decline in the intensity of the peaks from impurities. When $x = 0.5$, the impurity phases disappear and a single brownmillerite phase is observed. Figure 8.4 shows the X-ray powder diffraction data collected from $La_xSr_{2-x}CoGaO_{5+\delta}$ ($0.5 < x < 1$) samples. These data indicated that samples are single phases without any observed impurity.

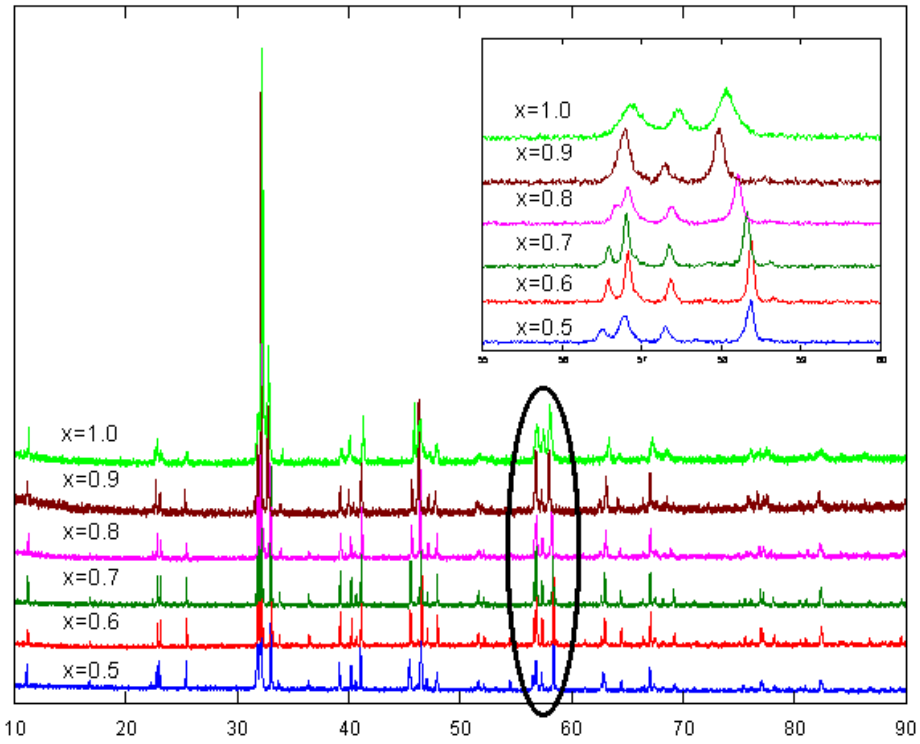

Figure 8.4 X-ray powder diffraction data collected from $La_xSr_{2-x}CoGaO_{5+\delta}$ ($0.5 < x < 1$) samples.

As can be seen in Figure 8.4, the diffraction features of $La_xSr_{2-x}CoGaO_{5+\delta}$ ($x = 0.9$ and 1.0) samples in the X-ray powder diffraction data are much broader than that of other $La_xSr_{2-x}CoGaO_{5+\delta}$ ($x = 0.5$, 0.6 and 0.7) samples, especially for the peaks at high angle. Given that all the samples were ground under the similar conditions, the influence of sample particle

sizes on the peak shape of the X-ray diffraction features should be slight. Thus the difference in the shape of diffraction peaks could be led by the changes in structure and/or composition. As discussed in Chapter 7, the presence of additional oxide ions in the lattice could disrupt brownmillerite structures, which could lead to the broadening of peak shape of X-ray powder diffraction observed for x = 1.0 member. Thus the exact oxygen stoichiometry of all the $La_xSr_{2-x}CoGaO_{5+\delta}$ ($0.5 < x < 1$) samples was determined by iodometric titration. The compositions and average oxidation state of cobalt in each $La_xSr_{2-x}CoGaO_{5+\delta}$ phase are shown in Table 8.2. The average oxidation state of cobalt in $La_xSr_{2-x}CoGaO_{5+\delta}$ changes from +2.52 (x = 0.5) to +2.36 (x = 1.0). It can be clearly seen that additional oxide ions are present in all the $La_xSr_{2-x}CoGaO_{5+\delta}$ ($0.5 < x < 1$) samples compared to the 'perfect' $La_xSr_{2-x}CoGaO_{5.00}$ brownmillerite phases.

Composition	Co oxidation state
$La_{0.5}Sr_{1.5}CoGaO_{5.01}$	2.52(1)
$La_{0.6}Sr_{1.4}CoGaO_{5.02}$	2.44(1)
$La_{0.7}Sr_{1.3}CoGaO_{5.05}$	2.40(1)
$La_{0.8}Sr_{1.2}CoGaO_{5.09}$	2.38(1)
$La_{0.9}Sr_{1.1}CoGaO_{5.13}$	2.36(1)
$LaSrCoGaO_{5.18}$	2.36(1)

Table 8.2. Compositions of $La_xSr_{2-x}CoGaO_{5+\delta}$.

8.3.2 Structural refinements

In order to determine the structures adopted by $La_xSr_{2-x}CoGaO_{5+\delta}$ ($0.5 < x < 1.0$) samples, neutron powder diffraction data were collected from each sample at room temperature. Due to the limitation of neutron beam time, neutron powder diffraction data were collected from $La_xSr_{2-x}CoGaO_{5+\delta}$ (x = 0.5, 0.6, 0.7, 0.8 and 1.0) samples at different beam sources as listed in Table 8.3.

Neutron powder diffraction data collected from $La_xSr_{2-x}CoGaO_{5+\delta}$ (x = 0.5, 0.6, 0.7, 0.8 and 1.0) could be indexed using body-centred orthorhombic unit cells that have a $\sqrt{2}a_p \times 4a_p \times \sqrt{2}a_p$ geometric expansion relative to a simple cubic perovskite cells. Thus models based on two known body-centered brownmillerite structures were constructed in space groups of *I2mb* and *Imma* as shown in Figure 7.1 in Chapter 7.

Composition	Data
$La_{0.5}Sr_{1.5}CoGaO_{5.01}$	Polaris, UK
$La_{0.6}Sr_{1.4}CoGaO_{5.02}$	Polaris, UK
$La_{0.7}Sr_{1.3}CoGaO_{5.05}$	Gem, UK
$La_{0.8}Sr_{1.2}CoGaO_{5.09}$	Polaris, UK
$LaSrCoGaO_{5.18}$	D2b, France

Table 8.3 Beam sources of the neutron diffraction data collected from different samples.

$La_xSr_{2-x}CoGaO_{5+\delta}$ (x = 0.5, 0.6 and 0.7). The two structural models (*I2mb* and *Imma*) were refined against neutron powder diffraction data collected from $La_xSr_{2-x}CoGaO_{5+\delta}$ (x = 0.5, 0.6 and 0.7) samples. During each refinement the Co/Ga B-site distributions were allowed to vary within the constraint of the overall composition. The atomic positions of all atoms were refined along with anisotropic displacement factors. Table 8.4 lists fitting statistics for the refinement of the *Imma* and *I2mb* brownmillerite models against neutron powder diffraction data collected from $La_xSr_{2-x}CoGaO_{5+\delta}$ (x = 0.5, 0.6 and 0.7) phases. It can be clearly seen that refinements of the *I2mb* model give better statistical fitting than that of *Imma* model. The final refined values of the lattice parameters, atomic positions and selected bond valence sums of each sample are listed in Tables 8.5 - 8.10.

Sample	Space group	χ^2	*wRp (%)*	*Rp (%)*
$La_{0.5}Sr_{1.5}CoGaO_{5.01}$	***I2mb***	**2.261**	**1.41**	**2.25**
	Imma	17.31	3.91	4.73
$La_{0.6}Sr_{1.4}CoGaO_{5.02}$	***I2mb***	**2.917**	**1.46**	**2.18**
	Imma	22.96	4.12	4.75
$La_{0.7}Sr_{1.3}CoGaO_{5.05}$	***I2mb***	**3.474**	**2.64**	**2.22**
	Imma	11.12	4.74	3.67

Table 8.4. Fitting statistics for the refinement of the brownmillerite models against neutron powder diffraction data collected from $La_xSr_{2-x}CoGaO_{5+\delta}$ (x = 0.5, 0.6 and 0.7) at room temperature.

Atom	site	*x*	*y*	*z*	fraction	$U_{equiv}(Å^2)$
La/Sr(1)	*8c*	0.0167(7)	0.1085(2)	0.4946(4)	0.25/0.75	0.0070
Co/Ga(1)	*4a*	0.9999(4)	0	0	0.870(2)/0.130(2)	0.0122
Co/Ga(2)	*4b*	0.9298(11)	¼	0.9570(4)	0.130(2)/0.870(2)	0.0048
O(1)	*8c*	0.2523(19)	0.9930(3)	0.2455(4)	1	0.0100
O(2)	*8c*	0.0531(8)	0.1462(3)	0.0180(4)	1	0.0148
O(3)	*4b*	0.8700(15)	¼	0.6132(4)	1	0.0084
$La_{0.5}Sr_{1.5}CoGaO_5$ -space group *I2mb*. *a* = 5.4306(2) Å, *b* = 15.9579(7) Å, *c* =5.6336(2) Å, V= 488.22(6) $Å^3$ χ^2 = 2.261, wRp = 1.41 %, Rp = 2.25 %						

Table 8.5 Refined structure of $La_{0.5}Sr_{1.5}CoGaO_{5.01}$ at room temperature.

Atom	site	*x*	*y*	*z*	fraction	$U_{equiv}(Å^2)$
La/Sr(1)	*8c*	0.4946(4)	0.1082(1)	0.0170(1)	0.3/0.7	0.0067
Co/Ga(1)	*4a*	0.9999(4)	0	0	0.872(2)/0.128(2)	0.0112
Co/Ga(2)	*4b*	0.9575(1)	¼	0.9302(1)	0.128(2)/0.872(2)	0.0053
O(1)	*8c*	0.2455(2)	0.9927(1)	0.2519(2)	1	0.0099
O(2)	*8c*	0.0187(1)	0.1462(1)	0.0542(1)	1	0.0151
O(3)	*4b*	0.6127(1)	¼	0.8706(1)	1	0.0090
$La_{0.6}Sr_{1.4}CoGaO_5$ -space group *I2mb*. *a* = 5.4326(2) Å, *b* = 15.9667(7) Å, *c* = 5.6402(2) Å, V= 489.22(3) $Å^3$ χ^2 = 2.917, wRp = 1.46 %, Rp = 2.18 %						

Table 8.6 Refined structure of $La_{0.6}Sr_{1.4}CoGaO_{5.02}$ at room temperature.

Atom	site	*x*	*y*	*z*	fraction	U_{equiv}(Å^2)
La/Sr(1)	*8c*	0.4942(1)	0.1079(1)	0.0169(1)	0.35/0.65	0.0063
Co/Ga(1)	*4a*	0.9999(7)	0	0	0.844(3)/0.156(3)	0.0105
Co/Ga(2)	*4b*	0.9592(3)	¼	0.9311(2)	0.156(3)/0.844(3)	0.0073
O(1)	*8c*	0.2475(3)	0.9924(1)	0.2523(3)	1	0.0084
O(2)	*8c*	0.0194(3)	0.1455(1)	0.0545(1)	1	0.0153
O(3)	*4b*	0.6108(3)	¼	0.8719(2)	1	0.0105
$La_{0.7}Sr_{1.3}CoGaO_5$ -space group *I*2*mb*. *a* = 5.4445(9) Å, *b* = 15.9604(9) Å, *c* = 5.6411(8) Å, V= 490.19(30) Å^3 χ^2 = 3.474, wRp = 2.64 %, Rp = 2.22 %						

Table 8.7 Refined structure of $La_{0.7}Sr_{1.3}CoGaO_{5.05}$ at room temperature.

cation	anion	multiplicity	Bond (Å)	BVS
La/Sr (1)	O(1)	1	2.598(8)	La+2.49/Sr+2.15
	O(1)	1	2.588(8)	
	O(1)	1	2.644(7)	
	O(1)	1	2.636(7)	
	O(2)	1	3.268(6)	
	O(2)	1	2.665(3)	
	O(2)	1	2.913(3)	
	O(2)	1	2.500(6)	
	O(3)	1	2.489(4)	
Co/Ga(1)	O(1)	2	1.955(2)	Co+2.33/Ga+2.52
	O(1)	2	1.964(2)	
	O(2)	2	2.354(5)	
Co/Ga(2)	O(2)	2	1.826(2)	Co+2.60/Ga+2.82
	O(3)	1	1.890(1)	
	O(3)	1	1.897(1)	

Table 8.8 Selected bond lengths from the refined structure of $La_{0.5}Sr_{1.5}CoGaO_{5.01}$ at room temperature.

cation	anion	multiplicity	Bond (Å)	BVS
La/Sr (1)	O(1)	1	2.594(8)	La+2.49/Sr+2.15
	O(1)	1	2.587(8)	
	O(1)	1	2.643(12)	
	O(1)	1	2.637(8)	
	O(2)	1	3.280(6)	
	O(2)	1	2.663(3)	
	O(2)	1	2.919(3)	
	O(2)	1	2.493(4)	
	O(3)	1	2.497(6)	
Co/Ga(1)	O(1)	2	1.952(2)	Co+2.31/Ga+2.51
	O(1)	2	1.971(2)	
	O(2)	2	2.357(2)	
Co/Ga(2)	O(2)	2	1.829(2)	Co+2.58/Ga+2.80
	O(3)	1	1.895(1)	
	O(3)	1	1.903(1)	

Table 8.9 Selected bond lengths from the refined structure of $La_{0.6}Sr_{1.4}CoGaO_{5.02}$ at room temperature.

cation	anion	multiplicity	Bond (Å)	BVS
La/Sr (1)	O(1)	1	2.638(2)	La+2.50/Sr+2.16
	O(1)	1	2.661(2)	
	O(1)	1	2.494(4)	
	O(1)	1	2.583(2)	
	O(2)	1	2.645(1)	
	O(2)	1	2.492(3)	
	O(2)	1	2.588(2)	
	O(2)	1	3.281(3)	
	O(3)	1	2.930(2)	
Co/Ga(1)	O(1)	2	1.963(2)	Co+2.31/Ga+2.51
	O(1)	2	1.965(3)	
	O(2)	2	2.344(1)	
Co/Ga(2)	O(2)	2	1.837(4)	Co+2.51/Ga+2.72
	O(3)	1	1.926(1)	
	O(3)	1	1.899(1)	

Table 8.10 Selected bond lengths from the refined structure of $La_{0.7}Sr_{1.3}CoGaO_{5.05}$ at room temperature.

$La_{0.8}Sr_{1.2}CoGaO_{5.09}$. Refinement of the *I2mb* model against the neutron powder diffraction data collected from the x = 0.8 member at room temperature gives a large χ^2 value of 4.986 and a significant anisotropic displacement of Ga/Co cations localized in the tetrahedral sites, as shown in Figure 8.5, suggesting that the cations and anions in the chains of tetrahedra within $La_{0.8}Sr_{1.2}CoGaO_{5.09}$ adopt a disordered arrangement.

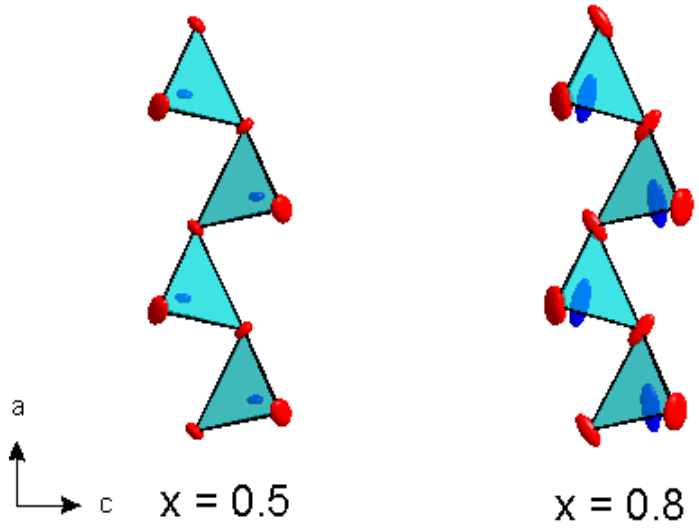

Figure 8.5 Refined tetrahedral chains of $La_{1.5}Sr_{1.5}CoGaO_{5.01}$ (left) and $La_{0.8}Sr_{1.2}CoGaO_{5.09}$ (right) in *I2mb* model with anisotropic thermal ellipsoids.

Space group	χ^2	*wRp (%)*	*Rp (%)*
I2mb	4.986	2.19	2.97
Imma	**3.294**	**1.78**	**2.48**

Table 8.11 Fitting statistics for the refinement of the brownmillerite models against neutron powder diffraction data collected from $La_{0.8}Sr_{1.2}CoGaO_{5.09}$ at room temperature.

Refinement of an *Imma* model with disordered chains of tetrahedra gives a better statistical fitting (χ^2 = 3.294) than that of *I2mb* model as shown in Table 8.11, confirming this view. The lattice parameters, atomic positions and selected bond valence sums of $La_{0.8}Sr_{1.2}CoGaO_{5.09}$ are listed in Table 8.12 and 8.13. As shown in Table 8.12, the refinements exhibit a clear preference for locating Co cations in the octahedral sites and Ga cations in the tetrahedral sites of the lattice. It should be noted that iodometric titrations

indicate that the phase has excess oxygen content. Given the modest level of oxygen excess in $La_{0.8}Sr_{1.2}CoGaO_{5.09}$ from which neutron diffraction data were collected, it was not possible to locate the additional oxide ions within the structural model, however it is assumed that the additional oxide ions fill some of the anion vacancies adjacent to the BO_4 tetrahedral cation sites.

atom	site	*x*	*y*	*z*	fraction	$U_{equiv}(Å^2)$
La/Sr(1)	*8h*	½	0.1081(1)	0.0169(1)	0.4/0.6	0.0074
Co/Ga(1)	*4a*	0	0	0	0.814(2)/0.186(2)	0.0136
Co/Ga(2)	*8i*	0.9596(1)	¼	0.9315(1)	0.093(1)/0.407(1)	0.0071
O(1)	*8g*	¼	0.9923(1)	¼	1	0.0095
O(2)	*8h*	0	0.1449(1)	0.0550(1)	1	0.0233
O(3)	*8i*	0.6151(1)	¼	0.8716(2)	0.5	0.0131
$La_{0.8}Sr_{1.2}CoGaO_5$ -space group *Imma*. *a* = 5.4606(3) Å, *b* = 15.9329(11) Å, *c* = 5.6468(4) Å, V= 491.29(10) $Å^3$ χ^2 = 3.294, wRp = 1.78 %, Rp = 2.48 %						

Table 8.12 Refined structure of $La_{0.8}Sr_{1.2}CoGaO_{5.09}$ at room temperature.

cation	anion	multiplicity	Bond (Å)	BVS
La/Sr(1)	O(1)	2	2.587(5)	La+2.90/Sr+2.51
	O(1)	2	2.646(6)	
	O(2)	1	3.282(8)	
	O(2)	2	2.801(1)	
	O(2)	1	2.487(8)	
	O(3)	2	2.486(6)	
Co/Ga(1)	O(1)	4	1.968(1)	Co+2.30/Ga+2.50
	O(2)	2	2.329(2)	
Co/Ga(2)	O(2)	2	1.827(1)	Co+2.55/Ga+2.77
	O(3)	2	1.911(1)	

Table 8.13 Selected bond lengths from the refined structure of $La_{0.8}Sr_{1.2}CoGaO_{5.09}$ at room temperature.

$LaSrCoGaO_{5.18}$. Refinements of two brownmillerite structural models (*I2mb* and *Imma*) against neutron diffraction data collected from $LaSrCoGaO_{5.18}$ give bad visual fits. Close inspection of the neutron powder diffraction data collected from $LaSrCoGaO_{5.18}$ indicated some peaks are much broader than the others. The peak shapes of the diffraction features with $l \neq 0$ are broader than those with $l = 0$. Thus a (0, 0, 1) anisotropic broadening axis was incorporated into both *I2mb* and *Imma* models as described in Chapter 2. The additional oxide ions were inserted to the vacant positions of the lattice, converting 4-coordinate tetrahedral sites to 5-coordinate pyramidal sites and even 6-coordinate octahedral sites. As shown in Figure 8.6, the extra oxide ions were added at the anion sites (0.25, ¼, 0.25).

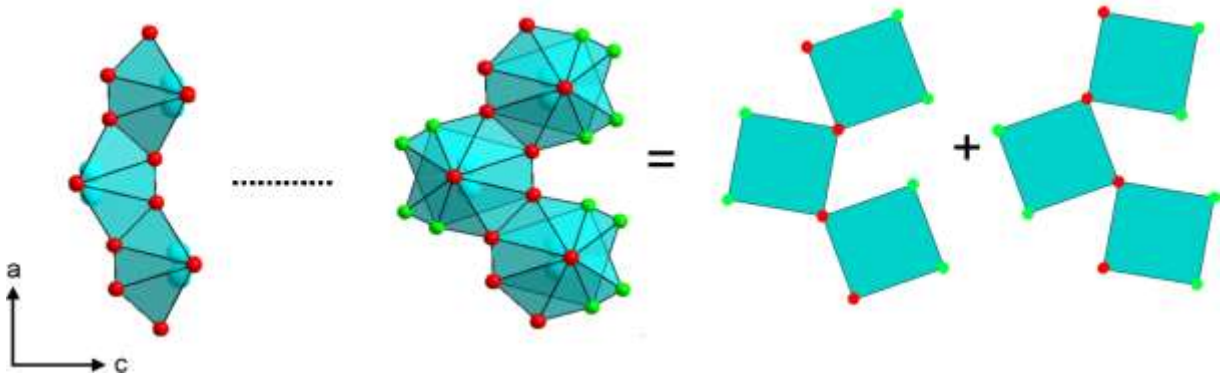

Figure 8.6. The positions of additional oxide ions in the lattice of $LaSrCoGaO_{5.18}$. Green spheres indicated the positions of additional oxides compared to the perfect $A_2B_2O_5$ brownmillerite.

Space group	χ^2	*wRp (%)*	*Rp (%)*
I2mb	5.632	6.86	5.78
Imma	**4.893**	**5.38**	**5.12**

Table 8.14 Fitting statistics for the refinement of the brownmillerite models against neutron powder diffraction data collected from $La_{1.0}Sr_{1.0}CoGaO_{5.18}$ at room temperature.

Refinements of the two modified models (*I2mb* and *Imma*) converged readily, to give χ^2 = 4.893 for *Imma* model and χ^2 = 5.632 for *I2mb* model. Thus $LaSrCoGaO_{5.18}$ is considered to adopt an *Imma* type brownmillerite structure. Figure 8.7 shows the observed, calculated and difference plots from the refinement of $LaSrCoGaO_{5.18}$ against powder neutron diffraction

data at room temperature. Refinement of the fractional occupancies of the additional oxide sites gives a value of 0.09(1), consistent with the result of iodometric titration. The lattice parameters, atomic positions and selected bond valence sums of $LaSrCoGaO_{5.18}$ are listed in Table 8.15 and 8.16.

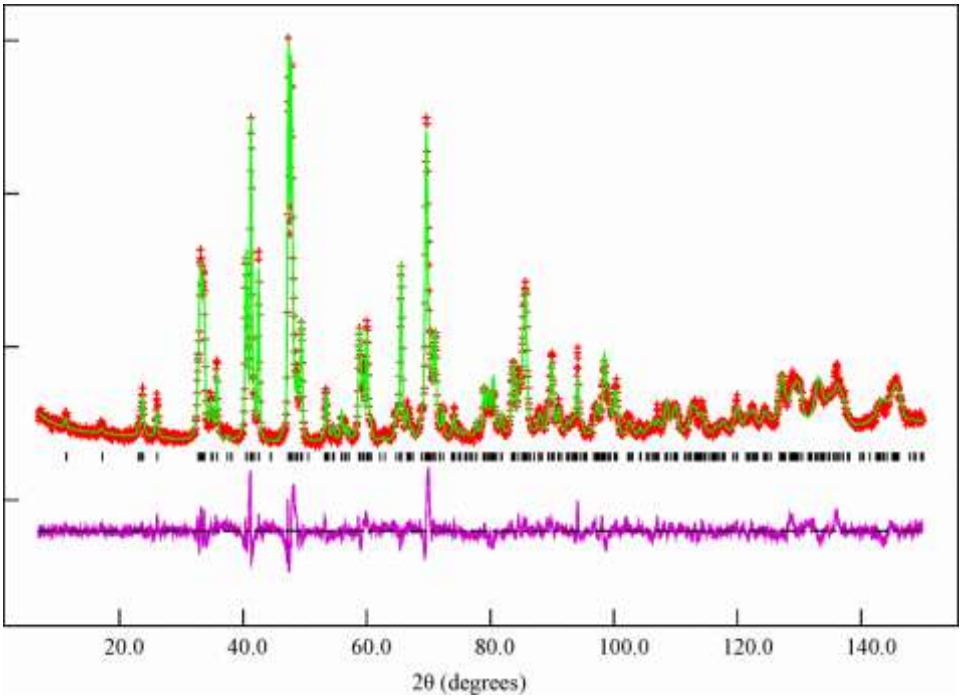

Figure 8.7 Observed, calculated and difference plots from the refinement of $LaSrCoGaO_{5.18}$ against powder neutron diffraction data at room temperature.

Atom	site	*x*	*y*	*z*	fraction	U_{iso} (Å^2)
La/Sr(1)	*8h*	½	0.1101(1)	0.0133(8)	0.5/0.5	0.0124
Co/Ga(1)	*4a*	0	0	0	0.795(13)/0.205(13)	0.0235
Co/Ga(2)	*8i*	0.9781(28)	¼	0.9308(10)	0.102(7)/0.398(7)	0.0149
O(1)	*8g*	¼	0.9929(2)	¼	1	0.0164
O(2)	*8h*	0	0.1430(2)	0.0605(8)	1	0.0270
O(3)	*8i*	0.6286(14)	¼	0.8676(16)	0.5	0.0251
O(4)	*8i*	0.2016(89)	¼	0.3352(87)	0.090(12)	0.0251
$LaSrCoGaO_{5.18}$ -space group *Imma*. *a* = 5.4786(5) Å, *b* = 15.8574(16) Å, *c* = 5.6316(5) Å, V= 489.26(13) Å^3 χ^2 = 4.893, wRp = 5.38 %, Rp = 5.12 %						

Table 8.15 Refined structure of $LaSrCoGaO_{5.18}$ at room temperature.

cation	anion	multiplicity	Bond (Å)	BVS
La/Sr(1)	O(1)	2	2.587(5)	La+2.90/Sr+2.51
	O(1)	2	2.646(6)	
	O(2)	1	3.282(8)	
	O(2)	2	2.801(1)	
	O(2)	1	2.487(8)	
	O(3)	2	2.486(6)	
Co/Ga(1)	O(1)	4	1.967(1)	Co+2.35/Ga+2.54
	O(2)	2	2.293(3)	
Co/Ga(2)	O(2)	2	1.851(4)	Co+1.92/Ga+2.08
	O(3)	2	2.184(17)	
	O(4)	1	2.195(50)	

Table 8.16 Selected bond lengths from the refined structure of $LaSrCoGaO_{5.18}$ at room temperature.

8.3.3 Magnetization

Zero-field-cooled and field-cooled magnetization data were collected from $La_xSr_{2-x}CoGaO_{5+\delta}$ ($0.5 < x < 1.0$) phases in an applied field of 100 Oe in the temperature range $5 < T/K < 300$. Figure 8.8 shows the zero-field-cooled and field-cooled magnetization data collected from $La_{0.5}Sr_{1.5}CoGaO_{5.01}$ which are typical of all the $La_xSr_{2-x}CoGaO_{5+\delta}$ ($0.5 < x < 1.0$) samples. The data can be fitted to the Curie-Weiss law in the temperature range 100 to 300 K, to yield values of $C = 2.227(1)$ cm^3 K mol^{-1}; $\theta = 52.6(1)$ K. Below ~ 60 K the zero-field-cooled and field-cooled data diverge. The field-cooled magnetization-field isotherm collected from $La_{0.5}Sr_{1.5}CoGaO_{5.01}$ at 5 K exhibits hysteresis and is displaced from the centre, as shown in Figure 8.9.

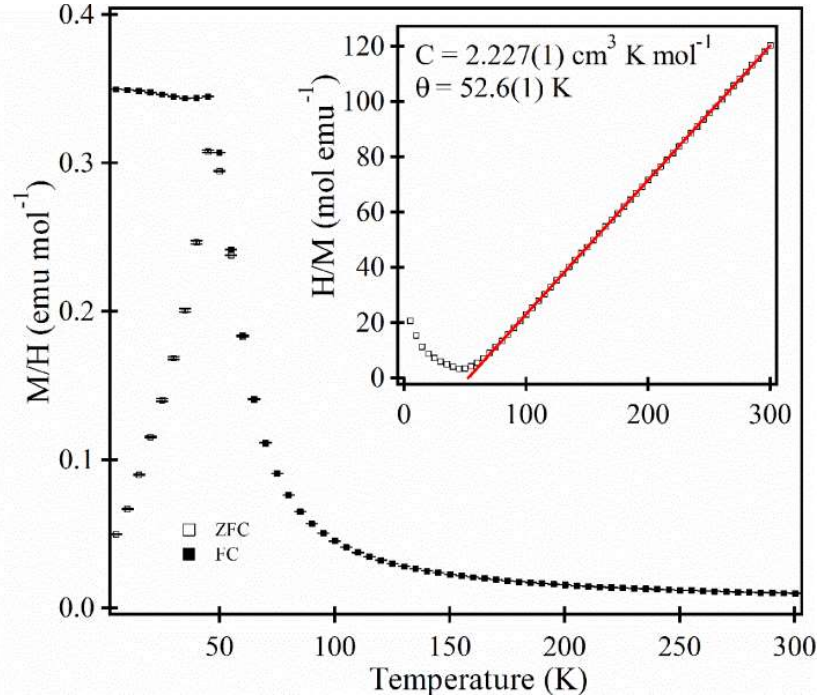

Figure 8.8 Zero-field-cooled and field-cooled magnetization data collected from $La_{0.5}Sr_{1.5}CoGaO_{5.01}$ (top). Inset shows fit to the Curie-Weiss law.

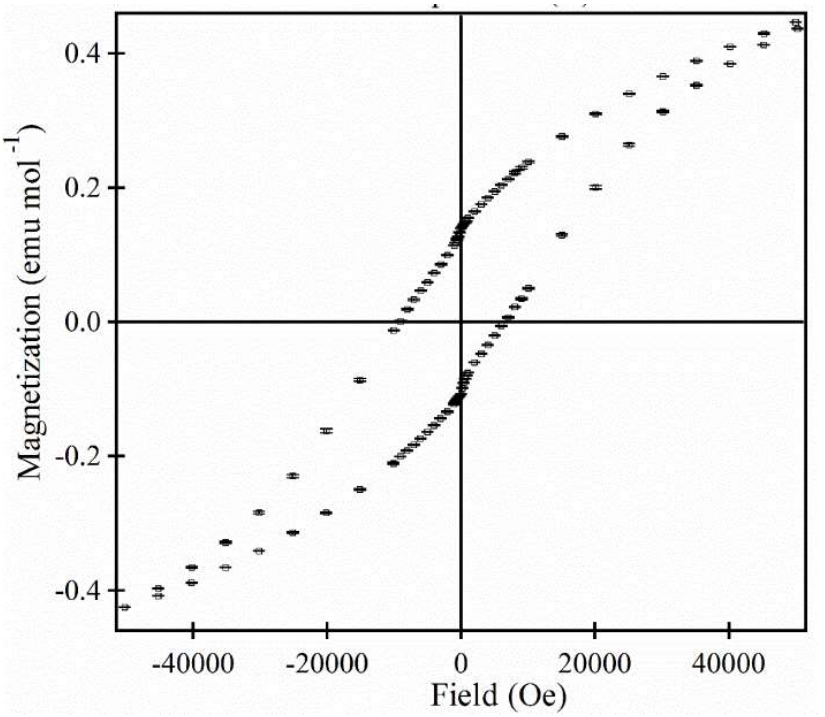

Figure 8.9 Magnetization-field isotherm collected at 5 K from $La_{0.5}Sr_{1.5}CoGaO_{5.01}$.

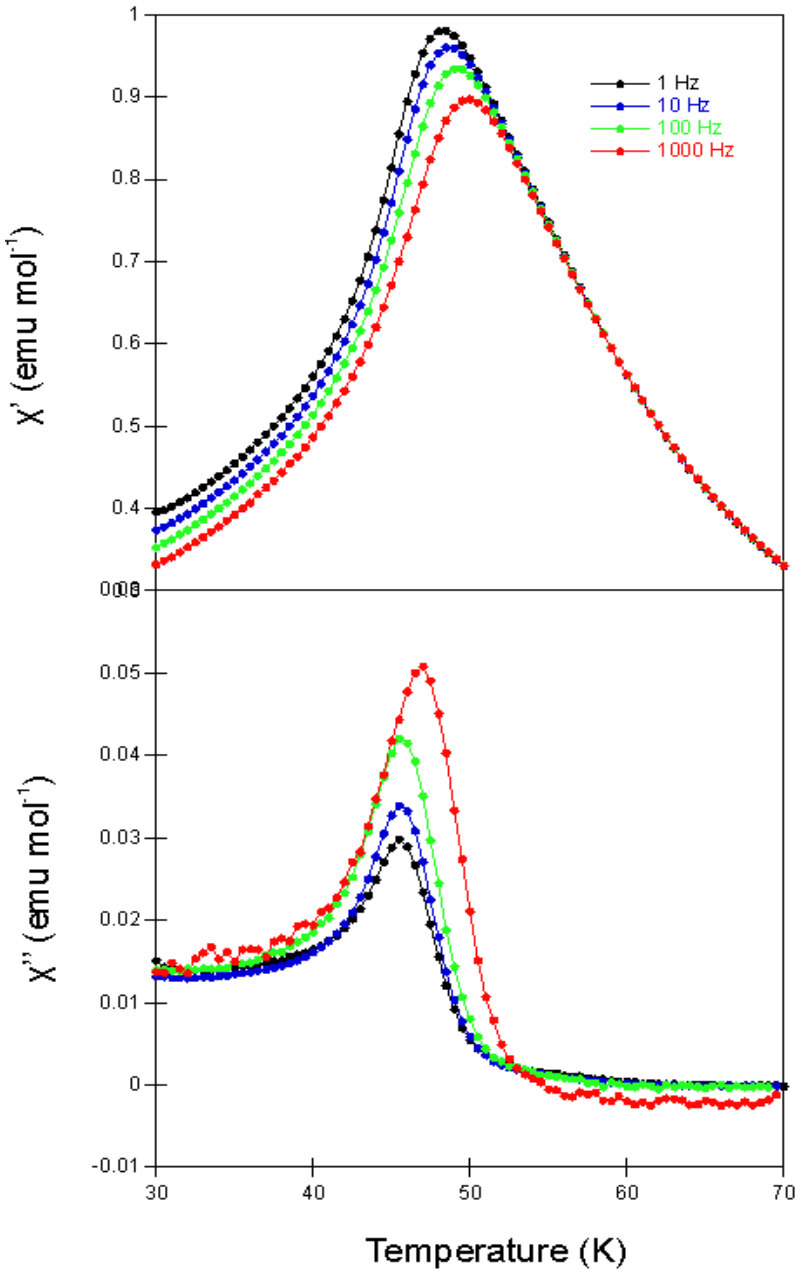

Figure 8.10 Real part and imaginary part of the AC susceptibility as a function of temperature (30 < T/K < 70) at frequencies of 1, 10, 100 and 1000 Hz for $La_{0.5}Sr_{1.5}CoGaO_{5.01}$.

AC susceptibility data collected from $La_{0.5}Sr_{1.5}CoGaO_{5.01}$ in the temperature range of 30 < T/K < 70 at frequencies of 1, 10, 100 and 1000 Hz (Figure 8.10) exhibit a frequency dependence, indicating spin-glass behaviour. Neutron powder diffraction data collected from $La_{0.5}Sr_{1.5}CoGaO_{5.01}$ at 5 K do not exhibit additional diffraction features, consistent with the spin-glass behaviour observed in AC susceptibility measurements.

All the $La_xSr_{2-x}CoGaO_{5+\delta}$ ($0.5 < x < 1.0$) samples exhibit similar magnetic behaviour to the $x = 0.5$ member, as shown in Figure A8.7 - A8.14 in the appendix. Zero-field-cooled and field-cooled data obey the Curie-Weiss law in the temperature range $100 < T/K < 300$ and the low temperature magnetization-field isotherms indicate spin-glass behaviours (Figure A8.8 - A8.12).

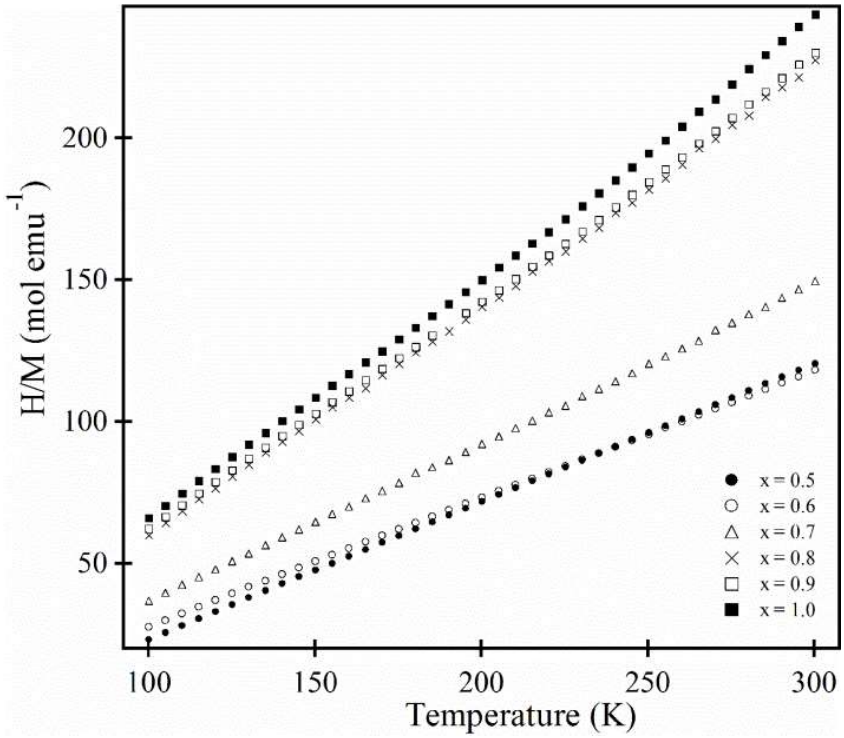

Figure 8.11 Plots of H/M against temperature for the $La_xSr_{2-x}CoGaO_{5+\delta}$ phases in the paramagnetic regime, illustrating the dramatic change in Curie constant with composition.

Composition	C (cm^3 K mol^{-1})	θ (K)
$La_{0.5}Sr_{1.5}CoGaO_{5.01}$	2.227(1)	52.6(1)
$La_{0.6}Sr_{1.4}CoGaO_{5.02}$	2.212(3)	38.9(2)
$La_{0.7}Sr_{1.3}CoGaO_{5.05}$	1.792(7)	34.7(3)
$La_{0.8}Sr_{1.2}CoGaO_{5.09}$	1.216(6)	28.3(8)
$La_{0.9}Sr_{1.1}CoGaO_{5.13}$	1.210(5)	26.0(8)
$LaSrCoGaO_{5.18}$	1.149(5)	25.5(8)

Table 8.17 Curie constants and Weiss temperatures of the $La_xSr_{2-x}CoGaO_{5+\delta}$ phases.

Figure 8.11 shows the plots of H/M against temperature for all the $La_xSr_{2-x}CoGaO_{5+\delta}$ ($0.5 < x < 1.0$) samples in the temperature range $100 < T/K < 300$. Table 8.17 lists the Curie constants and Weiss constants of $La_xSr_{2-x}CoGaO_{5+\delta}$ ($0.5 < x < 1.0$) samples. It can be clearly seen that the Curie constant changes from 2.227 (x = 0.5) to 1.210 (x = 1.0) cm^3 K mol^{-1} across the $La_xSr_{2-x}CoGaO_{5+\delta}$ series. Iodometric titrations indicated that the $La_xSr_{2-x}CoGaO_{5+\delta}$ phases have mixed valance of Co^{2+}/Co^{3+}, with an average oxidation state of cobalt which changes from +2.52 (x = 0.5) to 2.36 (x = 1.0). Despite this small change in average oxidation state of cobalt, there is a dramatic change in Curie constant across the series. This change in Curie constants cannot be explained by a simple replacement of HS Co^{3+} (S = 2) with HS Co^{2+} (S = 3/2) but can be understood by a change of Co^{3+} spin state from high-spin (HS) state to low-spin state (LS).

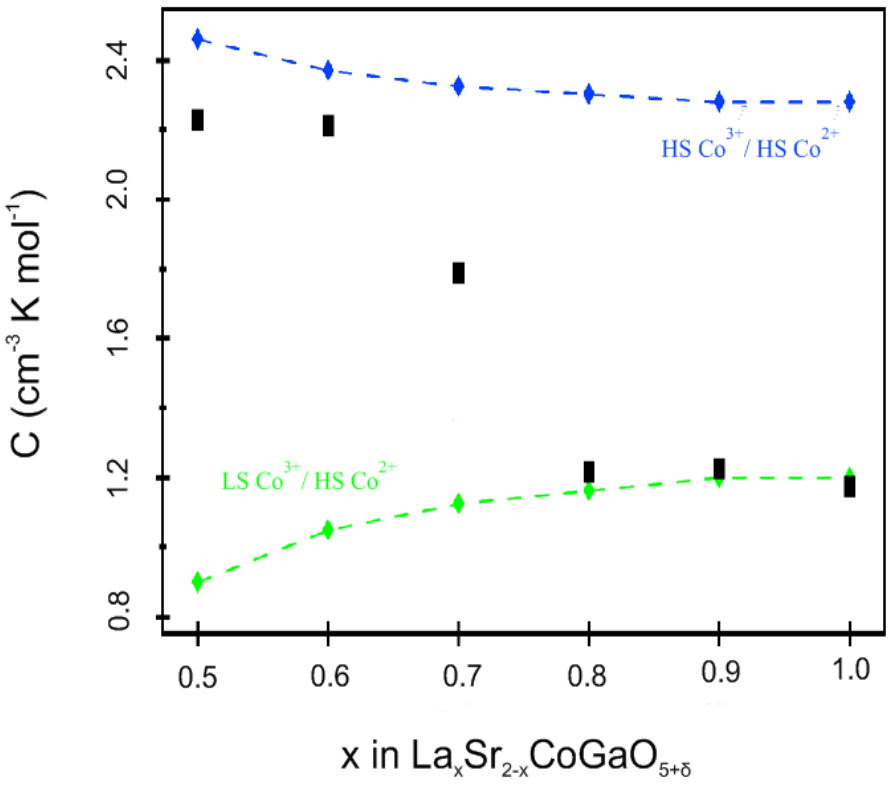

Figure 8.12 Curie constant as a function of La/Sr ratio in $La_xSr_{2-x}CoGaO_{5+\delta}$. Black squares correspond to 'as-made' samples. The blue line indicates the expected Curie-constant of 'as-made' samples for a HS Co^{3+}/ HS Co^{2+}, the green line LS Co^{3+}/ HS Co^{2+}.

As shown in Figure 8.12, the Curie constants of the x = 0.5 and 0.6 members are about 2.22 cm^3 K mol^{-1}, approximately equal to the value expected from a combination of HS Co^{3+} (S = 2) and HS Co^{2+} (S = 3/2) in a ratio determined by average oxidation state of cobalt (the blue dotted line in Figure 8.12). In contrast, the Curie constants extracted from x = 0.8 - 1.0 members are about 1.2 cm^3 K mol^{-1}, approximately equal to the value expected from a combination of LS Co^{3+} (S = 0) and HS Co^{2+} (S = 3/2) (the green dotted line in Figure 8.12). These values are therefore consistent with a change of Co^{3+} spin state accompanying the change in the La/Sr ratio across the $La_xSr_{2-x}CoGaO_{5+\delta}$ series.

8.3.4 Conductivity

Conductivity measurements were carried out on the as–prepared $La_xSr_{2-x}CoGaO_{5+\delta}$ sample bars. Figure 8.13 shows the conductivity of $La_{0.5}Sr_{1.5}GaCoO_{5.01}$ in the temperature range 230 < T/K < 300, which is typical of all the $La_xSr_{2-x}CoGaO_{5+\delta}$ samples.

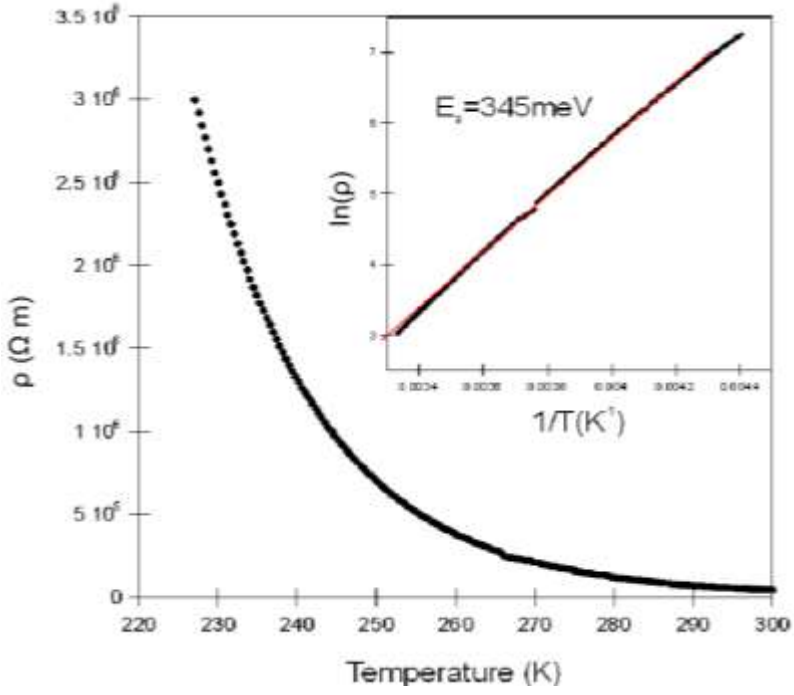

Figure 8.13 Temperature dependence of the electrical resistance of $La_{0.5}Sr_{1.5}GaCoO_{5.01}$ samples. Insets show logarithmic plots with the fit to the Arrhenius law.

The plots of *ln ρ* vs *1/T* in the measured temperature ranges follow the Arrhenius law with the fitting activation energy of 345 meV for $La_{0.5}Sr_{1.5}GaCoO_{5.01}$, indicating semiconducting behaviour. Conductivity measurements performed on other members of $La_xSr_{2-x}CoGaO_{5+\delta}$ samples indicate all the samples are semiconducting. The band gaps of $La_xSr_{2-x}CoGaO_{5+\delta}$ phases are in the range 0.3 - 0.4 eV. The conductivity behaviours of other members are shown in the Figure A8.15 and A8.16.

8.4 Discussion

The $La_xSr_{2-x}CoGaO_{5+\delta}$ series is an unusual example of a set of brownmillerite phases with an aliovalent La^{3+}/Sr^{2+} solid solution on the 10-coordinate A-cation site of the material, which allows the phases to exhibit a changeable average cobalt oxidation state. In addition, the $La_xSr_{2-x}CoGaO_{5+\delta}$ phases adopt nonstoichiometric compositions compared with the 'perfect' $A_2B_2O_5$ brownmillerite phase and exhibit a composition-related Co^{3+} spin state. As discussed below, these unusual properties can be rationalized on the basis of the chemical pressure from lattice strain.

8.4.1 Non-stoichiometric brownmillerite structure of $La_xSr_{2-x}CoGaO_{5+\delta}$

The $La_xSr_{2-x}CoGaO_{5+\delta}$ series has variable oxygen content and average cobalt oxidation state. Figure 8.14 shows that as the La/Sr ratio increases the cobalt oxidation state decreases from $Co^{+2.52}$ ($x = 0.5$) to $Co^{+2.36}$ ($x = 1.0$). However unlike the $La_xA_{2-x}Mn_2O_5$ (A = Ba^{2+}, Sr^{2+} and Ca^{2+}) brownmillerite series reported previously[27], which rigorously retains an $A_2B_2O_5$ stoichiometry and thus has a smoothly varying manganese oxidation state as a function of La:A ratio (red dotted line in Figure 8.14), the $La_xSr_{2-x}CoGaO_{5+\delta}$ series has a variable oxygen content which moderates the effect of the A-site composition on the cobalt oxidation state of phases. When x in $La_xSr_{2-x}CoGaO_{5+\delta}$ changes from 0.5 to 0.7 the average oxidation

state of cobalt drops from +2.52 to +2.40. However, for $x > 0.8$, the oxidation state of cobalt remains approximately a constant due to the incorporation of additional oxygen.

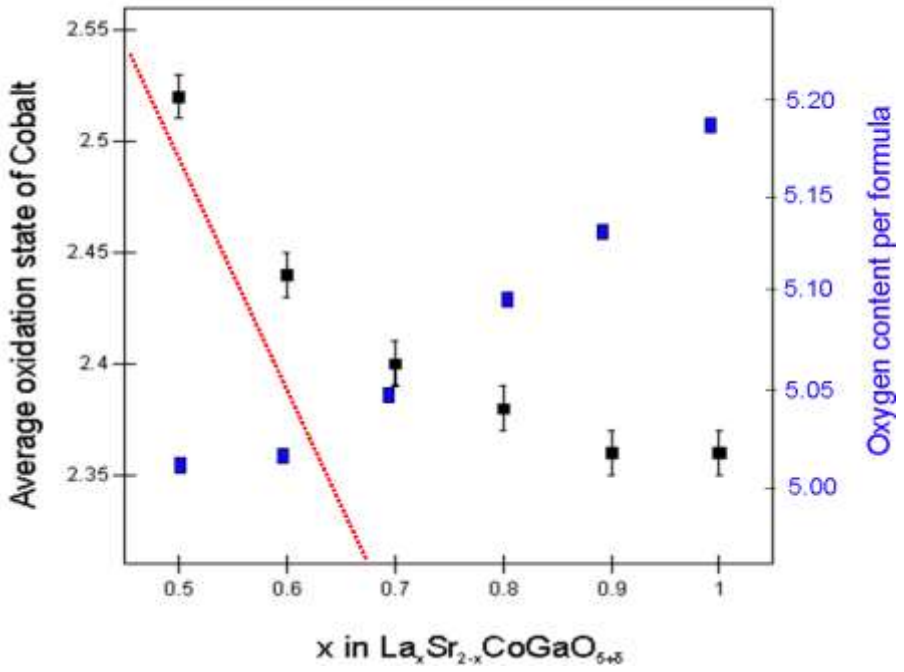

Figure 8.14 The oxidation state of cobalt as the compositions of $La_xSr_{2-x}CoGaO_{5+\delta}$ ($0.5 < x < 1.0$).

As mentioned in the Chapter 1, size mismatches between cations in perovskite structures can cause an internal strain to build up within phases, which is quantified as a tolerance factor. Cooperative tilting and twisting of octahedra can release internal strain and structural distortions such as tilting and twisting are commonly observed in perovskite structures. In the $A_2B_2O_5$ brownmillerite structure, size mismatches occur not only between A- and B- site cations but also between different B-site cations. For example, in the $La_xSr_{2-x}CoGaO_{5+\delta}$ series lattice strain can arise not only from the size difference between La^{3+}/Sr^{2+} cations in the A sites and $Co^{2+}/Co^{3+}/Ga^{3+}$ cations in the B sites, but also from the size difference between Co^{2+}/Co^{3+} and Ga^{3+} cations.

The internal strain in brownmillerite structures could in principle be released by cooperative tilting of octahedra. However the cooperative twisting of octahedra is not

observed in any of the five variants of brownmillerite structure (*I2mb, Pnma, Icmm, Pcmb* and *C2/c*). It is speculated that the different directions of internal strain field between octahedral and tetrahedral layers limits the cooperative twisting of octahedra in brownmillerite phases.[27] In the structure of $La_{0.5}Sr_{1.5}CoGaO_{5.01}$, the majority of cobalt cations are in the octahedral sites and majority of gallium cations are in the tetrahedral sites. The tetrahedral 'GaO_4' layers remain almost unchanged across the $La_xSr_{2-x}CoGaO_{5+\delta}$ series. In contrast, when the Co^{2+}/Co^{3+} ratio increases across the $La_xSr_{2-x}CoGaO_{5+\delta}$ series, an internal strain is built up in the 'CoO_6' octahedral layers due to the change of average cation size in the octahedral sites as the concentration of large Co^{2+} centres increases (HS Co^{2+} CN6 = 0.745 Å, HS Co^{3+} CN6 = 0.61 Å). The rigidity of the brownmillierite structure prevents the twisting of octahedra relieving this internal strain. Instead, additional oxygen is incorporated into the lattices, restricting to build-up of Co^{2+}. The formation of non-stoichiometric composition of $La_xSr_{2-x}CoGaO_{5+\delta}$ and presence of additional oxides in the lattice could be considered as a way to relieve the lattice strain. The internal lattice strain in the structure of $La_xSr_{2-x}CoGaO_{5+\delta}$ prevents the formation of the 'perfect' stoichometric $La_xSr_{2-x}CoGaO_{5.00}$ which has a large concentration of large Co^{2+} cations. The presence of additional oxide ions in the lattice controls the ratio of Co^{2+}/Co^{3+} cations, maintaining the lattice strain in an 'appropriate' range, which could explain the unusual stoichiometry of $La_xSr_{2-x}CoGaO_{5+\delta}$.

8.4.2 Magnetism-lattice coupling

Magnetization data indicate that the Co^{3+} spin state in $La_xSr_{2-x}CoGaO_{5+\delta}$ changes from HS (x = 0.5 and 0.6) to LS (x = 0.8, 0.9 and 1.0). As discussed above, the internal strain built up in lattice arises across the $La_xSr_{2-x}CoGaO_{5+\delta}$ series when the ratio of Co^{2+}/Co^{3+} increases.

Given the size difference between large HS, S = 2 Co^{3+} centres (HS Co^{3+} CN6 = 0.61 Å) and smaller LS, S = 0 Co^{3+} centres (LS Co^{3+} CN6 = 0.545 Å), the change of Co^{3+} spin state with increasing x across the $La_xSr_{2-x}CoGaO_{5+\delta}$ series can also be rationalized on the basis of relieving the internal strain. Apart from 'capturing' the oxide ions in the lattice, the change of Co^{3+} spin state can be considered as an alternative or additional mechanism to relieve the lattice strain arising from an increasing ratio of Co^{2+}/Co^{3+}. It should be noted that the cobalt centres are under compression from the surrounding lattice which would increase the splitting gap Δ between e_g and t_{2g} orbitals of the octahedral cobalt centres, further confirming that the internal strain is present in the lattice. Thus it would be proposed that the change of Co^{3+} spin state can be rationalized on the basis of internal chemical pressure arising from lattice strain.

8.4.3 Composition-magnetism coupling

Previous studies indicated that chemical pressure can induce a change in Co^{3+} spin state. In the $La_xSr_{2-x}CoGaO_{5+\delta}$ series, chemical pressure can be applied via the A-cation sites or the B-cation sites. Based on the compositions of $La_xSr_{2-x}CoGaO_{5+\delta}$, two parameters vary across the series: a) the ratio of La/Sr cations in the A sites; b) the ratio of Co^{3+}/Co^{2+} cations in the B sites. In order to determine which parameter induces the change of Co^{3+} spin state in $La_xSr_{2-x}CoGaO_{5+\delta}$, two sets of experiments were designed.

1. Effect of A-site substitution. Partial substitution of Sr^{2+} with smaller La^{3+} cations in $La_xSr_{2-x}CoGaO_{5+\delta}$ leads to the change of Co^{3+} spin state from HS (x = 0.5 and 0.6 member) to LS (x = 0.8 - 1.0 members). Thus the effect of the average cation size on the A sites of $La_xSr_{2-x}CoGaO_{5+\delta}$ is considered. Calcium-doped samples $La_{0.7}Sr_{1.3-y}Ca_yCoGaO_{5+\delta}$ ($0 < y < 0.2$) were prepared because the size of Ca^{2+} (CN10 = 1.23 Å) is similar to that of La^{3+}

(CN10 = 1.27 Å). If the average size of A-site cations influences the Co^{3+} spin state in $La_xSr_{2-x}CoGaO_{5+\delta}$, a change of Curie constants would be expected upon calcium substitution.

$La_{0.7}Sr_{1.3-y}Ca_yCoGaO_{5+\delta}$ ($0 < y < 0.2$) samples were synthesized under the same conditions as that of $La_{0.7}Sr_{1.3}CoGaO_{5.05}$ sample (1175 ^oC). Figure 8.15 shows the X-ray diffraction patterns collected from the $La_{0.7}Sr_{1.3-y}Ca_yCoGaO_{5+\delta}$ ($0 < y < 0.2$) samples. It can be seen that the samples with low levels of calcium doping ($0 < y < 0.15$) form single brownmillerite phases and the sample with higher level of calcium doping ($y > 0.2$) form mixtures with $Ca_2Co_{2-x}Ga_xO_{5+\delta}$ as an impurity.

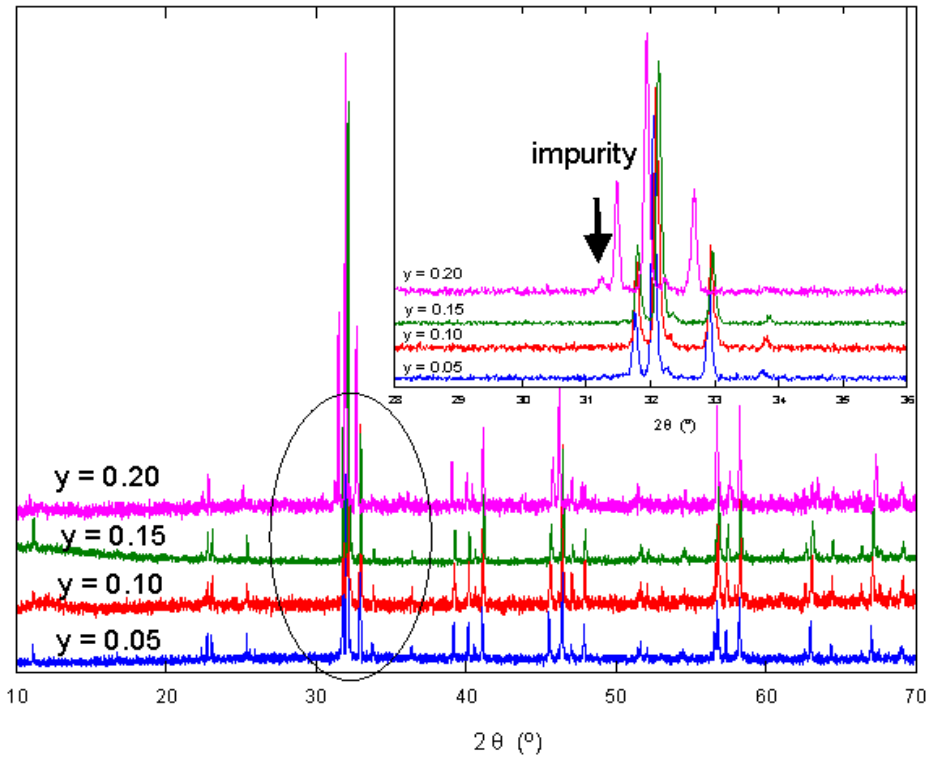

Figure 8.15 X-ray powder diffraction data of $La_{0.7}Sr_{1.3-y}Ca_yCoGaO_{5+\delta}$ ($0 < y < 0.2$).

As shown in Figure 8.16 the Curie constant of the calcium-doped sample $La_{0.7}Sr_{1.15}Ca_{0.15}CoGaO_{5.06}$ (C = 1.823(3) cm^3 K mol^{-1}) is almost identical to the undoped $La_{0.7}Sr_{1.3}CoGaO_{5.05}$ (C = 1.792(7) cm^3 K mol^{-1}), indicating partial substitution of Ca^{2+} on

the A site of $La_{0.7}Sr_{1.3}CoGaO_{5.05}$ has little influence on the Curie constant and Co^{3+} spin state.

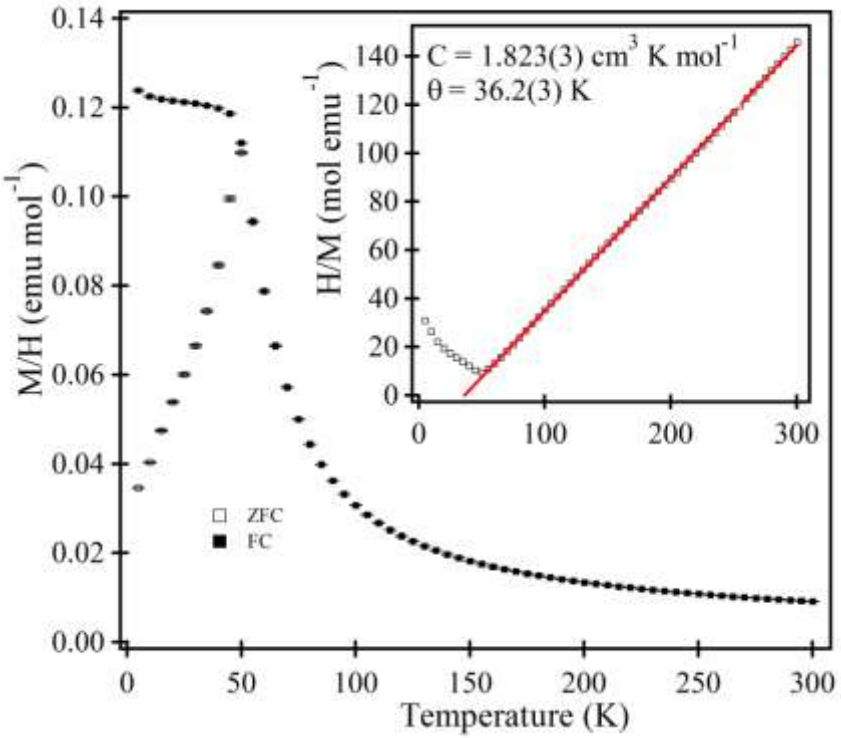

Figure 8.16 Zero-field-cooled and field-cooled magnetisation data collected from $La_{0.7}Sr_{1.15}Ca_{0.15}CoGaO_{5.06}$ as a function of temperature. Inset shows fit to the Curie-Weiss law.

2. Effect of Co^{2+}/Co^{3+} ratio. Experiments were also designed to confirm the influence of the Co^{2+}/Co^{3+} ratio on the Co^{3+} spin state. $La_{0.7}Sr_{1.3}CoGaO_{5.05}$ was 'reduced' by heating at 1275 ^{o}C under flowing argon for 40 h to form $La_{0.7}Sr_{1.3}CoGaO_{5.02}$, confirmed by iodometric titrations. $La_{0.8}Sr_{1.2}CoGaO_{5.09}$ was 'oxidized' by heating the sample at 1000 ^{o}C under flowing argon for 40 h to form $La_{0.8}Sr_{1.2}CoGaO_{5.16}$. Figure 8.17 shows the change in average oxidation state of cobalt in the redox processes described above.

It should be noted that the commercial argon used in this study contains ~ 2 ppm O_2. By adjusting the annealing temperature, samples can be reduced or oxidized slightly, yielding a change in Co^{3+}/Co^{2+} ratio.

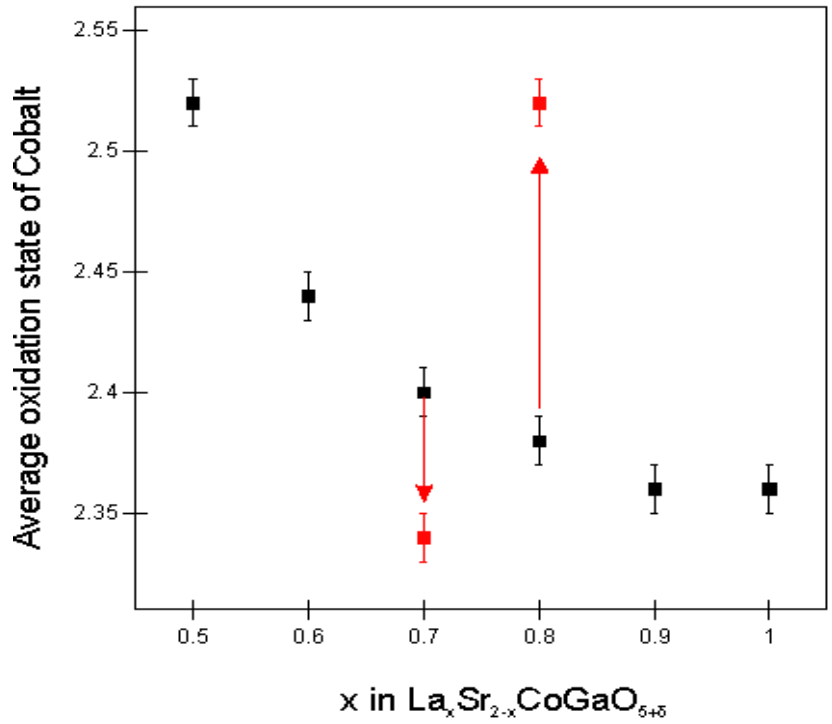

Figure 8.17 The average oxidation state of cobalt of $La_{0.7}Sr_{1.3}CoGaO_{5.02}$ and $La_{0.8}Sr_{1.2}CoGaO_{5.16}$ compared with $La_xSr_{2-x}CoGaO_{5+\delta}$ ($0.5 < x < 1.0$).

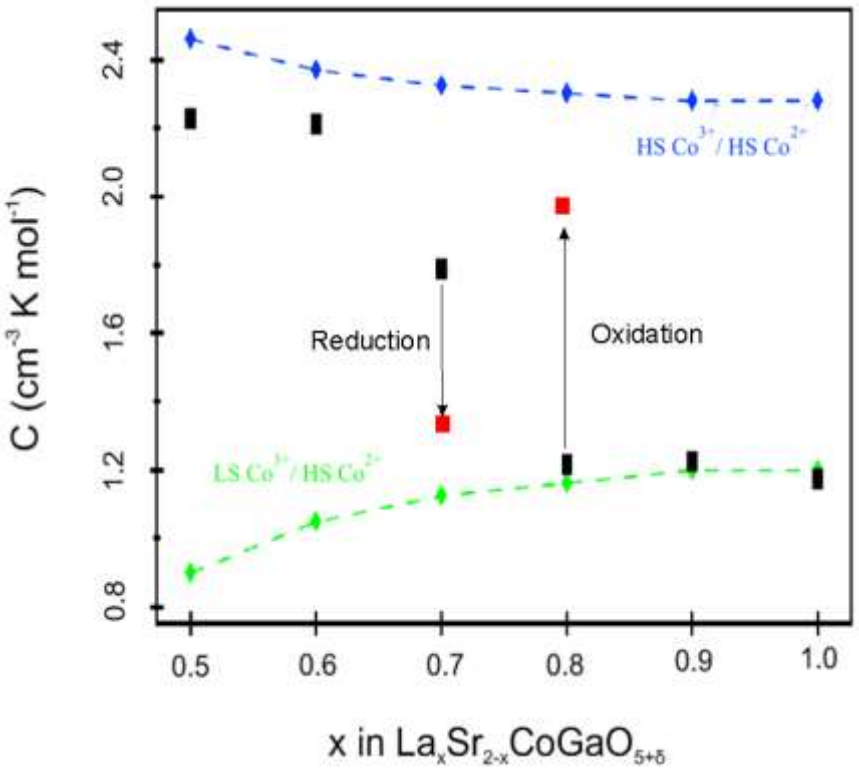

Figure 8.18Curie constant as a function of La/Sr ratio in $La_xSr_{2-x}CoGaO_{5+\delta}$. Black squares correspond to 'as-made' samples, red diamonds to oxidized and reduced samples.

The Curie constants are extracted from the magnetization data of the 'reduced' $La_{0.7}Sr_{1.3}CoGaO_{5.02}$ phase and the 'oxidized' $La_{0.8}Sr_{1.2}CoGaO_{5.16}$ phase. As shown in the Figure 8.18, the 'reduced' $La_{0.7}Sr_{1.3}CoGaO_{5.02}$ yields a smaller Curie constant than the as-prepared $La_{0.7}Sr_{1.3}CoGaO_{5.05}$ phase, while the 'oxidized' $La_{0.8}Sr_{1.2}CoGaO_{5.16}$ phase gives an increase in Curie constant compared to the as-prepared $La_{0.8}Sr_{1.2}CoGaO_{5.09}$ phase. Thus the relationship between the Co^{3+} spin state and the composition of $La_xSr_{2-x}CoGaO_{5+\delta}$ on the basis of a Co^{2+}/Co^{3+} redox reaction can be confirmed.

Based on the analysis above, the changing ratio of Co^{2+} (HS, CN6 = 0.745 Å) to Co^{3+} (HS, CN6 = 0.61 Å) leads to the internal strain which cannot be relieved by twisting of octahedra. The change of Co^{3+} spin state should be attributed to a compressive strain in the brownmillerite lattice when the ratio of Co^{2+}/Co^{3+} increases. In addition, the relationship between the Co^{3+} spin state and the average oxidation state of cobalt via the internal chemical strain is achieved over a small oxidation state range (~$Co^{+2.44}$-$Co^{+2.38}$). In this small range, the Co^{3+} spin state which is coupled with the compositions of $La_xSr_{2-x}CoGaO_{5+\delta}$ is determined by the oxygen stoichiometry of the sample, as shown in the following equation.

$$La_xSr_{2-x}CoGaO_{5+\delta} + y/2\ O_2 \rightarrow La_xSr_{2-x}CoGaO_{5+\delta+y}$$

Thus this class of sample could be used as a monitor of partial pressure of oxygen via the change in the Co^{3+} spin state.

The response of the Co^{3+} spin state to the oxygen content of samples has already observed in the $La_xSr_{2-x}CoGaO_{5+\delta}$ system. Although a similar composition-dependant Co^{3+} spin state was observed in metallic systems such as $La_{1-x}Sr_xCoO_3$ which stabilizes an intermediate Co^{3+} spin state by an itinerant electron or a dynamic Jahn-Teller distortion, the reason leading to the change of Co^{3+} spin state is different. In the $La_xSr_{2-x}CoGaO_{5+\delta}$ system, the

features of brownmillerite lattice limit the twisting of octahedra as a manner of relieving the internal chemical pressure arising from a changing ratio of Co^{2+}/Co^{3+}. The internal chemical pressure is proposed as a reason to understand the change of Co^{3+} spin state in this system.

8.4.4 *I2mb*-*Imma* structural transition

In the $La_xSr_{2-x}CoGaO_{5+\delta}$ phases, a structural change is observed from an *I2mb* (x = 0.5 – 0.7 members) to an *Imma* (x = 0.8 – 1.0 members) type brownmillerite. The change of Co^{3+} spin state in the $La_xSr_{2-x}CoGaO_{5+\delta}$ system occurs at a similar composition. The x = 0.5 and 0.6 members adopt a combination of HS Co^{3+} and HS Co^{2+}, while the x = 0.8 – 1.0 members adopt a combination of LS Co^{3+} and HS Co^{2+}. Previous studies indicated that a structural change from polar type to centrosymmetric type in $BiCoO_3$ brought about a change of Co^{3+} spin state. Is there a relationship between the structural transition and the change of Co^{3+} spin-state in $La_xSr_{2-x}CoGaO_{5+\delta}$?

It should noted that the extracted Curie constant of x = 0.7 members is smaller than that of the x = 0.5 or 0.6 members, suggesting the change Co^{3+} spin state has occurred to a portion of Co^{3+} centres. However, the x = 0.7 member adopts an *I2mb* type brownmillerite structure, similar to the x = 0.5 or 0.6 members. This indicates the Co^{3+} spin state is not directly related to the structural change in the $La_xSr_{2-x}CoGaO_{5+\delta}$ series as the structural change and spin-state change are not simultaneous.

As discussed in Chapter 1, the choice of a structural variant adopted by a brownmillerite phase can be influenced by several factors, principly the dipole moment established by the twisting of the tetrahedra, local electronically driven distortions and structural disruption by additional oxides. In order to understand the structural change in $La_xSr_{2-x}CoGaO_{5+\delta}$ the interactions of dipole moments and the structural choice is considered. These interactions

can be can be quantified as a function of two factors: twisting of tetrahedral chains (the O – O – O angle, φ) and the distance between tetrahedral layers (l).[27] The structural data from the $La_xSr_{2-x}CoGaO_{5+\delta}$ phases are listed in Table 8.18 and compared with the structural data extracted from other brownmillerite structures as shown in Figure 8.19.

Composition	$x = 0.5$	$x = 0.6$	$x = 0.7$	$x = 0.8$	$x = 1$
Space group	I2mb	I2mb	I2mb	Imma	Imma
Tetrahedral distortion ( )	52.87(2)	53.21(2)	53.61(2)	53.40(2)	51.61(9)
Layer separation (Å)	7.9789(7)	7.9833(7)	7.9802(9)	7.9664(11)	7.9285(8)
Cation Ordered Fraction (%)	73.8	74.4	68.8	62.8	59.0

Table 8.18 Selected parameters from the structural refinement of $La_xSr_{2-x}CoGaO_{5+\delta}$ phases. Oxygen concentrations determined by iodometric titration. Tetrahedral distortion angle = 180 °- (O-O-O) angle.

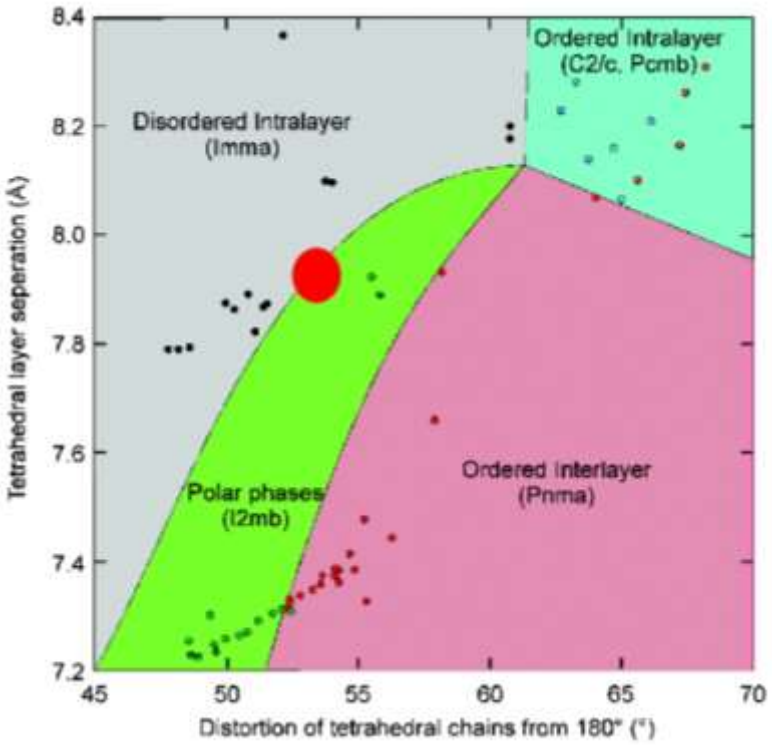

Figure 8.19 Brownmillerite structure map as a fuction of interlayer separation and tetrahedral chain distortion.[27] The red circle is the area of $La_xSr_{2-x}CoGaO_{5+\delta}$ phases discussed in this chapter.

As shown in Figure 8.19, the interlayer separations and twist angles of the $La_xSr_{2-x}CoGaO_{5+\delta}$ phases place these members close to the *I2mb/Imma* structural boundary on the

brownmillerite structure map. As listed in Table 8.18 the x = 0.8 member has a larger twisting angle of tetrahedra and a smaller distance of layer separation than the x = 0.5 or 0.6 members, and thus would be expected to adopt an *I2mb* type structure. However, structural analyses indicate that the x = 0.8 member adopts an *Imma* type structure. It should be noted that additional oxides are inserted into the tetrahedral layers in the nonstoichiometric $La_xSr_{2-x}CoGaO_{5+\delta}$ phases. The presence of additional oxides would lead to a conversion from the BO_4 centres to BO_5 and even BO_6 centres, which disrupts the cooperative twisting of the tetrahedral chains, to give a disordered arrangement of 'tetrahedra' in *Imma* structures. In addition, the disruption of the inserted additional oxides leads to a similarity between the octahedral sites and 'tetrahedral' sites in *Imma* members, confirmed by a dramatic of decrease in cation ordered fraction in $LaSrCoGaO_{5.18}$ phase.

Thus the *I2mb* - *Imma* structural transition observed in the $La_xSr_{2-x}CoGaO_{5+\delta}$ phases is attributed to the disruption by additional oxides in the lattice. As analyses above, no obvious evidence can be observed to support the direct relationship between the structural change and the change of Co^{3+} spin state.

8.4.5 Spin-glass behaviour

As noted above, zero-field-cooled and field-cooled magnetization data collected from $La_xSr_{2-x}GaCoO_{5+\delta}$ samples diverge when the temperature is below 60 K. AC susceptibility data collected from $La_xSr_{2-x}CoGaO_{5+\delta}$ exhibit a frequency-dependent response, indicating spin-glass behaviour. The materials which exhibit spin-glass behaviour must adopt disordered structures

The $La_xSr_{2-x}CoGaO_{5+\delta}$ phases adopt partial cation ordered structures in which majority of cobalt cations were located in octahedral sites and majority of gallium cations were located

in ‘tetrahedral’ sites. Thus two types of magnetic interaction occur in the phases. As shown in Figure 8.20, in a cation ordered micro-region, the phase is expected to adopt a G-type antiferromagnetically ordered arrangement of cobalt centres in octahedral sites. The presence of cobalt cations in ‘tetrahedral’ sites leads to a C-type antiferromagnetic order. The co-existence of these two magnetic interactions frustrates long-range magnetic ordering, to yield spin-glass behaviour. Similar magnetic frustration can be observed in $Sr_2Mn_{2-x}Al_xO_5$ brownmillerite system, in which the cation disorder in the tetrahedral layers leads to spin-glass behaviour.

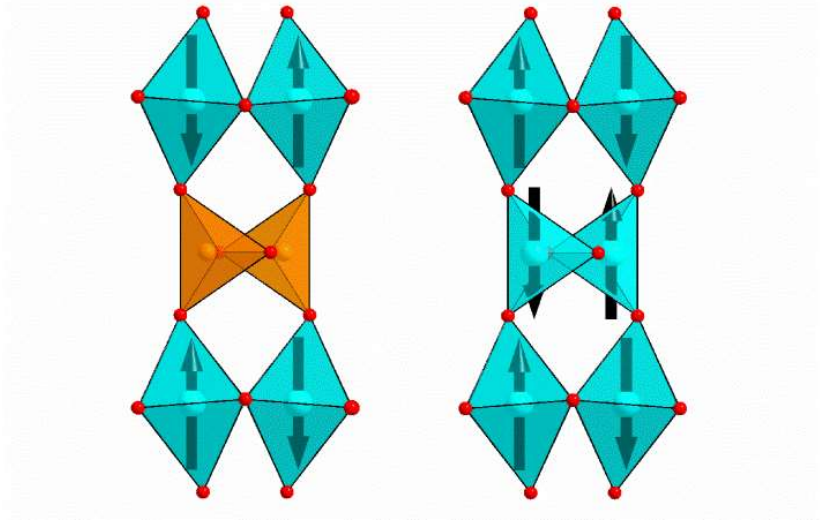

Figure 8.20 Regions with rigorous Co_{oct}/Ga_{tet} cation order adopt G-type antiferromagnetic order (left) within the layers of octahedra. The presence of cobalt on tetrahedral sites leads to C-type antiferromagnetic order within layers of octahedra, thus partial Co/Ga cation disorder leads to magnetic frustration and spin-glass behaviour.

The magnetic frustration is further achieved by a complex magnetic interaction. The combination of HS Co^{2+} and LS Co^{3+} cations in octahedral layers is another factor leading to spin-glass behaviour. $La_xSr_{2-x}CoGaO_{5+\delta}$ (x = 0.8 - 1.0) phases have a non-magnetic LS Co^{3+} and HS Co^{3+} cations. According to the Goodenough-Kanamori rules[103], Co^{2+} – O – Co^{2+} and Co^{3+} – O – Co^{3+} interactions are antiferromagnetic while Co^{2+} – O – Co^{3+} interactions are ferromagnetic. The combination of antiferromagnetic and ferromagnetic

interactions in a disordered manner also frustrates long-range magnetic ordering and yields spin-glass behaviour.

8.5 Conclusion

In this chapter, $La_xSr_{2-x}CoGaO_{5+\delta}$ (x = 0.5 - 1.0) phases were synthesized via a conventional solid-state route. The phases in this system adopt anion-vacancy ordered brownmillerite-type structures. The substitution of Sr^{2+} with La^{3+} results in a mixed Co^{2+}/Co^{3+} valence, with the average oxidation state of cobalt declines ($Co^{+2.52}$ – $Co^{+2.36}$) when the ratio of La^{3+}/Sr^{2+} increases. Magnetization data collected from the members of $La_xSr_{2-x}CoGaO_{5+\delta}$ system indicate that all the samples exhibit paramagnetism in the temperature range 100 < T/K< 300. The Curie constants extracted from the curves of each member indicate Co^{3+} centres undergo a change of Co^{3+} spin state from HS, S = 2 to LS, S = 0 as a function of the composition of $La_xSr_{2-x}CoGaO_{5+\delta}$. The coupling of the Co^{3+} spin state and the composition in $La_xSr_{2-x}CoGaO_{5+\delta}$ can be rationalized on the basis of internal chemical pressure due to the structural features of brownmillerite phases.

Appendix

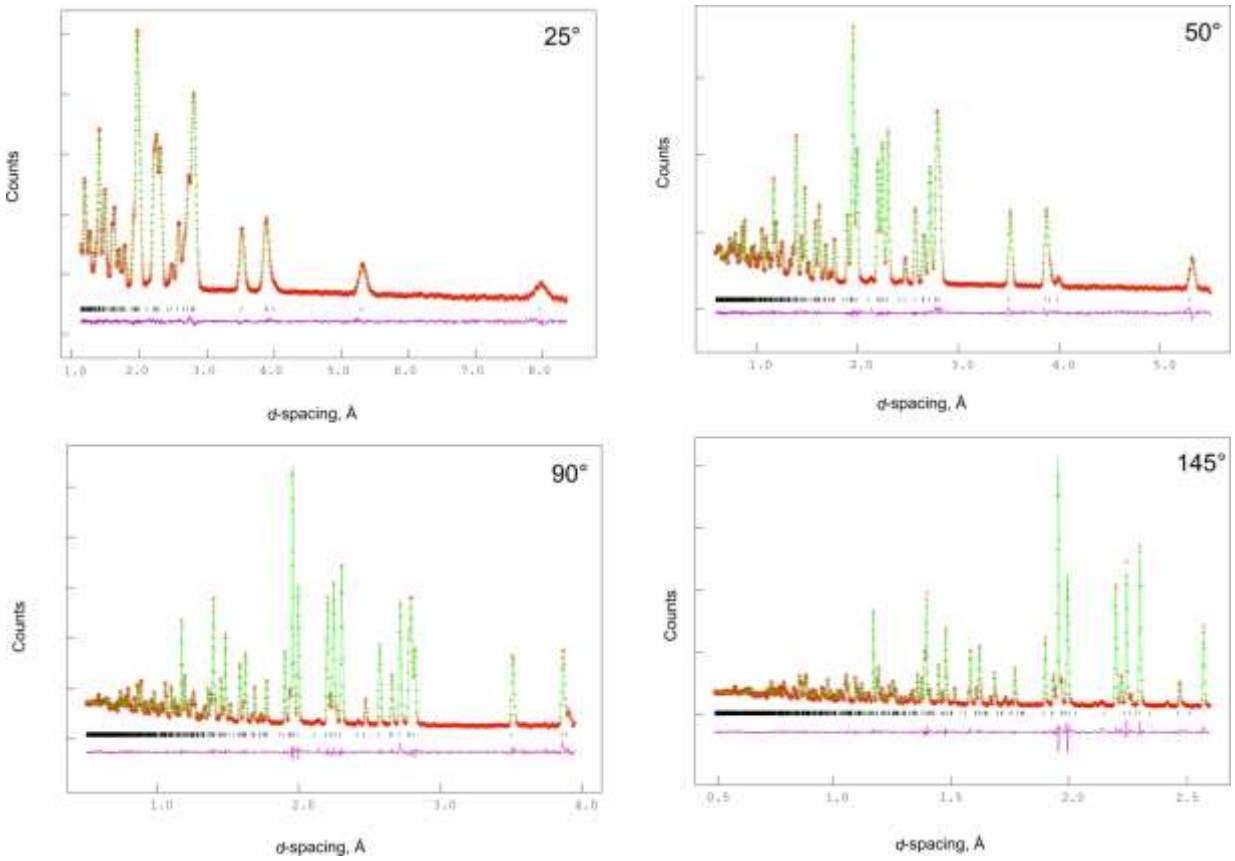

Figure A8.1 Observed, calculated and difference plots from the refinement of $La_{0.5}Sr_{1.5}CoGaO_{5.01}$.

Atom	U_{11}(Å)	U_{22}(Å)	U_{33}(Å)	U_{12}(Å)	U_{13}(Å)	U_{23}(Å)
La/Sr(1)	0.0064(1)	0.0064(1)	0.0081(1)	0.0001(1)	0.0004(2)	-0.0013(2)
Co/Ga(1)	0.0016(4)	0.0297(7)	0.0053(5)	0.0006(3)	0	0
Co/Ga(2)	0.0081(2)	0.0035(2)	0.0028(3)	0	-0.0004(2)	0
O(1)	0.0101(2)	0.0111(2)	0.0086(2)	-0.0012(3)	0.0011(1)	-0.0014(2)
O(2)	0.0141(3)	0.0096(2)	0.0206(3)	0.0068(2)	0.0034(2)	0.0067(2)
O(3)	0.0098(4)	0.0069(3)	0.0083(4)	0	-0.0004(2)	0

Table A8.1 Anisotropic thermal parameters refined against neutron powder diffraction data collected from $La_{0.5}Sr_{1.5}CoGaO_{5.01}$ at room temperature.

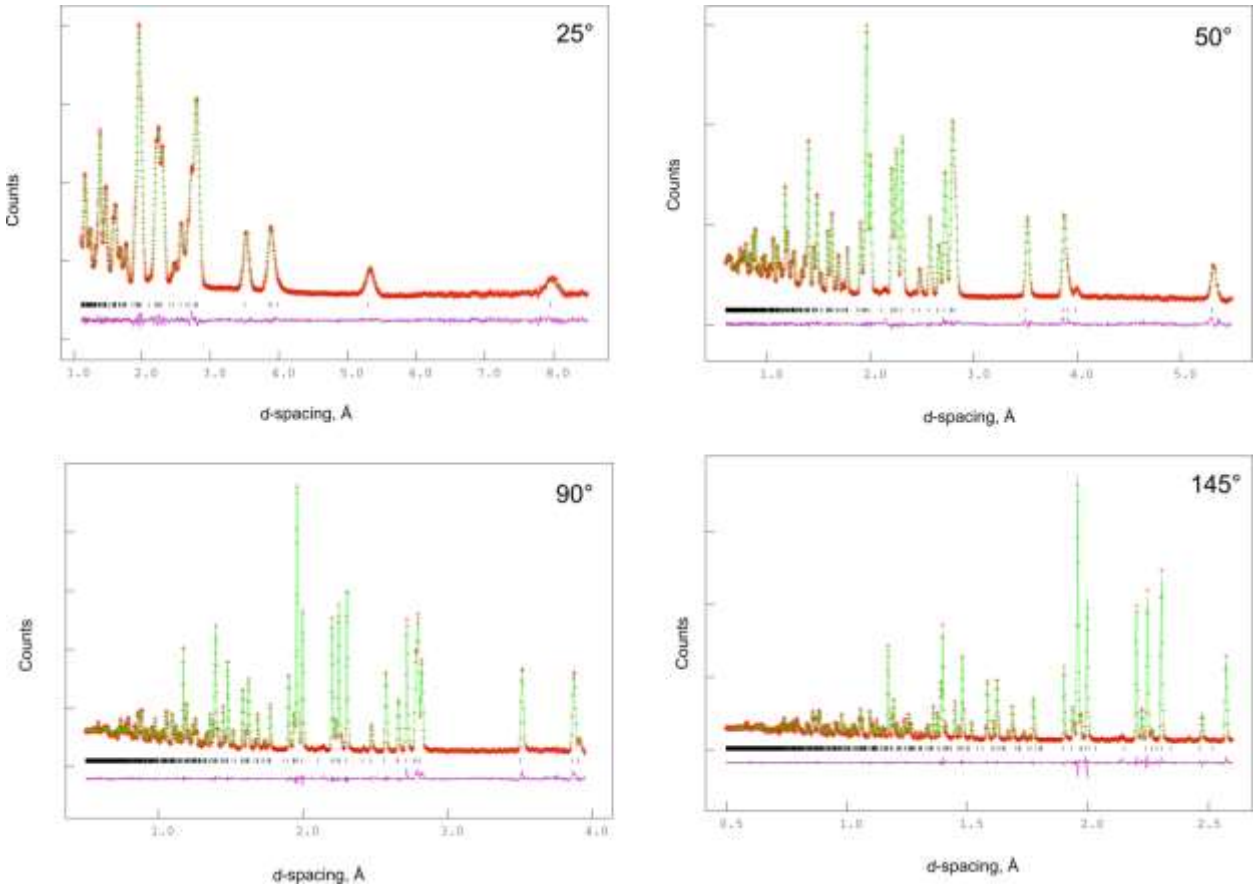

Figure A8.2 Observed, calculated and difference plots from the refinement of $La_{0.6}Sr_{1.4}CoGaO_{5.02}$.

Atom	U_{11}(Å)	U_{22}(Å)	U_{33}(Å)	U_{12}(Å)	U_{13}(Å)	U_{23}(Å)
La/Sr(1)	0.0065(1)	0.0059(1)	0.0077(1)	0.0001(1)	0.0009(2)	-0.0010(2)
Co/Ga(1)	0.0011(5)	0.0276(8)	0.0046(5)	0.0001(1)	0	0
Co/Ga(2)	0.0081(3)	0.0038(2)	0.0038(3)	0	-0.0001(1)	0
O(1)	0.0094(2)	0.0119(2)	0.0083(2)	-0.0009(3)	0.0009(2)	-0.0015(3)
O(2)	0.0142(3)	0.0105(2)	0.0205(4)	0.0072(2)	0.0035(3)	0.0066(3)
O(3)	0.0098(4)	0.0064(3)	0.0106(4)	0	-0.0043(3)	0

Table A8.2 Anisotropic thermal parameters refined against neutron powder diffraction data collected from $La_{0.6}Sr_{1.4}CoGaO_{5.02}$ at room temperature.

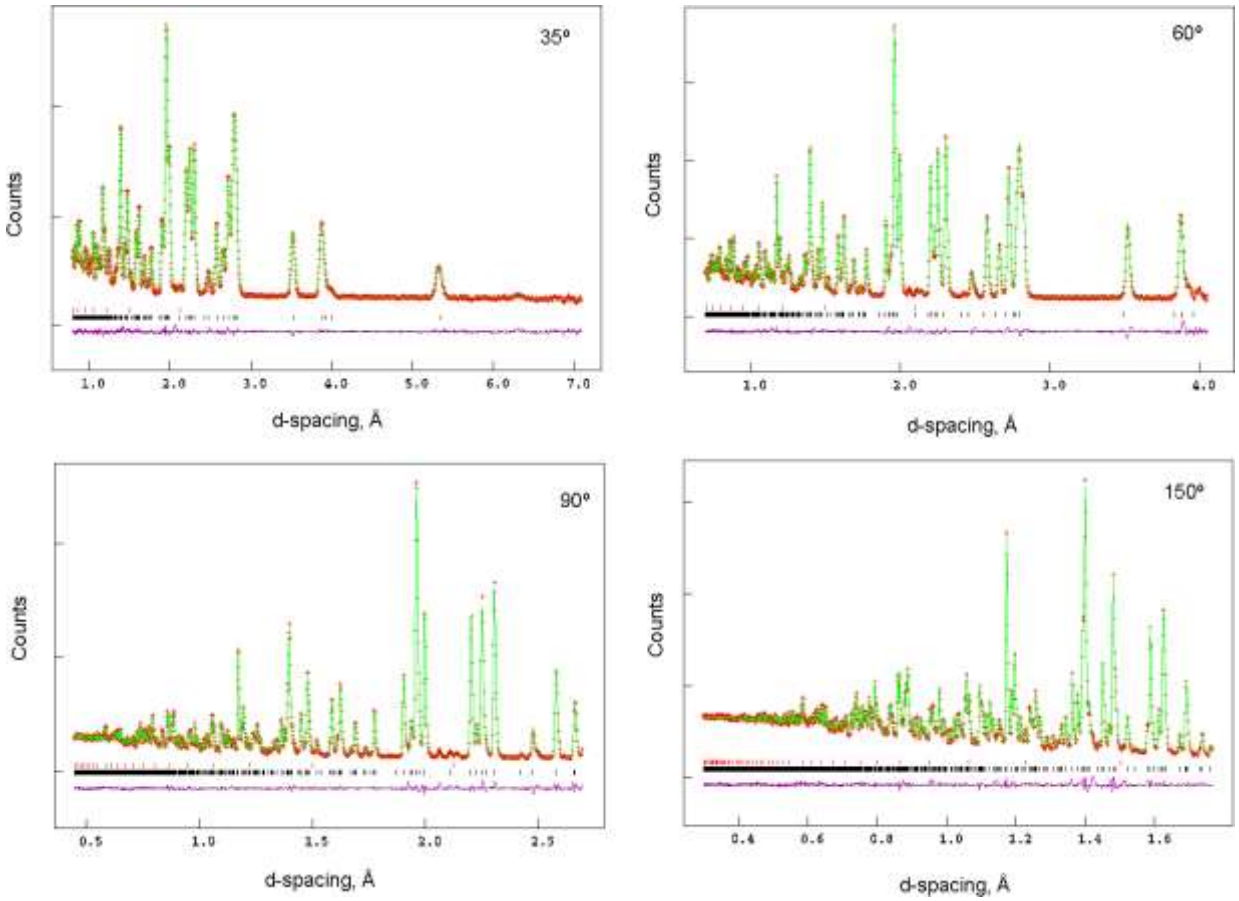

Figure A8.3 Observed, calculated and difference plots from the refinement of $La_{0.7}Sr_{1.3}CoGaO_{5.05}$.

Atom	U_{11}(Å)	U_{22}(Å)	U_{33}(Å)	U_{12}(Å)	U_{13}(Å)	U_{23}(Å)
La/Sr(1)	0.0061(3)	0.0049(3)	0.0079(3)	0.0009(2)	0.0011(4)	0.0003(2)
Co/Ga(1)	0.0034(1)	0.0276(13)	0.0015(8)	-0.0001(1)	0	0
Co/Ga(2)	0.0087(6)	0.0050(5)	0.0082(8)	0	-0.0002(1)	0
O(1)	0.0070(4)	0.0118(5)	0.0059(3)	-0.0002(1)	0.0008(3)	0.0002(1)
O(2)	0.0158(5)	0.0133(5)	0.0168(7)	0.0075(4)	0.0023(5)	0.0065(6)
O(3)	0.0118(8)	0.0061(7)	0.0139(8)	0	-0.0046(6)	0

Table A8.3 Anisotropic thermal parameters refined against neutron powder diffraction data collected from $La_{0.7}Sr_{1.3}CoGaO_{5.05}$ at room temperature.

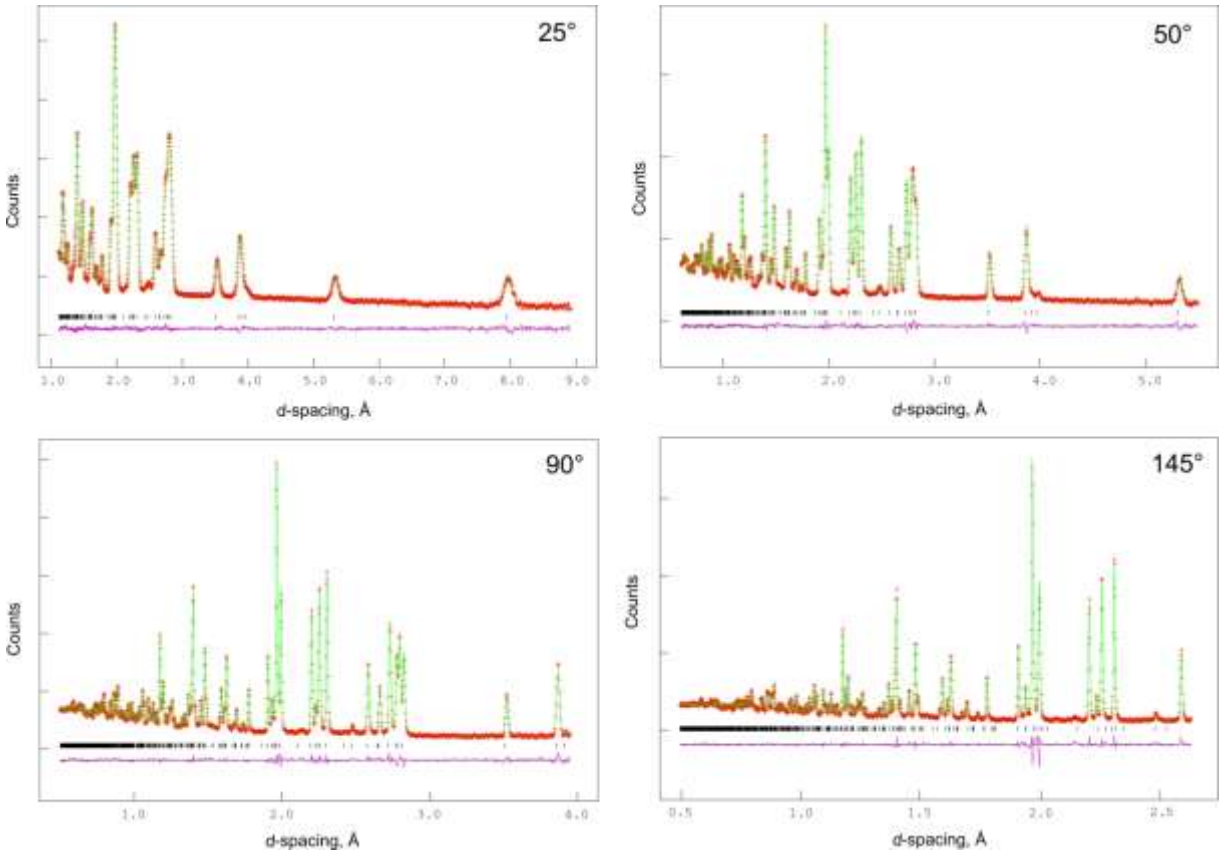

Figure A8.4 Observed, calculated and difference plots from the refinement of $La_{0.8}Sr_{1.2}CoGaO_{5.09}$.

Atom	U_{11}(Å)	U_{22}(Å)	U_{33}(Å)	U_{12}(Å)	U_{13}(Å)	U_{23}(Å)
La/Sr(1)	0.0082(2)	0.0058(1)	0.0080(1)	-0.0004(1)	0	0
Co/Ga(1)	0.0028(5)	0.0307(8)	0.0071(5)	0.0078(6)	0	0
Co/Ga(2)	0.0126(4)	0.0061(3)	0.0026(6)	0	0.0012(3)	0
O(1)	0.0077(2)	0.0143(3)	0.0064(2)	0	0.0001(1)	0
O(2)	0.0124(3)	0.0141(3)	0.0433(4)	0.0076(2)	0	0
O(3)	0.0146(5)	0.0049(5)	0.0198(6)	0	-0.0077(4)	0

Table A8.4 Anisotropic thermal parameters refined against neutron powder diffraction data collected from $La_{0.8}Sr_{1.2}CoGaO_{5.09}$ at room temperature.

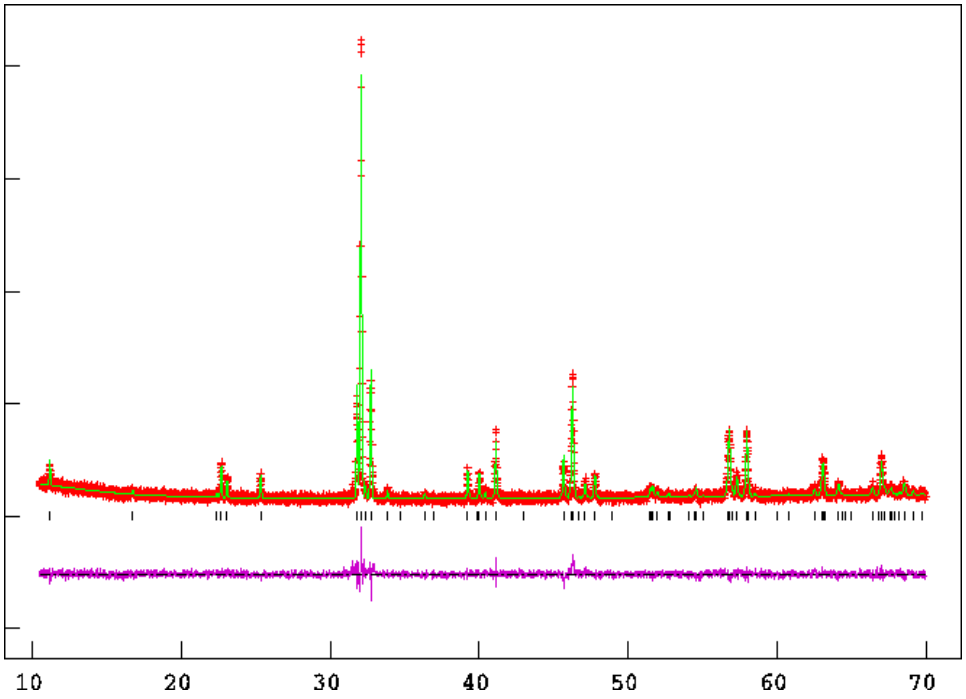

Figure A8.5 Observed, calculated and difference plots from the refinement of $La_{0.9}Sr_{1.1}CoGaO_{5.13}$ against powder X-ray diffraction data at room temperature.

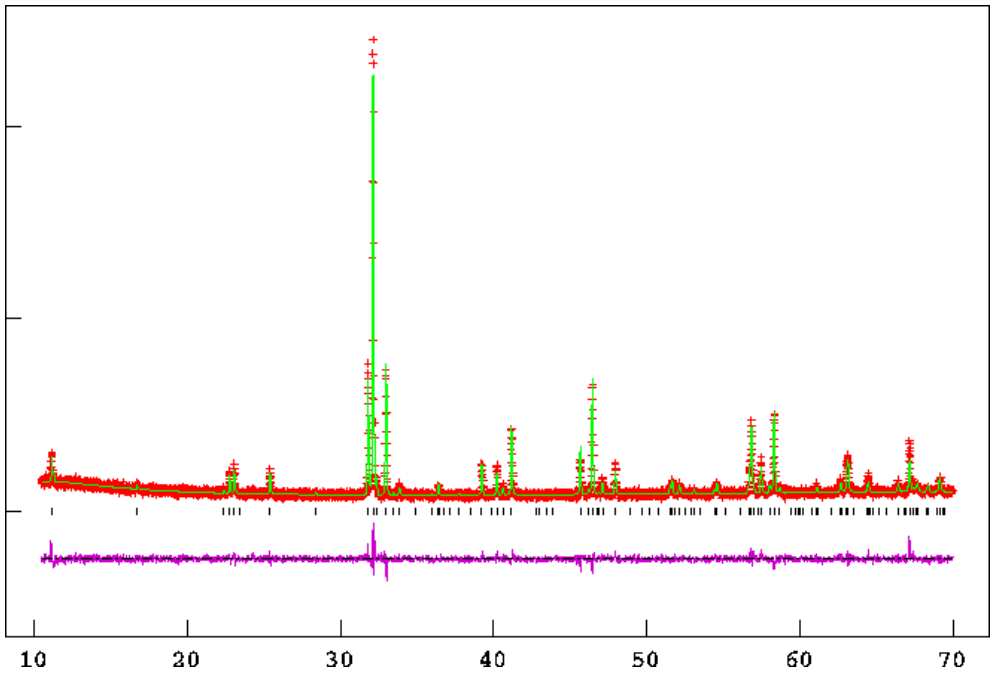

Figure A8.6 Observed, calculated and difference plots from the refinement of $La_{0.7}Sr_{1.15}Ca_{0.15}CoGaO_{5.06}$ against powder X-ray diffraction data at room temperature.

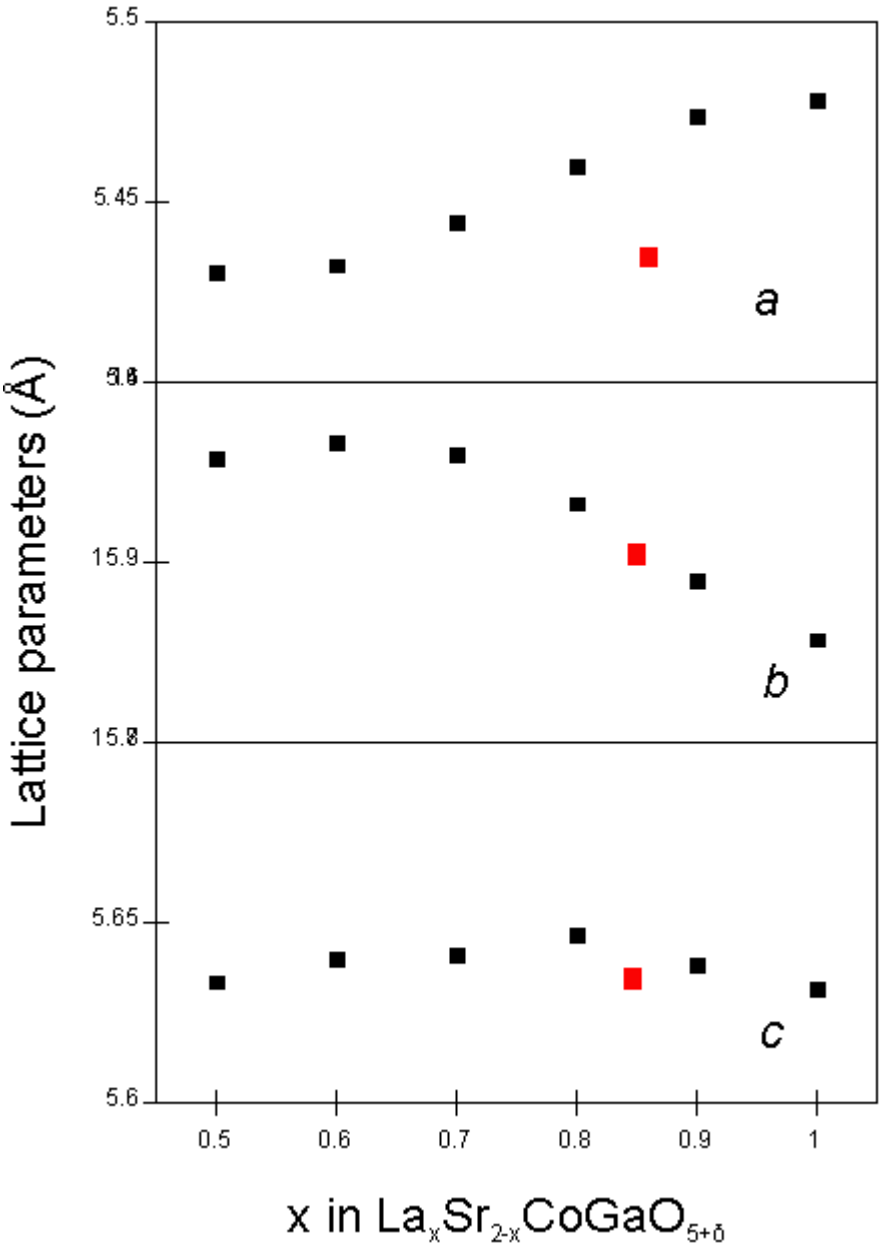

Figure A8.7 Lattice parameters of the $La_xSr_{2-x}GaCoO_{5+\delta}$ phases (black dots). The red dots indicated the lattice parameters of $La_{0.7}Sr_{1.15}Ca_{0.15}CoGaO_{5.06}$ phase

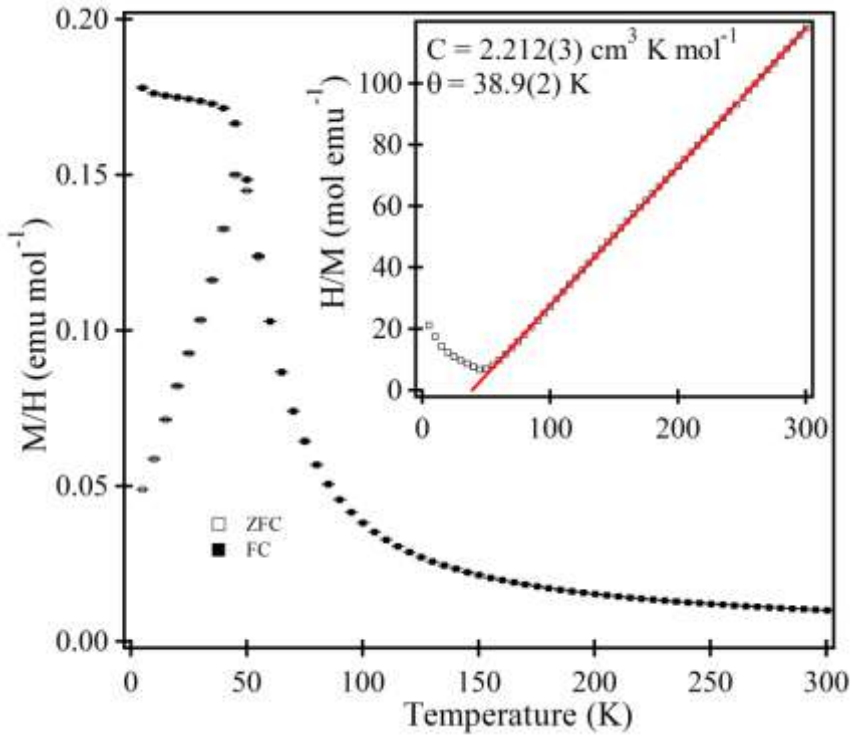

Figure A8.8 Zero-field-cooled and field-cooled magnetisation data collected from $La_{0.6}Sr_{01.4}CoGaO_{5.02}$ as a function of temperature. Inset shows fit to the Curie-Weiss law.

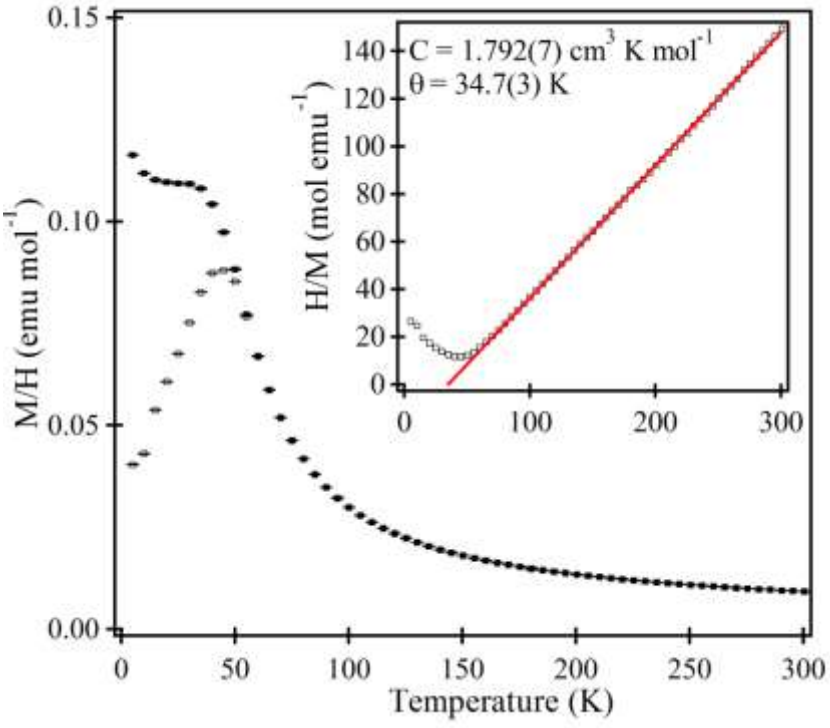

Figure A8.9 Zero-field-cooled and field-cooled magnetisation data collected from $La_{0.7}Sr_{01.3}CoGaO_{5.05}$ as a function of temperature. Inset shows fit to the Curie-Weiss law.

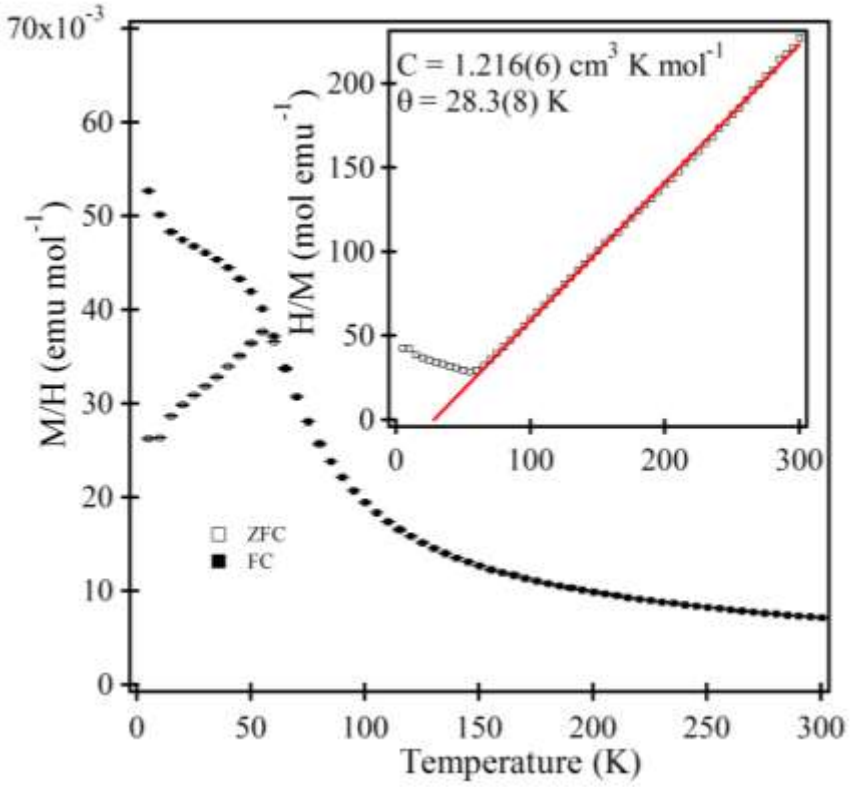

Figure A8.10 Zero-field-cooled and field-cooled magnetisation data collected from $La_{0.8}Sr_{1.2}CoGaO_{5.09}$ as a function of temperature. Inset shows fit to the Curie-Weiss law.

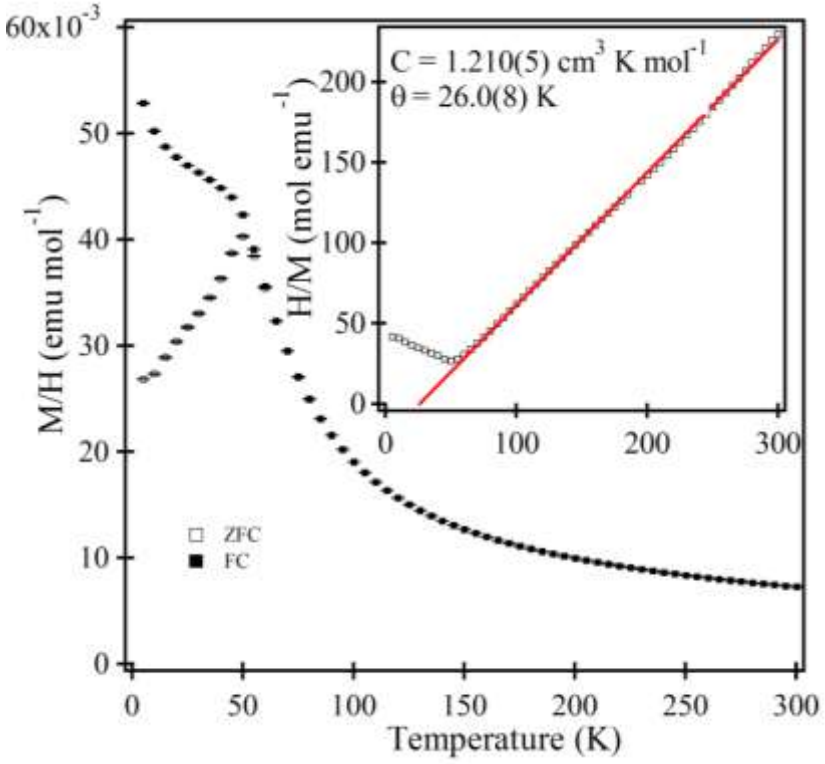

Figure A8.11 Zero-field-cooled and field-cooled magnetisation data collected from $La_{0.9}Sr_{1.1}CoGaO_{5.13}$ as a function of temperature. Inset shows fit to the Curie-Weiss law.

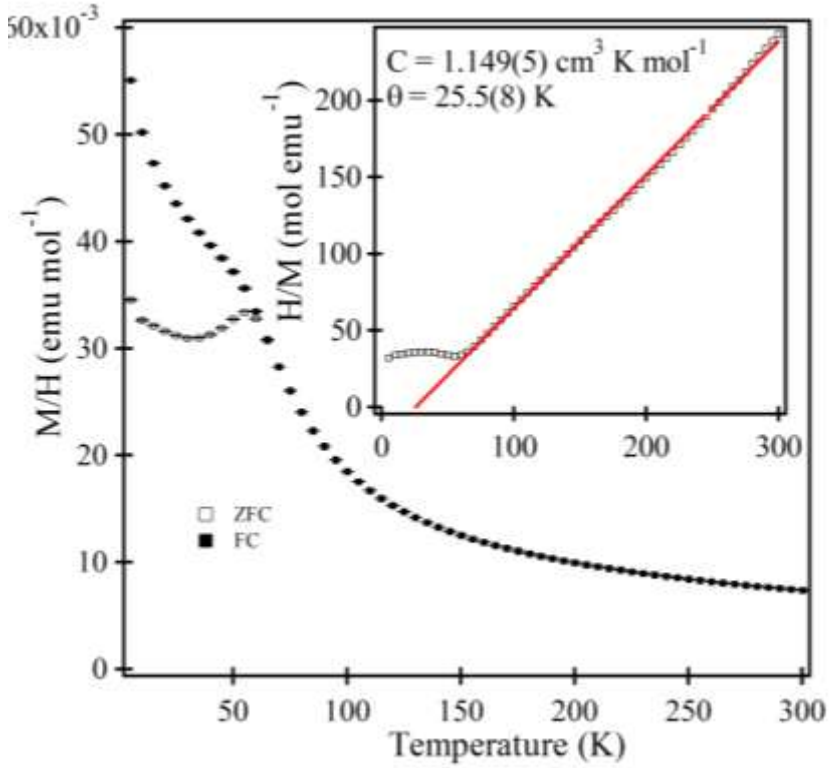

Figure A8.12 Zero-field-cooled and field-cooled magnetisation data collected from $LaSrCoGaO_{5.18}$ as a function of temperature. Inset shows fit to the Curie-Weiss law.

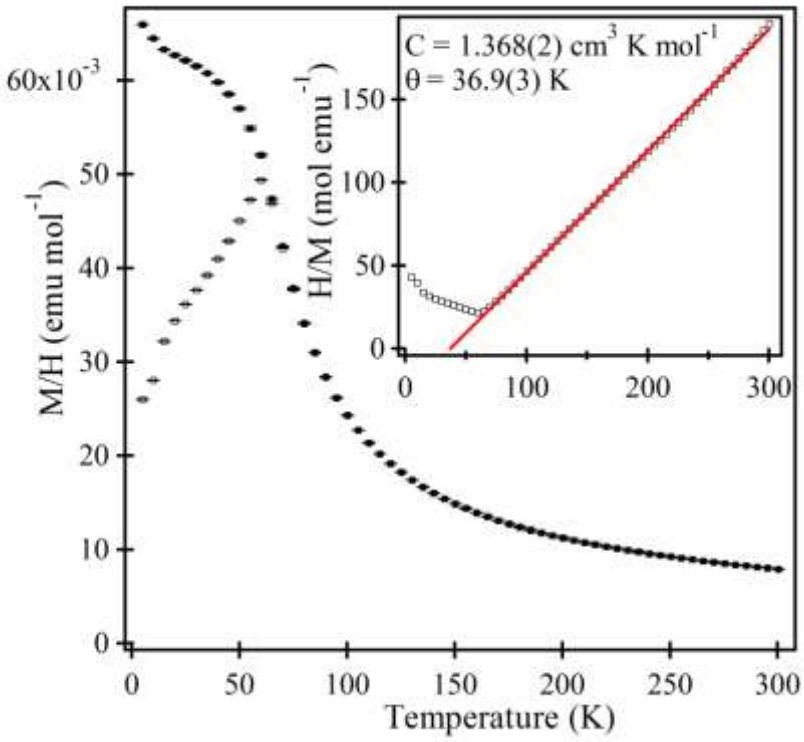

Figure A8.13 Zero-field-cooled and field-cooled magnetisation data collected from $La_{0.7}Sr_{1.3}CoGaO_{5.02}$ as a function of temperature. Inset shows fit to the Curie-Weiss law.

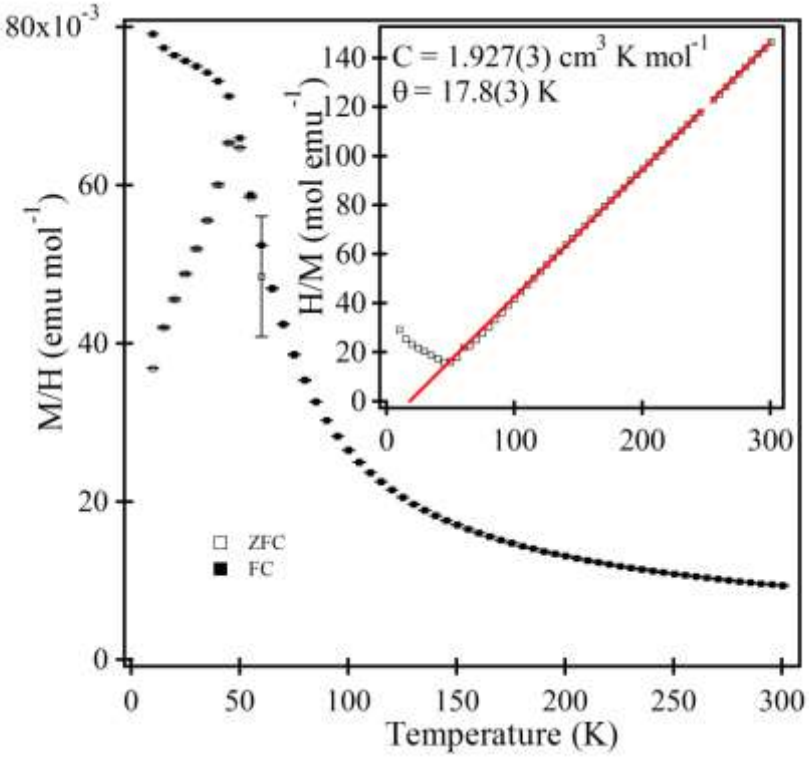

Figure A8.14 Zero-field-cooled and field-cooled magnetisation data collected from $La_{0.8}Sr_{1.2}CoGaO_{5.16}$ as a function of temperature. Inset shows fit to the Curie-Weiss law.

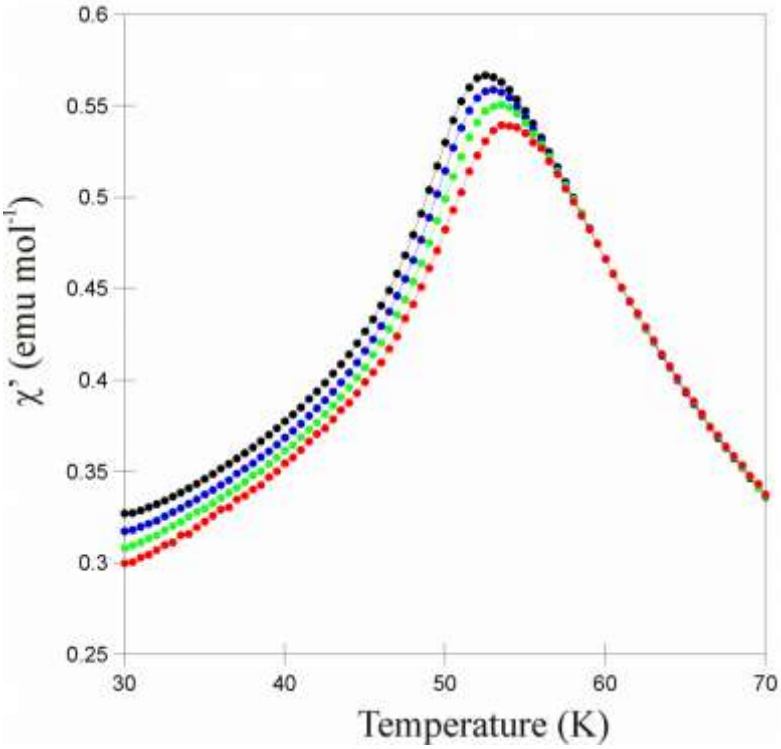

Figure A8.15 AC susceptibility data collected as a function of temperature from $La_{0.6}Sr_{1.4}CoGaO_{5.02}$ at 1, 10, 100 and 1000Hz.

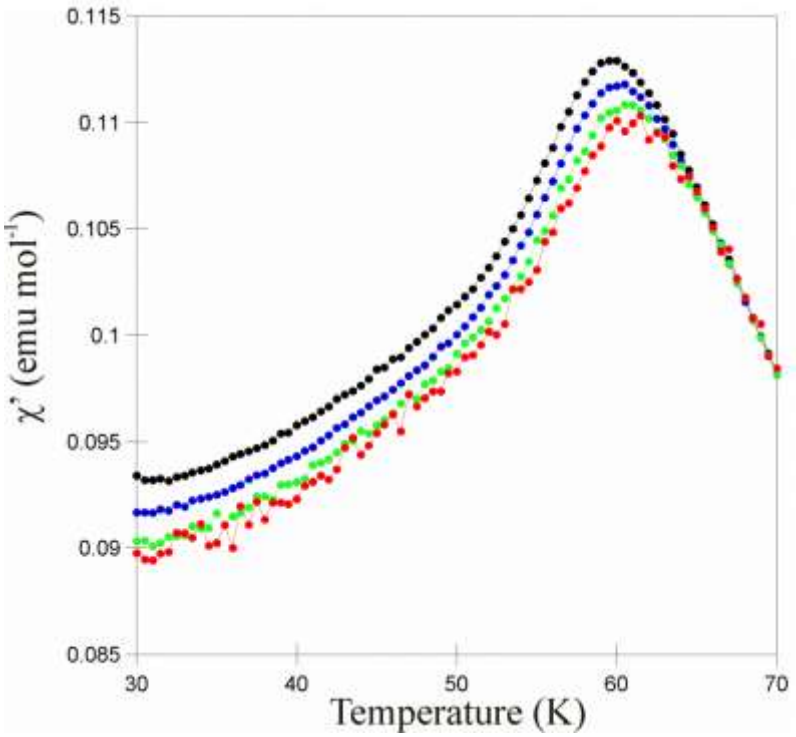

Figure A8.16 AC susceptibility data collected as a function of temperature from $La_{0.8}Sr_{1.2}CoGaO_{5.09}$ at 1, 10, 100 and 1000Hz.

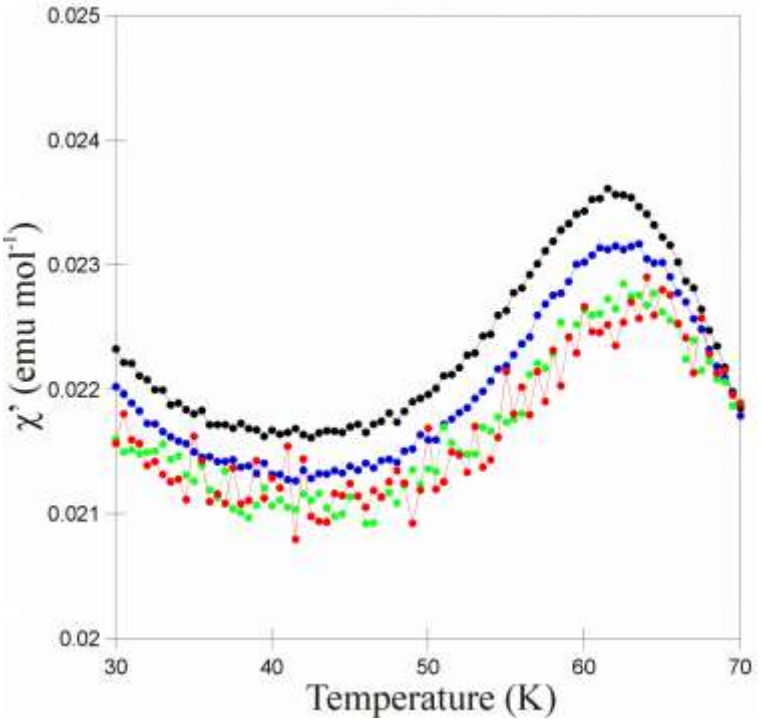

Figure A8.17 AC susceptibility data collected as a function of temperature from $LaSrCoGaO_{5.18}$ at 1, 10, 100 and 1000Hz.

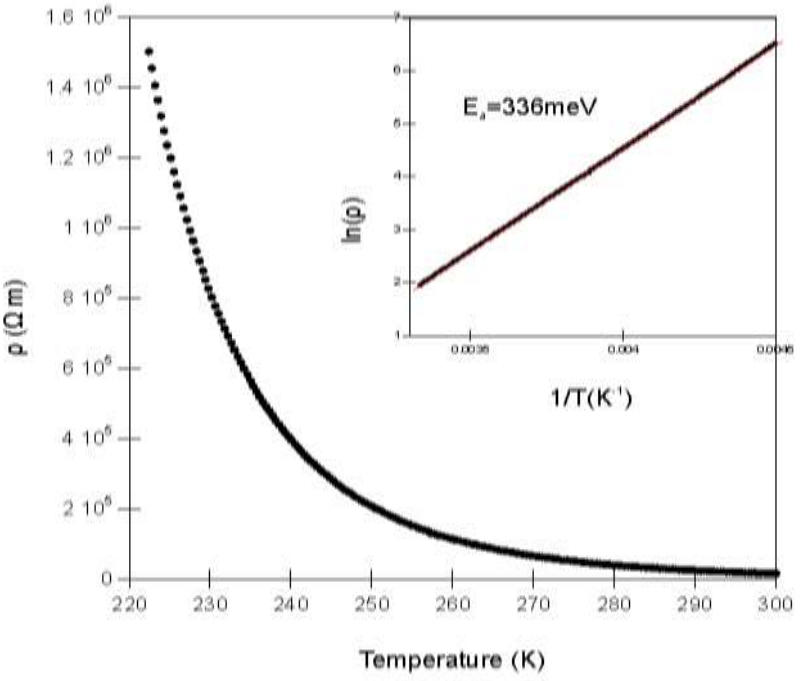

Figure A8.18 Temperature dependence of the electrical resistance of $La_{0.6}Sr_{1.4}GaCoO_{5.02}$ samples. Insets show logarithmic plots with the fit to the Arrhenius law.

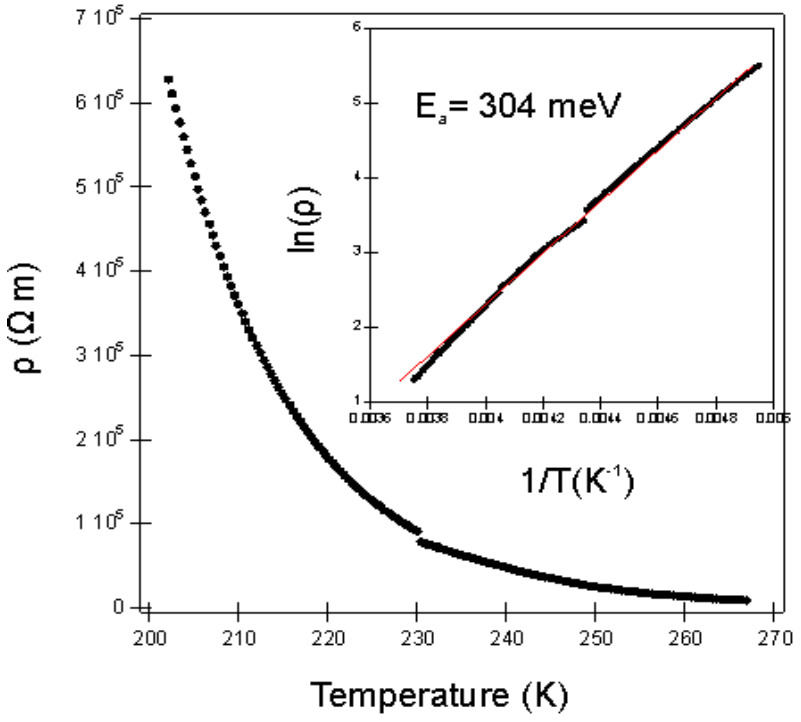

Figure A8.19 Temperature dependence of the electrical resistance of $La_{0.8}Sr_{1.2}GaCoO_{5.09}$ samples. Insets show logarithmic plots with the fit to the Arrhenius law.

Chapter 9 Summary

This thesis focuses on the synthesis of several perovskite phases with complex cation ordering and anion-vacancy ordering. Chapter 3 and 4 describe the complex cation and anion-vacancy ordered $Ba_nYM_{n-1}O_{2.5n}$ (M = Fe, Co; n = 2, 3) phases, which consist of YO_6 octahedra and MO_4 tetrahedra. The analysis of the structures of four $Ba_nYM_{n-1}O_{2.5n}$ (M = Fe, Co; n = 2, 3) phases indicates that complex cation ordering can be achieved by carefully controlling the size difference of pairs of B-site cations and the oxygen content, which offers the possibility of preparing phases with new cation ordering patterns. In principle, $Ba_nREM_{n-1}O_{2.5n}$ (RE = Ho, Nd, etc, M = Fe, Co; n = 2, 3) can be synthesized. The size difference between RE^{3+} and M^{3+} cations could lead to a different cation-ordered structure.

Chapter 5 and 6 describe the anion insertion into the structural lattice of Ba_2YMO_5 (M = Fe, Co). The insertion of oxide ions into Ba_2YFeO_5 breaks the inversion symmetry of the host lattice, which allows the material to exhibit second-harmonic generation activity. However, the lack of switchability of the polarization of $Ba_2YFeO_{5.5}$ in an applied electric field limits this material to exhibiting pyroelectric behaviour, rather than ferroelectric behaviour. By adjusting the size difference of two B-site cations (e.g. Lu^{3+}/Fe^{4+}), a switchable polarization in an applied electric field could be achieved, which could lead to a new type of multiferroic material.

The triple-layered ($LaCa_2Fe_2GaO_8$) and brownmillerite ($La_xSr_{2-x}CoGaO_{5+\delta}$, $0.5 < x < 1.0$) phases are described in Chapter 7 and 8 respectively. Magnetization data collected from $La_xSr_{2-x}CoGaO_{5+\delta}$ indicates a composition-related Co^{3+} spin state. A change of the Co^{3+} spin state from high spin (HS) to low spin (LS) is observed as the La^{3+}/Sr^{2+} ratio increases. This change of Co^{3+} spin state in $La_xSr_{2-x}CoGaO_{5+\delta}$ can be rationalized on the basis of an applied internal chemical pressure. This study motivates the interests in exploring other systems

which could exhibit a similar composition-related Co^{3+} spin state to the brownmillerite $La_xSr_{2-x}CoGaO_{5+\delta}$ phases. For example, the rigidity of the Ruddlesden-Popper structure offers the possibility of constructing a system that could exhibit a composition-related spin state.

Chapter 10 Bibliography

(1) Abramov, Y. A.; Tsirelson, V. G.; Zavodnik, V. E.; Ivanov, S. A.; Brown, I. D. *Acta Crystallogr B* **1995**, *51*, 942.
(2) Chamberland, B. L.; Katz, L. *Acta Crystallogr B* **1982**, *38*, 54.
(3) Mather, G. C.; Islam, M. S.; Figueiredo, F. M. *Adv Funct Mater* **2007**, *17*, 905.
(4) Nagai, I.; Shirakawa, N.; Ikeda, S.; Iwasaki, R.; Nishimura, H.; Kosaka, M. *Appl Phys Lett* **2005**, *87*.
(5) Callagha.A; Moeller, C. W.; Ward, R. *Inorg Chem* **1966**, *5*, 1572.
(6) Jin, S.; Tiefel, T. H.; Mccormack, M.; Fastnacht, R. A.; Ramesh, R.; Chen, L. H. *Science* **1994**, *264*, 413.
(7) King, G.; Woodward, P. M. *J Mater Chem* **2010**, *20*, 5785.
(8) Kobayashi, K. L.; Kimura, T.; Sawada, H.; Terakura, K.; Tokura, Y. *Nature* **1998**, *395*, 677.
(9) Howard, C. J.; Barnes, P. W.; Kennedy, B. J.; Woodward, P. M. *Acta Crystallogr B* **2005**, *61*, 258.
(10) Bos, J. W. G.; Attfield, J. P. *Phys Rev B* **2004**, *70*.
(11) Darriet, J.; Drillon, M.; Villeneuve, G.; Hagenmuller, P. *J Solid State Chem* **1976**, *19*, 213.
(12) Rijssenbeek, J. T.; Saito, T.; Malo, S.; Masaki, A. T.; Takano, M.; Poeppellmeier, K. R. *J Am Chem Soc* **2005**, *127*, 675.
(13) Alonso, J. A.; Mzayek, E.; Rasines, I. *Mater Res Bull* **1987**, *22*, 69.
(14) Nakatsuji, S.; Kuga, K.; Kimura, K.; Satake, R.; Katayama, N.; Nishibori, E.; Sawa, H.; Ishii, R.; Hagiwara, M.; Bridges, F.; Ito, T. U.; Higemoto, W.; Karaki, Y.; Halim, M.; Nugroho, A. A.; Rodriguez-Rivera, J. A.; Green, M. A.; Broholm, C. *Science* **2012**, *336*, 559.
(15) Zhou, H. D.; Xu, C. K.; Hallas, A. M.; Silverstein, H. J.; Wiebe, C. R.; Umegaki, I.; Yan, J. Q.; Murphy, T. P.; Park, J. H.; Qiu, Y.; Copley, J. R. D.; Gardner, J. S.; Takano, Y. *Phys Rev Lett* **2012**, *109*.
(16) Susuki, T.; Kurita, N.; Tanaka, T.; Nojiri, H.; Matsuo, A.; Kindo, K.; Tanaka, H. *Phys Rev Lett* **2013**, *110*, 267201.
(17) Ting, V.; Liu, Y.; Noren, L.; Withers, R. L.; Goossens, D. J.; James, M.; Ferraris, C. *J Solid State Chem* **2004**, *177*, 4428.
(18) Shimoda, Y.; Doi, Y.; Hinatsu, Y.; Ohoyama, K. *Chem Mater* **2008**, *20*, 4512.
(19) Nakahara, Y.; Kato, S.; Sugai, M.; Ohshima, Y.; Makino, K. *Mater Lett* **1997**, *30*, 163.
(20) Battle, P. D.; Blundell, S. J.; Brooks, M. L.; Hervieu, M.; Kapusta, C.; Lancaster, T.; Nair, S. P.; Oates, C. J.; Pratt, F. L.; Rosseinsky, M. J.; Ruiz-Bustos, R.; Sikora, M.; Steer, C. A. *J Am Chem Soc* **2004**, *126*, 12517.
(21) Greaves, C.; Slater, P. R. *Physica C* **1989**, *161*, 245.
(22) Gomezromero, P.; Palacin, M. R.; Rodriguezcarvajal, J. *Chem Mater* **1994**, *6*, 2118.
(23) Turp, S. A.; Hargreaves, J.; Baek, J.; Halasyamani, P. S.; Hayward, M. A. *Chem Mater* **2010**, *22*, 5580.
(24) Floros, N.; Michel, C.; Hervieu, M.; Raveau, B. *J Solid State Chem* **2002**, *168*, 11.
(25) Dunstone, S. J.; Clark, J. H.; Hayward, M. A. *Chem Commun* **2007**, 1905.
(26) Clark, J. H.; Hayward, M. A. *Chem Mater* **2008**, *20*, 4612.
(27) Parsons, T. G.; D'Hondt, H.; Hadermann, J.; Hayward, M. A. *Chem Mater* **2009**, *21*, 5527.

(28) D'Hondt, H.; Abakumov, A. M.; Hadermann, J.; Kalyuzhnaya, A. S.; Rozova, M. G.; Antipov, E. V.; Van Tendeloo, G. *Chem Mater* **2008**, *20*, 7188.
(29) Hadermann, J.; Abakumov, A. M.; D'Hondt, H.; Kalyuzhnaya, A. S.; Rozova, M. G.; Markina, M. M.; Mikheev, M. G.; Tristan, N.; Klingeler, R.; Buchner, B.; Antipov, E. V. *J Mater Chem* **2007**, *17*, 692.
(30) Gregory, D. H.; Weller, M. T. *J Solid State Chem* **1993**, *107*, 134.
(31) Jiang, P.; Li, J.; Ozarowski, A.; Sleight, A. W.; Subramanian, M. A. *Inorg Chem* **2013**, *52*, 1349.
(32) D'Hondt, H.; Hadermann, J.; Abakumov, A. M.; Kalyuzhnaya, A. S.; Rozova, M. G.; Tsirlin, A. A.; Nath, R.; Tan, H. Y.; Verbeeck, J.; Antipov, E. V.; Van Tendeloo, G. *J Solid State Chem* **2009**, *182*, 356.
(33) Casey, P. S.; Barker, D.; Hayward, M. A. *J Solid State Chem* **2006**, *179*, 1375.
(34) Hayashi, N.; Yamamoto, T.; Kageyama, H.; Nishi, M.; Watanabe, Y.; Kawakami, T.; Matsushita, Y.; Fujimori, A.; Takano, M. *Angewandte Chemie-International Edition* **2011**, *50*, 12547.
(35) Li, R. K.; Greaves, C. *Phys Rev B* **2000**, *62*, 3811.
(36) Hagerman, M. E.; Poeppelmeier, K. R. *Chem Mater* **1995**, *7*, 602.
(37) Kay, H. F.; Wellard, H. J.; Vousden, P. *Nature* **1949**, *163*, 636.
(38) Goodey, J.; Broussard, J.; Halasyamani, P. S. *Chem Mater* **2002**, *14*, 3174.
(39) Halasyamani, P. S.; Poeppelmeier, K. R. *Chem Mater* **1998**, *10*, 2753.
(40) Cross, E. *Nature* **2004**, *432*, 24.
(41) Catalan, G.; Scott, J. F. *Adv Mater* **2009**, *21*, 2463.
(42) Antokhina, T. F.; Ignat'eva, L. N.; Savchenko, N. N.; Tkachenko, I. A.; Kaidalova, T. A. *Russ J Inorg Chem* **2003**, *48*, 472.
(43) Heier, K. R.; Norquist, A. J.; Wilson, C. G.; Stern, C. L.; Poeppelmeier, K. R. *Inorg Chem* **1998**, *37*, 76.
(44) Izumi, H. K.; Kirsch, J. E.; Stern, C. L.; Poeppelmeier, K. R. *Inorg Chem* **2005**, *44*, 884.
(45) Marvel, M. R.; Pinlac, R. A. F.; Lesage, J.; Stern, C. L.; Poeppelmeier, K. R. *Z Anorg Allg Chem* **2009**, *635*, 869.
(46) Norquist, A. J.; Heier, K. R.; Stern, C. L.; Poeppelmeier, K. R. *Inorg Chem* **1998**, *37*, 6495.
(47) Vaughey, J. T.; Harrison, W. T. A.; Dussack, L. L.; Jacobson, A. J. *Inorg Chem* **1994**, *33*, 4370.
(48) Kim, Y. H.; Lee, K. S.; Kwon, Y. U.; Han, O. H. *Inorg Chem* **1996**, *35*, 7394.
(49) Abrahams, S. C.; Sherwood, R. C.; Bernstei.Jl; Nassau, K. *J Solid State Chem* **1973**, *8*, 274.
(50) Sykora, R. E.; Wells, D. M.; Albrecht-Schmitt, T. E. *J Solid State Chem* **2002**, *166*, 442.
(51) Sykora, R. E.; Ok, K. M.; Halasyamani, P. S.; Albrecht-Schmitt, T. E. *J Am Chem Soc* **2002**, *124*, 1951.
(52) Kunz, M.; Brown, I. D. *J Solid State Chem* **1995**, *115*, 395.
(53) Marvel, M. R.; Lesage, J.; Baek, J.; Halasyamani, P. S.; Stern, C. L.; Poeppelmeier, K. R. *J Am Chem Soc* **2007**, *129*, 13963.
(54) Choi, T.; Horibe, Y.; Yi, H. T.; Choi, Y. J.; Wu, W. D.; Cheong, S. W. *Nat Mater* **2010**, *9*, 253.
(55) http://www.ill.eu/instruments-support/instruments-groups/instruments/d2b/how-it-works/simulated-experiment/
(56) http://www.isis.stfc.ac.uk/instruments/polaris/

(57) http://www.isis.stfc.ac.uk/instruments/polaris/data-analysis/polaris-data-analysis4649.html
(58) http://www.isis.stfc.ac.uk/instruments/gem/
(59) http://www.isis.stfc.ac.uk/instruments/gem/data-analysis/gem-data-analysis2513.html
(60) http://english.cas.cn/Ne/CASE/200911/t20091112_47074.shtm
(61) Ok, K. M.; Chi, E. O.; Halasyamani, P. S. *Chem Soc Rev* **2006**, *35*, 710.
(62) Kurtz, S. K.; Perry, T. T. *J Appl Phys* **1968**, *39*, 3798.
(63) Rieckhof.Ke; Peticola.Wl *Science* **1965**, *147*, 610.
(64) Antipov, E.V.; Lykova, L.N.; Korba, L.M. Koordinatsionnaya Khimiya (Coordination Chemistry (USSR)) 1985, 11, 1151-1153
(65) Izumiyama, Y.; Doi, Y.; Wakeshima, M.; Hinatsu, Y.; Nakamura, A.; Ishii, Y. *J Solid State Chem* **2002**, *169*, 125.
(66) Wright, A. J.; Palmer, H. M.; Anderson, P. A.; Greaves, C. *J Mater Chem* **2001**, *11*, 1324.
(67) Akimoto, J.; Gotoh, Y.; Oosawa, Y. *J Solid State Chem* **1998**, *141*, 298.
(68) Takahashi, Y.; Gotoh, Y.; Akimoto, J. *J Solid State Chem* **2003**, *172*, 22.
(69) Jansen, M.; Hoppe, R. *Z Anorg Allg Chem* **1975**, *417*, 31.
(70) Sullivan, E.; Hadermann, J.; Greaves, C. *J Solid State Chem* **2011**, *184*, 649.
(71) Abakumov, A. M.; Shpanchenko, R. V.; Lebedev, O. I.; Van Tendeloo, G.; Amelinckx, S.; Antipov, E. V. *Acta Crystallogr A* **1999**, *55*, 828.
(72) Wang, C. H.; Guo, D. F.; Li, Z. F.; Wang, X. M.; Lin, J. H.; Zeng, Z. Z.; Jing, X. P. *J Solid State Chem* **2012**, *192*, 195.
(73) Shannon, R. D. *Acta Crystallogr A* **1976**, *32*, 751.
(74) de Muro, I. G.; Insausti, M.; Lezama, L.; Rojo, T. *J Solid State Chem* **2005**, *178*, 1712.
(75) Delattre, J. L.; Stacy, A. M.; Slegrist, T. *J Solid State Chem* **2004**, *177*, 928.
(76) Barry, T. L. *J Electrochem Soc* **1968**, *115*, 733.
(77) Ruter, I.; Mullerbuschbaum, H. *Z Anorg Allg Chem* **1989**, *573*, 89.
(78) International Tables for Crystallography, ISBN: 978-1-4020-4969-9, doi: 10.1107/97809553602060000001
(79) Fukunaga, M.; Noda, Y. *J Phys Soc Jpn* **2008**, *77*.
(80) Lin, Y. Q.; Chen, X. M.; Liu, X. Q. *Solid State Commun* **2009**, *149*, 784.
(81) Lunkenheimer, P.; Bobnar, V.; Pronin, A. V.; Ritus, A. I.; Volkov, A. A.; Loidl, A. *Phys Rev B* **2002**, *66*.
(82) Palmer, H. M.; Snedden, A.; Wright, A. J.; Greaves, C. *Chem Mater* **2006**, *18*, 1130.
(83) Takano, M.; Nakanishi, N.; Takeda, Y.; Naka, S.; Takada, T. *Mater Res Bull* **1977**, *12*, 923.
(84) Woodward, P. M.; Cox, D. E.; Moshopoulou, E.; Sleight, A. W.; Morimoto, S. *Phys Rev B* **2000**, *62*, 844.
(85) Carpenti.Cd; Nitsche, R. *Mater Res Bull* **1974**, *9*, 1097.
(86) Banerjee, S.; Malliakas, C. D.; Jang, J. I.; Ketterson, J. B.; Kanatzidis, M. G. *J Am Chem Soc* **2008**, *130*, 12270.
(87) Lobanov, M. V.; Abakumov, A. M.; Sidorova, A. V.; Rozova, M. G.; D'yachenko, O. G.; Antipov, E. V.; Hadermann, J.; Van Tendeloo, G. *Solid State Sci* **2002**, *4*, 19.
(88) Romero, F. D.; Bingham, P. A.; Forder, S. D.; Hayward, M. A. *Inorg Chem* **2013**, *52*, 3388.
(89) Brese, N. E.; Okeeffe, M. *Acta Crystallogr B* **1991**, *47*, 192.

(90) Case, G. S.; Hector, A. L.; Levason, W.; Needs, R. L.; Thomas, M. F.; Weller, M. T. *J Mater Chem* **1999**, *9*, 2821.
(91) Battle, P. D.; Gibb, T. C.; Nixon, S. *J Solid State Chem* **1988**, *77*, 124.
(92) Hudspeth, J. M.; Goossens, D. J.; Studer, A. J.; Withers, R. L.; Noren, L. *J Phys-Condens Mat* **2009**, *21*.
(93) Battle, P. D.; Gibb, T. C.; Lightfoot, P. *J Solid State Chem* **1990**, *84*, 237.
(94) Allix, M.; Battle, P. D.; Frampton, P. P. C.; Rosseinsky, M. J.; Ruiz-Bustos, R. *J Solid State Chem* **2006**, *179*, 775.
(95) Goossens, D. J.; Henderson, L. S. F.; Trevena, S.; Hudspeth, J. M.; Avdeev, M.; Hester, J. R. *J Solid State Chem* **2012**, *196*, 238.
(96) Abakumov, A. M.; Rozova, M. G.; Pavlyuk, B. P.; Lobanov, M. V.; Antipov, E. V. *J Solid State Chem* **2001**, *160*, 353.
(97) Wang, Y.; Sui, Y.; Ren, P.; Wang, L.; Wang, X. J.; Su, W. H.; Fan, H. J. *Inorg Chem* **2010**, *49*, 3216.
(98) Green, M. A.; Neumann, D. A. *Chem Mater* **2000**, *12*, 90.
(99) Goodenough, J. B.; Longo, J. M. Landolt-Börnstein Tabellen; Springer: Berlin, 1970
(100) Oka, K.; Azuma, M.; Chen, W. T.; Yusa, H.; Belik, A. A.; Takayama-Muromachi, E.; Mizumaki, M.; Ishimatsu, N.; Hiraoka, N.; Tsujimoto, M.; Tucker, M. G.; Attfield, J. P.; Shimakawa, Y. *J Am Chem Soc* **2010**, *132*, 9438.
(101) Sun, J. R.; Li, R. W.; Shen, B. G. *J Appl Phys* **2001**, *89*, 1331.
(102) Kobayashi, Y.; Mogi, T.; Asai, K. *J Phys Soc Jpn* **2006**, *75*.
(103) Goodenough, J. B. Magnetism and the Chemical Bond; Wiley: New York, 1963

Publication list

1. **Kun Luo**, Michael A. Hayward. Redox Responsive Co^{3+} Spin-state in $La_{2-x}Sr_xCoGaO_{5+\delta}$ Brownmillerite Phase. Dalton Transaction **doi:** 10.1039/C3DT52355A

2. **Kun Luo**, ThanhThao Tran, P. Shiv, Halasyamani, Michael A. Hayward. Synthesis and Selective Topochemical Fluorination of the Cation and Anion-vacancy Ordered Phases Ba_2YCoO_5 and $Ba_3YCo_2O_{7.5}$, Inorganic Chemistry. 2013, 52 (23), 13762–13769

3. **Kun Luo**, Roger Johnson, ThanhThao Tran, P. Shiv, Halasyamani, Paolo Radaelli, Michael A. Hayward. $Ba_2YFeO_{5.5}$: A Ferromagnetic Pyroelectric Phase Prepared by Topochemical Oxidation. Chemistry of Materials. 2013, 25, 1800-1808.

4. **Kun Luo**, Michael A. Hayward. The Synthesis and Characterisation of $LaCa_2Fe_2GaO_8$, Journal of Solid State Chemistry, 2013, 198, 203-209.

5. **Kun Luo**, Michael A. Hayward. Complex Cation order in anion-deficient $Ba_nYFe_{n-1}O_{2.5n}$ perovskite phases, Inorganic Chemistry. 2012, 51, 12281-12287.